



UNIVERSITY  
OF  
JOHANNESBURG

## COPYRIGHT AND CITATION CONSIDERATIONS FOR THIS THESIS/ DISSERTATION



- Attribution — You must give appropriate credit, provide a link to the license, and indicate if changes were made. You may do so in any reasonable manner, but not in any way that suggests the licensor endorses you or your use.
- NonCommercial — You may not use the material for commercial purposes.
- ShareAlike — If you remix, transform, or build upon the material, you must distribute your contributions under the same license as the original.

### How to cite this thesis

Surname, Initial(s). (2012). Title of the thesis or dissertation (Doctoral Thesis / Master's Dissertation). Johannesburg: University of Johannesburg. Available from: <http://hdl.handle.net/102000/0002> (Accessed: 22 August 2017).

# CHARACTERISATION OF CONCENTRATING SOLAR OPTICS BY LIGHT FIELD METHODS

DISSERTATION

submitted in partial fulfilment for the requirements for the degree

MASTER OF ENGINEERING

in

MECHANICAL ENGINEERING SCIENCE

in the

FACULTY OF ENGINEERING AND THE BUILT  
ENVIRONMENT

at the

UNIVERSITY OF JOHANNESBURG

Supervisor: **Prof. Andre Nel**

Co-Supervisor: **Dr. Philip Robinson**

Document Date: **September 2019**

## ABSTRACT

This dissertation develops ideas and techniques for the measurement of the light field produced by the concentrating optics that are used in solar thermal power systems. The research focussed on developing a framework and the principles for the implementation of a scalable technology that is suitable, in principle, for cost effective industrial implementation in the field. Investigation from first principles and technological surveys resulted in formulation of a number of model techniques, from which one was developed.

A key component of the proposed model was evaluated using a novel reformulation and application of electrical impedance tomography (EIT). This was to implement an information transform effecting a highly non-linear compressive sensing mechanism, offsetting manufacturing and material complexity in the measurement of high solar flux levels. The technique allows sensing of a wide range of phenomena over arbitrary manifolds in three-dimensional space by utilizing passive transducers.

An inverse reconstruction method particular to the structure of the device was proposed, implemented, and tested in a full simulation of intended operation. The parameter space of internal configurations of the method were the subject of a uniform, statistical search, with results also indicating geometrical properties of the transform used. A variety of design guides were developed to better optimize the implementation of the techniques in a range of applications.



## Acknowledgements

I thank my supervisor, Prof. Andre Nel, for the material opportunity to engage in this project, patience with what must have appeared to be very fragmented progress, and much direction and support.

I thank my co-supervisor, Dr. Philip Robinson, for his equal patience, much advice and time spent in guidance. I was exposed to many important technical areas in the lab that you and Dr. Yuko Roodt head.

## Dedication

*I have tested all this by wisdom. I resolved, "I will be wise," but it was beyond me.*

*What exists is beyond reach and very deep. Who can discover it?*

*I turned my thoughts to know, explore, and seek wisdom and an explanation for things,  
and to know that wickedness is stupidity and folly is madness.*

*- Ecclesiastes 7:23-25*

I must thank my parents for their wholehearted support during this project, Andrew and Marion, as well as my most significant other, Heather, who bore my detachment with patience, support, kindness and encouragement.

UNIVERSITY  
OF  
JOHANNESBURG



# Table of Contents

1	Introduction.....	6
2	Hypothesis and Research Methodology.....	7
2.1	Problem Definition.....	7
2.2	Research Methodology.....	7
2.3	Research Objectives.....	9
2.4	Research Process.....	9
2.5	Overview of the Dissertation.....	10
2.5.1	Literature Study.....	10
2.5.2	Design.....	10
2.5.3	Experimental Design.....	10
2.5.4	Results and Conclusion.....	10
2.6	Contributions.....	11
2.7	Chapter Summary.....	11
3	Literature Study.....	12
3.1	Introduction.....	12
3.2	Why Solar Thermal Power.....	13
3.3	Solar Thermal Power Generation Systems.....	14
3.3.1	General Solar Power Issues.....	14
3.3.2	System Layouts.....	15
3.3.3	Types of Receiver.....	18
3.3.4	Types of Convective Shield.....	19
3.3.5	Types of Mirror.....	19
3.3.6	Concentration.....	20
3.3.7	Exergy Analysis at the Collector.....	22
3.3.8	Prime movers used in the conversion of heat to mechanical power.....	25
3.3.9	Optical Losses in Solar Concentration.....	29
3.3.10	Governing Relationships Determining System Capacity and Efficiency.....	29
3.3.11	Design and Optimization Methods.....	35
3.4	Principles of Optics.....	36
3.4.1	The ray model.....	36
3.4.2	The wave model and diffraction.....	36
3.5	Solar Flux Measurement and Metrology.....	37
3.5.1	Measurement of Radiative Flux.....	40
3.5.2	Components of Irradiation.....	41
3.5.3	Measurement of the spectrum.....	42
3.6	Representation of Optical Fields.....	43
3.6.1	Computer Vision.....	43
3.6.2	Image-Based Rendering.....	43
3.7	Camera Models.....	47

3.7.1	The arthropod eye model.....	49
3.7.2	The pinhole aperture model.....	49
3.8	Metrology of General Surfaces.....	50
3.8.1	Principles of surface metrology.....	51
3.8.2	Interferometry.....	51
3.8.3	Structured Light Methods.....	51
3.8.4	Laser Scanning Methods.....	52
3.8.5	Other Methods.....	52
3.9	Holography.....	53
3.9.1	General principles.....	53
3.9.2	Reconstruction.....	53
3.9.3	Practicalities of Implementing Holographic System.....	53
3.9.4	Applicability to the current problem.....	53
3.10	A Holographic Theory of Measurement.....	54
3.11	Chapter Summary.....	54
4	Design.....	56
4.1	Measurement Technique Design Requirements.....	56
4.1.1	Cost-effective.....	56
4.1.2	Operable in production environments.....	56
4.1.3	Mouldable into a generic closed surface.....	57
4.1.4	Directly applicable.....	57
4.1.5	Technically comparable.....	57
4.1.6	Theoretically complete.....	58
4.2	The Sensing Problem.....	58
4.2.1	The Measurement of Phenomena.....	58
4.2.2	Material Sensor Characteristics.....	59
4.3	Development of a Measurement Solution.....	61
4.3.1	Selected Measurement Concept.....	61
4.3.2	Description of Light Field Capture Concept Design.....	65
4.3.3	Temperature Compensation.....	65
4.3.4	Considerations for the Concept Design.....	65
4.3.5	Manufacturability of the Sensor Surface.....	66
4.4	Mathematical Considerations for the Sensor Array.....	68
4.4.1	Introduction.....	68
4.4.2	Device Layout.....	68
4.4.3	Introducing the concept of tomographical boundary scan.....	72
4.4.4	Proof for ensuring distinct measurements under constant voltage excitation.....	73
4.4.5	Proof for ensuring distinct measurements under constant current excitation.....	75
4.4.6	A lemma in practical illustration of uniqueness.....	75
4.4.7	Derivation of the number of distinct measurements given a boundary in naive sampling .....	76

4.4.8	Information available for reconstructions.....	78
4.4.9	Representation of field state.....	79
4.4.10	Comments on the combinatorial nature of distinct measurements with respect to electrical properties.....	80
4.5	Initial Investigations into Design Parameters.....	81
4.5.1	Voltage and current excitation.....	81
4.5.2	Connection for the measurements.....	82
4.5.3	Design considerations for system configurations.....	82
4.5.4	Design considerations for sampler hardware.....	86
4.5.5	Template system design procedure.....	89
4.5.6	Discussion of boundary scan in comparison to multiplexing and further conclusions.....	90
4.6	Optimization of the Tomographical Boundary Scan idea.....	91
4.6.1	Connectivity requirement for measurability.....	91
4.6.2	Minimal connectivity topology.....	91
4.6.3	Boundary Inversion to Produce Continuous Fields.....	93
4.6.4	Topological Properties of a Continuous Field with Regards Foveal Node Positioning.....	97
4.6.5	Element Value Distribution.....	98
4.7	The Literature on EIT.....	100
4.7.1	The applicability of previous work on EIT to the current problem.....	102
4.7.2	Classification of applications in previous work with regard to EIT.....	104
4.7.3	The current problem in light of EIT.....	104
4.8	Sensor-Layer Manufacturing Methods.....	105
4.9	The Forward Transform.....	106
4.9.1	The Conductivity-state view.....	106
4.9.2	Connectivity-state view.....	107
4.9.3	Simulation of the forward transform.....	108
4.10	The Inverse Transform Recovery.....	110
4.10.1	Introduction.....	110
4.10.2	Inverse by global optimization.....	111
4.10.3	The traditional approach of EIT – Backpropagation.....	112
4.10.4	Inverse by piecewise linearisation.....	113
4.10.5	Inverse by global constant-current field interpolation.....	116
4.11	Chapter Summary.....	127
5	Experimental Design.....	130
5.1	Experimental procedure.....	130
5.2	Test Sample Space.....	131
5.3	Objective Functions Used in Evaluation.....	132
5.4	Chapter Summary.....	133
6	Experimental Results and Discussion.....	134
6.1	Parameter-Space Slice and Aggregation Analysis.....	134
6.1.1	Discussion for Figure 48 – The total number of F-nodes.....	137

6.1.2	Discussion for Figure 49 – The Total Number of Outer Loop Iterations.....	138
6.1.3	Discussion for Figure 50 – The Number of Sub-Models Used.....	138
6.1.4	Discussion for Figure 51 – The Number of Iterations within Each Sub-Model.....	140
6.1.5	Discussion for Figure 52 – The Method of Measurement State Selection.....	140
6.1.6	Discussion for Figure 53 – The Radius of Gaussian Blur Used within Sub-Model Filtering .....	142
6.1.7	Discussion for Figure 54 – The Median Filter as a Function of Morphological Radius.....	142
6.1.8	Discussion for Figure 55– The Method of Aggregation of the Sub-Model Results.....	143
6.1.9	Discussion for Figure 56 – The Effect of Oversampling Factor.....	143
6.1.10	Discussion for Figure 57 – The Electrical Path Distance Between H and F-Nodes.....	146
6.1.11	Discussion for Figure 58 – The Multiplier of the Field Width X-Axis.....	146
6.1.12	Discussion for Figure 59 – Field Width Multiplier in the Y-Axis.....	147
6.1.13	Discussion for Figure 60 – The Effect of Total F-Nodes.....	148
6.1.14	Discussion for Figure 61 – the number of measurement states used.....	149
6.2	Principal Component Analysis Results.....	151
6.2.1	Discussion for Plots of PCA Vectors and Distributions.....	152
6.3	Chapter Summary.....	156
7	Conclusion.....	157
7.1	A Brief Review of the Investigation Process.....	157
7.2	Results of the Tests.....	159
7.3	Final Remarks and Main Contributions.....	160
7.4	Chapter Summary.....	160
8	Appendices.....	161
8.1	Concepts for Measurement.....	161
8.1.1	Zeroth Generation “Scanning” .....	161
8.1.2	First Generation Scanning.....	161
8.1.3	Second Generation Scanning (Line Scanners).....	162
8.1.4	Third Generation Scanning (Imaging Sensors).....	163
8.2	Sample time consideration design.....	165
8.3	Sensor-Layer Manufacture Methods.....	166
8.3.1	Discrete Component Implementation.....	166
8.3.2	Printed-Paste Method.....	169
8.3.3	Inkjet Printing + Gas Developer Method.....	170
8.3.4	Conductive Film Continuous-Element Fields.....	171
8.4	Electrical Layout.....	172
8.4.1	The Foveal Node Sensing Cell.....	173
8.4.2	Management of electrical noise.....	174
8.4.3	Sources of Measurement Error.....	174
8.5	Calibration and characterisation.....	175
8.5.1	Overview of assumptions in base model.....	175
8.5.2	Identifying sources of deviation from the model.....	178

8.5.3 Calibration Routines.....	179
8.5.4 Device failure modes.....	180
8.6 Boundary Connectivity.....	181
8.6.1 Path Length Sensitivity Profiles.....	182
8.7 Proposed Methods of Reconstruction.....	188
8.7.1 Inverse by linearity of response.....	188
8.8 The Linear Pinhole Model.....	189
Bibliography.....	192



## List of Figures

Figure 1: Design science research method as proposed by Baskerville et al.....	7	Figure 18: Simple topological representation of a synthetic construction of an arthropod eye. .	49
Figure 2: Design science research steps and their outputs.....	8	Figure 19: Solar Light Field Capture Assembly Drawing.....	63
Figure 3: Main components of a flat-plate collector.....	16	Figure 20: Light Field Capture Concept, alternate view.....	64
Figure 4: The geometrical layout and effect of compound parabolic collectors.....	17	Figure 21: General sensor system layout.....	71
Figure 5: Basic structure of a concentrating parabolic collector.....	17	Figure 22: Example of sensing elements in a single layer field at the boundaries.....	72
Figure 6: Basics of Fresnel lensing.....	18	Figure 23: Circuit equivalent of voltages applied in tomographical boundary scan.....	73
Figure 7: Picture of an experimental concentrating central receiver-tower.....	18	Figure 24: The connection situation for one measurement state.....	73
Figure 8: Visualization of the geometric concentration ratio.....	20	Figure 25: Superposition sub-circuits for one measurement state.....	74
Figure 9: Exergy balance at the solar collector. .	22	Figure 26: A measurement state with two sources and one sink.....	74
Figure 10: Non-dimensional exergetic and energetic efficiencies against normalized receiver temperature.....	24	Figure 27: Subsystems as a result of a double source excitation.....	74
Figure 11: Normalized exergy balance from test data for a CPC on Kyushu Island, Japan, 19 March 1990.....	25	Figure 28: Number of measurements for a flexibly-driven field of symmetric elements.....	79
Figure 12: Maximal work efficiency as a function of receiver operating temperature.....	31	Figure 29: Multiplexing optimization to reduce design footprint.....	82
Figure 13: Aggregate Temperature Receiver Heat-Transfer Model.....	33	Figure 30: Minimum resolution system sizing curves.....	83
Figure 14: Visualized Airy disc.....	37	Figure 31: System supply and demand curves, plots holding the total number of nodes constant.....	84
Figure 15: Solar irradiance spectral content prior to the atmosphere.....	38	Figure 32: Plot showing the geometric properties of defined measures.....	85
Figure 16: Terrestrial spectral absorption due to multiple factors.....	39	Figure 33: Graphs of information resolution relative to multiplexing complexity.....	87
Figure 17: Visualization of four of the eight camera models in the General Linear Camera.	48	Figure 34: Cost relationships for a given	

information resolution, plotted in series for total number of nodes for cost structure for (Line : Multiplexer Cell : Active Driver).....	88	Figure 45: Bias images that form errors in reconstruction for a given prior.....	118
Figure 35: Minimal topology tiling.....	92	Figure 46: Iterative reconstruction using voltage-interpolated fields.....	122
Figure 36: Three types of continuous boundary connectivity.....	94	Figure 47: Alternative visualization of reconstruction process.....	123
Figure 37: Effect of boundary continuity.....	95	Figure 64: Sample time as a function of information resolution for system configurations.....	165
Figure 38: Field of minimal connectivity, 3-space connectivity.....	99	Figure 65: Sense cell for one Foveal Node.....	173
Figure 39: Printed photoresistive form examples .....	106	Figure 66: Types of continuous boundary connectivity.....	182
Figure 40: Parsing an image into an EITMSA graph.....	108	Figure 67: Virtual image principle demonstrating first order sensitivity analysis.....	183
Figure 41: Map representation of example system matrix structure.....	110	Figure 68: Manhattan connectivity path sensitivity analysis for F-node pattern A.....	185
Figure 42: Reconstruction by optimization routine.....	111	Figure 69: Bridged-Manhattan connectivity layout for F-node pattern A.....	186
Figure 43: Voltage fields due to a conductivity change.....	117	Figure 70: Euclidean connectivity sensitivity analysis for F-node pattern A.....	187
Figure 44: Gradient of voltage field of measured states.....	117		

## List of Experiment Results

Figure 48: Performance plot for parameter "Total Nodes".....	135	Figure 54: Performance for variations in median filter radius within inner sub-models.....	141
Figure 49: Performance for various numbers of chained iterations of the main algorithm.....	136	Figure 55: Performance for method of aggregation of the results of the sub-models in the outer loop.....	143
Figure 50: Performance for variations on the number of sub-models in the inner loop.....	136	Figure 56: Scatterplot of medians for classes of parameter for the number of states used as a ratio to total information required, with fitted lines up to the first order to show mean and trend.....	144
Figure 51: Performance for the number of iterations within the inner sub-models.....	139	Figure 57: Performance for variations in the mean of the minimum path length between any H-node and the nearest F-node.....	145
Figure 52: Performance for variations in method of measurement state selection.....	139		
Figure 53: Performance for variations in magnitude of Gaussian blurring within inner sub-models.....	141		

Figure 58: Performance for scaling of the field size in the X axis during reconstruction.....	Figure 61: Box-and-whisker plot for the effect of measurement data quantity.....
145	150
Figure 59: Performance effects for scaling field shape in the Y axis during reconstruction.....	Figure 62.1: PCA Components for objective function - "Combined Performance Accuracy".....
147	152
Figure 60: Box-and-whisker plot for the effect of the number of F-nodes used.....	Figure 63 PCA Components for objective function - "Mean-Squared Accuracy".....
148	154





# List of Symbols

This catalogues the symbols used in formulas.

Sym bol	Unit	Description	Sym- bol	Unit	Description
<b>Standardized Constants</b>			<b>Thermal State Properties</b>		
$\sigma$	$\frac{W}{m^2 K^4}$	Stephan-Boltzmann constant = 5.67e-08	$T_r$	$K$	Temperature of the receiver.
<b>Measures of Energy Flow</b>			$T_a$	$K$	Average ambient environment temperature.
$\dot{Q}_u$	$J/s$	The usable energy collected at the receiver.	$T_{in}$	$K$	Fluid temperature entering the collector.
$\dot{Q}_r$	$J/s$	Instantaneous energy gained by the receiver.	$T_{out}$	$K$	Fluid temperature exiting the collector.
$\dot{Q}_{conv}$	$J/s$	Heat transfer to the environment by convective means.	$T_s$	$K$	Temperature of the sun surface.
$\dot{Q}_{rad}$	$J/s$	Heat transfer to the environment by radiative means.	$T_p$	$K$	Average temperature of the receiver surface.
<b>Radiative Flux</b>			$T_{r,o}$	$K$	Outer temperature of the receiver.
$\Phi_T$	$W/m^2$	Solar flux incident on the tilted collector.	$T_{r,i}$	$K$	The inner temperature of the receiver.
$\Phi_r$	$W/m^2$	Solar energy flux at a point on the receiver.	<b>Geometrical Properties</b>		
$\Phi_a$	$W/m^2$	Solar energy flux over the aperture of the collector.	$A_r$	$m^2$	Area of the receiver.
<b>Optical Properties</b>			$A_a$	$m^2$	Collector aperture area, the frontal opening of the collector.
$\tau$	1	Coefficient of transmissivity.	$C$	1	The aggregate concentration ratio.
$\alpha$	1	Coefficient of absorptivity.	$\theta_{accept}$	$rad$	Acceptance angle for radiation entering the collector.
$(\tau\alpha)_{eff}$	1	Eff. optical fraction absorbed.	<b>Heat Transfer Coefficients</b>		
$\epsilon_{eff}$	1	Effective emissivity of the collector.	$h$	$\frac{W}{m^2 K}$	Convection heat transfer coefficient.
$C_L$	1	A constant defined by the emissivity of the receiver coating.	$k$	$\frac{W}{m K}$	Heat transfer coefficient of conduction.
<b>Fluid Properties</b>			$U$	1	Overall heat loss coefficient.
$\dot{m}$	$kg/s$	Mass flow for heat transfer fluid.	$F_R$	1	The "Effectiveness Removal Factor", for relating actual and reference heat exchanger performance.
$\rho$	$kg/m^3$	The fluid density.	$C_p$	$J/kg K$	Constant pressure specific heat.
$P_{in}$	$N/m^2$	The pressure of the inlet.			



# 1 Introduction

Renewable energy sources are an inevitable consideration for our generation. There are a myriad of technologies that are considered, with solar electricity generation presenting a flexible and available form of energy that can be produced in areas of earth that would otherwise have little to no perceived value. This necessitates the development of techniques and technologies that lower the material cost of construction of solar energy conversion, while maintaining or increasing the energy yield and consistency.

The most effective technology for deployment at scale is that of solar thermal power generation, when assessed from a materials-availability perspective. Concentration solar thermal is suitable for partial or total supply of industrial heat, which can offset a large amount of electrical capacity used for that purpose. Large scale deployment has the lowest material cost per unit energy, and the greatest usable life expectancy (considering maintenance), in comparison with other forms of solar to electricity energy conversion. In comparison to photovoltaic technologies, solar thermal has a distinct theoretical advantage over the losses of an intermediate form of energy transmission.

The low-grade availability of solar energy on the earth's surface makes some form of concentration a pre-requisite for material-efficient deployment of related system. Building on previous observations, this study seeks to develop a new method for the refinement of devices that concentrate solar energy, specifically for but not limited to thermal applications.



## 2 Hypothesis and Research Methodology

The problem is defined, along with the most applicable research methodology, with both being introduced to frame the approach taken.

### 2.1 Problem Definition

The design of concentrating solar collecting systems requires information about the real characteristics of the concentrating system, it is the methods and apparatus used to acquire this information that is the chosen basis of the design problem. To enable the characterization of a wide range of types and scales of concentrating solar system, a method is needed that will enable characterization with accuracy suitable to inform the design problem of the solar collecting system. This design should strive to operate in as close to field conditions as is possible, where as-yet unaccounted-for effects may occur. Simultaneously it should remain relatively low cost, while in concept being able to service a wide range of applications.

The problem is augmented by a knowledge heuristic; that there is a suitable amount of information available in the characteristic of the light made available by the concentrating optics. This heuristic is a justified requirement if large solar systems are to be serviced, since a large number of known techniques are unsuitable to be applied to full scale solar systems.

### 2.2 Research Methodology

Research was conducted according to the design science research methodology, which is a relatively modern (1969) methodology that seeks to mediate between the process of science and the application of scientific knowledge in a technical sense [1]. A general mode of design science thought is given in Figure 1 [1].

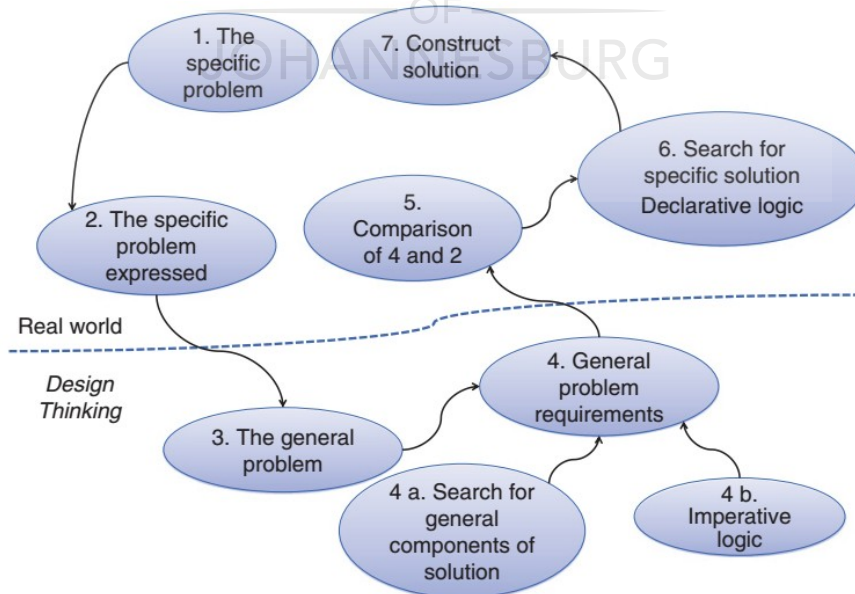


Figure 1: Design science research method as proposed by Baskerville et al.

Design science (DS) seeks to apply consistent, repeatable investigation in the development of techniques and rules that can be applied in a technical application of a development process [1]. The product object of DS is an artefact, either physical or abstract, that has characteristics

determined by deductive, inductive or hypothesis-inductive investigations into the problem that the artefact seeks to solve [1]. The artefact may vary from a tool in physical form, to a body of rules that are optimized for the design of other artefacts.

The design science method uses iterative processes as are used in engineering design, however the difference is a focus on greater rigour in the design decisions made. This process is shown in Figure 2 [1], along with the outputs of each step.

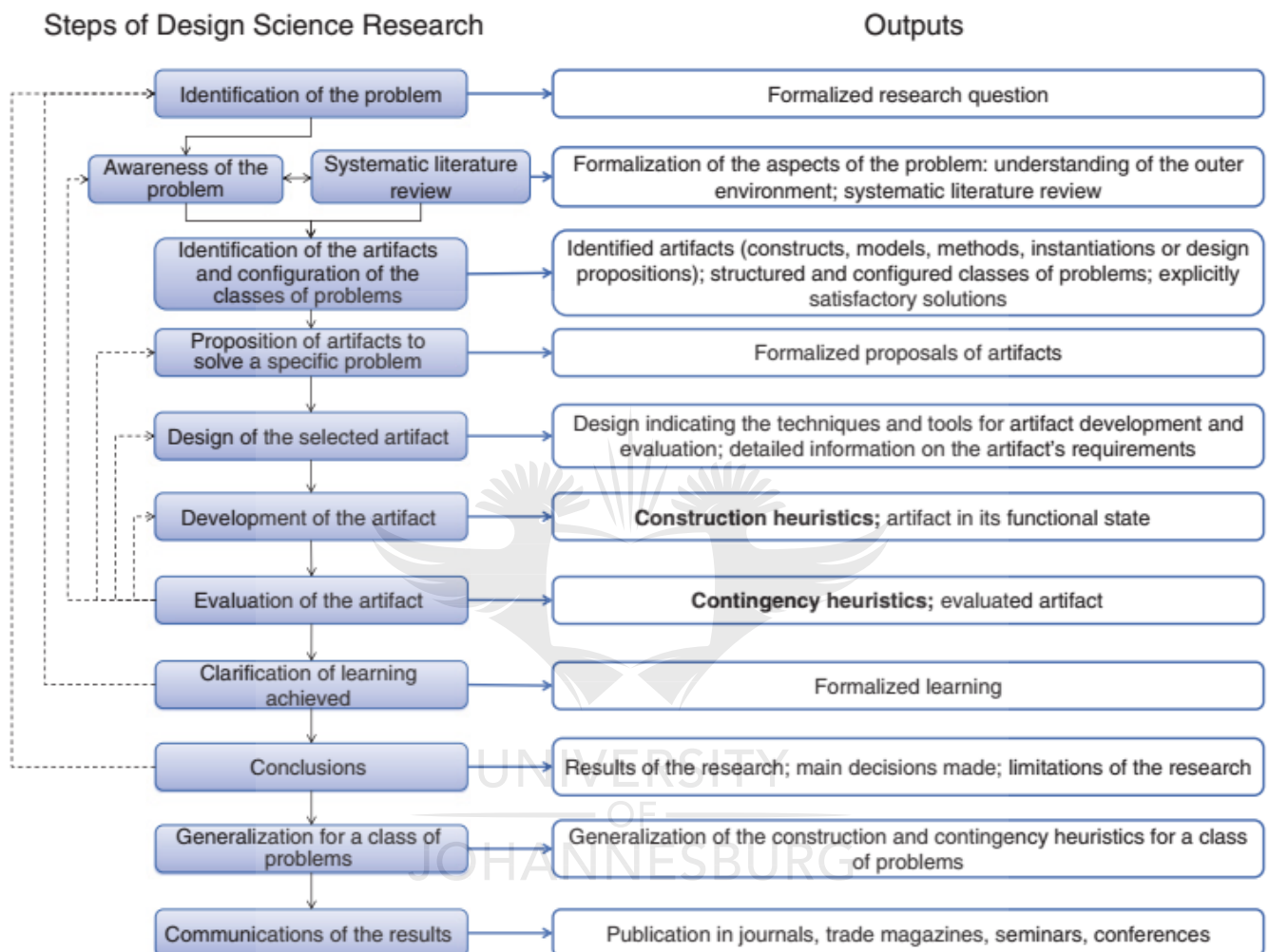


Figure 2: Design science research steps and their outputs

The deductive method was used in concept development, while later developments were based on the inductive-deductive method, specifically with regard to the problem solution [2]. The style was chosen in light of previous experience that indicated that previous methods to solve the problem were inextensible. As a result, such methods were investigated in so far as forming a good base for comparison rather than providing a base of further effort.

The design was quantitatively evaluated in part using performance metrics with reference to theoretical limitations, rather than in terms of improvements on existing solutions. Learning obtained from the evaluation process was in the form of general characterizations that are of direct use in further design processes. This method suitable for development of a flexible base of new technology, which invariably will have poorer initial performance but greater promise of performance in future iterations.

## 2.3 Research Objectives

The overall research objectives, being target solutions, were as follows:

1. Determination of the range and scope of the techniques used in the measurement of solar thermal systems and general solar properties. These steps are in order to evaluate the opportunities for new developments in improvements and descriptive functionality, based on an understanding of the overall operating principles in operation.
2. Determination of the analytical tools used in the solar thermal design process, in order to cater techniques developed to the form of these tools.
3. Development of a generalized model for optical measurement of solar collecting optics, suitable for the reasoning and development of a family of optical measurement devices that are able to inform the solar thermal design process with pertinent information.
4. Development of a particular measurement technique for the optical measurement of solar collecting optics, based on easily implementable and inexpensive, accessible technology. This technique is ideally to provide a different complement of characteristics to existing technologies, and thus be suitable to areas of weakness that current technologies present.

## 2.4 Research Process

Research progressed according to the following structure:

- 1) An initial study on existing technologies dealing with the problem space and areas similar to the problem space. In each of the previous technologies of (to be explained later) VSHOT, LANSIR, Flow Calorimetry, Speckle Metrology, Laser Surface Metrology, Structured Light Surface Metrology, Scanning Interferometry, and Moire Metrology; the aims of this phase were to:
  - 1.1) Determine the fundamental operating principles in order to generate a database of possible routes of attack on the base problem.
  - 1.2) Identify the assumptions in the methodology and implementation, and their epistemological impact.
  - 1.3) Identify the previous challenges in the physical implementation and mathematical characteristics of the measurement solution.
  - 1.4) Compare the solutions to the particular problems against one another and build a reference standard for the design.
- 2) An initial study on the manufacturing techniques used to produce the sensors and structures used in problems that have application domains somewhat similar to the core problem. This was to understand the relationship between desired physical characteristics and realizability.
- 3) Formulation of the problem from first principles, by applying the abstract models of the phenomena being measured, formulating the effects in general terms for the entire problem space.

- 4) Formulation of an ideal model for the measurement of the desired phenomena, to form the reference to the judge the quality of design candidates against one another without the burden of the compromises made in previous instruments.
- 5) Creation of a range of design candidates, with a major focus on the application of differing methodologies or physical relationships. Followed by a selection process according to a design value specification, considering in order of preference: The dimensionality of the information, expected final accuracy, research extensibility of the method, application to other problem domains and economic extensibility in deployment.
- 6) Creation of a model simulation of the methodology chosen to implement the prototype implementation chosen.
- 7) Analysis of the results in the light of the ideal model instrument and prior instrumentation as studied in earlier phases of the project.

## **2.5 Overview of the Dissertation**

A high level view of the dissertation is as follows:

### **2.5.1 Literature Study**

The importance of solar thermal power and is introduced. This continues with an investigation of existing solar thermal power systems, and the background of fundamental physical optical phenomena and models for such phenomena. These investigations are complemented by investigations into measurement of solar radiation and tied together to generalize the measurement problem.

### **2.5.2 Design**

Requirements are laid out for design procedure and the sensing problem is evaluated. Concepts based on this evaluation are described based on these principles. The sensing problem is then reduced to a fundamental mathematical problem in order to reduce complexity in the physical domain. This technique is investigated and methods of reconstruction are proposed, one of which is developed for investigation. This technique is chosen as the topic of investigation since it is a limiting factor in overall system performance, and of key importance to the design form of instruments presented.

### **2.5.3 Experimental Design**

The reconstruction method is investigated by simulation: where measurements are generated from an ideal sensing device, the effects of electrical noise and quantization are applied and the reconstruction method applied with varying parameters. Latin hypercube sampling is used to investigate the parameter space, and the aggregate effects of the important parameters visualized. The sampling scheme is adjusted to account for the combination of both discrete and continuous dimensions in the parameter space, and dimensionality reduction applied in further analysis.

### **2.5.4 Results and Conclusion**

The distinctions proposed with regard to the mathematical method are analysed given the test results, in order to develop design heuristics. The characteristics of the reconstruction method and



the test method are discussed with regard to design decisions, in order to inform design and further applications. Directions for further development are proposed and commentary given on the ultimate usefulness of the technique in the intended physical device framework that has been proposed.

## **2.6 Contributions**

The dissertation brings a number of contributions at the time of the research:

1. A framework for thought with regard the use of light field methods in the characterization and design of concentrating solar thermal collectors. These are justified according to the well-established principles used in existing collector design, and according to thermodynamic principles with clear use potential in the experimental research currently underway with regard to volumetric and multiphase systems.
2. The introduction of a novel form of concrete measurement device, based on the abstract principles in the framework. This device is suitable for the light field measurement in concentrating solar parabolic tube receivers, and was developed to be practically achievable using relatively inexpensive production techniques.
3. Application of linear programming models to the problem of measurement system design, for the purposes of determining practical design heuristics that assist in reducing the parameter space and improving economic viability of the technique.
4. Introduction of a number of novel image sensor design forms for investigation with regard to the problem space that are economically minded. These open possibilities for direct electrical sensing of related properties at low resolution over a large-space manifold at reduced cost.
5. Development and characterization of a novel reconstruction algorithm to achieve suitable results for the particular application of Electrical Impedance Tomography developed as part of the manifold sensing topology called for by the light field characterization framework.

## **2.7 Chapter Summary**

The problem has been defined along with the research methodology and a high-level plan as to the structure and goals for the research. In summary; the research seeks to improve the tools and methodologies currently used in the design of solar thermal collectors. To this end, development of modelling and apparatus suited to the kinds of analysis required by the design process are the principal targets of the research. This requires extensive survey of the models, tools and apparatus used in the current design process. In order to be of greater relevance, research is also targeted toward the development of an informational model as to the information required and the means of acquisition of such information given the constraints on the problem domain. The chapter motivates the purpose of the research and outlines the methodology used, being “design science”, as well as the steps the research took to fulfil the spirit of this relatively new research methodology.



### 3 Literature Study

An extensive literature study was performed as part of a broad search into the overall problem space, due to the interlinked concerns of different layers of the problem.

#### 3.1 Introduction

The design of solar energy systems of any nature has as a primary aim; to address the parameters of a subsystem to increase the quality of the available exergy prior to conversion of this energy into more usable form [3], [4], [5], [6], [7]. This concentrating subsystem is typically ignored by mobile systems that cannot afford the added mass, but is a requirement for any fixed installation that is expected to be material-cost effective.

The capture of solar energy is not as straightforward as it may seem at first [8]. The systems that are available at present are attempting to be generalized solutions to a problem that is inherently quite complex [9], [10], [11], [12]. In terms of systems engineering, the use of modular components and defined interfaces has been the primary mode of reducing complexity. This has come at a cost of decreased total efficiency of energy production, where a specific solution often has the potential to do much better. These complexities are evident in applications of integration [13]. An example of such an approach is the conversion of solar radiation into electricity that will be eventually be used in a primarily thermal application, with intermediate losses that are unnecessary [14]. Process heat can be supplemented by solar thermal heat [15], chemical reactions can be utilized directly using suitable catalysts [16], [17], [18], or by interaction with biological agents [19], [20], and moisture can be driven off from adsorbents [21], [22]. In addition, thermal energy storage needs no unique materials [23], and is thus suitable for many economic environments.

The designer has a relative lack of tools for the initial specification, evaluation and monitoring of solar concentrating systems. Current methods of system implementation are covered by a few expensive or sub-optimal methods that are focussed on a subset of solar thermal systems, and remain unable to provide continuous information in the field [4].

In addition to enabling the development of more specific solutions, better tools would facilitate the analysis (and improvement) of current solutions under real conditions and the development of foreseeable solutions with greater active control. The latter is a sufficient justification in-of itself, since active control would mitigate many of the challenges with systems using problematic multi-phase heat transfer fluids, or allow tighter, cheaper closed-loop control of large central receiver tower mirror arrays. Examples of research into general issues in solar control include [24], [25] and importantly [26]. This would help alleviate some of the reliability issues present in current deployments due to non-uniform solar flux concentrations [27].

The current tools that are available can be briefly summarized into a providing a few categories of information:

1. Scalar measurements of the output of the solar power production system, measured in overall output. This information is unsuitable and theoretically unavailable for some envisioned solar system developments. It remains of limited use in optimizing a system in

design or operation. These examples use a calorimetric approach to solar thermal system evaluation [4]: ASHRAE 93 (2003), ISO 9806-1 (1994), and EN12975-2 (2001).

2. Statistical measurements of the characteristics of concentrating subsystems, in terms of images projected by the optics under ideal test conditions. These cannot be made in-field and cannot be used in a dynamic control situation. The example of this is LANSIR, as used by the National Renewable Energy Laboratory [28]. Another sampling mechanism for use in volumetric concentrating systems is a solar-blind system that provides a directional point sample in [29].
3. Measurements of the physical characteristics of the concentrating and other subsystems, with the application of Monte-Carlo light and surface models in order to predict the performance of the system as a whole. These measurements can be done non-interactively in the field, but the current methods scale in proportion to the size of system being measured. As solar thermal energy systems scale up with increasing energy cost, this will result in measurement technologies of a size that are absurd in practical terms. The Video Scanning Hartmann Optical Test (VSHOT) is a primary example [28].

These sensing methodologies are not suitable for various classes and scales of possible solar energy capture system. In view of these factors further investigation was targeted toward the development of a measurement solution that is complementary to and extends beyond the current tools, by using an optical sensing methodology that utilizes the radiation present during normal operation.

### **3.2 Why Solar Thermal Power**

Solar thermal power is less well known than photovoltaics, both in research activity and in the technical implementation community (from the material available). The total amount of concentrating solar power in deployment is however dominated by solar thermal technologies [30]. The reasons for this have not been studied well, however by familiarity with the literature and techniques in general it is possible to propose a number of factors:

1. There are lower barriers to research for many aspects of photovoltaics, especially for prototype development.
2. Photovoltaic systems have a lower initial cost and thus lower barriers to entry, especially for small installations that are intended to be expanded [31].
3. The technical requirements for the specification and installation of a photovoltaic power producing system are lower than a solar thermal system. This makes it attractive for introductory solar research in applications [32], [33].
4. Solar thermal technologies require a greater intensity and frequency of maintenance by skilled technicians, making them unsuitable for small installations. These effects are primarily a consequence of fluid containment requirements, mechanical wear and thermal fatigue.

5. Solar thermal systems require fluids, moving parts and multiple systems to be matched correctly. Whereas photovoltaic components are most often static and can handle a wider degree of design variation.

These economic factors however discount the fundamental benefits of a solar thermal solution, as opposed some physical realities [34]:

1. Photovoltaic panels have issues in recycling due to the chemical nature of the panels and the use of rare earth metals therein. Solar thermal plants can however be broken down and fully recycled with relative ease.
2. Photovoltaic panels require rare earth metals that are not widely distributed with regard to the political economy of nation states, this makes dependence a strategic issue due to the promotion of trade imbalances. This problem is magnified since the primary solar resource is also not equally distributed.

It is for these reasons that it is likely that concentrating solar thermal power generation will be the most useful in the long run.

### **3.3 Solar Thermal Power Generation Systems**

This section will introduce a number of solar power generation systems, since these dominate the research into the use of solar energy and are the most widespread current and future applications of concentrating solar power besides domestic heat<sup>1</sup>. A system to measure the performance of such systems must be mindful of their general form, their installation particulars and the scaling effects with increased size.

The formulas and modelling techniques covered are for demonstrating the informational requirements at each level. A robust development tool should provide greater certainty in measurement and feedback of actual performance to the designer in a flexible way, independent to, but complementary of, a particular design methodology.

#### **3.3.1 General Solar Power Issues**

The energy present in solar radiation is abundant but subject to great variation in a number of aspects. The direction from which it originates varies on a continual basis, the magnitude will vary rapidly with local weather conditions and global factors [35], [36]. The system may be contaminated on a continual basis with particulates, condensation or other residue [37], [38]. Wind loading will affect the shape of mirrors and the direction of active control systems. Material components of the system will age relatively rapidly with exposure to radiation and daily-continual thermal cycles [39].

It is important that these real effects on the concentrating phenomenon be measured, and the variation in originating effects on the radiation accounted for. This compensation is in order to normalize an ideal measurement to practical power output in real world situations, thereby allowing for less of a safety-factor in system design.

---

<sup>1</sup> This exception of domestic heat from the subject and analysis will persist throughout the document.

### *The scale in relation to efficiency and efficacy*

There are a number of factors that affect the performance of solar thermal systems, turbomachinery and in general any system that functions as a heat engine attached to an electrical generator:

1. Fluid friction due to the interaction of viscosity and fluid velocity.
2. Heat loss to the environment, a property proportional to the surface area of the exposed to the environment by a combination of conductive, convective and radiative means.
3. Temperature loss due to thermal resistance in heat transfer surfaces.
4. Magnetic containment due to tolerance and structural limitations in construction.
5. Magnetic hysteresis losses due to materials and cycle rates.

The net effect is that almost universally; a larger thermal system has lower losses, lower maintenance and thus has higher potential and actual efficiency. These are the primary factors in operational expenditure (OPEX). In commercial implementation the construction cost scales with increasing capacity, the source of capital expenditure (CAPEX). The interaction of OPEX, CAPEX and return on investment favours larger systems when the general cost of energy increases. It is expected that as general energy costs increase with the exhaustion of fossil fuel sources, the need for tools to handle larger systems will similarly increase.

### **3.3.2 System Layouts**

Solar thermal concentrating systems are laid out in configurations that are highly dependent on the structure of the concentrating mirror system. This dependency is due to a number of factors that cannot be avoided [34]:

1. A concentrating system, in order to be effective, needs to intercept a large area of directional sunlight. This presents structural problems where the stability of a lensing or mirror system needs to be maintained at a low material cost.
2. A tracking system, that is required to swivel the mirror or lens system in order to keep the directed radiation to within a determined "acceptance angle" that depends on the design of the lensing system. A given design has a higher performance in concentrating ability if the acceptance angle is allowed to be smaller. Movement is required to track the sun, and may be effected by actuation of the whole lensing sub-assembly, sections of the lensing system or moving the energy capture mechanism to track the point of concentration presented by a fixed mirror system.
3. An energy transport mechanism that moves acquired energy to the prime mover responsible for the conversion into useful form, or that removes waste heat from a local energy transducer in order to maintain its' required heat difference.
4. A supporting framework and placement of solar concentrating units into a field that may be very large. The parameters of the units and their spacing come as dependent parameters of the concentrating lensing used.

In commercial use at present there are a number of primary forms, used depending on the (perceived) use criterion:

1. Flat-plate collectors and static vacuum-tube collectors of various forms, a non-concentrating or low-concentrating solar thermal energy capture that is limited by heat transfer considerations to low temperature. Figure 3 [4] demonstrates a classic example of flat-plate designs. Design of such systems is limited by the large acceptance angle that is a requirement for static operation. This limits the concentration that can be provided by internal structured reflective surfaces, or structured lensing surfaces on the inward-facing side of the outer cover. The more recent advances in concentrating ability have come from treating the mirror or lensing system as a non-imaging design. The understanding being that what is to be optimized is not the point-focus capability but rather the effect on the absorbing surface in general. This has resulted in static concentrating designs based on multiple concentrating surfaces: the compound parabolic collector, the principle of which is illustrated in Figure 4 [4].

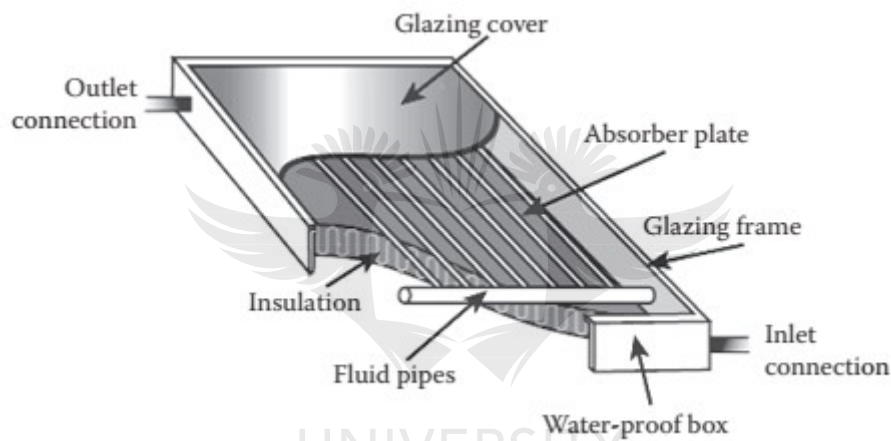


Figure 3: Main components of a flat-plate collector.

The central characteristic in the class is the lack of active control possible, and as such tunable performance parameters are limited to design and installation time.

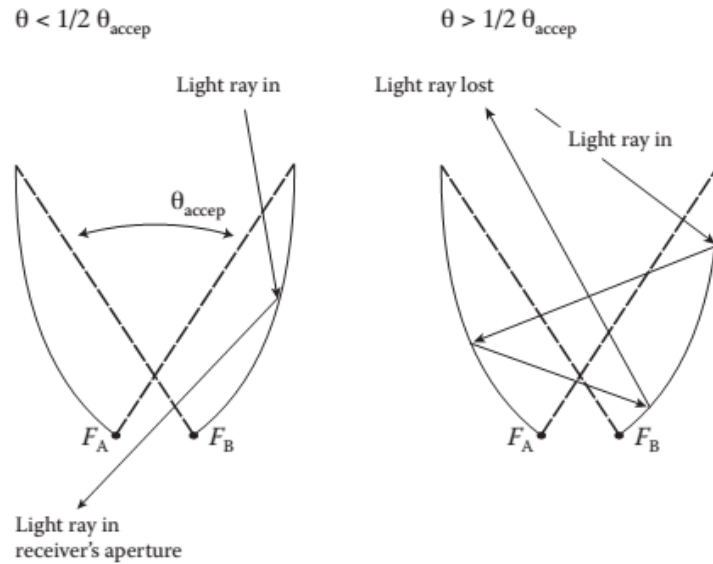


Figure 4: The geometrical layout and effect of compound parabolic collectors.

2. Concentrating parabolic collectors (CPCs), that are a modular approach with regard to overall solar power plant design. A parabolic or compound-parabolic reflecting mirror directs radiation onto a glass-tube encased conducting tube. The system is actuated to follow the sun based on direct sun-sensors or by coordinate control. Examples of such systems are given in [40], [41], [8], [42]. In Figure 5 [4] a basic example of the construction and principles of operation is shown.

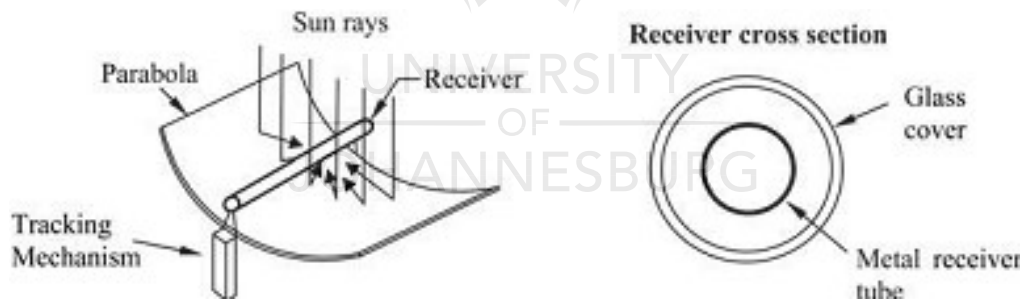


Figure 5: Basic structure of a concentrating parabolic collector.

3. Fresnel lens concentrators, where a transparent lens is placed between the sun and the absorbing surface to concentrate the incoming radiation using refraction. These systems are limited in scale due to structural limitations in the presence of gravitational forces on the lens itself. The use of lensing materials is an important design trade-off, since polymers that would permit larger lenses are subject to lower operational lifespans due to weathering effects. A tracking system is required, and the performance is highly dependent on the manufacture of the lens facets [4]. The principle of operation is illustrated in Figure 6 [4].



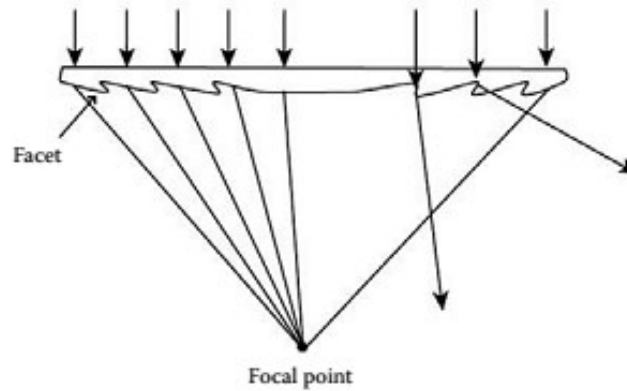


Figure 6: Basics of Fresnel lensing.

4. Central receiver-tower systems (Heliostats), where a large number of actuated concentrating solar mirror paraboloids direct radiation toward an elevated absorber system. The system as a whole acts as a very large adaptive concentrating lens that has the greatest theoretical concentrating performance. In practice a large number of factors combine to reduce performance by orders of magnitude below theoretical limits, primarily as a result of accuracy in design, deployment and control. Examples of small implementations include that described in [43]. In Figure 7 [249], a functional prototype operating from these principles is shown below.

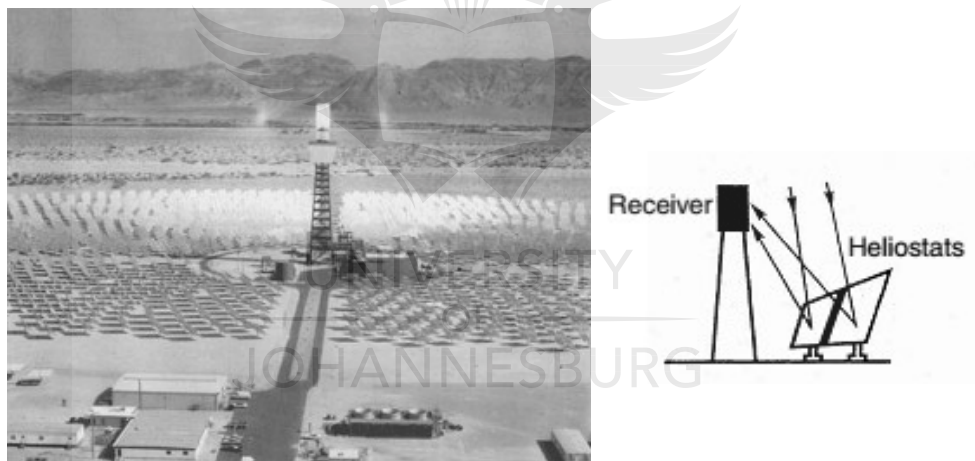


Figure 7: Picture of an experimental concentrating central receiver-tower.

These systems represent a range of design approaches to the general problem of capturing useful amounts of energy at different grades from solar irradiation, as a natural clustering of mechanisms that have been investigated up to the present day. This list is not complete, there are a few other non-conventional technologies that do not use a lensing concentrating system [7], [44], [45].

### 3.3.3 Types of Receiver

The receiver is the subsystem that absorbs solar energy in the form of multiple light spectra, primarily in the visible range, and captures this radiation in the form of heat on the absorbing surface. A coating that has a high emissivity in the visible wavelengths and low emissivity in the infra-red wavelengths is applied to a highly thermally conductive substrate. The substrate allows heat transfer to the transfer fluid and provides mechanical stability to the coating and resists pressures that result from the heated fluid.

The fluid can be single or multiphase, the latter has been a subject of greater difficulty and presents significant problems. The performance of the receiver has conflicting requirements:

1. In order to deliver high-quality energy (high exergy) fluid to the prime mover, a high concentration ratio is required for high temperature of the outlet fluid.
2. In order to achieve a high temperature in a typical fluid, a pressure must be applied by suitable containment. This requires a structural skin, which presents either a thermal resistance or an optical attenuation depending on the design.

Broadly there are a number of receiver implementations:

1. Fluid-filled pipe, including finned designs. The selective coating is located on the outside of the pipe and fluid is cycled through the internal volume.
2. Solid conductive or heat pipe, where heat is transferred by conductive or phase-change means to a header that is in contact with the transfer fluid.
3. Volumetric air receivers, where a high-emissivity surface is heated through an optically transparent window and a contained gaseous heat-transfer fluid is passed over the surface.

### 3.3.4 Types of Convective Shield

Convective shields are required to reduce the losses due to primary modes of heat transfer [46], [47]: Conduction through a static air mass, movement of a normally static air mass against gravity, and movement of a dynamic air mass due to local atmospheric conditions.

The convective shield is required to surround the receiver surface, this presents a problem with regard to [14]: The material of the shield, sealing the interface between the shield and receiver, pressure containment by the shield, and chemical interactions of the filling gas.

There are a number of basic designs used in practice, based the economical formability of transparent glasses and plastics [4], [47]: Containment boxes that are used in flat plate collectors, multi-receiver tubes, and the most common design of the single-receiver tubes.

### 3.3.5 Types of Mirror

The best case mirror is often taken as a 3D paraboloid, on the assumption that solar irradiation is a point source at near infinite distance, resulting in parallel rays. This assumption is not accurate, since the size of the sun is significant at the Earth's surface, and as a result must be modelled in any calculations requiring accuracy. *The effect of this non-point source is often mistakenly understood as diffraction*, especially with regards to shadows formed on surfaces. However, when considering incoherent light sources, diffraction effects only dominate with regard to the small-scale of the edge quality of the surface casting the shadow.

The best case performance for a real (non-point) sun is given by a compound parabolic mirror in 3D rotation, however construction of such mirrors is difficult in practice due to varying curvature. There are a number of lensing systems that are simplifications based on various principles, with varying trade-offs and extensions that enable differing options to the designer [14], [46]:

1. Fresnel mirrors, where a compound concentrating mirror is created by stacking horizontally an array of near-linear mirror surfaces such that each surface redirects incoming radiation



onto the target. The degree of concentration increases with decreasing size of the individual surfaces. These are of a few main types: Static segments without independent movement, used in small low-cost systems. Adaptive segments with a common control mechanism, sometimes used in medium scale systems. Independent adaptive segments with independent control mechanisms, used in large scale systems such as central receiver towers [48].

2. Linear parabolic mirrors, formed in one continuous piece these are easier to manufacture than compound parabolic types and are effective when the focal length is not short relative to the mirror rim angle. A high quality parabolic mirror developed for commercial purposes has used a pressure difference maintained across a thin metal skin to form the paraboloid, this however did not prove an economic advantage [34].
3. Spherical mirrors, formed by dish spinning, or bending sheet with stiff formers. These are the simplest to manufacture and model, however rim angles must be kept small and focal lengths relatively long, which hinders performance [49].

### 3.3.6 Concentration

The principles of solar concentration are covered by [48], [4] [23], [46].

The geometrical concentration ratio is defined by:

$$C = A_a / A_r \quad (1)$$

The geometric concentration ratio is visualized below:

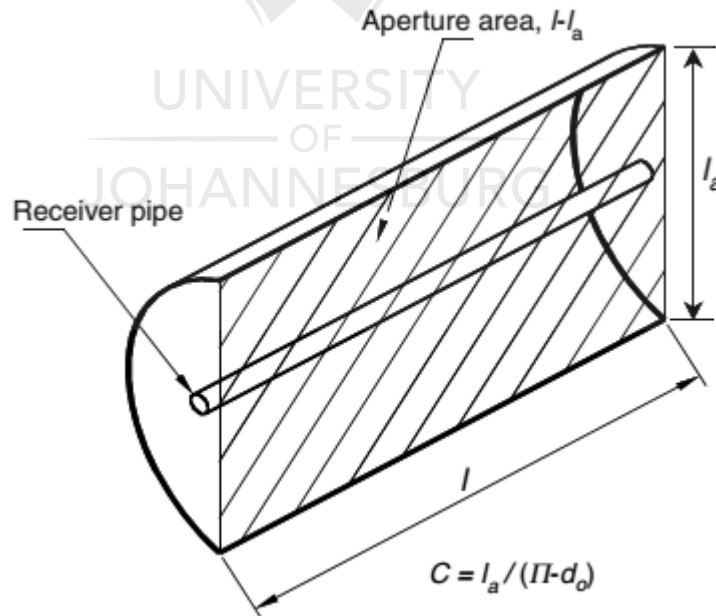


Figure 8: Visualization of the geometric concentration ratio

The flux concentration ratio is defined by:

$$C = \Phi_r / \Phi_c \quad (2)$$

This can be applied on the local and the macro level. The geometrical and macro flux concentrations are equivalent if there is no loss in the concentrating optics. The macro effective

concentration ratio can also be found by surface integration of the solar irradiance over the receiver, where irradiance is the spatial derivative of the flux:

$$C = \frac{\Phi_r}{\Phi_c} = \frac{\iint E_r}{\Phi_c} \text{ where } E = \frac{\partial \Phi}{\partial A} \quad (3)$$

This irradiance is defined as the energy density in the radiation, and can be further regarded as the energy density per unit wavelength, known as spectral irradiance. By integration over the wavelength and spatial domain this becomes:

$$C = \frac{\int \frac{\partial E}{\partial \lambda}}{\Phi_c} = \frac{\iint \int \frac{\partial \Phi}{\partial A d\lambda} \cdot d\lambda}{\Phi_c} \quad (4)$$

### *Theoretical Limits of Concentrating Optics*

The best performance of a two-dimensional ideal concentrating mirror profile, in geometrical terms is given by:

$$C_{g, \max} = \frac{n}{\sin(\theta_{\text{accept}}/2)} \quad (5)$$

where  $n$  in this context is the refractive index of the material that solar irradiance last encountered, and  $\theta_{\text{accept}}$  is the acceptance angle of collecting system. The three-dimensional case is described by:

$$C_{g, 3D \text{ ideal}} = \frac{n^2}{\sin^2(\theta_{\text{accept}}/2)} \quad (6)$$

Geometrical properties of the collector in relation to the sun, both of which are finite in size and interact with each other radiatively, result in a maximum theoretical concentration ratio and temperature profile. The two-dimensional case as is found in parabolic troughs is limited to:

$$C_{\max, 2D} = \frac{n}{\sin(\epsilon/2)}, \text{ typically } C_{\max, 2D} = 216 \text{ in air.} \quad (7)$$

where  $\epsilon$  is the angular size of the sun's disc as seen by the collector, the minimum acceptance angle possible. The three-dimensional case as is found in central receiver towers is given by:

$$C_{\max, 3D} = \frac{n^2}{\sin^2(\epsilon/2)}, \text{ typically } C_{\max, 3D} \approx 46000 \text{ in air.} \quad (8)$$

These are theoretical upper limits for a perfectly implemented system. Theoretical maximum saturation temperatures occur in radiative equilibrium, when there is no heat removal by the heat transfer system or by non-radiative losses. Maximum concentration can only occur at the minimum acceptance angle, and only when the sun is tracked perfectly such that there is no deviation between the centre of the acceptance angle and the sun centre. Saturation temperatures can be found by:

$$T_r = T_s \left\{ \frac{(1-\eta)\eta_0 C}{\epsilon_{\text{eff}} C_{\text{ideal}, 3D}} \right\}, \text{ giving, } T_{r, 3D} \approx 5800 \text{ } ^\circ\text{C} \quad (9)$$

where in this context is the sun temperature at approximately  $5800^{\circ}\text{C}$ . The efficiency  $\eta$  is the fraction of energy used by the collector in conversion to heat accounting for losses, and  $\eta_o$  is the optical efficiency resulting from reflectance, transmittance and absorbance.

The relationships indicate that it is possible to enhance the concentrating ability by using a material other than air in the interface between collector and receiver, up to the point that special reflective surfaces can be eliminated entirely with internal reflection. Such materials are not usually a cost-effective option in relation to better designed and larger mirror systems, though smaller systems have been experimented on using materials which have a high refractive index.

### 3.3.7 Exergy Analysis at the Collector

Exergy is a state property of the system that describes the energy that is available to do work between two thermal states in an ideal heat engine such as a Carnot engine. The transfer of radiation occurs between two thermal sinks, and is modified by the concentrating properties of the lensing system.

The maximum efficiency in terms of the work that can be extracted from a given quantity of heat moving between two thermal reservoirs [3]. This efficiency is applied to a heat flow, resulting in an exergy flow that is converted to work [3]:

$$\dot{E} = \dot{Q} \left( 1 - \frac{T_{\text{cold}}}{T_{\text{hot}}} \right) \quad (10)$$

Using the elementary definitions of exergy besides these it is possible to analyse the receiver and fluid as a black-box. Taking a control volume around the collector an exergy flow relationship results when considering the inputs and outputs and annihilation, shown in Figure 9 [3]:

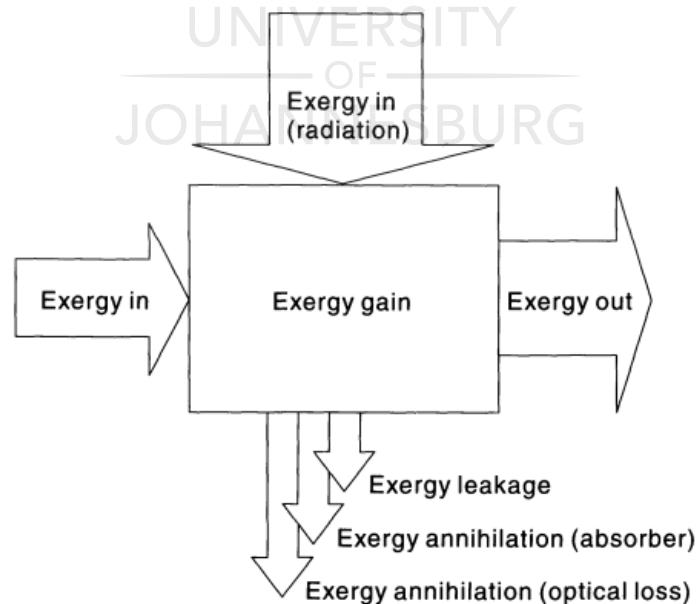


Figure 9: Exergy balance at the solar collector.

This is expressed as:

$$\dot{E}_o + \dot{E}_{i,f} + \dot{E}_{i,r} + \dot{E}_l + \dot{E}_{a,p} + \dot{E}_{a,r} + \dot{E}_{a,c} + \dot{E}_s = 0 \quad (11)$$

where flows are positive-in by convention. Terms that include density apply to static pressure in the working fluid, the effects of which may be non-negligible in the case of gasses. These flows are given in the relationships below, given that  $P_{in} > P_{out}$  :

Equation	Exergy Flow	No.
$\dot{E}_o = -C_p \dot{m} (T_{out} - T_a (1 - \ln(\frac{T_{out}}{T_a}))) + \frac{1}{A_r} \cdot (\frac{1}{2} \frac{(A_r \dot{m})^3}{(\rho A_a)^2} + \frac{\dot{m} \Delta P_{out}}{\rho})$	Exergy carried by the mass transport out of the collector.	(12)
$\dot{E}_{i,r} = (\tau \alpha) \Phi_T (1 - \frac{T_a}{T_s})$	Flow into the system by solar irradiation.	(13)
$\dot{E}_{i,f} = C_p \dot{m} (T_{out} - T_a (1 + \ln(\frac{T_{out}}{T_a}))) + \frac{1}{A_r} \cdot (\frac{1}{2} \frac{(A_r \dot{m})^3}{(\rho A_a)^2} + \frac{\dot{m} \Delta P_{in}}{\rho})$	Flow into the system by fluid transfer.	(14)
$\dot{E}_l = -C_L (T_p - T_a) (1 - \frac{T_a}{T_p})$	Radiative leakage to the environment from the receiver.	(15)
$\dot{E}_{a,p} = -(\frac{\dot{m}}{\rho A_r}) \Delta P T_a \ln(\frac{T_{out}/T_{in}}{T_{out} - T_{in}})$	The loss due to pressure drop.	(16)
$\dot{E}_{a,r} = (\tau \alpha) \Phi_T T_a (\frac{1}{T_p} - \frac{1}{T_s})$	The major loss due to the difference between the sun temperature and the receiver temperature.	(17)
$\dot{E}_{a,c} = -C_p \dot{m} T_a (\ln(\frac{T_{r,o}}{T_{r,i}}) - \frac{T_{r,o} - T_{r,i}}{T_p})$	Loss due to the conductive thermal resistance from the receiver inner and outer surfaces.	(18)
$\dot{E}_c = -C_{receiver} m_{receiver} (1 - \frac{T_a}{T_p}) \frac{dT_p}{dt}$	Exergy storage due to thermal changes in the receiver material.	(19)

Accumulating all these components, collecting terms and re-arranging gives a fundamental relationship in terms of exergy [3]:

$$\begin{aligned}
& (C_p \dot{m} (T_{out} - T_{in}) - \frac{\dot{m}}{\rho A_r} \Delta P) (1 - \frac{T_a \ln(T_{out}/T_{in})}{T_{out} - T_{in}}) + C_{receiver} m_{receiver} (1 - \frac{T_a}{T_p}) \frac{dT_p}{dt} \\
& = \Phi_T (1 - \frac{T_a}{T_s}) - \Phi_T (1 - (\tau \alpha)) (1 - \frac{T_a}{T_s}) + \Phi_T (\tau \alpha) T_a (\frac{1}{T_p} - \frac{1}{T_s}) \\
& \quad + C_L (T_p - T_a) (1 - \frac{T_a}{T_p}) + C_p \dot{m} T_a (\ln(\frac{T_{r,o}}{T_{r,i}}) - \frac{T_{r,o} - T_{r,i}}{T_p})
\end{aligned} \tag{20}$$

The dimensionless exergetic efficiency is the ratio between the collector output exergy and the solar input exergy [3]:

$$\varepsilon = \frac{\dot{E}_{out}}{\dot{E}_{in}} \tag{21}$$

When previous results are substituted into it this becomes [3]:

$$\begin{aligned}
\varepsilon = & \frac{C_p \dot{m} (T_{out} - T_{in} - T_a \ln(T_{out}/T_{in}))}{\Phi_T (1 - T_a/T_s)} = 1 - (1 - (\tau \alpha)) + (\tau \alpha) \frac{1/T_p - 1/T_s}{1/T_a - 1/T_s} \\
& + \frac{C_L (T_p - T_a)}{\Phi_T} \frac{1 - T_a/T_p}{1 - T_a/T_s} + \frac{C_p \dot{m} T_a}{\Phi_T (1 - T_a/T_s)} (\ln(\frac{T_{r,o}}{T_{r,i}}) - \frac{T_{r,o} - T_{r,i}}{T_p})
\end{aligned} \tag{22}$$

The term  $C_L$  here includes the effect of the concentration provided by the lensing or mirrors of the collector. A simplification of the energetic efficiency, for an assumed linearity in the temperature rise in the fluid, is defined as:

$$\eta = \frac{c_p \dot{m} (T_{out} - T_{in})}{\Phi_T} = F_p (\tau \alpha) - F_p U_L \frac{(T_p - T_a)}{\Phi_T} \quad (23)$$

where  $F_p$  is a simplification for short collectors of the efficiency factor for heat exchangers: the ratio of the heat transfer resistance from the fluid to ambient air, to the heat transfer resistance from the absorber to the ambient air.

The results of the exergetic analysis around the collector are similar to that of the energetic analysis that purely accounts for energy flows. Plotting the non-dimensional efficiency above, gives Figure 10 [3], where  $G_T = \Phi_T$ . The lower axis is in units of temperature above ambient per total radiative intake of the collector [3]:

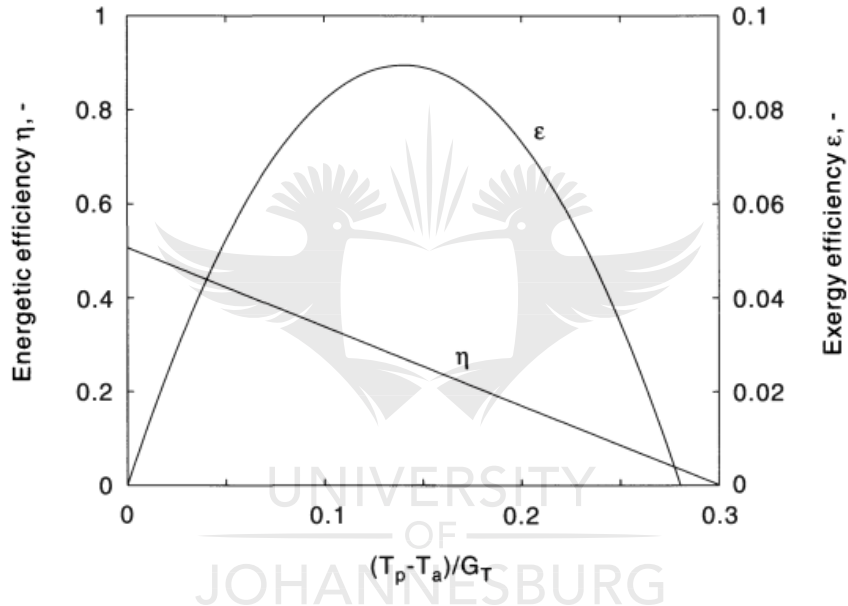


Figure 10: Non-dimensional exergetic and energetic efficiencies against normalized receiver temperature.

The exergetic analysis here considers the effects of exergy loss due to wall temperature gradients. The real effects on an evacuated tube type concentrating parabolic collector are shown in fitted test results in Figure 11 [3] below, normalized for clarity:

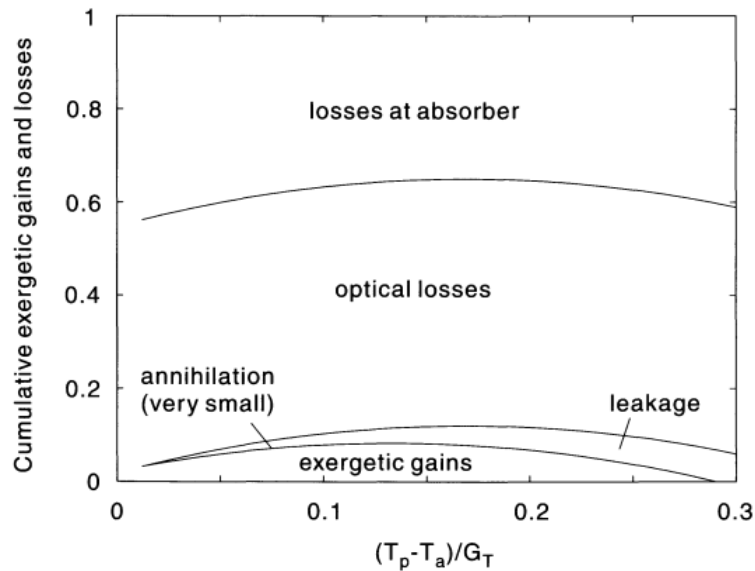


Figure 11: Normalized exergy balance from test data for a CPC on Kyushu Island, Japan, 19 March 1990.

This demonstrates the added information provided by assessing the exergy at part of the solar system, as such an exergy analysis is a powerful tool often used in optimizing solar collector design.

*It is clear that in order to maintain optimal exergetic efficiency, the outlet temperature must be adjusted according to the total irradiance on the receiver.* This motivates accounting for the variation in received irradiation, due to likely effects of sun shading and dynamic optical distortions induced by wind and active components.

*The analysis here can benefit from further granularity in modelling the local heat distributions on the receiver surface, and most importantly the local flux distributions on the receiver surface.* The relationships described can be applied to independent regions of receiver as long as the thermal interactions between regions are low, effecting a thin-wall assumption as has been previously described. This can be motivated due to non-linear effects of multiphase operation; some regions have a limiting liquid temperature at phase change, while sidewall regions exposed to the gaseous phase will experience a greater temperature. *An exergy analysis itself is inherently non-linear, which makes bulk aggregation an inaccurate process, the more so the greater the temperature variation.* Any improvement in the application of exergy analysis would require a finer accounting of local temperatures in a FEM-like process, especially when considering systems with fluid-related non-linearities. *This section thus shows the analytical value supporting the design premise, and the intended use for a greater resolution of information regarding solar flux.*

### 3.3.8 Prime movers used in the conversion of heat to mechanical power

The prime mover is the heat engine used between the high temperature source as provided by the concentrating solar system and the sink of environmental temperatures. These may be closed or open cycle, and may utilise the solar system as their only source of energy or use a bouquet of energy sources of which the solar system is supplemental.

This section is included in review in order to gain appreciation of the accuracy that is required for various systems in the predictive capability of a measurement scheme “in the loop” of a control

system that seeks to regulate toward greatest energy output. A control scheme would have at its disposal the ability to manipulate what dynamic mirror surfaces there are present, regulate the mass flow of circulating pumps and the pressure drop over actuated valves. *Such control would normally be informed by temperature sensors at the inlet and outlet of sections of the solar thermal infrastructure, however this information is a lagging indicator of flux conditions at the receiver surface, which are the actual energy input into the system.* The effect of lag in a feedback variable is to introduce poles into the compensated system response, this creates instability and has a tendency toward oscillatory behaviour that requires the designer to lower proportional feedback gain. This results in systems that are slower to respond, or that overshoot by significant margins if gain is not reduced.

It is expected that control informed by the actual flux on the receiver would enable differing control schemes that would not suffer the unbounded transients present in control based on inherently laggy indicators. *This would also enable specification of overcapacity in concentrating ability of collecting mirrors in order to compensate for local atmospheric scattering effects, thus maintaining operating temperatures.* Without adequate control, an overcapacity in concentration would damage receiver materials and coatings, either by temperature gradients or flux intensity itself.

Adaptive control of the distribution of flux on the receiver can only be done by accurately informed predictive models, or by use of reactive models informed by finding the actual flux concentration on the receiver surface. Predictive models rely on a system model or model estimate that is sufficiently accurate, this however is often a challenge in terms of data available and computational resources required for simulative models.

### *Rankine Cycle and its' Derivatives*

The Rankine cycle is the basic prime mover technology responsible for most of the world's prime mover technology, including prime movers used in solar thermal systems. The cycle is characterised by the following process [14], [50], [51]: An Isentropic compression (1-2), Isobaric heat addition (2-3), Isentropic expansion (3-4), and Isobaric heat removal (4-1). A large source of loss in a real non-ideal Rankine cycle is the exergy associated with a drop in temperature in the walls of the heat exchanger.

Efficiency of the cycle can be improved by among other methods, increasing the average temperature of the isobaric heating process [50]. This in turn raises the pressure after the pump and the heat exchanger wall thickness required. Greater wall thickness leads to an increased loss of exergy in heat transfer, and is limited by temperature and pressure associated metallurgical creep. The cycle efficiency depends heavily on temperature, which can be regulated against a varying energy input by control of the feed pump rate. This however may increase pump inefficiency due to operation out of optimal pump rotational speed. In solar thermal applications the use of series stages makes the system better able to efficiently manage varying hot-side temperatures. Thermal storage systems can be used to provide buffers to variations in energy input, and provide limited operation after sundown.

Since thermal storage can be effectively used and multi-stage systems implemented, the sensitivity of the cycle to short-term thermal variations is low, and the control timing requirements less



stringent. In conclusion it is possible to determine the required sample rate for solar flux measurement, depending on the relative capacity of the collection area:

1. If there is overcapacity, the time constant for measurement must be less than the time constant for temperature rise in the outer shell of the receiver, given a step increase in solar irradiation<sup>2</sup>.
2. If there is no overcapacity, it must be less than the time constant for temperature rise in the working fluid.

### *Brayton Cycle*

The Brayton cycle may be of the open or closed type, where the open type is the most common. It is philosophically composed of processes using air as a transfer medium [52], [53]: An Isentropic compression process. (1-2), an Isobaric heat addition (2-3), an Isentropic expansion process (3-4), and an Isobaric cooling process (4-1). The efficiency of the ideal cycle can be derived in simple form by assuming constant specific heats [52]:

$$\eta = 1 - \frac{(T_4 - T_1)}{(T_3 - T_2)} = 1 - (r_p)^{(k-1)/k} \quad (24)$$

Where the pressure ratio is defined as:

$$r_p = \frac{p_2}{p_1} \quad (25)$$

This reveals the sensitivity of the cycle to load variations on compression as a result of turbine rotational speed. This also creates positive feedback for any reduction in heat addition, since the lower energy provided to the turbine results in further efficiency losses due to lower compression. An attempt to control the load-sensitivity is evident in the split-shaft design, where the Brayton cycle is implemented in two stages:

1. The compression pair, where a compression turbine is powered by an expansion turbine.
2. The work pair, where an expansion turbine powers the load with the remaining power.

The cycle efficiency is improved by increasing the turbine inlet temperature (3), using reheating, intercooling and regeneration. Temperature is a key factor due to metallurgical limits in a high stress situation, with over-temperature a cause of catastrophic failure if left unchecked.

The cycle must be open if a fuel is combusted, and energy can be supplemented into the system by solar thermal systems in a central receiver tower configuration using a volumetric collector. The initial heat source is provided by concentrated solar irradiation, with supplemental heating by fuel in order to achieve desired turbine inlet temperature. This also allows backup operation with fossil fuels when the sun is obscured by weather.

In the case of a grid-independent system, control is required to manage excess capacity to prevent over-temperature at the turbine inlet. Since solar irradiation is highly variable in the presence of cloud cover, the regulation of power output can be managed by:

---

<sup>2</sup> The use of "time constant" will implicitly refer to the temperature rise as a consequence of a step increase in solar irradiation, for the remaining commentary on prime movers.



1. Consistent operation of the solar field below the required power output, with supplemental fuel providing regulation against the load.
2. Consistent underutilization of the solar field capacity, with regulation provided by a combination of adaptive concentrating optics, supplementary fuel and variations in the air bypassing the burner.

*The second option requires information about the effects of concentration and the real solar flux on the receiver, since atmospheric conditions vary the effective sun-shape.*

The conclusion for purposes of control in systems where heating is provided by solar means only;

1. Without overcapacity present, the measurement sample separation time must be less than the time constant for fluid temperature rise.
2. In the more stringent case of overcapacity, this limiting time constant is that of temperature rise in the receiver material.

### *Stirling Cycle*

The Stirling cycle is used in small parabolic concentrating solar power plants, since given sufficient development it can be made relatively maintenance-free and efficient. The Stirling Cycle is a closed ideal cycle, often using external combustion, with the following layout [54]: Isothermal compression, effected by compression while under thermal contact with a heat reservoir (1-2). Constant-volume addition of heat (2-3). Isothermal expansion, effected by expansion while under thermal contact with a heat reservoir (3-4). Constant-volume removal of heat (4-1).

Being a closed-cycle heat engine, supplemental energy from fossil fuels can only be provided with a heat exchanger. This however comes at the cost of increased inactive gas volume, which significantly lowers the cycle efficiency. This implies that regulation against a varying load can only effectively come from varying the energy input provided by the hot thermal reservoir. There is possibility to use thermal storage at the hot reservoir if transfer fluid is valved between supply and storage, in a separate loop to the main cycle, which can account for short variations in energy input.

Stirling engines have been used in various sizes to provide work from various scales of concentrated solar irradiation. In this application and others the materials of construction are the primary concern, with cracking a common problem in heat transfer surfaces at the irradiated surfaces. This problem is exacerbated by irregular concentration of flux with respect to a cyclic removal of heat, this could be better managed by control of the flux distribution with respect to variations in real sun-shape due to local atmospheric conditions. In addition to this, since most loads are coupled directly to the prime mover, a partial load situation requires dynamic control of total flux on the receiver to prevent overheating and overspeed.

The conclusion is that the measurement sample interval must be less than the time constant of the temperature rise in the external receiver material, which can be estimated to be on the order of a second or less in small systems with low pressures.

### 3.3.9 Optical Losses in Solar Concentration

Concentration is primarily done by reflective means, either external reflection by specular surfaces or internal reflection in transmission media. The process of concentration has a number of loss factors that are the result of material and manufacture processes [47]:

1. Reflectivity of the surface, which is less than 1 and typically is around 0.93 for clean silvered glass mirrors. This parameter is primarily a function of wavelength and is affected by dusting, which is a major factor in areas of high solar irradiance.
2. Intercept factor, which is the portion of direct solar radiation incident on the receiver. This factor is less than unity due to microscopic imperfections in the reflecting surface and in the macroscopic shape of the mirror. A properly assembled and calibrated system has an intercept factor at 0.95.
3. Transmissivity, which is the factor of flux that is not absorbed by the transparent cover of the receiver. This factor is primarily a material property of wavelength, and is usually about 0.93 for sunlight passing through glasses used in solar systems.
4. Absorptivity of the coating on the receiver, which is the fraction of radiation absorbed as a property of wavelength. This factor is subject to change over the life of a receiver tube due to “greying” effects of high flux concentrations. It is primarily a function of wavelength and is typically 0.95 for a cermet coating.

The optical efficiency of a concentrator and receiver system is the product of all the loss factors, since solar flux encounters each in series:

$$\eta_{\text{optical}} = \rho(\lambda) \cdot \tau(\lambda) \cdot \alpha(\lambda) \cdot \gamma \quad (26)$$

### 3.3.10 Governing Relationships Determining System Capacity and Efficiency

An energy balance at the absorbing surface gives the heat input accounting for losses, over the convective, conductive heat transfer and emissivity. The instantaneous energy gained by the receiver at the absorber surface is given by [4], [46]:

$$\dot{Q}_r = \dot{q}_r A_c = \eta_{\text{optical}} \Phi_T A_c \quad (27)$$

where  $\Phi_T$  is the solar energy flux in the target acceptance angle of the concentrating system and  $A_c$  is the cross-sectional area of the collecting mirror, which is a function of the position of the sun and collector system.

The convective losses are generalized by [4], [46]:

$$\dot{Q}_{\text{conv}} = \dot{q}_{\text{conv}} A_r = U A_r (T_r - T_a) \quad (28)$$

The radiative losses are generalized by [4]:

$$\dot{Q}_{\text{rd}} = \dot{q}_{\text{rad}} A_r = \epsilon_{\text{eff}} \sigma A_r (T_r^4 - T_a^4) \quad (29)$$

The energy balance is thus [4]:

$$\dot{Q}_u(t) = \dot{q}_u A_c = \eta_{\text{optical}} \Phi_T A_c - U A_r (T_r - T_a) - \epsilon_{\text{eff}} \sigma A_r (T_r^4 - T_a^4) \quad (30)$$

where the available energy is  $\dot{Q}_u(t)$  and in balance is taken up by the heat exchange fluid. It is often the case that the radiative component is neglected when dealing with low temperature systems. The properties  $\epsilon_{\text{eff}}$  and  $U$  are the mean effective coefficients that depend on spectral content, materials and construction particulars. The  $\epsilon_{\text{eff}}$  is the particular mean  $\epsilon$  defined by integration over the spectral response of the absorber coating with regard to the black-body radiation curve. The “constant”  $U$  is highly dependent on operating conditions, and is best defined empirically and physically controlled by the use of flow shields or vacuum-filled spaces. The most manageable method is to use a fitted polynomial, taking as it's parameter the difference in temperature between the receiver surface and the ambient conditions. More complicated models would include the average ambient air velocity, but in practice a vacuum tube has a thermal resistance of approximately  $5 \text{ W/m}^2\text{K}$  [48].

By taking  $C$  as the geometric concentration ratio, this becomes:

$$\dot{q}_u = (\tau\alpha)_{\text{eff}} \Phi_T - \frac{U}{C}(T_r - T_a) - \frac{\sigma\epsilon_{\text{eff}}}{C}(T_r^4 - T_a^4) \quad (31)$$

The instantaneous thermal efficiency is thus given by:

$$\eta_{\text{receiver}} = \frac{\dot{Q}_u}{\Phi_T A_c} = \frac{\int_{t_1}^{t_2} \dot{Q}_u dt}{A_c \int_{t_1}^{t_2} \Phi_T dt} = \eta_{\text{optical}} - \frac{U A_r}{\Phi_T A_c}(T_r - T_a) - \frac{\epsilon \sigma A_r}{\Phi_T A_c}(T_r^4 - T_a^4) \quad (32)$$

where the effective  $\dot{Q}_u$  and  $I_T$  is measured over some finite time interval. This results in a heat transfer relationship for a fluid-filled receiver, without modelling heat transfer losses in conduction within the receiver [4]:

$$\dot{Q}_u = \eta \Phi_T A_c = \Phi_T A_c F_R \left[ \eta_{\text{optical}} - \frac{U A_r (T_r - T_a)}{\Phi_T A_c} - \frac{\epsilon \sigma A_r (T_r^4 - T_a^4)}{\Phi_T A_c} \right] \quad (33)$$

Where the average receiver temperature is defined in approximation by:

$$T_r \approx (T_{\text{out}} - T_{\text{in}})/2 \quad (34)$$

The usable energy is taken up by a heat transfer fluid, this can be expressed as the average calorific heating between average inlet and outlet temperature:

$$Q_u = \dot{m} C_p (T_{\text{out}} - T_{\text{in}}) \quad (35)$$

The design usually minimizes the convective loss by suitable shielding, this allows manipulation toward a receiver-only efficiency based on the operating temperature:

$$\eta_{\text{receiver}} = \eta_{\text{optical}} - \frac{\sigma\epsilon_{\text{eff}}}{C\Phi_T}(T_{\text{in}}^4 - T_{\text{amb}}^4) \quad (36)$$

*This implies fundamental design criteria in order to maximize receiver efficiency:*

1. Maximize the concentration ratio ( $C$ ).
2. Minimize the operating temperature ( $T_{\text{in}}$ ).
3. Maximize the coefficient of absorptivity  $\alpha$  of the receiver coating in the wavelengths of sunlight.

4. Minimize the emissivity  $\varepsilon$  of the receiver coating in the wavelengths of the black-body radiation emitted from the receiver.

These criteria are augmented by the maximum heat engine efficiency for mechanical work purposes, which is the topic of primary interest:

$$\eta_{\text{work}} = \eta_{\text{rec}} \cdot \eta_{\text{carnot}} = \frac{T_{\text{in}} - T_a}{T_{\text{in}}} \cdot \left\{ \alpha - \varepsilon \frac{(T_{\text{in}}^4 - T_{\text{amb}}^4)}{C \Phi_T} \right\} \quad (37)$$

This results in a system operating condition that favours higher concentration ratios both in overall efficiency and in sensitivity of operating point, visualized in Figure 12 [48]:

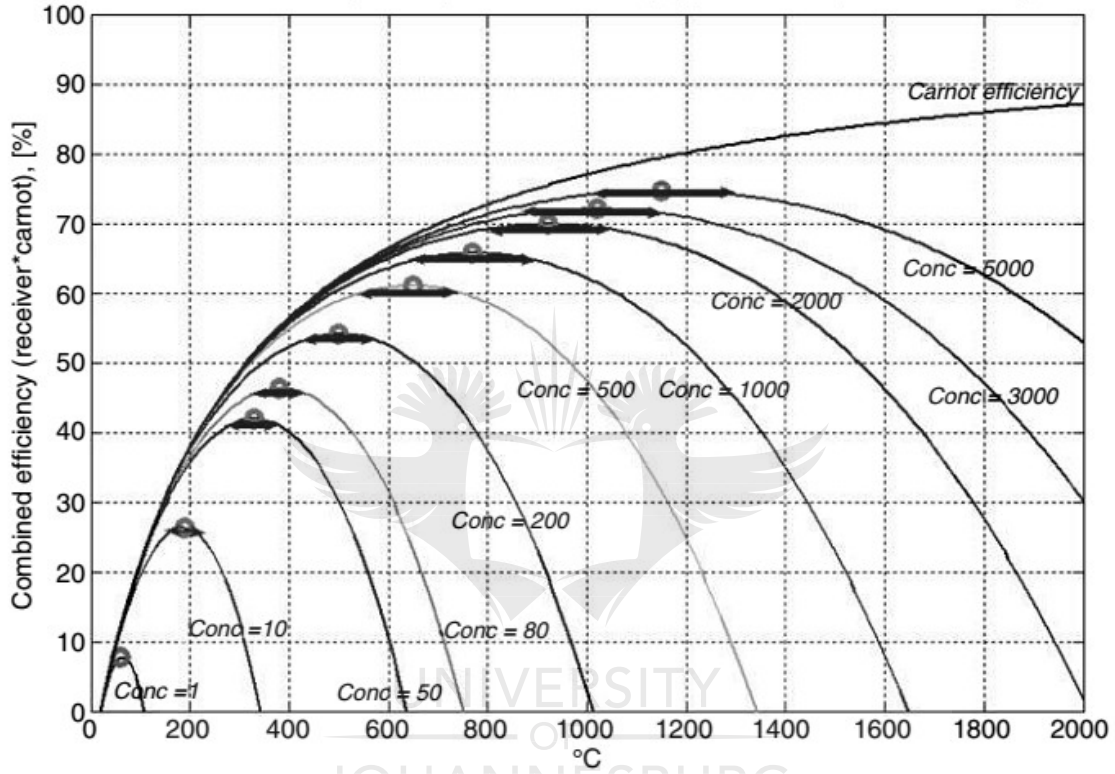


Figure 12: Maximal work efficiency as a function of receiver operating temperature.

The optimal point is found by finding the real roots of the equation [48]:

$$4\sigma T_a^5 - 3\sigma\varepsilon T_a^4 T_{\text{in}} - (\sigma T_a^5 + \alpha C \Phi_T T_a) = 0 \quad (38)$$

There are two definitions of concentration ratios for solar collectors. In each case it may either be a local or aggregate global property of the system, defined as a property of an area on the receiver in relation to an area on the collector. *However, these concentration ratios are geometrical in nature and only approximate the actual flux intensity ratio present on the absorber surface due to non-ideal effects.*

Without heat extraction from the system by a transfer fluid the system reaches stagnation state where radiative and convective losses balance with radiative heat input by solar irradiance. This temperature is given by [48]:

$$T_{\text{stagnation}} = \left[ \frac{(\tau\alpha)_{\text{eff}} C \Phi_T}{\varepsilon\sigma} + T_a^4 \right]^{1/4} \quad (39)$$

### *Heat Transfer to the Primary Fluid*

The primary heat transfer fluid may be single or multiphase, with the useful component being liquid or gaseous. There are two types of systems in this regard:

1. Direct cycle, where the heat transfer fluid in contact with the solar receiver is used directly in the prime mover.
2. Indirect cycle, where different fluids are used in the solar field and the prime mover, with a heat exchanger interface between the two.

The primary heat exchange fluid is usually kept single phase in an indirect cycle, this is due to:

1. Simplification of the calculation of heat exchanger component parameters and the system operating point.
2. Reduction in the stress in containment of pressure, since multiphase operation implies a vapour-pressure associated with the gaseous portion.
3. Consistency in the heat transfer behaviour over regions of the receiver tubing in contact with possibly oscillating multiple fluid phases.

There are multiphase systems in operation and development, since direct generation of gas is advantageous in Rankine cycle plants for thermal efficiency and cost reduction due to elimination of a heat exchanger. These avoid some of the material sealing issues with heat transfer fluids such as synthetic oil, but have shown complications in maintaining stable operating states among other issues.

There are a few models of the heat transfer to the primary fluid, based on the nature of the fluid, which are presented below:

#### *Thick-Wall Aggregate Receiver Temperature for a Single Phase*

This first model is the most common due to its simplicity. The core assumptions in this model are that [55]:

1. The conductivity of the wall is high in relation to the thickness of the wall, such that the temperature gradient is radial and there is almost uniform temperature through a iso-radial slice of the receiver wall.
2. The radiation impinging on the receiver tube is largely uniform, producing a largely uniform temperature at the surface.
3. The phase of the fluid in contact with the inner surface of the receiver wall is uniform, with correspondingly uniform thermal properties.
4. The velocity of the fluid in contact with the inner surface of the receiver is uniform in an iso-radial slice, and gravitational forces are negligible.
5. The heat capacity of the receiver tube is small with regard to the rate of change of the energy transients present in typical operation.

The model aggregates the collector-receiver-fluid system into a single-dimension system in series-parallel, without taking into account losses the model is such. A visualization of this simple model is shown in Figure 13, created here for clarity:

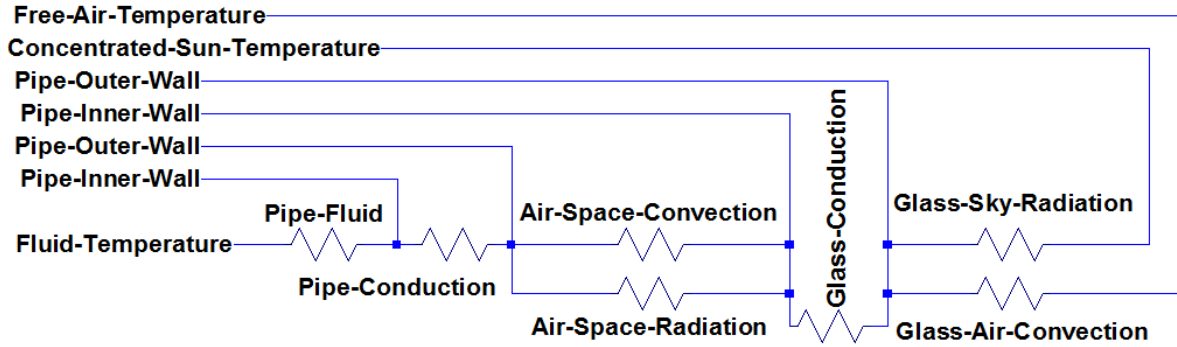


Figure 13: Aggregate Temperature Receiver Heat-Transfer Model

The convection to the heat transfer fluid is given by:

$$q_{f-pi, conv} = h_{fluid} \pi D_{pipe\ inner} (T_{pipe\ inner} - T_{fluid}) \quad (40)$$

where the convection constant is non-dimensionally found by:

$$h_{fluid} = \frac{Nu_{D_{pipe\ inner}} \cdot k_{fluid}}{D_{pipe\ inner}} \quad (41)$$

where the constant  $k_{fluid}$  is the thermal conductivity of the fluid and  $Nu_{D_{pipe\ inner}}$  the Nusselt number that is characteristic to the geometry of the system. In order to increase heat transfer efficiency, the flow in the system is usually kept in the turbulent region. A correlation that finds the Nusselt number for transition and turbulent flow is given in. [46]

The conduction of heat through the receiver pipe wall is modelled by simple conduction through a cylinder:

$$q_{pi-po, conduction} = \frac{2\pi k_{pipe} (T_{pi} - T_{po})}{\ln(D_{po}/D_{pi})} \quad (42)$$

where  $k_{pipe}$  is the thermal conductivity of the pipe wall, and  $D$  the diameter of the subscript variable, at either the pipe outer,, and pipe inner,. Thermal conductivity is itself a property of temperature that depends on the material used. Thermal conductivity for 304L stainless steel can be found by [46]:

$$k_{pipe} = (0.013) T_{pi-po} + 15.2 \quad (43)$$

The stainless steel 321H can be found by:

$$k_{pipe} = (0.0153) T_{pi-po} + 14.775 \quad (44)$$

These are common steels used in heat transfer surfaces where water may be used, systems that use hydrocarbons may use other materials more freely.

The convection through the gas between the receiver and the glass cover is different depending on the pressure of the gas therein; in the low pressure state the convection is dominated by inter-



particle gas conduction, while in the high pressure state the dominating effect is buoyant movement of the gas with respect to gravitational forces.

Radiation heat transfer between the receiver and the glass envelope occurs at infra-red wavelengths, which is the spectral region in which typical glasses are opaque. Since there is little transmission of infra-red through the envelope, allowing the modelling of the radiative component as:

$$q_{po-gi, radiative} = \frac{\sigma \pi D_{po} (T_{po}^4 - T_{gi}^4)}{\frac{1}{\epsilon_{po}} + \frac{(1 - \epsilon_{gi}) D_{po}}{\epsilon_{gi} D_{gi}}} \quad (45)$$

where the subscripts  $gi$  and  $po$  are the glass inner surface and the receiver pipe outer surface respectively.

#### *Thin-Wall Non-Aggregate Receiver Temperature for a Single Phase*

In the second model, the situation at the receiver can be modelled by a differentially small portion of cylindrical wall [56]. The assumptions in this model are:

1. The thermal conductivity of the receiver wall is such that temperatures on the receiver wall is consistent over a finite area.
2. The temperature gradient through the receiver wall is such that heat flow is primarily in the radial direction.
3. The receiver wall thickness is at least almost uniform under the finite area of interest.
4. The fluid in contact with the receiver inner wall is single phase and has a consistent aggregate flow behaviour.
5. The heat capacity of the receiver wall is low relative to the typical transients in the receiver outer-wall temperature.

This scheme uses the same relationships as the aggregate temperature thick-wall temperature, evaluated over a small finite area of the receiver. The model expands in specificity on the previous aggregate model by consideration of:

1. Variation in the distribution of concentrated solar flux over the receiver surface due to the directional characteristics of the concentrating mirror.
2. Variation in the conductive heat transfer properties through the receiver wall.
3. Variation in the characteristics of convective heat transfer at the fluid interface.

The relationships are practically the same as the aggregate model, just evaluated with regard to a small area of receiver tube. This can be done completely locally or in a scheme that assumes finite elements over which a linear, quadratic or other interpolation can be applied. *In order to perform such an analysis, either an assumed flux distribution or a measured flux distribution that the intended measurement framework should provide.* The surface flux measurement will only be accurate if the location of the absorber surface is known with good certainty relative to the concentrating optics. If reflectivity of the absorber is low, it is sufficient that only the flux intensity on the area be



measured. If reflectivity is angle dependent, then measurement of the directionality of the flux is required.

#### *Finite Element Model of the Receiver Tube in General*

Making no assumptions of the dynamics of the sky-receiver-fluid except that there is geometrical stability in the receiver tube and a known concentrated solar flux over the receiver surface. The characteristics of the model are particular to the information provided, and require implementation in a finite element scheme. The details of such models are more involved than would be useful here, except to say that there is a great accuracy benefit in an increase in available information with regard to:

1. The geometry and positioning of the receiver tube.
2. The distribution of solar flux on the receiver surface.
3. The flow regime in the heat transfer fluid.

#### **3.3.11 Design and Optimization Methods**

Design for solar thermal power plants occurs in a macro and micro level, the most popular method is a *thermoeconomic* analysis. In this method the system as a whole is minimized with regard to the *cost per unit exergy*, this is an iterative non-linear process that treats the components block with varying levels of variance [57], [58], [59]. Cost is treated as a flow variable, being presented to the system by fuel and solar energy to flow through the system and eventually becomes the product in the form of excess exergy. The analysis requires lookup in the thermodynamic tables of the transfer and working fluid to account for multiple phase effects.

The thermoeconomic method is in principle applicable to solar collector design, however the cost surface is monotonic for a single component. Since available exergy is a function of the concentration ratio, component optimization requires:

1. Concentration as a function of structural design, with a cost associated with the amount of material used.
2. Concentration as a function of material choice, with associated material costs.
3. Concentration as a function of tolerance in manufacturing technology.
4. Tracking and automation costs per unit exergy.

A suitable method for assessing the concentration effect is by simulation of the optical effects of the structure under real expected loads, by raytrace technique. There is little evidence of research into such methods, likely due to the large parameter space that makes generalization of results difficult. It would be of benefit to this method that good tables of concentration with respect to economic variables be produced, including factors such as time from last cleaning. *The most accessible way is likely to acquire such data with continuous measurement of existing systems in the field, with a relatively low-cost measurement technique. This should be considered a design target for the measurement framework envisioned.*

### 3.4 Principles of Optics

There is practically no upper bound on the complexity that can occur in the design of optical systems, including accounting for the non-linear effects in real lenses and mirrors. The mathematical modelling that is possible under these circumstances is technical, time consuming and requires special simulation tools. A design model that will be extensible should use the most basic principles in order to remain extensible under real engineering constraints.

#### 3.4.1 The ray model

The ray model of light assumes that light can be modelled as photons that travel along a vector that has infinitesimal transverse area, and with infinite velocity. The photon will interact with any object in the path of its' flight from, starting at its' point of origin [60], [61], [60], [62]. The effect of the wave properties of light are predominant at the interactions with obstructions; and as such the ray model breaks down when spacing of obstructions and apertures comes to an order of magnitude of the wavelength of the light present.

Simulation of solar systems using the ray model can be done with a Monte-Carlo technique where rays are generated by a pseudo-random generation process and passed through the system to a point of measurement. This process is known as forward ray-tracing.

#### 3.4.2 The wave model and diffraction

The wave model as originated by Huygens can be formulated best by the Maxwell equations, satisfying the wave equation for the electric field [63], [64]. Simplification leads to the Helmholtz equation for monochromatic waves, however this only has a limited number of analytical solutions.

The evaluation of the wave model is far more cumbersome than the ray model for the requirements of integration over the surfaces of interest, however the core aspects of spectral differentiation require wave model assumptions. The design of any optical system that involves any combination of thin films, real lenses, nano-Fresnel lenses, or zone-diffraction optics will require evaluation of wave model effects. When a restriction on the wavefront occurs due to interactions with an obstruction, a complex pattern of diffraction will result.

In most current applications of solar lensing systems the practical manufacture tolerances make design for diffraction very uncommon. In the design of an optical measurement system it must be considered, at a minimum for the determination of modelling requirements.

##### *Airy Disc and Rayleigh Resolution*

The transfer function of a perfect, aberration free lens or perfect aperture to a point source is not a point at the objective. Diffraction results in the formation of a circular diffraction pattern known as an "Airy Disc". Real lenses are subject to more sources of error due to manufacturing imperfections, material realities, and edge effects due to non-infinite lens size. The objective intensity distribution of an infinitely-distant point is given by a first order Bessel function, with an argument dependent on the  $f$  number of the lens and the light wavelength [64]. The point source becomes a distribution with a radius of:

$$\Delta l = 1.22 \frac{\lambda f}{2a} = 1.22 \frac{\lambda f}{D} \quad (46)$$

The diameter  $a$  depends on the minimum of the lens diameter or the beam diameter. In the case of a simple lens, the distance between the lens and the objective surface is  $D$ , and the disc is dependent on the wavelength of the light. This is visualized below in Figure 14 [63]:

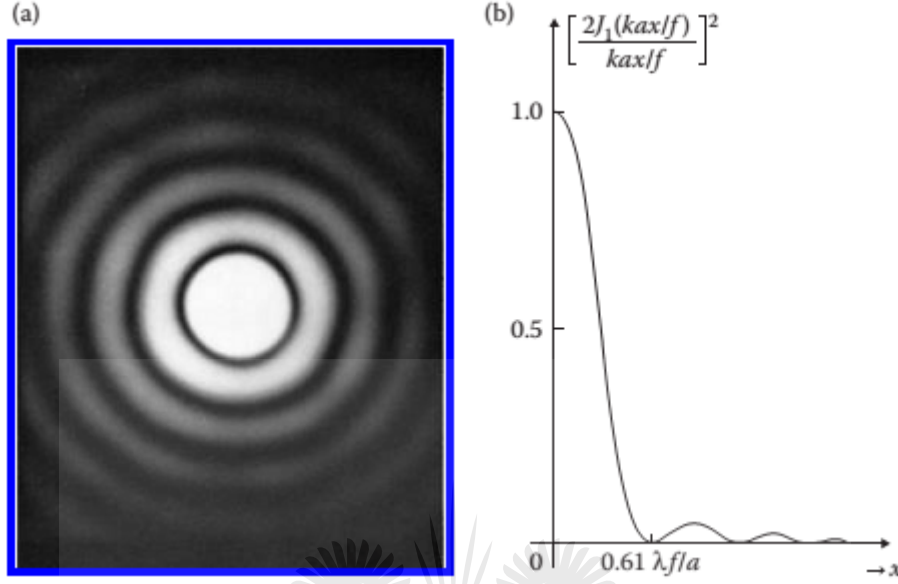


Figure 14: Visualized Airy disc.

The core effect can be seen to be a low-pass filter, the effects of which can be dramatically modified by apodization by an aperture mask placed on the lens. The interaction of multiple Airy Discs result in the Rayleigh criterion for the resolvability of two or more equally luminous points, which occurs when the maximum first point of an Airy disc falls over the minimum of another. This can also be seen as an expression of Nyquist theorem with respect to the spatial frequencies in the signal.

The Rayleigh criterion is the upper limit for packing of light-sensitive elements, it is also applicable to the most simple kind of optical element; a simple aperture with no lens material. A given spacing between light-sensitive elements will require a greater distance between the elements and the aperture.

### 3.5 Solar Flux Measurement and Metrology

This section seeks to overview the existing methodologies dealing with solar phenomena, thereby acquainting the reader with an overview of the ideas that pervade as a result of these technologies. *The techniques in current use are in a large part moulded by the measurements made available by these technologies.* Solar irradiation originating from the sun and not yet affected by Earthly effects has been studied by satellite measurements. The extraterrestrial irradiance distribution depends on the quantum effects in the solar reactor, a spectral intensity plot is shown in Figure 15 [71], below:

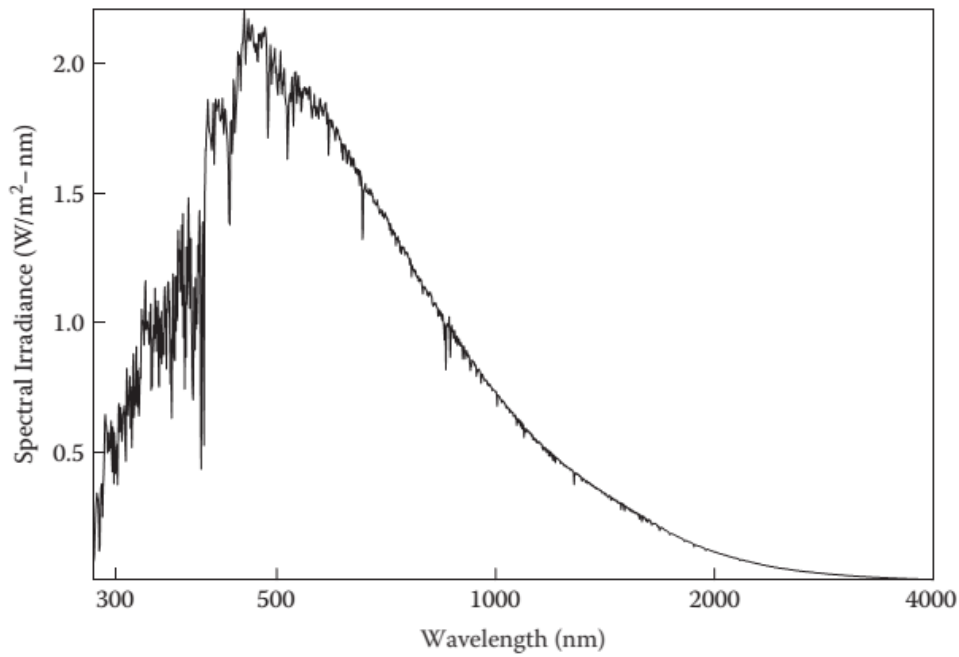


Figure 15: Solar irradiance spectral content prior to the atmosphere.

The first questions that arise with regards to solar energy deal with the energy as a natural phenomena, and a considerable amount of effort has been expended in determining the distribution of radiation over the surface of the earth, modelled as a function of [35], [65], [66]:

1. Location on the earth's surface, both along the surface and in terms of altitude.
2. The time of year and thus the effects of the inclination of the earth during solar transit.
3. Local and recurrent meteorological conditions in aggregate, such as the amount of water vapour, dust and chemical constituents in the atmosphere.

The radiation experienced by a location on earth is further studied by decomposing the constituent parts, which are the direct and indirect fractions, these are a function of [67], [68], [69], [70]:

1. The shape of the sun itself, being finite and thus producing non-parallel rays.
2. The region of atmosphere through which the radiation has passed to get to the location of interest, which is a function of the time of day and the geographical location.
3. The effects of local geographical structure, flora and buildings that tend to scatter radiation diffusely.

Atmospheric effects include Rayleigh scattering, aerosol scattering and absorption, and gas absorption. Rayleigh scattering is due to dust particles in the air mass, given by [71]:

$$I(\lambda)/I_0(\lambda) = e^{-\tau(\lambda)m} \quad (47)$$

where  $I$  is the strength of the attenuated original source, the optical depth is given by  $\tau$ , and  $m$  the amount of atmosphere traversed relative to the vertical.

Aerosols have a wavelength dependent property with regard to scattering and absorption, and is defined by the probability of absorption or scattering of a photon. This probability is given approximately by the Henyey-Greenstein function, where  $\theta$  is  $0^\circ$  in the primary direction of propagation and  $180^\circ$  in the opposing direction [71]:

$$p(\cos(\theta)) = \frac{1}{2} \left( \frac{1 - g^2}{2(1 + g^2 - 2g\cos(\theta))^{3/2}} \right) \quad (48)$$

Such that:

$$\int_{-1}^1 p(\cos\theta) d(\cos\theta) = 1 \quad (49)$$

And:

$$\int_{-1}^1 p(\cos\theta) \cos\theta d(\cos\theta) = g \quad (50)$$

Gas absorption is primarily accounted for by water vapour, ozone and  $NO_2$  when in polluted areas, the result is a transmission coefficient depending on the gas abundance and gas absorption coefficient:

$$\tau_g = \eta_g \dot{\alpha}_g \quad (51)$$

The result of these attenuation factors on the extraterrestrial spectral content is a situation-particular distribution, a typical situation is plotted in Figure 16 [248].

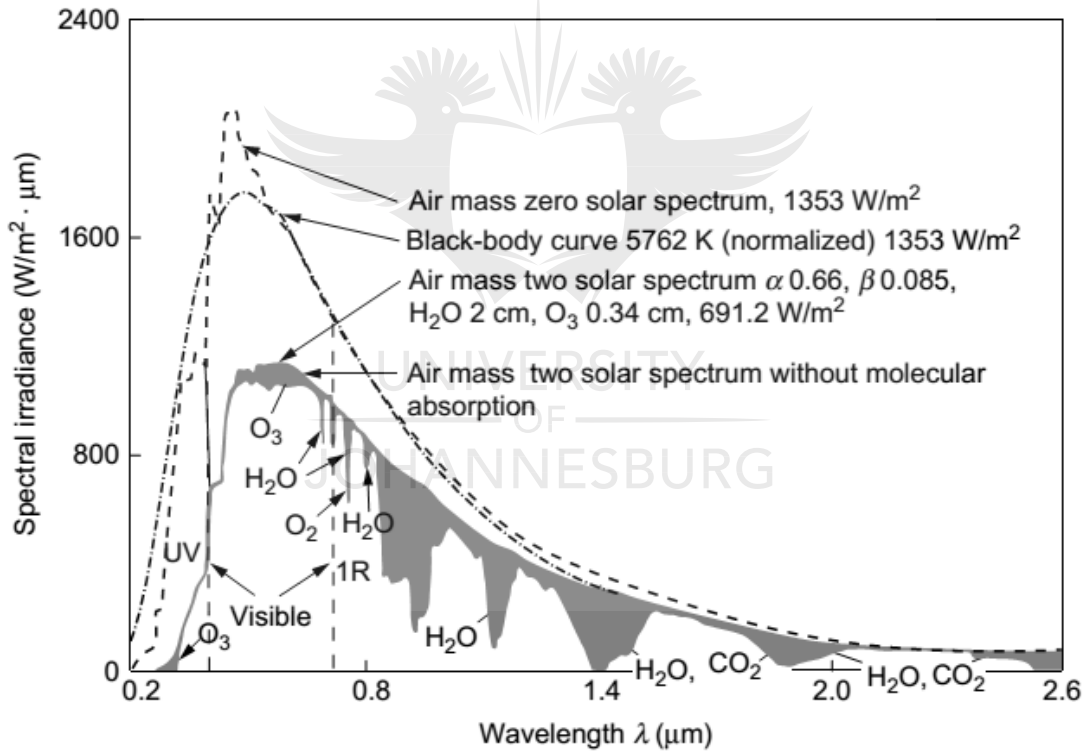


Figure 16: Terrestrial spectral absorption due to multiple factors.

*This clearly demonstrates the need for a multi-spectral measurement of the content of solar irradiation in any accurate measurement scheme.* There is a significant history of devices that are used in measurement of light and solar irradiance, the extensive details of which were covered in the process of literature review and concept design [72]. Their enumeration is however out of place here, since all are derivatives and improvements on a few basic measurement techniques. These are subject to similar issues as a result of their physical construction, and as a result are not directly applicable to the design purposes of the project. *A brief description of the principles will suffice to give sufficient background into later developments.*

### 3.5.1 Measurement of Radiative Flux

#### *Calorimetric Methods*

Calorimetry is the measurement of the change in internal energy of a reference substance as a result of heat input from a phenomena of interest, which can be set by interaction with the environment in any combination of the three modes of thermal systems: conduction, convection and radiation. In the case of solar measurements the energy is the absorbed fraction from the irradiance on the absorber that is transmitted to the reference material, while ensuring isolation of the system from conductive and convective effects. This requires a coating with a high coefficient of emissivity, ideally as close to that of a black body as possible, across the whole spectrum of irradiance on the device. The possible convective effects are mitigated by shielding through glass, and the conductive effects by insulation. The use of a suitable transducer for temperature into an electrical signal allows a measurement to be facilitated. The variations in the calorimetric technique hinge around the design of the device with regard to the window of radiation of interest, the transducer of the temperature information and the methods of continuous calibration of the device. In general the devices are subject to a number of considerations that are characteristic of their physical structure [73]:

1. Slow response due to thermal inertia of the mass of the absorber and the thermopile.
2. A requirement for a high quality double-walled evacuated glass dome in order to isolate the convective effects of the environment and ensure that contaminants do not enter into the device.
3. A sensitive and matched electrical measurement device that will translate the electrical potential into a thermal quantity for recording.

There are a number of transducers used in practice, which will be discussed below.

#### *Energy Balance Methods*

Energy balance methods rely on the accurate measurement of a heating effect rather than that of temperature, which is held constant by a less accurate measurement that serves merely as a calibrated reference point. A typical arrangement in this methodology is the radiative heating of a reference material by the irradiance being measured, while noting the time taken to reach a certain temperature. The exposure to the environment is then inhibited and the reference is then cooled to a local standard temperature before being heated artificially by electrical means to the same reference temperature. Other methods rely on an energy balance between the heat input by the radiation being measured and an artificial source of radiation, while keeping the temperature of a reference material constant. These methods can be made highly accurate as they inherently integrate the effects over time, and since the applied electrical heat can be measured accurately. The design consideration is either a measurement averaged over time, or a device that is slow to respond and settle [73], [72]. *It is unlikely that energy balance methods can be scaled down to a size small enough for any meaningful resolution without significant expense and effort.*



### *Thermopile Pyrometer*

The thermopile is a stack of thermoelectric (thermocouple) junctions that operate according to the Seebeck effect, which is the generation of a potential as a result of junctions of dissimilar conductive materials exposed to a temperature. The potential is small and needs a suitably sensitive electrical bridge and digital converter in order to get decent performance, however as a positive the response is very nearly linear. There are always two junctions in series by virtue of construction, one of which must be kept controlled so that its effects can be eliminated [73], [72]. *Minimization of the scale of such devices is likely possible, but would require interesting manufacturing techniques derived from those used in semiconductor manufacturing.*

### *Resistance Detectors*

All materials suffer some change in electrical resistance due to changes in temperature, the most linear of these are suitable for application in a bridge electrical configuration in order to measure temperature directly. A high-quality alloy or pure metal such as platinum is commonly used, which gives good linearity in response. Other cheaper options include semiconducting (ceramic) thermistors, which are non-linear and require subsequent compensation. The excitation of resistance detectors generate small amounts of heat that may skew a temperature measurement, but in practice the current passing through the device can be made so small as to reduce such effects to below the primary accuracy required of the measurement [73], [72]. Resistance detectors in the form of a small scale array are used in Forward-Looking Infra-Red (FLIR) camera detectors, however these are optimized for low-flux conditions in military and industrial purposes.

### *Photoelectric Detectors*

The photoelectric effect is the generation of an electric current when materials are illuminated by photons. This can be in the body of a semiconductor material or on the surface of a metal contained within a hard vacuum. The absorption of photons is frequency dependent in interaction with the material "band gap". *While most practical designs have at least some dependence on wavelength, it is this dependence that makes a photoelectric measurement of solar flux more of an indicator than other methods.* Given a known wavelength profile for the radiation being observed this is not an issue, though this is most often not the case. The lower cost of a semiconductor photoelectric detector makes them useful for indicator measurements. [73], [74], [75]

## **3.5.2 Components of Irradiation**

Irradiation has been traditionally decomposed into components that are based on a number of aggregates that categorise according to the radial distribution of the irradiance. This makes sense with regards to the typical uses of solar irradiation: in general the use of concentrating optics makes best use of direct solar flux, while less concentrating receivers are able to capture the direct and indirect fractions of irradiance. These classifications are commonplace for the purposes of most design involved with solar collectors, however they need not be used exclusively. At any point of measurement there are a number of distribution properties useful in design:



### *Direct Solar Flux*

The direct component of solar radiation is defined by a number of original measurement techniques, the nature of the techniques being now intrinsically linked with the definition [70]:

1. The total flux and indirect component is measured, the difference is the direct component.
2. The flux is measured by a shrouded energy measurement technique, so arranged in the bottom of a tube with baffles. The interior of the chamber is blackened and the pyrometric sensor shielded from re-radiation. The whole device is tracked toward the sun during measurements.

The angular spread of the direct component thus has a practical angular tolerance, however the direct component for practical purposes is the fraction within the acceptance angle of a system of interest. However the details of any particular standardisation are not useful in this context. *It is this angular tolerance in the direct component that limits the usefulness of the definition to bulk properties of the solar system as a whole.*

### *Indirect Solar Flux*

The indirect component, often known as the diffuse component, is measured by a pyrometer that is kept in shadow by a thin shield that tracks the sun, so as to only be affected by specular reflections off surfaces or particulates in the environment. This fraction is lower than the direct solar component, and cannot be effectively used by most concentrating designs, and is thus of little interest for our purposes [69].

## **3.5.3 Measurement of the spectrum**

### *Spectrometer*

Solar spectral measurements can be done by a regular spectrometer whereby a light ray impinges on a diffraction grating; distributing the spectrum according to angle in a distributed spatial region where a response-compensated intensity sensor measures the wavelength components [76], [77], [71].

The spectrometer is a well known device, used for many practical purposes. Some important generalizations become evident in any spectral differentiation scheme: since any sensor present can only measure intensity, thus in order to gain resolution in spectrum there must be distinction in the spatial arrangement of a set of sensors. *Since the sensor size is finite, any attempt in spectral differentiation using diffraction gratings trades resolution in space for resolution in wavelength* [76].

The geometry of the typical spectrometer is unsuited to being implemented in parallel for an imaging system. Spectral differentiation in remote sensing is most often performed by filters switched into the optical path. An exception to this is a scanning imaging system known as a heliograph, for the express use of imaging the sun [76].

### *Heliograph Imaging*

The heliograph is an imaging spectrometer implemented by scanning a selective diffraction grating over a presented image, using a tracking mechanism. If the scan rate is sufficient, the memory

effect of human persistence of vision can form an image of the selected wavelength, and a single photodiode is sufficient for electronic capture.

An overview with respect to the problem at hand indicates that: while useful in imaging the sun from Earth or low orbit, the cost, spatial requirements, complexity and fine tolerances of using a similar method in measuring solar radiation reflected off a collector would not be effective [76].

### 3.6 Representation of Optical Fields

Any computational application that seeks to model the light in an area of space will need a method of storing and manipulating the light field, or a model that will allow its' reconstruction. It is important to consider how this might be done, so that the measurement tool to capture the light field might facilitate it more effectively.

#### 3.6.1 Computer Vision

The techniques used in computer vision form the basis for most attempts at analysis of solar systems. These techniques will not be expounded on here, suffice to say that there is no attempt at capture of the light field; only the sources of light in the scene, and the objects or lenses therein.

This approach is evidenced in the tool used in combination with VSHOT, known as SolTrace. The software uses models for the sun, the captured shape of the mirrors, and the receiver surface, in order to predict light interactions.

#### 3.6.2 Image-Based Rendering

Image-Based Rendering (IBR) is a research discipline that takes a different approach to that of computer vision in the way visual information of the world is processed. With regard to the method of representation, objects have what is called a *source description*. This model is the ideal representation for storage, transmission and manipulation in digital form. The source description describes the objects in the scene, their properties and interactions [78].

The information obtained from a light-sensing device or number of devices provides what is called the *appearance description*. The task of computer vision has been to use an appearance description in order to determine a source description, which has had limited success with regard to the general problem. The goal of IBR is the recording, compression, transmission and manipulation of scene information using the appearance description rather than the source description [78].

The difference in source description and appearance description representations are in the scaling of algorithmic and computational complexity with respect to scene complexity. A source description is better for simple scenes that are built from primitive objects, but scales poorly as scene complexity increases. The appearance description has high overhead for simple scenes but has a low increase in computational complexity with increasing scene complexity. It is for these reasons that IBR is of interest for the next generation of media devices that intend to deliver content with multiple views. The techniques in IBR are a media extension of general light-field methods [78], and is useful in our context because it scales to any degree of complexity in the mirror system used. It is thus suitable to large fields of small mirrors, or infinitesimal effects on mirror surfaces.

### *The Plenoptic Function*

The light present in a scene can be represented, as an appearance description, by a continuous function of seven variables known as the *Plenoptic function* [78]:

$$l(V_x, V_y, V_z, \theta, \phi, \lambda, t) \quad (52)$$

This has the components  $(V_x, V_y, V_z)$  for the location in space, the angles  $(\theta, \phi)$  for the light incident on the location, over the wavelengths  $\lambda$  for a given time  $t$ .

The discretization of the function results in a state tuple in all parameters with an associated intensity, and as such the scene can be described as a collection of state tuples without ambiguity. This does not describe all the information in the scene since effects of polarization and phase are ignored. This approach is however sensible since intensity is the only directly measurable property of a light ray and the most useful for almost all purposes.

Thus a definition for IBR follows: A two stage process of discrete sampling from the Plenoptic function, and rendering a reconstruction of the continuous Plenoptic function at the desired view point. The challenge therein is the processing of a large amount of required data and its manipulation, with a core goal the reduction in the amount of data transmitted or stored.

### *Image-Based Processing Techniques*

Due to the lack of complete information available on the Plenoptic function and the large amount of information required, techniques in IBR include [78]:

1. Determining the minimum amount of captured information required for a given quality in result.
2. Constraint of the number of view points required for a target subject view.
3. Reduction in the number of dimensions in the Plenoptic function for a given purpose, such as time and wavelength.

Common assumptions made in constraining the viewing space include [78]:

1. Reduction of the number of wavelength discretizations to a three dimensional colour-space for human-centric quantitative applications. This assumption is applicable to media presentation not suitable for quantitative applications, and represents an integration of the wavelengths with respect to sensitivity response characteristics of the channels.
2. Assumption that the transmission medium for the radiation does not attenuate it to a significant extent, as such it is not necessary to measure the intensity along the ray path. This allows a complete representation of the Plenoptic function on a closed surface bounding the space of interest that has a view of all surfaces in the scene.
3. The scene is static such that information from different samples in time from the Plenoptic function can be integrated.

Common assumptions about the viewer that will interact with the reconstruction are [78]:

1. The scene of interest is bounded to a free-space region, and there are limitations in capturing only the light along a convex hull containing the scene. This requirement is often

made for practical purposes in capture, and allows a reduction of positional dimensions to two (since sampling occurs on a manifold in the three-dimensional space).

2. The viewer can only move through a predefined path through the space. This removes two dimensions from the full function.

The practical devices used for image capture result in a number of effects in sampling the Plenoptic function [78]:

1. The intensity of a camera pixel is the average of the intensity in an angular region around, and as such is dependent on the sample position, even along a given ray line.
2. The intensity of a camera pixel is the average of the intensity in the sensitive region over a certain shutter time window. Depending on the construction of the device this window may be universal for all pixels in the device or unique to each pixel, as is common with sequential mechanisms to read off the pixels into digital form. This time-sensitivity is a consideration for time-sensitive and time-position sensitive applications where images appear to be warped by camera or subject motion.

These assumptions result in a number of systems that have emerged based on the treatment of the Plenoptic function, which are summarized in Table 1, below on page 45. The assumptions applicable will have a great impact on the method of data storage and manipulation, it is thus necessary to consider the particular set of cases applicable to our design problem.

Plenoptic Dimen- sions	Example Representations	Assumptions					
		None	3D colour space	Static scene in time	Transparent transmission medium	Viewer in fixed position	Viewer moves along fixed path
7D	True Plenoptic Function	✓					
6D	Surface Plenoptic Function				✓		
5D	Plenoptic Modelling		✓	✓			
5D	Light Field Video		✓		✓		
4D	Light Field Lumigraph		✓	✓	✓		
3D	Concentric Mosaics		✓	✓	✓		
3D	Panoramic Video		✓			✓	
3D	Interactive Panoramic Video		✓	✓			✓
3D	Branch Movies		✓				✓
3D	Standard Video		✓			✓	
2D	Image Mosaicing		✓	✓		✓	
2D	Image		✓	✓		✓	

Table 1: Comparison of systems in terms of the Plenoptic function

The application of this categorisation and family of techniques to the measurement of the light field off a concentrating mirror results in an ideal feasible system handling the Plenoptic function accordingly:

1. A multi-dimensional colour-space based on hyper-spectral binning. This can be achieved by a suitable filter mask, and is well-known in actual implementations [79].

2. A viewer constrained to movement on a surface, which is not the surface of acquisition of the Plenoptic function.
3. The transmission medium does not significantly attenuate the radiation present, which is not true for the general solar situation. It is however representatively suitable to interpolate views geometrically near to the image capture device.
4. The rate of change of the radiation is relatively slow with respect to the functioning of the device. The scene is quasi-static and thus can be handled as a series of static scene snapshots at time points of interest.

This particular simplification of the Plenoptic function, as far as can be presently found, is not achieved by any existing technological implementation. Further, [80], and [78] indicate that there are as yet no implementations that allows the viewer to be free to move on a surface.

#### Discrete representations of the Plenoptic function

A key factor in the handling of data in computational terms in the representation of the data in structures that have an inherent layout, logic and ordering. The effect of data structures on data operations is an inherent function of the structure, with different structures requiring different amounts of computational resources. The architecture of the computational machine interacts with the data structure, further impacting the tractability of the problem in real terms.

There are a number of representations used to represent the Plenoptic function [78]:

1. The naive representation that is present by storing timestamped images taken by camera devices that have a known, recorded location (relative to one-another and to a reference origin), and known optical characteristics.
2. A ray database representation that stores tuples of ray intensities and parameters.
3. A cut-surface representation where ray position and direction is represented by the intersection of the rays with two planes or two cylinders.
4. A sphere-plane representation that records the ray direction and the intersection coordinates of the ray with plane passing through the origin and perpendicular to the ray itself. This representation does not allow for a pencil or rays that exist in a near region of space and parallel to one another.
5. A partial source representation that is an intermediate between the principles of IBR and traditional computer vision.
6. A representative surface representation that is used for fixed-point viewers of panoramic video, where the video is simultaneously captured by multiple cameras and projected onto a spherical or cylindrical surface. The view in any direction can be rendered by coordinate transformation or warping.

*The likely best fit for the purposes of the intended measurement tool is a combination of the representative surface representation and the naive positional representation. This will be evident as a natural consequence of the measurement tool internal geometry.*

## Operations used in Image Based Rendering

The core value in IBR is the construction of new views of a scene based on captured views taken of the Plenoptic function, which is independent of the complexity of the content of the scene. Functions toward this aim include [78]: Determining the minimum number of samples of the Plenoptic function allowing an anti-aliasing reconstruction. Splitting of a new view into discrete rays cast into the representation of the Plenoptic function. Quad-linear interpolation of light rays in order to compose new ray representations. Then finally the compression of the representation, since even with the minimum number of samples the amount of information is very large.

In this application the IBR pipeline will not be considered besides compression, which will be afforded a natural implementation as a result of the way pixel intensities are sampled. In general the process of forward ray-tracing is sufficient for reconstructing any view required.

## Capture for Image Based Rendering

The inherent representations used in IBR can be serviced by any feasible device, however the high level of development in focal-plane imaging devices make these the most useful device primitives. A general scan of the literature reveals that the majority light-field research has used camera devices located on a surface, either in a parallel or by serial replacement, and possibly with highly non-linear lensing or mirror systems.

Recent developments in image-based devices include work by a Stanford research group that resulted in the "Lytro" camera. The construction of this device presents a basic optical path, that includes a primary optic presenting light to an array of micro-lenses that form individual apertures for a regular CMOS imaging sensor. Each micro-lense thus acts as a pixel that measures the direction of incoming radiation. The benefit of a Lytro type camera for the user is the capture of a dataset that allows dynamic refocus of the image in post-processing, allowing depth of field to be changed after image capture. This allows a constructed image to be brought into focus on different subjects. *The principles of operation the Lytro can be extended toward our application, where they are specifically modified to suit the problem environment.*

## 3.7 Camera Models

The capture of 2D images is largely purpose dependent, the model of most use for most purposes is the pinhole model. The natural world has a number of types of eye, with associated models:

1. Eye's corresponding to the pinhole model, as used by most medium to large fauna. These can capture various depths of field, using variable lens characteristics. In order to maximally sample the Plenoptic function the lens geometry is swept through its' available focal lengths.
2. Ommatidia collections corresponding to vision systems in insects, arachnids and various crustaceans. These eyes have infinite depth of field, but do not function as well in static situations since it samples from a limited number of discrete angles. Motion of the eye (by the body itself), is used to interpolate the Plenoptic function over successive samples [81].
3. Low resolution "pit" sensors that consist of large radiation sensitive regions that have an inherent angular sensitivity pattern as a result of their construction. The sensor must be



moved through a region in order to construct an image of the scene. These correspond to body-heat sensors as used by viper snakes and the method used by various grubs.

A number of models are used in synthetic mechanisms, developed for specific purposes [80]:

1. The orthographic camera, where a pixel in the image depends on the intensity of the light in a pencil perpendicular to the image plane. The imaging plane needs to be of the same size as the objects in the scene, this makes it impractical as a single device.
2. Perspective cameras, the “pinhole” model, the most common imaging model which will be expanded upon.
3. Pushbroom cameras, that are often used in satellite imaging systems. A linear sensor is swept parallel to it's axis, thereby building an image sequentially in the columns. The result is a more orthographic image for objects that are near the viewer, and a more perspective image for objects at distance.
4. The “XSlit” camera, where rays pass through two oblique slits in 3D space and are collected on an imaging plane.
5. Catadioptric cameras, which are constructed by having a pinhole camera viewing a curved mirror surface. The curved mirror implements a transform that gives a wide field of view, the surface is required to be a 3D conic section. Actual physical implementation is highly sensitive to component positioning and vibration. This principle maps to multiple curved surfaces, producing a light-field imaging system where each mirror serves as a spatial pixel.

The pinhole, orthographic, pushbroom and XSlit cameras can be modelled with an inclusive manifold model known as the General Linear Camera (GLC), which is defined as the affine combination of three generator rays [80]. The GLC is capable of describing eight distinct types of camera model, however not all are of interest to the current problem. Referring to Figure 17 [80] there are the pinhole (a), orthographic (b), pushbroom (c), and XSlit (d). It is useful as a simple but flexible model for forward ray-tracing information from a captured light field, and the method should consider facilitating its' use directly.

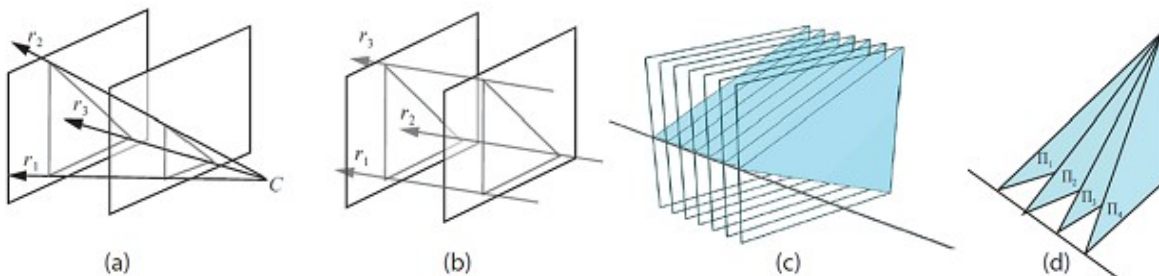


Figure 17: Visualization of four of the eight camera models in the General Linear Camera.

The more physical movement required by an imaging mechanism the slower the ultimate sample rate. This movement is an important factor for any real system involving control. *The two models of greatest interest will be now be considered: The arthropod eye model and the pinhole camera model.*



### 3.7.1 The arthropod eye model

The eye of insects is composed of a collection of individual lens and sensor arrangements known as *Ommatidia*. Each can be modelled as aggregating the intensity of a conic angle of incoming light, and are positioned such that there is minimal overlap in the conic angles of any two ommatidia. The actual conic angle can range from the practical maximum, given by the number of ommatidia in the collection and the total field of view, to a minimum of a parallel pencil that is the width of the lens itself.

Recent work has shown a practical implementation of a synthetic arthropod-like eye, made using flexible circuitry interlinking sensors on a flexible substrate and a flexible microlens array. This construction is visualized in Figure 18 [81]. Application of pressure under the structure produces a hemispherical array of ommatidia that are sensed using a multiplexing technique to sequentially sample the sensor elements [81].

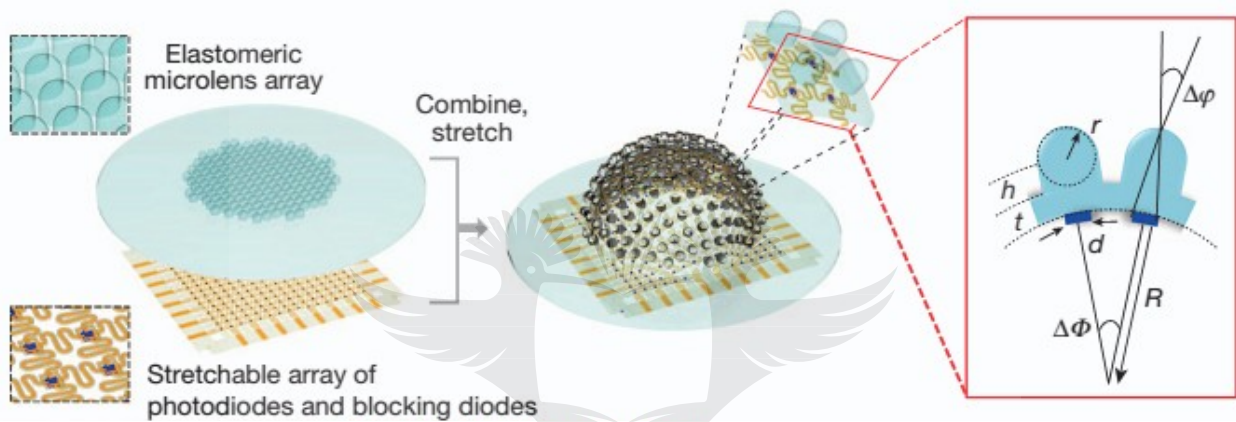


Figure 18: Simple topological representation of a synthetic construction of an arthropod eye

The model of system behaviour can be approximated by the pinhole model at more significant distances from the device, while visualization of nearer objects is subject to effects due to device geometry. At these distances the model is non-linear and should be piecewise defined by local models for each pixel, defined as a linear model that is modified by pixel-dependent parameters.

*The model is attractive to the current problem due to the feasible robustness of using photodiodes under some form of selective aperture for limiting the amount of light present, along with the wide field of view required for analysis of certain solar concentrators.* It is easy to postulate an array of shrouded tubes with radiation-limiting apertures before photodiode detectors. The prospective suitability of this method will be discussed later.

### 3.7.2 The pinhole aperture model

The pinhole model is a linear model that models light as vector rays that pass through a point and intersects a focal plane, it is the simplest model available that takes into account perspective effects. The assumptions in the model allow the interaction of the camera with the scene as a linear transformation. This assumption is not applicable for large fields of view and systems with inherent significant distortions [82], [80].

The implementation of a pinhole can in practice be applied when the *virtual aperture* is made small by the optic system. The use of an actual pinhole is also suitable, which can be implemented in

practical terms by a very small hole made through enclosure of the image sensor. This can be done by laser cutting or drilling and shaving the area of the pinhole to be as thin as structurally practical, in order to reduce *vignetting* which occurs with attenuation of rays of increasing incidence angle relative to the surface. The resolution of the pinhole is improved with decreasing size, up until diffraction effects (Rayleigh criterion) start to dominate. *This reduces the total available energy available to the sensor, which results in lower signal to noise ratios given a fixed shutter time. This effect is useful in a naturally high energy (high radiative flux) environment as long as black-body radiation of the enclosing body is kept low.*

The depth of field is infinite, eliminating the inherent need for a focusing lens and making it suitable for large depth ranges and uncertainty in the scene. A focusing lens presents a control issue and attenuates the radiation spectral content based on the material transfer characteristics, it also requires special manufacture techniques that tend to be expensive in short runs. *It is these factors that make the use of lensing material generally unsuitable for inexpensive prospective techniques.*

The effect of a pinhole as a transfer function can be modelled as a convolution of a Dirac delta function in two dimensions with the original image, neglecting diffraction effects [83]. The pinhole model can be defined virtually, by sampling the image using a set of matrix-like apertures and reconstructing the effect of a delta function [84], [85], [86]. This technique is known as *coded aperture imaging*, however once this initial step is performed a virtual pinhole can be used in a standard pinhole model. The implementation of a coded aperture can be static by a laser-cut sheet of foil, or dynamically by a Liquid Crystal Display (LCD), Digital Mirror Device (DMD), mechanical switch-plate or other reconfigurable mask [86]. *Coded aperture techniques are be suitable for our purposes, however the increased complexity should ideally be avoided.*

The details of how the model is constructed are given in the Appendix: "8.8 - The Linear Pinhole Model" on page 189.

### **3.8 Metrology of General Surfaces**

The effects of a concentrating mirror, or set of mirrors, can be predicted by both ray and diffraction models, given a sufficient knowledge of the geometry of the mirror surface. A direct route to determining system performance is to acquire a source description of the reflective and refractive surfaces present, as they exist in the system. This predictive relationship is the reason for including techniques of surface metrology in our investigation.

In addition to reflective surfaces, prediction would require knowledge of the refractive components in the optical path, which will include thin films. These can occur both by design and by unwanted deposits. The assumption is most often made that these structures are insignificant with regards to the geometry of the system, and that thin film effects can be considered by modification of the transmission function in the system. Thin films are used almost universally in optical lensing systems, and well covered in [87]. Measurement of thin films can be done by interferometric techniques as described in [88].

The Video Scanning Hartmann Optical Technique (VSHOT) is a direct implementation of the principle of acquisition of a source description. The geometry acquired is processed using the

software package SolTrace developed by the National Renewable Energy Laboratory, wherein a Monte-Carlo technique of forward ray-casting is used to sample the effect on the target surface. A similar method is demonstrated in [89]. A variety of sun-shapes can be used to probabilistically generate rays that are each checked for collision with the system geometry, then reflected or refracted and checked for interaction with other objects in the system. At each step the optical properties of the reflecting material are applied. The result is a flux-map over the geometry of the absorbing surfaces.

VSHOT requires a fine source of coherent radiation that can be accurately scanned over the mirror, and measured on its' path to a measurement surface. The angle of the source, the position of the measurement surface and the angle of the radiation hitting the measurement surface is cumulatively sufficient to generate a point-cloud representation of the mirror surface. Surface fitting techniques are then used to generate a polynomial or spline-polynomial representation of the surface. It may be possible to estimate surface characteristics such as propensity for scattering, however it appears that this is not implemented in SolTrace, and information on VSHOT is otherwise not available.

### **3.8.1 Principles of surface metrology**

Surface metrology is an application of the practical applications of geometry, using the path and wave-nature of light as a tool of geometrical measurement. Given a suitable number of measurements the path length may be resolved under reconstruction assumptions that often include smoothness and continuity in the surface being measured [90], [91].

Applications of such methods include depth cameras used in interactive computer interfaces, in part identification and orientation in production systems, in quality control of shape and integrity, and in digitization of environments and artefacts for multimedia uses.

### **3.8.2 Interferometry**

The distance along a ray of light can be taken as a multiple of the number of wavelengths by measuring the interference of a coherent beam of light with its' reflection off a specular surface. This principle is used in system control for measuring equipment spacing and in manufacturing for part dimensions [92], [93], [94], [91].

The shape of a surface can be acquired by scanning over the surface with a coherent beam, or in two dimensions with a snapshot of the interference with the environment of a coherent spherical wavefront. The method cannot be used in traditional form on a mirror-like surface of arbitrary orientation, and has been found to be prohibitively slow for industrial applications in scanning parts for quality control purposes.

### **3.8.3 Structured Light Methods**

By projection of a known pattern onto the scene of interest, one is able to acquire information about local changes in geometry on the surface by the way the pattern is modified. This pattern is typically a sinusoidal, triangular or square spatial arrangement of lines, which may be rotated during the course of measurements. The local changes are accumulated by integration over the image in order to get absolute distance relative to some reference in the scene, which may be

arbitrary. Other methods may project an array of coded shapes into the scene, each shape identifiable by its' form and measurable by perspective depth from the camera [90], [95], [91], [96], [97], [98], [99]

The account in review of these methods need not go further than the requirement that structured light methods have that the surface be an opaque, largely non-specular acceptor and re-radiator of visual information. There have been a number of limited experiments applicable for specular surfaces, however these have been limited to close-up projection of the pattern, which is unsuitable for the current task. Industrial uses with specular surfaces require a dusting of the surface prior to measurement [91].

#### **3.8.4 Laser Scanning Methods**

Besides the VSHOT method, a similar method is general laser triangulation. Instead of a structured light projection leading to detection of local changes, a spot is projected onto the scene with a known global angle with respect to the camera. With a known projection angle and a known measurement angle, the point can be triangulated in the space in front of the camera. The resolution of the system is a function of the angular precision, and size of the projection. The VSHOT method is an implementation of laser triangulation catered toward measurement off the mirror surface, whereas general laser triangulation requires a diffuse surface, much like a structured light method. The requirements for laser triangulation with regard to the scene are particular to the view desired and the view available from a given vantage point, while for VSHOT the orientation and size of the scene objects must be considered [91], [90], [100], [95].

The VSHOT sensor plate can be implemented as a translucent filter, diffusively scattering the spot for measurement by camera. Details on the method of measurement of the angle of the ray coming off the mirror are difficult to obtain. By inspection this can be measured by movement of the plate along its' normal vector, using the difference between the spot locations over the displaced distance to calculate incoming angle.

#### **3.8.5 Other Methods**

*There is very little research in the area of metrology of specular surfaces*, the reason primarily being due to the nature of information transmission. A diffuse surface effects a complex transform on incoming radiation, removing a large amount of information on the original path taken and distributing information on intensity to any viewer able to observe the surface. This decouples the observer from the scene, allowing a limited number of observers access to a portion of all radiation in the scene given few constraints. Without such a transform, an arbitrary scene would require an infinite number of observation locations on a surface bounding the scene, or a number of observers that are sequentially swept through all locations on the bounding surface.

The scene complexity is however almost always constrained, both in object surface complexity and in the number of light sources, allowing development of particular solutions to the general problem. Since particular solutions are less useful from an industrial and research perspective, and a large number of observation points is expensive to implement, it is natural that less research effort would be directed to solve them.

### 3.9 Holography

Holography is a complementary method to structured light methods, and has been used to determine scene structure in a range of scales. It is necessary to consider this method as a candidate solution to our fundamental problem.

#### 3.9.1 General principles

Assume that the scene is filled with a transfer substance that does not attenuate the light appreciably, such as clear air. When a coherent wavefront is presented to a scene, it interacts with objects in the scene in terms of transmission, and specular and diffuse reflection. The interactions result in phase and intensity changes, which when compared with the original wavefront produces a diffractive pattern that can be measured in intensity. The comparison of the light rays from the scene with the reference allows information on the phase to be recorded [101].

By projecting a reference waveform through the film used in the capture of the field, the resulting light field is the same as that of the original. This allows observation of the original scene from any viewpoint. The information on phase is distributed throughout the recording film, such that any region of the film contains full information on the whole scene. The limited, finite resolution of the film results in a lower-quality reconstruction for smaller film sizes [101].

#### 3.9.2 Reconstruction

The reconstruction can be performed digitally with low computational cost, since the fundamental interactions that result in the observed waveform can be computed by Fourier transform. This makes it possible to record the hologram digitally and reconstruct at any point in the scene, including an observation plane that cuts through a physical object. This allows measurement of shape properties of every visible surface, and by taking a multitude of cutting planes a 3D surface can be found. This technique is used in microscopy for the measurement of cell shape [101].

#### 3.9.3 Practicalities of Implementing Holographic System

The challenges in holographic recording and reconstruction have been in the physical expression of the recording mechanism:

1. The implementation of a high intensity coherent light source, requiring a laser light source or sufficient power. The source must be sufficiently powerful to provide sufficient signal against background light sources that constitute noise.
2. The comparison of the observed and reference waveform, requiring a stable structure.
3. A high-speed, and thus highly-sensitive recording device, since micro-structural vibrations in the physical implementation over the shutter time will corrupt the phase interactions and thus the recorded image.

#### 3.9.4 Applicability to the current problem

The principle of holography initially appeared to be most suited to shape measurement of solar concentrating mirrors and their general analysis, however the light source requirements over the range of scales of solar system in use make this a practical impossibility. *The size of the system in*



*terms of observation film is on the order of the focal region of the optics, while the size of the source is on the order of the system itself.*

### **3.10 A Holographic Theory of Measurement**

The principles laid out in holography present an interesting situation for defining the limits of information in describing a system. The Plenoptic function at any visible point in the space can be captured on the surface of a film, where *visible* is having an optical path to the source and to observer. This defines a region where a holographic measurement can be made, which is distinct from other regions that are optically bounded from it. In the case of an object whose voids are not of interest, the shape of the exterior of the object is encoded entirely by a holographic film enclosing the object.

Comparing the application of holography and the application of image based rendering, it becomes evident that the two approaches are complementary with their approach to capture of the Plenoptic function. Holographic measurements hold the wavelength constant and measure the phase, while light field methods ignore phase and can resolve wavelength. Given different physical implementations the two methods are equivalent in capability when directed toward the problem of shape measurement in the bounded region, though each has its' difficulties in practice.

*In either case, if it is possible to restrict the sources of electromagnetic energy to being outside the enclosing region containing the object of interest, the effect of the object on radiation flow can be completely characterized by sufficient measurements on the boundary. In cases where the source of radiation is known, the object surface shape can be found. This general observation will thus form the basis for the design of our measurement method.*

### **3.11 Chapter Summary**

This chapter contains a literature study focussed on understanding the design process for concentrating solar thermal collectors, the analytical tools used in this process, the physical phenomena that are relevant, the current constraints on the design process and the physical constraints emerging from the fundamental nature of the problem. A comparatively large emphasis is placed on this understanding within the current tools available to the design process, and the physical form of the current solar thermal energy capture systems. The latter are investigated due to the combination of information requirements and constraints that arise from the models and real-world challenges these modular designs bring. The possible solution space for information capture is large, and such investigations allows ascertaining the real requirements toward producing an economically relevant research output.

The analytical methods used for such systems are covered in order to inform on what are the useful quantities to be determined by a measurement system, and at what spatial and temporal resolutions. The more recent developments of solar thermal technologies were found to benefit from information as to the flux distributions in the focal region, with active control benefiting from a temporal response better than the thermal inertia at the absorber surface.

The non-linear aspects of exergy and entropy production were shown to be vital with regard to the ideal operating point of such systems, as opposed to the linear relationships in pure energy terms.

Due to this non-linearity a whole-system optimization is required, factoring in the prime mover and the thermodynamic effects of the prime mover was shown to be important, both for overall system efficiency and for dynamic operating characteristics.

The effect of losses were covered due to the effect of dusting and other real-world effects that cause deviations in field conditions. The heat transfer models used in modelling interactions between the collector, receiver and the environment were covered to determine useful measurement quantities and characteristics.

The measurement techniques used in characterization of solar flux were covered in order to determine the methods by which measurement has been and can be made, each of which has particular constraints. The storage and representation of such information was covered due to the relevance in computability and the ability to predict new views between known points of prior measurement. The methods by which images are acquired were covered, including differing camera models, in order to supplement understanding of the techniques used in measuring solar flux. These are all aspects that are important in the design of a measurement device.

Metrology of surfaces was briefly covered in order to demonstrate the lack of suitability of existing techniques in mapping general specular surfaces. Holography was covered due to the importance of the technique for understanding the information requirements of the problem, however despite the great theoretical suitability, direct applicability of existing techniques in holography is not possible due to the light source requirements.

Finally, a parallel with the informational content of light fields and holography was identified, allowing a reasonably complete understanding of the general information problem and thus a better theoretical handle on the design of the intended measurement system.



## **4 Design**

This chapter addresses the design requirements, process and models with regard to the core objectives.

### **4.1 Measurement Technique Design Requirements**

In the literature, design requirements for a suitable sensor have been outlined by inspecting the methods of modelling irradiance interactions at the receiver. The measurement of the radiant energy passing through a closed surface around a region of interest is desired. The method proposed will be discussed from the material realities that constrain the task in general and the project in specific. The aim is a best attempt at meeting the theoretical requirements discussed previously.

What is required is a method that is:

#### **4.1.1 Cost-effective**

Cost effectiveness is a general as well as a project specific requirement, since an instrument that is of great accuracy and great expense has arguably less cumulative economic effect than one of reasonable accuracy with reasonable expense. This can be achieved by the following requirements:

1. No requirement for special production equipment, where “special” is indicated by a significant cost and singular purpose.
2. Controlled and reasonable tolerance of manufacturing error in the instrument production process, with sufficient production yield in batch processes. The yield is a function of the particular manufacture method and the effect of a unit failure, the total probability of such a failure, and the sensitivity to the total number of failures.
3. Use of inexpensive materials, preferably chemicals and structures that are available from commercial providers.
4. Competitive pricing even when production is in job-shop or small batch quantities, where “competitive” is defined as being of lower or equal cost-benefit to existing methodologies, if they should exist.

#### **4.1.2 Operable in production environments**

The power-production environment is where some of the main sources of calibration-related loss occur during construction and operation. It is also the least understood area in the practicality of solar thermal power generation, as is evidenced by a not insignificant shortfall between what is predicted during design and what is achieved after a large amount of capital is expended.

This criterion is stringent as it precludes any form of artificial radiation, be it structured or scanning, that requires a radiation controlled environment. A desired property is the direct use of the solar radiation coming from the collector in production operating environments. This requirement is both for reasons of general applicability and the problems associated with implementing, servicing and powering any sources of radiation.

Some of the expected factors present in operation environments that are most often not present during controlled testing in the design phase are:

1. Alignment of the concentrating optics required during installation.
2. Lensing effects of heat shimmer from air in contact with the hot surface of the optics.
3. Dusting of the optics and collector with respect to the site specific nature.
4. Drift in the structural shape of optics and collectors due to settling of joints, material property changes under temperature and continuous cyclic operation.
5. Real world weathering of radiation absorbing, reflecting and transmitting surfaces and materials under the effects of constant cyclic operation. Accelerated weathering is used to simulate this effect in a controlled environment, however this may not account for all effects present in the field.

#### **4.1.3 Mouldable into a generic closed surface**

To account for the variations in concentrating solar power system form and scale, the measurement technique should be general and not inherently limited in size or shape by the physical relationships governing implementation of the technology. Limits on size are technical and practical. There may be a fundamental physical relationship limiting the size of the produced measurement surface or that a measurement device would be required that is comparable in size to the system being measured. In the largest solar thermal systems a measurement device of comparable size would be completely unworkable.

The goal of an arbitrary surface is achievable by either manufacturing the primary sensor surface directly in the final form, deforming it to the desired shape, or simulating it by stitching together partial surfaces swept over the region.

#### **4.1.4 Directly applicable**

It would be more useful in a general sense if the measurement problem were to be solved by a direct route, rather than by problem transformation, in order to be more easily adapted to the variety of solar systems in current use. If the transformation is to be avoided the measurement technique would need to directly measure the predominant fractions of solar irradiation, using electrical transducers. The response time should be faster than the expected rate of change of radiation, under the influence of earth's rotation, cloud cover, and deviations in the solar tracking system that may be present in the system being measured.

#### **4.1.5 Technically comparable**

In order to be relevant the technique should be sufficiently accurate to enable informing finite-element style analyses that have been reviewed, this constraint is however difficult to quantify. It will be assumed that a discretization increasing modelling resolution by  $10^3$ , over the case of a single aggregate measurement, is sufficient for demonstration purposes.

Measurement of the energy flux is desired, however sensor material constraints will make it possible to only measure indicator variables in the form of weighted subsets of the incoming radiation. In order to relate these indicator variables to energy flux, either normalization is required

against a calibrated primary energy measurement, or against an estimate prior distribution of energy against the indicator variables. In this way, a close link that is complementary to existing solar-related measurement solutions is naturally present.

#### **4.1.6 Theoretically complete**

Since the problem is similar to that of other forms of optical measurement, developmental trends present in this area can be used to gauge the development of a solar-specific optical technique. With this in mind the solution developed should attempt to cover all the factors pertinent to the measurement problem, and thus capture of all the information designated as useful to its' purpose. An intermediate solution would both not provide a good base for further development, or optimize existing instrumentation, and should thus be avoided.

## **4.2 The Sensing Problem**

In this section the desirable physical characteristics of the previous section are discussed, and the requirements of a sensor most suited to the problem of solar collector characterisation are developed. The aim being for finding a technically useful and economically feasible solution.

### **4.2.1 The Measurement of Phenomena**

In the literature on light fields and holography it can be seen that: given the understanding that obtaining complete information about the state of the radiative flux (that is the direction, intensity, polarization, wavelength and phase) passing through a closed surface around an object, it is possible to determine:

1. The amount of radiation absorbed, transmitted and reflected in scalar terms.
2. The directions, wavelength and source strength from which the radiation originated both inside and outside the region.

It cannot be determined from these measurements alone whether a specific packet of radiation was absorbed, transmitted or reflected. Integrating over the surface allows determination of how much radiation has been absorbed by objects within the surface, regardless of knowledge about the objects themselves.

Obtaining complete information about this radiative flux in both directions through the surfaces is not possible, given that any conceivable sensor would occlude the path of incoming radiation at least to a certain degree. The nature of the radiation passing through the surface would also otherwise be corrupted to a certain degree, whether it be direction, intensity, polarization, phase or wavelength. It thus makes sense, with respect to the general problem, either to:

- Restrict our sensing to radiation passing from the outside inward, or
- sample a portion of incoming radiation, allowing the remaining to pass unimpeded, and further sample a portion of the outgoing radiation.

Partial sampling is more challenging given structural implications in a real sensor, but is not infeasible when considering multi-layer photovoltaic devices relying on such an arrangement. The measurement should be taken in a way that the regions of the surface that do not form part of the sample regions can have their values estimated, given that most images formed on surfaces are:

- piecewise smooth, and
- without an expected distribution, that is of an arbitrary general nature.

The sampled regions should be ideally be arranged such that the number of measurements are equally spaced on the surface. This would allow interpolation of the radiation over the surface dependent on the spacing of the sample points. Accuracy in interpolation is limited to the assumption of spatial value change.

Given that the general problem is one of a time varying radiative flux, the samples should be made at a representative instant in time, simultaneously for all points on the surface. The special case of a static flux can be sampled over a period of time, and samples from each point need not be synchronous. However, any method that may require integration over time in its' response will need to account for this. Further development should bear in mind that compressive sensing techniques may be used to sample spatial frequencies greater than traditional sampling theory would allow.

Several factors complicate the process of partial sampling of the radiation:

1. Errors in position and orientation of the element.
2. Errors in performance of the measuring element, with regard to the response to radiation intensity, angular distribution and wavelength.

Understanding and compensation for these errors is the task of calibration, in particular the elimination of the positioning and wavelength errors. Deviations in orientation have an uncertain effect depending on the specifics of the element construction. In the case of most current technologies the effect of the cosine angle response characteristic is to desensitize any basic flat sensor element from these errors.

More elaborate constructions and structures that are sensitive to position are more difficult to calibrate, since these are particular to the individual device and not a property of the batch. Calibration of structures and positions of such components as lenses and mirrors is time consuming and expensive unless performed by specialised tools and amortised over large production runs.

#### **4.2.2 Material Sensor Characteristics**

In order to sense radiation in an efficient manner in the current paradigm, it is required to transduce the radiation into an electrical signal that can be processed and recorded. A study of the sensors developed for solar and general light measurement purposes show the possibilities to be in two general classes:

1. Direct Measurement: Whereby the radiation is transduced directly to electrical currents or voltages, which can be measured directly.
2. Indirect Measurement: Whereby the radiation stimulates some other measurable phenomena that has a functional relationship to the radiation, is itself measurable.

The direct measurement methods are more modern methods than the indirect methods traditionally used for solar measurement purposes, made possible by advancements in

semiconductor manufacturing. However direct methods have a greater specificity in response and do not generalize well to the problem of accounting for the spectral composition of solar radiation.

Direct methods are dependent on a few effects:

1. Active photoelectric emission in a semiconductor material: The basic form of sensors constructed in this way can be operated in two modes:
  - a. Photovoltaic mode (Open Circuit), with increased sensitivity but slower response times.
  - b. Photoconductive mode (Short Circuit), with reduced sensitivity but faster response times.
2. Passive photoelectric emission resulting in the photoelectric effect, in which an increase in radiation on the sensor results in a decrease in resistance over the sensor. This mode is the only possibility when an irregular junction structure is present.

Indirect measurement methods are derived from methods that have traditionally been more useful, especially with regard to historical availability of analogue signal capture and processing. Mechanical recording devices and manually operated instrumentation based on the heating effects of radiation on physical devices have been the basis of some of the most accurate measurements of solar radiation phenomena. *An extensive study was performed in the early stages of this project in an attempt to re-develop some of the well proven measurement methodologies for use in the problem at hand. It was determined these methods are not well suited to the problem this study is concerned with.*

The indirect methods are advantageous in that they are better at integrating over the properties of the radiation. They have a broad response to wavelength, polarization, phase, orientation and intensity. This results in a measurement in the terms that are most useful to investigation into power generation; that of radiative power incident on the sensor. This would make them ideal if it were not for their extremely poor spatial resolution as a result of their physical size, the great costs and technical hurdles in miniaturization of such methods, and slower response times in comparison with the direct methods.

The direct methods are easier to miniaturize, cheaper to produce and have faster response times. The wavelength dependence of the semiconductor material is chemistry dependent, with maximum response centred around the wavelength determined by the bandgap of the semiconductor. This frequency response can be accounted for to a certain extent by the use of multiple semiconductor materials, either separately in distinct sensor elements or blended together to form a composite chemistry of multiple layers, or a single bulk lattice. It proved difficult to find any information on the response function to radiation of composite chemistries in bulk form. This may be due to the focus of research on the power generation properties of multiple layers with semiconductor bandgaps, so-tuned to cover the energy-carrying regions of solar irradiation.

By definition a bulk composite chemistry for the explicit purposes of having a desirable sensor response function would only be possible in photo-conductive mode. This been an unattractive idea, due to the greater commercial viability of photovoltaic sensors that can be produced with generic silicon semiconductor technology.

The back-to-back serial-parallel electrical connections of the junctions in the substrate in photo-conductive mode necessitate the formation of channels of differing chemistry that are connected in parallel to the terminals. If these channels were connected in series, an increase in conductivity due to one wavelength response would not be detected, since the photo-conductive effect is to raise the limiting leakage current through the semiconductor junction. This indicates that in a series connection a lack of response in one channel will limit the response of another.

### **4.3 Development of a Measurement Solution**

This section focusses on alternative solutions that were considered, the presentation of which is necessary to illustrate the difficulty in meeting design objectives using technology available in the current landscape, and the justification for the proposed methodology with respect to these challenges. The measurement problem can logically be broken down into two fundamental problems, this reductionist method was applied at the outset in order to transform the problem to a domain that had already been solved. The final solution is however non-reductionist, the benefits of which became apparent when the interfacing of possible solutions to the fundamental problems presented undesirable performance.

#### **4.3.1 Selected Measurement Concept**

The appendix section titled "Concepts for Measurement" on page 161 describes a number of design concepts considered, which successively add complexity. These sample the Plenoptic function with varying degrees of simplification, with considerations as to the manufacturability of the measurement scheme. This process resulted in a design based on complete light field capture, which will be expounded upon below.

##### *Light Field Capture – 4<sup>th</sup> Generation Imaging?*

The concentration of solar flux decreases with distance from the focal region, consider then an arbitrary surface that can be made to pass through a region of low concentration. This possibility is important when material properties of sensor cannot handle the saturation temperatures present in the region of the receiver, introducing complications with cooling and attenuating high irradiances. Since the measurement surface is not identical to the receiver surface; directional information is required to predict the intensities of concentrated flux on the receiver by projection. This approach is a process of light field capture, corresponding to a 5D light field video or a 4D light field lumigraph, depending on whether the capture time is relatively low.

A complete implementation of light field capture without a slow process of positioning requires multiple spatial pixels with their own directional measurement surfaces. In the solar measurement situation this can be implemented by an aperture plate with multiple apertures spaced at regular intervals, projecting images onto an imaging surface. The aperture-imaging complex is curved to enclose a region that includes the focus, since if both location and direction are captured in a light-field structure this surface can be made arbitrary in size. In addition to this a spectral filter mask over the imaging layer can provide spectral differentiation, and interpolation between locations allows an estimate of spectral content for every direction. A polarization filter mask can be similarly applied, however this is not useful for our purposes.

A specific implementation of this concept is demonstrated in Figure 19 and Figure 20, below on pages 63 and 64. The assembly describes a light field camera in a frame that mounts around a collector tube, with a photosensitive layer and a curved aperture plate that simultaneously acts as a lens and limits the solar flux on the sensor.





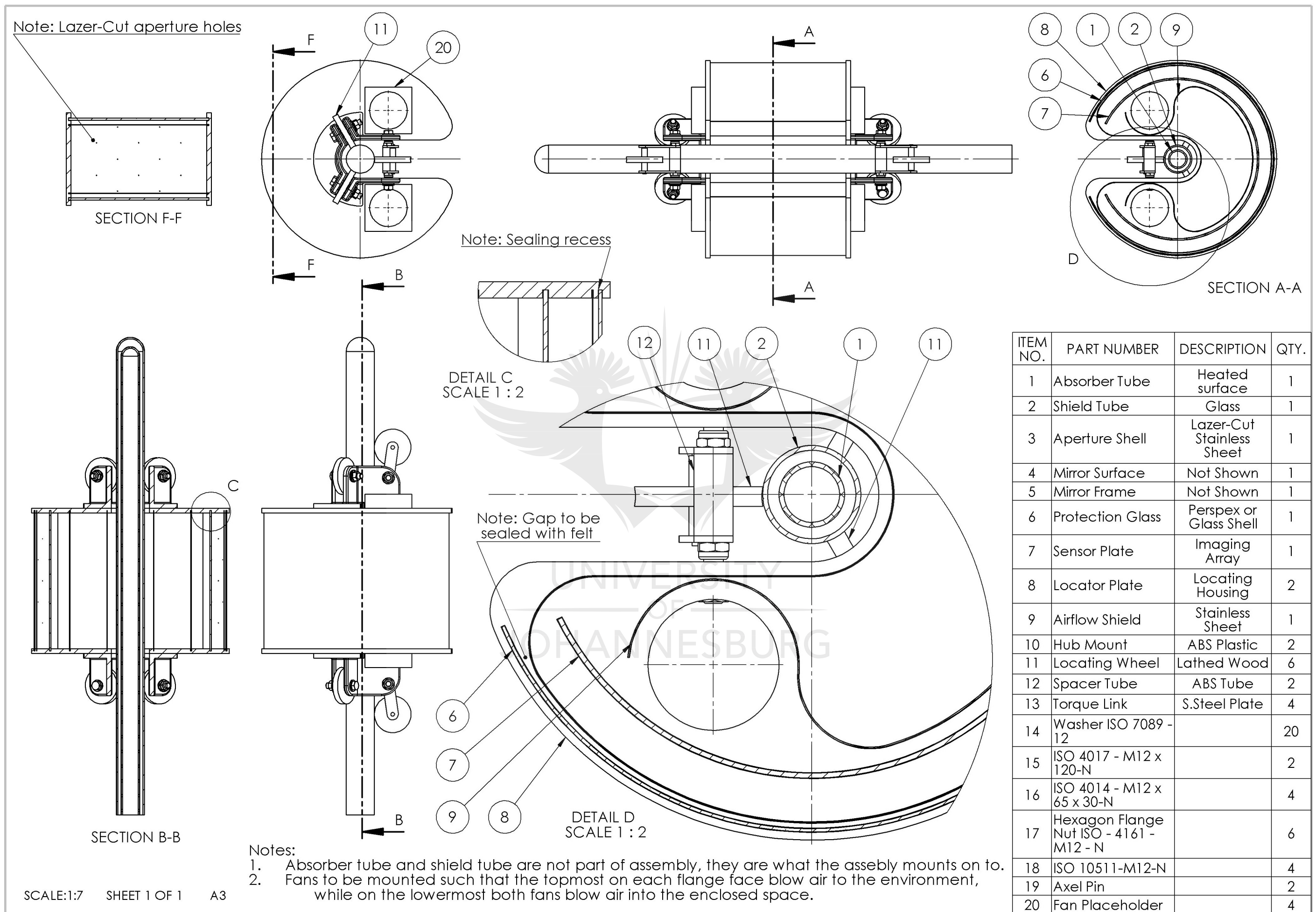


Figure 19: Solar Light Field Capture Assembly Drawing

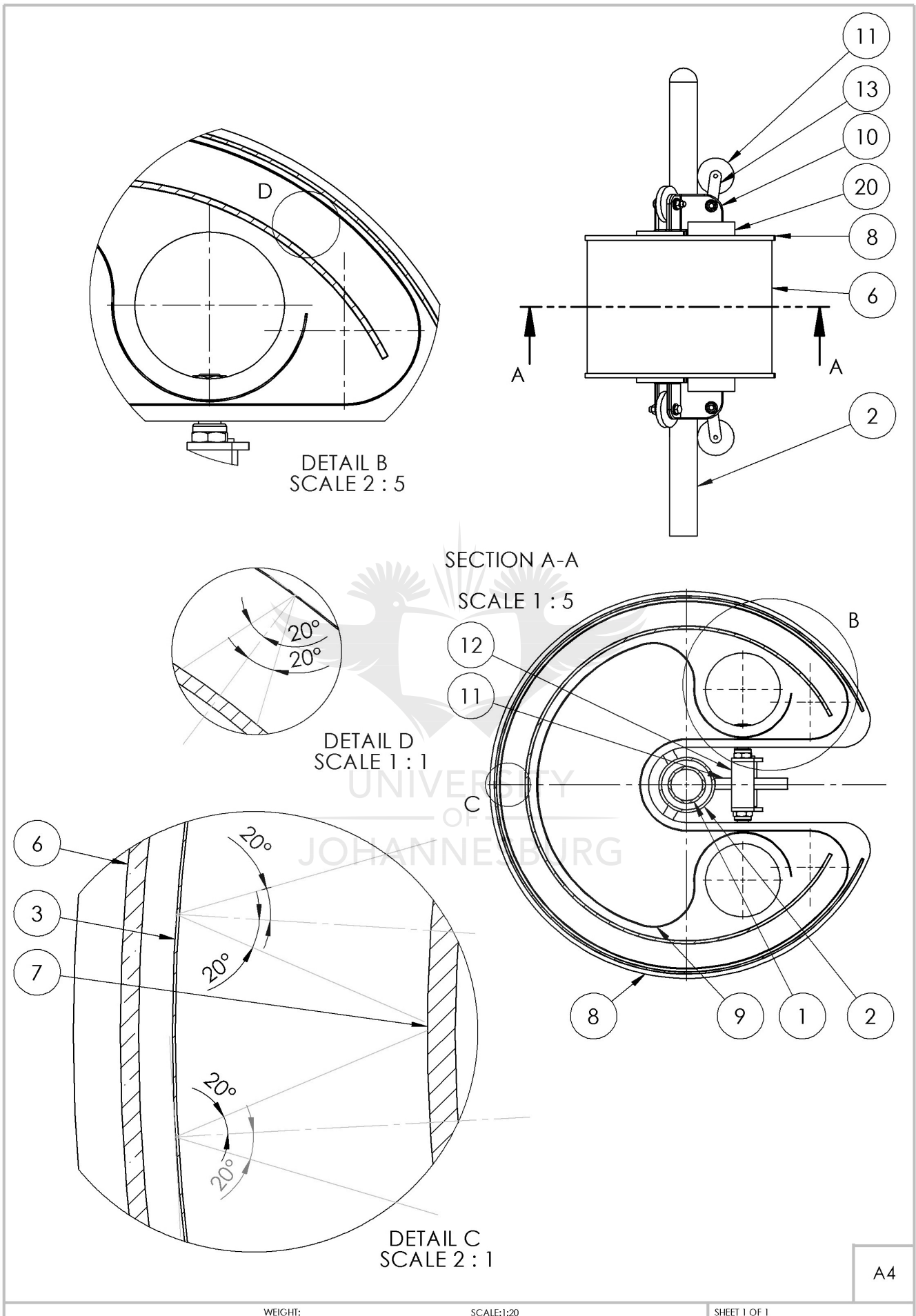


Figure 20: Light Field Capture Concept, alternate view.

### 4.3.2 Description of Light Field Capture Concept Design

The system in Figure 20 is a specific instance of the measurement concept, for the purposes of demonstrating the principles of operation. The design is to scale for a common, standard size of receiver tube used in parabolic trough designs, however dimensions have been omitted for clarity. This concept is representative of the technological form, which scales in proportion to the size of the receiver tube.

The form is cylindrical, with a cut-out for attaching to the receiver tube. The locating shroud (item 8) holds the parts in location and shields the internals from radiation. There are four layers which form the basis for the design:

1. An outer shield (item 6), which is either glass or perspex and serves to keep dust out.
2. An aperture plate (item 3), which is a thin stainless steel sheet with apertures laser-cut in a hexagonally-packed structure. These form spatial pixels that form pinhole cameras that project images onto the sensor array (item 7). The plate thickness at the apertures is thinned by localized grinding in order to improve the quality of the pinhole effect, thereby reducing vignetting effects.
3. A sensor array (item 7), which is a two-dimensional array of light sensitive elements which is temperature-controlled by airflow that is managed by fans and an air-flow shroud (item 9), which also serves to shield the sensor array from light contamination through the fan ducts.
4. An air-shroud (item 9), with a black coating to minimize internal reflection. The form allows approximately uniform air-flow over and under the sensor layer, the fans on the upper ducts extracting hot air and the fans on the lower ducts pressurizing the chamber.

Inspecting detail view C and detail view D, there are multiple pinhole projections from the aperture plate onto the sensor array. These interact with one another at the overlap, however vignetting due to a finite thickness of aperture results in a practical conic angle.

The physical design parameters of interest here are: the overall diameter of the aperture shield, the aperture hole size, the distance between aperture plate and sensor plate. A less important parameter is the air-flow thickness as a result of the form of the air shroud.

### 4.3.3 Temperature Compensation

Every available direct sensor technology is subject to response due to both irradiance and temperature, the latter needing to be compensated against. This requires active cooling and local calibration against operating temperature, and is an important design feature that is common to most possible arrangements. The core issue in temperature compensation is mathematical processing for the decorrelation of the resulting signals, this will be covered in the section on calibration.

### 4.3.4 Considerations for the Concept Design

The outer shield, aperture plate, and air shroud are straightforward to specify and design. The distance between aperture plate and sensor array, and the distance between aperture pinholes can be easily specified. By application of Rayleigh resolution and the trade-off between spatial

resolution and angular resolution at each aperture, the size of the device is specified for a given resolution at the sensor array.

*The primary problem is identified as the construction of the sensor array.* This construction is relatively simple in the case of smaller systems, however as the concept scales to systems like central receiver towers this becomes a significant challenge. *This has become the primary focus of the investigation, since it is common to other methods of sampling the Plenoptic function that require large sensor arrays.*

#### **4.3.5 Manufacturability of the Sensor Surface**

The physical nature and inherent limitations of sensor technology must be considered if the technology is to be implementable in a practical way with limited, low technology resources for manufacture. This consideration is the component of the method with the greatest complexity in reliable implementation, and is of prime importance if such a technology is to rapidly and widely adopted in an environment with inherently low production volumes.

Consider the manufacture process for a semiconductor sensor of passive or active nature: In general, the active sensor junctions are either made in an amorphous, crystalline processes, or by organic methods:

1. Amorphous sensors can be made by chemical deposition or composite mixtures; a solvent is evaporated from a controlled film, with multiple chemistries being applied under controlled temperature and pressure. The photovoltaic efficiency of these sensors is poor, but there are multiple exploitable chemistries that are easily produced without special equipment. A simple passive photoresistor can be made by reaction on a substrate or by film application that is controlled by spraying or various applications of ink printing technology. In relation to this project these sensors are:
  - a) Suitable for manufacture in a job-shop environment due to the simple chemistry and methods of deposition.
  - b) Manufacturable using a modification of the commercial inking processes.
  - c) Technically able to be applied to any closed region without regions of high-curvature or self-occlusion, with respect to an instrument that would apply the chemistry to a substrate.
  - d) Of a response that is dominated by the chemistry of the semiconducting material used rather than the physical construction. This response is due to the averaging effects of imperfections that tend to destroy quantum effects that rely on specific physical structures.
  - e) Unable to be tuned reliably to specific wavelengths of radiation and subject to greater variation in process and response to wavelength and intensity, thus requiring greater amounts of post-manufacture calibration and possibly re-calibration as the material ages with use.
2. Crystalline sensors are produced by the controlled growth of a semiconductor wafer that is later doped to produce P and N type semiconductor materials. This process is expensive,



energy intensive and require rare earth materials. These sensors require tight structural and chemical control in order to have good photovoltaic performance, with wavelength responses as much a result of the physical dimensions of the junction as it's chemistry. Much effort and research has been concerned with the economical production of consistent and accurate crystalline sensors for photovoltaic power production. In relation to the project these sensors can be seen to have the following problems:

- a) Requiring of specialist equipment and great technical skill in order to obtain a custom sensor of sufficient accuracy and repeatability.
  - b) Are relatively expensive when obtained in discrete form from commercial processes, since the packaging cost is a significant portion of the overall cost of a semiconductor device. This expense is magnified in the amalgamation of a global sensor using discrete components, along with the expense and difficulty in quality control of a final product using possibly thousands of discrete components to be produced in low quantities without automated integrity testing equipment.
  - c) Are currently not manufacturable as a single device with the shape of an arbitrary closed region. There has been little to no investigations to this effect, the equipment for manufacturing such devices has not been developed and there is little commercial interest in doing so.
3. Organic sensors, which are a modern alternate that are based on the production of layered junctions of semiconducting carbon chains. The current techniques produce relatively inexpensive cells with low efficiencies and relatively poor lifetime under solar radiation. Organic semiconductors can be used to form both active junctions and photoresistive layers, and there is continued active research into improving the performance of active junctions for photovoltaic power purposes. In relation to the project these sensors are:
- a) more difficult to manufacture in terms of obtaining the chemical precursors, most of which do not currently have uses outside of laboratory research; and
  - b) a highly promising avenue of further research due to their formability into arbitrary shapes, along with an inherent plasticity that would allow more reliable mechanical adjustment of a sensor without the risks of cracking.

It is evident that what is needed is a design that tackles the problem from first principles, that seeks to reduce physical complexity, for which a few observations can be made.

1. The manufacture of amorphous photoresistive films is a straightforward and inexpensive process that may benefit from additive deposition provided by inkjet, transfer and silk screen printer technology. The semiconductors are fairly readily available, although they often have environmental and health risks associated which will limit the commercial application of their use under RoHS agreements. Techniques shown in [102] can be used in this regard.

2. A photoresistive film is an entirely passive single layer device that is less sensitive to radiation than layered junction sensors, however in this application the lower sensitivity and passive operation allow greater levels of radiation to be detected.
3. A photoresistive film can be deposited directly on a heat transfer surface. This possibility is imperative if a sensor exposed to high fluxes is to be operated under steady state conditions, and while other junctions can be cooled just as efficiently, there is currently no commercial motivation to do so for high-irradiance imaging sensors. The CCDs used in imaging low light conditions or in the infra-red region are cryogenically cooled, however the methods of cooling are not suitable for solar purposes due to low cooling capacity and great expense.
4. There arise greater issues in initial calibration of an amorphous photoresistive sensor, and possibly greater sensor drift with use than the discrete commercially available components that could be used.

Since photoresistance is a passive effect the application of linear circuit techniques makes the behaviour less mathematically complicated and more numerically stable to simulate than the exponential functions found in junction devices.

In this project the issues around manufacture are secondary to the measurement technique itself. The use of discrete, quality controlled components of low cost would benefit the evaluation of the measurement technique, bearing in mind that a production version of the technique would avoid using discrete components. An initial prototype would best use discrete photoresistive elements of an amorphous structure that are commercially available at low cost: Light Dependent Resistors (LDRs).

#### **4.4 Mathematical Considerations for the Sensor Array**

A key design aspect are the theoretical constraints on the design in terms of physical nature, along with mathematical and algorithmic treatment. This section aims to address these.

##### **4.4.1 Introduction**

*The sensor array is of primary interest, however current photosensitive array technologies cannot scale without significant problems.* This section seeks to develop another method of sampling a large array of sensors using a mathematical mechanism for reducing physical complexity.

The system that will be developed is an implementation of a non-linear compressive sampling system, and represents a non-linear compressive sensing mechanism with deterministic rather than probabilistic sampling system. *This system is being dubbed "Electrical Impedance Tomography Manifold Sensor Array" (EITMSA).*

##### **4.4.2 Device Layout**

After consideration of the manufacturability of sensor elements from the point of view of the sensor technology, questions arise with regard to implementation in the context of the sampling of points around a region of interest:

1. How can the sensor elements be pixellated in order to sample a sufficient resolution? This entails that:
  - (a) the elements be made small;
  - (b) the spacing between the elements be made small; and
  - (c) the elements have integrity relative to one another, that is elements do not share responses in an indeterminate manner, resulting in spontaneous loss of resolution due to unquantifiable amounts of sympathetic bleed, local averaging or other such effects.
2. How can the sensor elements be integrated into a measurement field? This entails that:
  - (a) the elements be addressable, in that their response must be identifiable with respect to the response of their neighbouring elements and any element in the field; and
  - (b) every element in the field must have a position that can be determined, either during manufacture or during calibration, given that the substrate may be deformed as part of the manufacture process.
3. How can the information made available in their material responses under radiation be obtained in a direct manner? This entails that:
  - (a) a *manageable* amount of interconnect between the equipment reading the sensor response be present;
  - (b) the interconnect does not contribute in a significant way to the final measurement, either by the introduction of spurious energies or the loss of components of the signal; and
  - (c) the interconnect be able to transmit the responses of each element in a way that each element response can be identified as distinct to a desired degree from the other elements. Without this it would be impossible to identify regions of the surface being sampled.

In order to increase the amount of information available for optimization to be possible, it is necessary to consider answering question (1) in a way that generates a significantly large amount of pixels. In order to answer the questions of field integration (2) and information retrieval (3), while maintaining the requirement of (3.1), it is necessary to investigate ways to multiplex the signal from possibly millions of sensor elements in a way that makes practical sense.

There currently exist a few ways to do this that are suitable for the interconnect required for sensing passive photoresistive elements. Unlike charge-inducing sensors found in a CCD, photoresistors require that an electric field be actively set up across the elements and the current passing through the element measured. Alternately a current may be set up and the voltage field measured:

1. Direct, separate connections on a common supply bus.
2. Grid Multiplexing.
3. Grid Multiplexing with shift registers.
4. Charlieplexing (but only with tristate switching).



These methods all suffer from the significant drawback of requiring an amount of interconnect that scales either linearly or with the square root of the number of elements being sensed.

The issues of multiplexing is also present when excitation is not required, as evidenced in CCD and CMOS imagers where a grid multiplexing technique is used in a shift register fashion to capture an image. The complexity of this interconnect is a very large part of the manufacturing and electrical complexity of such devices, with the actual area being sensed being on average only about 50% the silicon area of the device.

This huge amount of interconnection is completely unacceptable when using discrete elements to make up a larger device due to manufacture time, complexity, expense and quality control issues. In addition to this, the interconnect is a major factor in the scalability of a technique, since the length of the interconnect (and thus associated cost) scales with the square root of the coverage area of the array.

*The problem of interconnect is severe to the point of making the sensing of a large, arbitrary region almost practically impossible without significant difficulties and investment in manufacture.* The number of joints and separate conductors to implement a typical grid multiplexing scales with the square root of the number of elements being addressed, which is a function of sensor array area. There is a linear scaling in the product of sampling time and the number of analogue to digital converters (ADCs) on the scheme.

The use of these multiplexing methods require an entirely new conductive layer that would be forced to lie behind the sensor elements. This complicates the manufacture process, the routing of long tracks of interconnect underneath a photoresistive layer would introduce many possible locations of manufacturing errors that would render sections unusable. This problem would be exacerbated by decreasing the size of components and under the application of thermal or mechanical stress. The connections between the underlying layer and the sensor layer occupy physical space that reduces the overall resolution of the field, and most importantly the manufacture of a flexible substrate for interconnect along with reliable connection with the sensor elements themselves is expensive and technologically constrained.

The practicalities of sampling such a region require new thinking. *What is ideally required to reduce the amount of interconnect is a method of multiplexing that scales with a function that grows at an exponentially decreasing rate*, i.e. the number of addressable elements grows at an exponential rate with increased interconnect capacity.

The largest problems in interconnect are in the primary layer (see Figure 21), this is followed by multiplexing that is used to reduce the amount of distinct data to an amount compatible with the choice of analogue measurement bus, which is the secondary interconnect. It is from the measurement bus that analogue data is digitised and processed to extract relevant information by Analogue to Digital converters. The control of the multiplexing scheme is coordinated with the conversion process, and is distributed by a digital control bus to the multiplexers. The primary interconnect is the subject of this section, since it represents the greatest burden on scalability and manufacture.

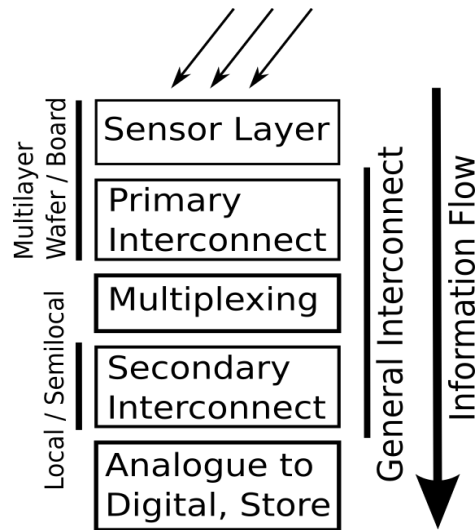


Figure 21: General sensor system layout

In avoiding the issues with manufacturing a multi-layer field, an entirely single layer field would require primary interconnect that runs through the sensing element structure itself. This structure is a possibility if it is accepted that measurements will influence each other, requiring recovery in a later process.

The degree of influence of measurements on one another is a design criterion, how much interconnect is required is a function of:

1. The number of measurements from which a reconstruction is made. The application of rank theorem requires at least as many distinct measurements as there are sensors to be measured in the field.
2. The distribution of the information of each sensor element to the measurements made. If a sensor element does not influence a measurement to a detectable degree of what is capable by the equipment, it will be impossible to ascertain any information about the state of that sensor element from the measurement. The design of the system should consider the spread of the amount of information over the measurements, giving a best attempt to distribute measurement resolution equally to all sensor elements.

In such a scheme the interconnect layer still exists, the quantity and complexity of which can be varied according the structures used in the sensor layer. The question of what structures to use in the sensor layer is a function of the degree of difficulty in separation of elements from each other, and is subject to the competing design criteria of:

1. Minimum effective intensity resolution of a set of sensor elements.
2. Scan time as a function of the total number of samples taken in parallel.
3. Hardware complexity in terms of the number of parallel measurements.
4. The total number of physical links to be routed during manufacture.

#### 4.4.3 Introducing the concept of tomographical boundary scan

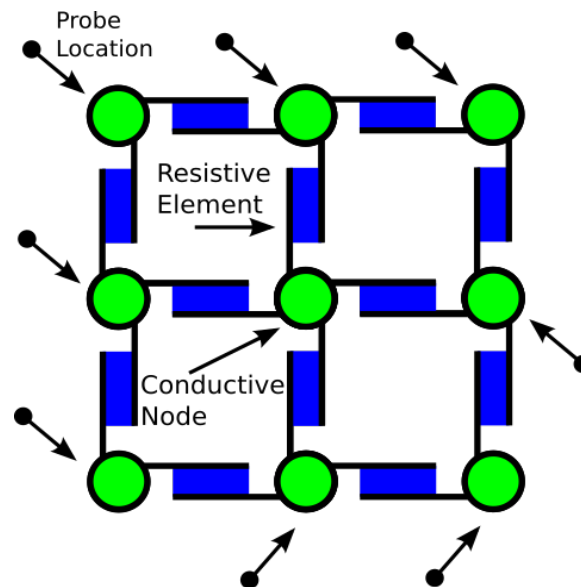


Figure 22: Example of sensing elements in a single layer field at the boundaries

Consider the arrangement in Figure 22; the layout is a uniform grid of sensor elements that are connected to each other by conductive nodes. The elements and nodes can be implemented on a single layer, adjacent to one another. The primary interconnect layer is integrated into the layout of the elements themselves, with measurements available at the boundaries of the field and multiplexing throughout the primary interconnect formed by the structure of the grid and the method of measurement. What is most useful in reducing the amount of interconnect is the way measurements can be made on this grid:

1. A boundary node may either be attached to a measurement probe or unattached.
2. Every attached boundary node can be driven by a voltage or current source and measurements taken of the resulting currents or voltages produced.
3. The number of non-distinct measurements from boundary nodes is proportional to the number of combinations of driven/undriven boundary nodes. *The result is an exponential scaling in measurements against interconnect capacity, a property previously identified as necessary.*

In order to resolve the responses of the elements, a sufficient number of *distinct* measurements is required. The principle of superposition in circuitry is well known and can be applied in reverse; that is by purposely ensuring that superposition cannot occur, in order to guarantee that measurements are distinct from one another. The principle of superposition states that:

1. Electronic circuits of passive continuous elements (ideal resistors, capacitors, inductors, memristors, operational amplifiers, transformers and transistors) are linear with respect to their excitation but not linear with respect to their values, in terms of reactances and response. Discontinuous elements such as switches and ideal diodes violate superposition, and must therefore be considered in each of their possible combination of states or simulated in a dynamic manner in order to ascertain likely state.

2. The excitation of a circuit by a number of voltage and current sources is equivalent to the sum of the contributions of each source taken separately, with the other sources all being made inactive:
  1. In order to render a *voltage* source inactive and ensure the circuit remains linear, a short circuit replaces the terminals of the source.
  2. In order to render a *current* source inactive, an open circuit is substituted across the terminals, inhibiting current flow.

The conditions for the production of distinct measurements differs depending on whether the excitation of the circuit is by voltage, current or a mixture of sources. This consideration is important, as the methods of ensuring distinct measurements differ in each case.

#### 4.4.4 Proof for ensuring distinct measurements under constant voltage excitation

In order to maximize the number of distinct measurements; it is necessary to ensure that superposition not apply, thus ensuring that no measurement is a linear combination of another measurement. If a system is equivalent to a linear combination of the responses of other systems, then this system does not add further information to the measurement scheme.

Consider a circuit with a number of nodes that are able to be driven tristate, shown in Figure 23, below on page 73. The square block to which the voltages connect is the field of a structure like that shown in Figure 22, and contains an arbitrary number of elements and nodes without internal short circuits. Each connection of a voltage source is to a different boundary node on the field.

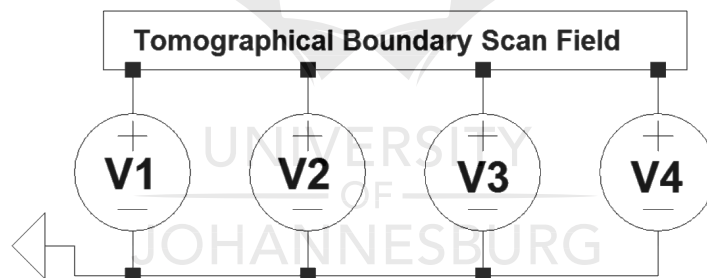


Figure 23: Circuit equivalent of voltages applied in tomographical boundary scan

A single measurement state with two active nodes is shown in Figure 24, with one excitation source and one node made to sink by connection to ground. The other nodes are disconnected by high-impedance switches.

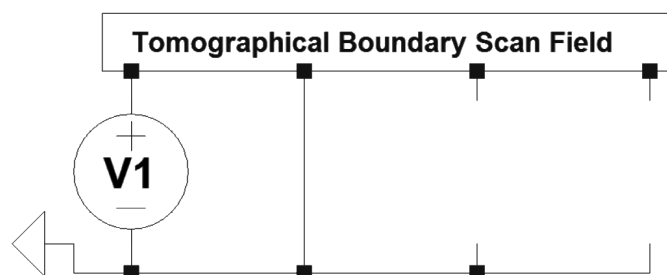


Figure 24: The connection situation for one measurement state

Any number of nodes can be made active for a particular measurement state; in Figure 25 an excitation source is connected to boundary node 1, while nodes 2 and 3 are made sink by

connection to ground. This represents a measurement state distinct from that in Figure 24, and thus supplies further information about the field. In practice it is possible to measure the current flow through all boundary node connections.

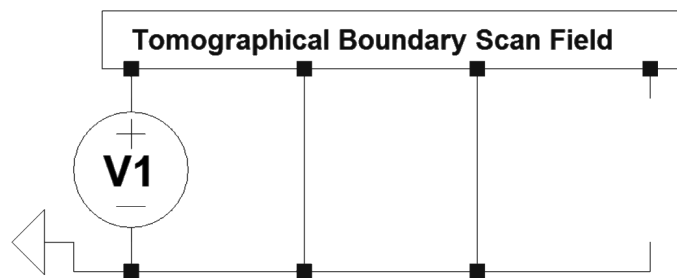


Figure 25: Superposition sub-circuits for one measurement state

In each of these measurement states it is evident that superposition techniques cannot be used to decompose the response into responses of subsystems. It is also evident that for a given node as sources, there are as many measurement states as there combinations of sink connections.

Consider the situation where there is more than one excitation source, as in Figure 26 below, in order to determine whether there is additional information in the state.

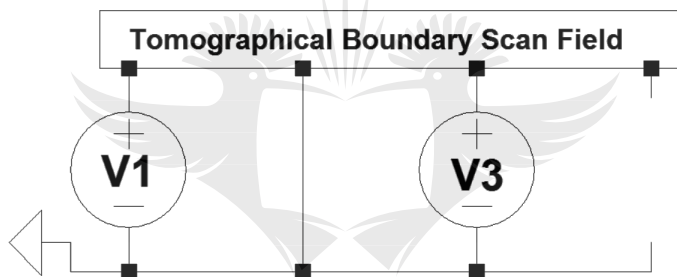


Figure 26: A measurement state with two sources and one sink

The system can be decomposed into a linear combination of two subsystems, as shown in Figure 27, one system for each source of excitation. It is immediately evident that two single-source excitations here would be present in the complete set of measurements possible with single source excitations.

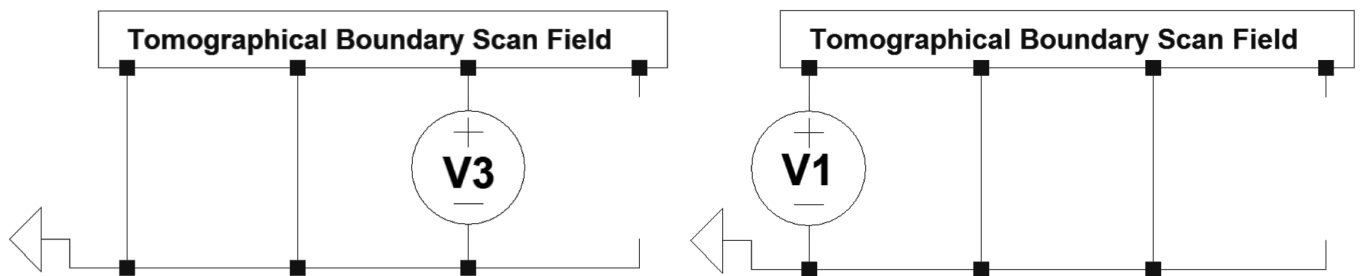


Figure 27: Subsystems as a result of a double source excitation

By induction this observation is true for more than one source in general, and thus it isn't possible to have unique measurements under these conditions. Since for every parameter a unique measurement is required, this forms the basis for comparing resolvability of the measurement scheme.

Thus it can be seen that a distinct measurement under voltage excitation is determined distinctly from other measurements by the use of only one source, a combination of “active nodes” that are any number of sinks that are connected to ground and “free nodes” that are in open-circuit isolation from interacting directly with either sources or sinks.

#### 4.4.5 Proof for ensuring distinct measurements under constant current excitation

It is possible to evaluate the use of current sources by use of logic similar to that above. In this case a distinct measurement under current current excitation is determined by a single current source, a combination of “free nodes” (maintaining previous functional convention) that are in short circuit with ground and a number of “active nodes” that are in isolation from any source or sink and thus open circuit.

This swap of roles (active v.s. free) between the voltage excitation mode and the current excitation mode is electrical only, the convention is maintained that the active nodes are nodes being “selected”, while the free (or “passive”) nodes are maintained in rest state particular to the type of excitation used.

#### 4.4.6 A lemma in practical illustration of uniqueness

The consequences of this uniqueness between states is borne out in the mathematical modelling of the response of the field. The details of modelling will be covered again in the section “The Forward Transform” on page 106, however a brief description is required here.

Using either Kirchoff's current law or Kirchoff's voltage law an identical system matrix can be derived using each. In this matrix every node in the field is connected to it's neighbours by conductances  $s_i$ , where  $i$  is the node index.

When using Kirchoff's current law to write equations for every node in the field, the following form is produced:

$$[S] \cdot \bar{v} = \bar{r} \quad (53)$$

where  $[S]$  is the system matrix of shape  $N \times N$  where  $N$  is the number of nodes in the field;  $\bar{v}$  is a vector of length  $N$  for the node voltages; and  $\bar{r}$  is a vector of length  $N$  for result of the equations. The result vector  $\bar{r}$  is normally  $\bar{0}$  when not augmented, representing current balance into and out of every node. It is possible to approach setting up the system for inversion to find  $\bar{v}$  in three ways, either;

1. the result  $\bar{r}$  is augmented with the currents at the boundary nodes,
2. the rows of  $[S]$  are augmented with unit diagonal entries, and the result  $\bar{r}$  is augmented with the applied boundary voltages for the corresponding rows.
3. A combination of (1) and (2) above.

*In the first case the system matrix remains static, that is there is one system description only.* In finding the response according to an application of voltage sources, an iterative method is required, since currents are inherent in the result vector. By assuming a set of boundary currents, a set of voltages at the boundaries can be found. These voltages then inform the boundary currents for further iterations. The system matrix is inverted once and applied to the augmented current vector at each

iteration, in order to find the voltages of all nodes in the system. These voltages are compared with the actual applied voltages at the boundary nodes in a process of gradient descent.

In this case, every zero entry in the result vector represents an open circuit with respect to the boundary node connection. The process is therefore forcing a particular response from a single system, rather than finding the natural response under applied voltage.

*In the second case the system matrix is itself augmented, producing as many system descriptions as there are measurements.* The rows of the system matrix  $[S]$  that correspond to the boundary nodes are given unit diagonal entries, and the result vector  $\bar{r}$  is augmented with the applied boundary voltages. The voltages of the other nodes in the system can be found by inversion of the particular augmented system matrix, and multiplication with the augmented result vector.

This demonstrates that for the natural response, *there are as many systems as there are unique measurements.* It is also evident that the type of excitation source matters to the uniqueness of the measurement, given a particular method of selecting a measurement by switching.

In the third case the system matrix is augmented at least once, and there may be anywhere up to and including as many systems as there are unique measurements. If all the rows are augmented as per case 2, all the properties of that case are maintained.

#### **4.4.7 Derivation of the number of distinct measurements given a boundary in naive sampling**

Since it is possible to express a measurement as consisting of a source, a number of free nodes and a number of active nodes: the procedure for defining a set of distinct measurements is a layered application of set combinations. The proof is slightly different from the case where elements are electrically symmetrical to where the elements have different responses in their V-I quadrants.

The procedure for proof under the *constant voltage excitation* is as follows:

1. The directionality of the elements is a function of the relationship between the source and active nodes. Since the free nodes are defined as high-impedance to any source or ground node, they do not participate in determining the direction of current flow.
2. The source can be of one potential that is higher or lower than the potential of any active node.
3. Every active node must be quantized to a set of possible potentials in order to allow a discrete solution, however this is not a requirement for proof as such: since an active node that is driven to a potential different from source will participate, rather it aids the ability to reconstruct from a measurement. This will be expanded upon later, but for now assume that the active nodes should all be driven to the same single potential that is distinct from the source.
4. Given a state of a source and active nodes, that is the source being of one potential and the nodes selected as being active having another, the direction of current through every element in the field will be reversed when the state is inverted. This means that by swapping the potentials of the source and collective active nodes, every element in the field will



operate in a different quadrant. This effect is important when the response of sensor elements is direction dependent, or when there are memory effects due to current flow.

5. The source is defined first in a particular voltage polarity, for which there is a known number of combinations  $\binom{n}{1}$  for boundary nodes. The remaining nodes are either sinks or disconnected. There are two further cases:
  1. The system contains elements with a symmetric response, in which case source or sink are interchangeable given only one source and one sink. There are  $\binom{n}{2}$  independent measurement states with only 2 active nodes.
  2. The system contains elements with an asymmetric response. Source and sink have independent identity. In this case there are  $\binom{n}{1} \times \binom{n-1}{1} = n \cdot (n-1)$  measurements with two active nodes.
6. The active nodes are defined from the remaining nodes other than the source, thus there are  $\sum_{k=1}^{n-1} \binom{n-1}{k}$  number of combinations for the active sink nodes. The number of nodes that can be defined as active is independent of the symmetry of the elements in the circuit, however in the case of asymmetric elements the source and sink nodes can swap polarity and the number of measurement double.
7. The free nodes are defined for every combinatorial state as the nodes that have not been made source or active.

Under constant current excitation the roles of the active and free nodes are interchanged, otherwise the method is the same. Thus the total number of measurements that can be made from  $n$  nodes is given by a sum of sums, in the case of symmetric elements:

$$\binom{n}{2} + n \cdot \sum_{k=1}^{n-1} \binom{n-1}{k} \quad (54)$$

In the case of asymmetric elements:

$$n \cdot (n-1) + 2n \cdot \sum_{k=1}^{n-1} \binom{n-1}{k} \quad (55)$$

The general asymmetric element has unique parameters for operation in the 1<sup>st</sup> and 3<sup>rd</sup> V-I quadrants, to solve for these parameters the combinatorial states that are inverses contain this information. Symmetrical elements have the same parameters for current flowing in their 1st and 3rd quadrants, thus there is no added information in the combinatorial states that are inverses. The number of distinct measurements in this case is the set of general distinct measurements with a particular source polarity and all inversions removed.

#### 4.4.8 Information available for reconstructions

The proofs and derivations thus far have assumed that measurements are only performed at the boundary nodes which are being driven by sources provided by the probes, with the induced currents flowing from the voltage sources to and from the boundary nodes. At this point it is possible to ensure that measurements made are distinct and that there are sufficient measurements to resolve all the elements in the field using this baseline method. It is also possible to attempt to maximize the amount of information captured by a measurement while still ensuring that the information remains distinct.

The amount of information is the standard that determines the ability of the system to solve for the state of elements when an appropriate mathematical algorithm is applied, the performance of the algorithm can be unambiguously measured against it. *This result is a simple application of rank theorem, and it seems sensible to talk about the amount of information made available by the system as "information resolution", since it is the information obtained that is key to differentiating between elements.*

Every measurement obtains two types of information:

1. Current flowing into or out of the active node
2. Voltage of the visible nodes, active or passive.

The sum of the currents into or out of the active nodes must sum to zero:

$$\sum i_n = 0 \quad (56)$$

This implies that there are only  $k$  sources of current information associated with a measurement, and all nodes that are not active are available for voltage measurement, being  $(n - (k + 1))$  in number. The total amount of information available for  $n$  nodes in a given state is; a sum of the free voltages and unique current. Since all currents sum to zero, one current measurement is made redundant.

The sum of the information over successive non-superimposed measurements is the total amount of information made available by the system. Given symmetrical elements, this quantity is given by a sum over the possible states:

$$q_{sym}^{flexible} = (n - 1) \cdot \left( \binom{n}{2} + n \cdot \sum_{k=2}^{n-1} \binom{n-1}{k} \right) \quad (57)$$

The amount of information available for asymmetric elements is similar:

$$q_{asym}^{flexible} = 2 \cdot (n - 1) \cdot \left( \binom{n}{2} + n \cdot \sum_{k=2}^{n-1} \binom{n-1}{k} \right) \quad (58)$$

It must be emphasized that these formulas are dependent on the  $k$  sources of current being entirely flexible in their connection to the nodes. That is there is a multiplexing system that allows the bank of  $k$  sources to be connected to any node in turn. There is a different formula in the case of fixed source connections, where only a subset of nodes can be driven and the rest are sampled purely passively. For elements with a symmetric response the relationship is:

$$q_{sym}^{fixed} = (n-1) \cdot \binom{k}{2} + k \cdot \sum_{i=2}^{k-1} \binom{k-1}{i} \quad (59)$$

For elements with an asymmetric response the relationship is:

$$q_{asym}^{fixed} = 2 \cdot (n-1) \cdot \binom{k}{2} + k \cdot \sum_{i=2}^{k-1} \binom{k-1}{i} \quad (60)$$

*This demonstrates that there is only a scaling factor increase by increasing the number of passive sampling points, since these points do not add variety in the states of the system that may be sampled. It is the flexible tristate attachment of current sources that is the source of information variety.*

Equation 67, for the number of unique states given symmetric elements, is plotted in Figure 28. Each line corresponds to the total number of boundary nodes on the field, the number of measurement channels. Variation along the horizontal axis is in the number of boundary nodes that are flexibly connected to excitation sources. It is evident that there are diminishing returns in the number of unique measurements as the number of these nodes that are driven actively increases.

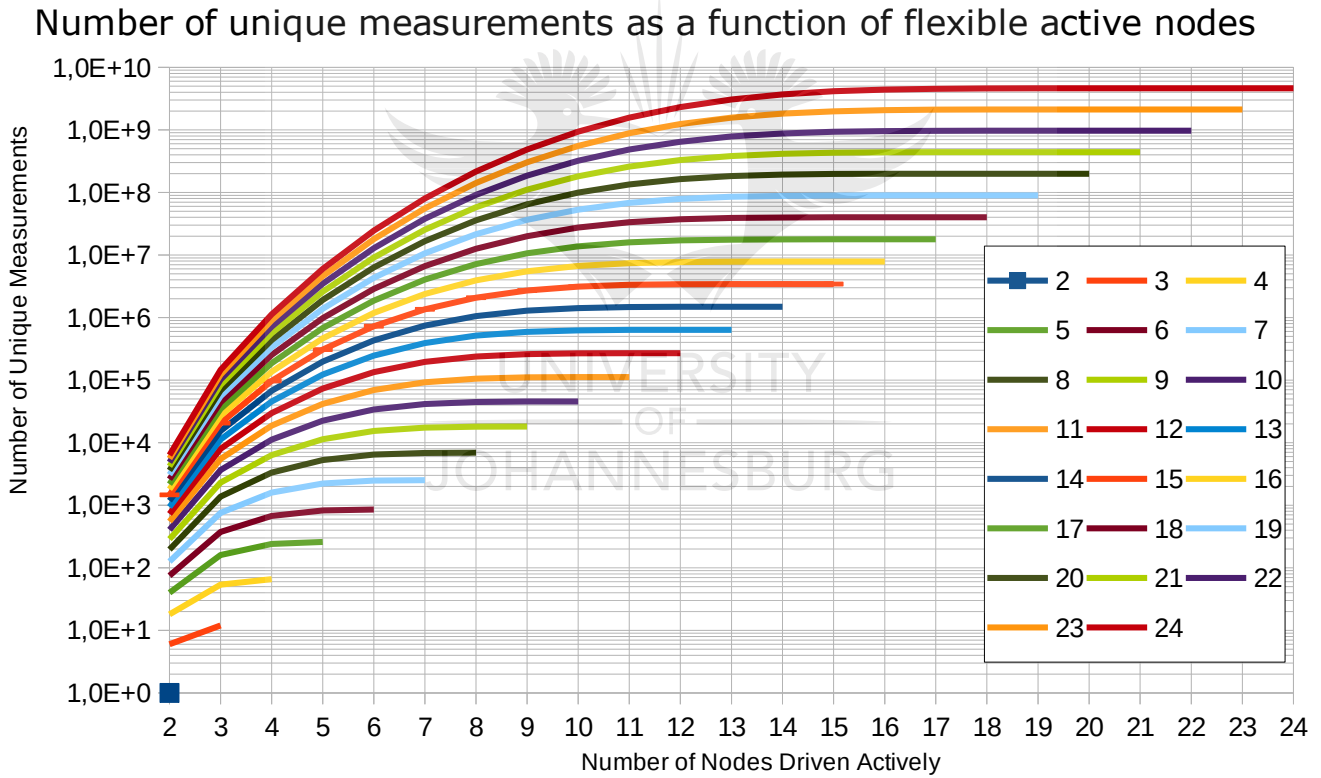


Figure 28: Number of measurements for a flexibly-driven field of symmetric elements

This finding is useful in design, since every active node requires an excitation mechanism, while nodes sampled passively can be read for voltage without as much associated hardware. By inspection it seems economical to only have 1/3 to 1/2 of the total number of boundary nodes driven actively, for a given number of boundary nodes present.

#### 4.4.9 Representation of field state

A maximal amount of information should be obtained from one measurement, which is defined by applying a “combinatorial state” of sources and sinks to the boundary nodes. The combinatorial

state  $k$  can be represented over the enumerated nodes by a state vector with a length of the number of boundary nodes  $F$ , using trinary logic:

$$\bar{c}_k \in C^F \text{ where } C \in [-1, 0, 1], \begin{matrix} -1 = Sink \\ 0 = Undriven \\ 1 = Source \end{matrix} \quad (61)$$

The resulting measurement can be fully described by two vectors, a voltage state and a current state:

$$\begin{matrix} \bar{v}_k \in \mathcal{R}^F, \bar{v}_k \in [0, V_{excitation}] \\ \bar{p}_k \in \mathcal{R}^F, \bar{p}_k \in [0, I_{saturation}] \end{matrix} \quad (62)$$

The voltage state vector describes all the voltages on the boundary, including the driven voltages. The combinatorial state vector is implicitly encoded in the voltage state vector, since entries that are at the excitation voltages cannot come from boundary nodes unless there is a short between nodes. This implicit encoding is not true if multiple sources are applied, however this situation has already been excluded as it results in non-distinct measurements.

The current state similarly describes all the currents in and out of the boundary nodes, the non-driven nodes are represented uniformly as nodes with zero current. The range of values in the current state are practically limited by the ability of the constant voltage source to deliver current, this boundary is important since if an upper limit of current is reached the conditions for a distinct measurement in voltage mode are violated. The method developed should detect such conditions to avoid false reconstructions.

In the case where the field has elements that have a leakage current to ground, the source and sink currents will not balance. This imbalance is useful to detect failures of the device and may further be of use as a sensing principle; given an array of known resistances, the shorting of any number of nodes to ground should be detectable by attempting to reconstruct the equivalent resistance value of the short. This possibility is an interesting aside which will not be considered for our purposes.

#### **4.4.10 Comments on the combinatorial nature of distinct measurements with respect to electrical properties.**

The number of distinct measurements available shows divergence in the behaviour of excitation modes. The largest number of combinatorial states occur when there are a comparable number of active and free nodes. Thus there are three main classes of combinatorial state:

1. Single-sink, with a single active node and the rest free.
2. Multi-sink, with a mix of active and free nodes.
3. Omni-sink, with all the foveal nodes that aren't source being active and no free nodes.

The classes 1 and 2 have a large amount of information present in the free nodes as values of either current or voltage depending on the excitation method. The measurement of such poses some design options:

### *Constant Voltage*

The free nodes under constant voltage excitation are left high-impedance and the floating voltage defined by interactions on the field is measured. Since the field may be composed of photoresistive elements with a high mean resistance, the macro equivalent resistance into the field as seen from a free node may be large. This puts the free node at the risk of picking up large amounts of interference from electromagnetic sources and reduces the quality of information received by the free nodes under constant voltage excitation. The remedy for this is to choose photoresistive elements of a lower value to decrease the equivalent resistance, however this will increase current draw for a given excitation voltage and thus the overall power consumption. The active nodes are low impedance to a set potential, and thus will contribute in their current measurements a large amount of information with greater noise resistance.

### *Constant Current*

Constant current excitation is expected to require a greater amount of excitation current in order to function, making it more power hungry. The free nodes in this scheme are grounded low-impedance to a set potential and the active nodes are switched high-impedance and measured for their floating voltage.

## **4.5 Initial Investigations into Design Parameters**

At this point some guarantees have been determined for the amount of unique information present in a boundary scan measurement scheme, however at this point it is not clear how to configure a system to capture the required amount of unique measurement. This section seeks to answer two questions:

1. what system configurations will be sufficient, and
2. what specific configuration is most economical to implement in a real world system?

### **4.5.1 Voltage and current excitation**

There are technical advantages to excitation by constant voltage in the simpler implementation of the circuitry, however as will be demonstrated later the developers of the technique in other applications prefer to use current sources rather than voltage sources. This preference is as a result of the mathematical construction of the backpropagation algorithm initially used in reconstruction. It is however generally true in circuit design that it is easier to match a target voltage rather than a target current. It is for this reason, and the greater ease in developing algorithms and techniques specific to the application at hand, that the convention will be disregarded. *Voltage excitation is the method that will be used throughout the document and all further references to "excitation" refer to voltage excitation unless otherwise stated.*

#### 4.5.2 Connection for the measurements

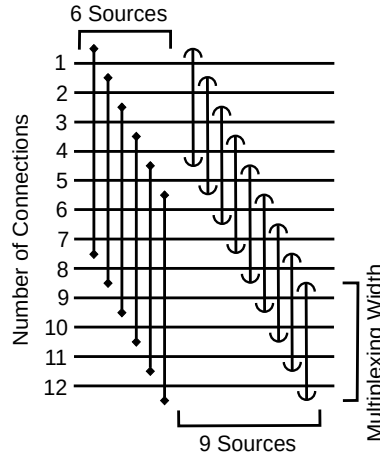


Figure 29: Multiplexing optimization to reduce design footprint

Any electrical sampling technique will require some form of multiplexing, this should be briefly considered prior to developing any further tools, since multiplexing will constitute a significant part of the sensor hardware implementation.

The complexity of the naïve fully-connected multiplexing interconnect scales with the square of the number of nodes. Optimizations can be made however, since the requirements are not equivalent to multiplexing the sensor array directly. A simple method is observed to achieve this, as Figure 29 demonstrates, by requiring on that every node be serviced by *some* active source. In this case it is only required to multiplex each source to an overlapping subset of possible nodes. Thus the amount of complexity, in terms of the number of multiplexing unit cells, is given by:

$$z_{links} = k \cdot (n - k + 1) \quad (63)$$

where  $n$  is the number of total nodes, and  $k$  the number of active boundary node drivers. This further increases the economy of sampling a field using tomographical boundary scan.

#### 4.5.3 Design considerations for system configurations

The first question, that of whether a configuration is sufficient, requires determining whether a configuration has a sufficient amount of unique measurement information across its' boundary nodes.

To this end, design curves may be plotted, as demonstrated in Figure 30 on page 83. This plot has lines holding the number of active nodes constant, while varying the total number of boundary nodes, the added nodes being voltage measurement only. The plot in Figure 31 on page 84 demonstrates the relationships when the total number of nodes is held constant, and the number of active nodes is varied. The size of the intended field is here in terms of the number discrete elements to be resolved, and should contain a safety factor necessary to account for imperfect reconstruction algorithms.

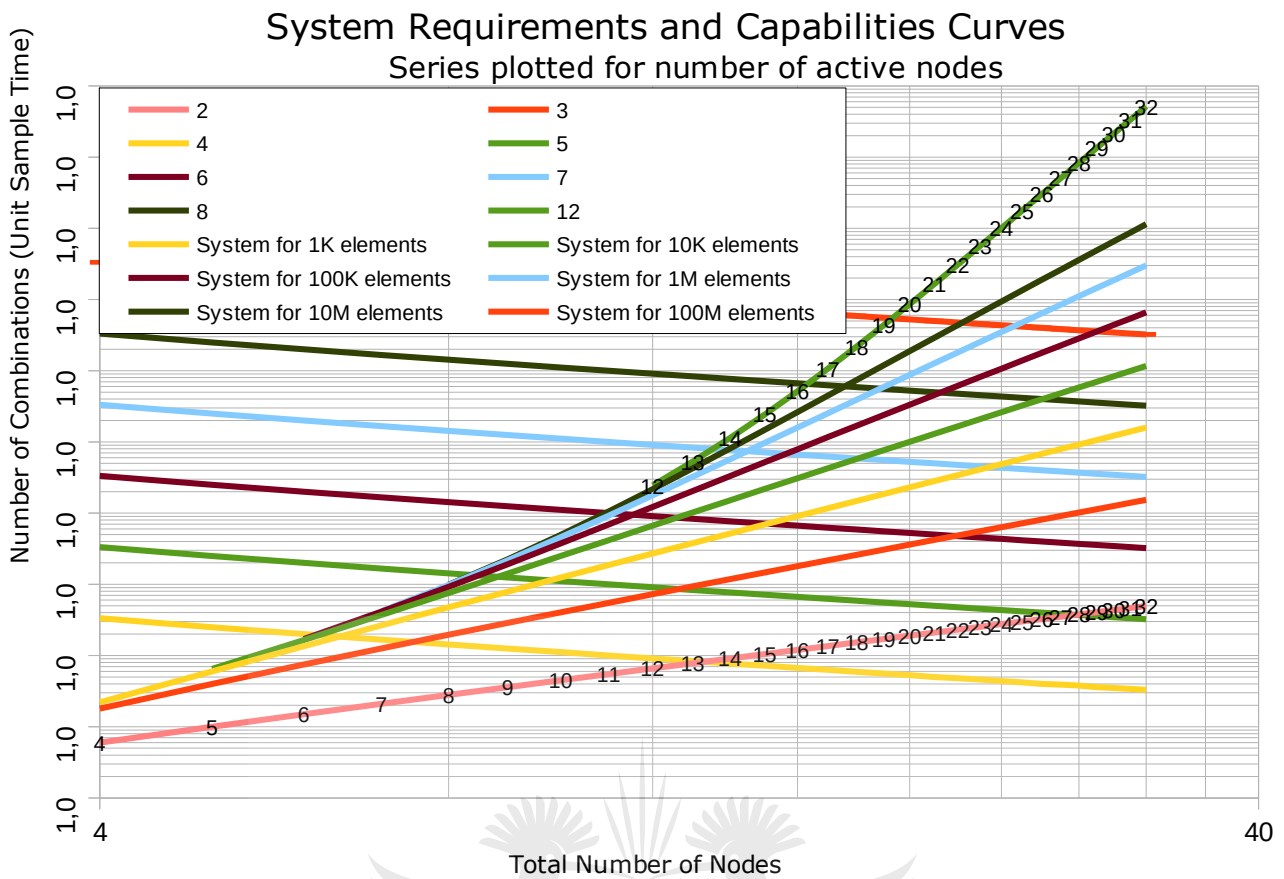


Figure 30: Minimum resolution system sizing curves

There are two families of curves plotted on the graph:

1. System demand curves, which hold constant the total amount of unique information required to solve for elements in the field. These are shown by "System for" in the plot legend.
2. System supply curves, which plot the maximum number of unique measurements available for the configuration at the point on the curve. These are shown in the plot legend by numbers only.

The point of intersection between the demand and supply curves defines the minimum number of total nodes required by the system (and thus hardware requirements in sampling), for a desired number of active nodes. This point will be called the **minimum defined measurement**. Any increase in the number of total nodes to the right of this point will give more flexibility in use, allowing a few basic options:

1. The system demand curve is followed rightward and downward, which will decrease the number of unique measurements required, and thus the sample time, for an expected desired reconstruction quality.
2. The system supply curve is followed rightward and upward, which will increase the number of unique measurements made of the system and thus improve the measurement performance at the expense of greater time in sampling.



3. A point is chosen rightward of the minimum feasible measurement, between the supply and demand curves in order to gain a mixed trade-off between measurement performance and sampling time.

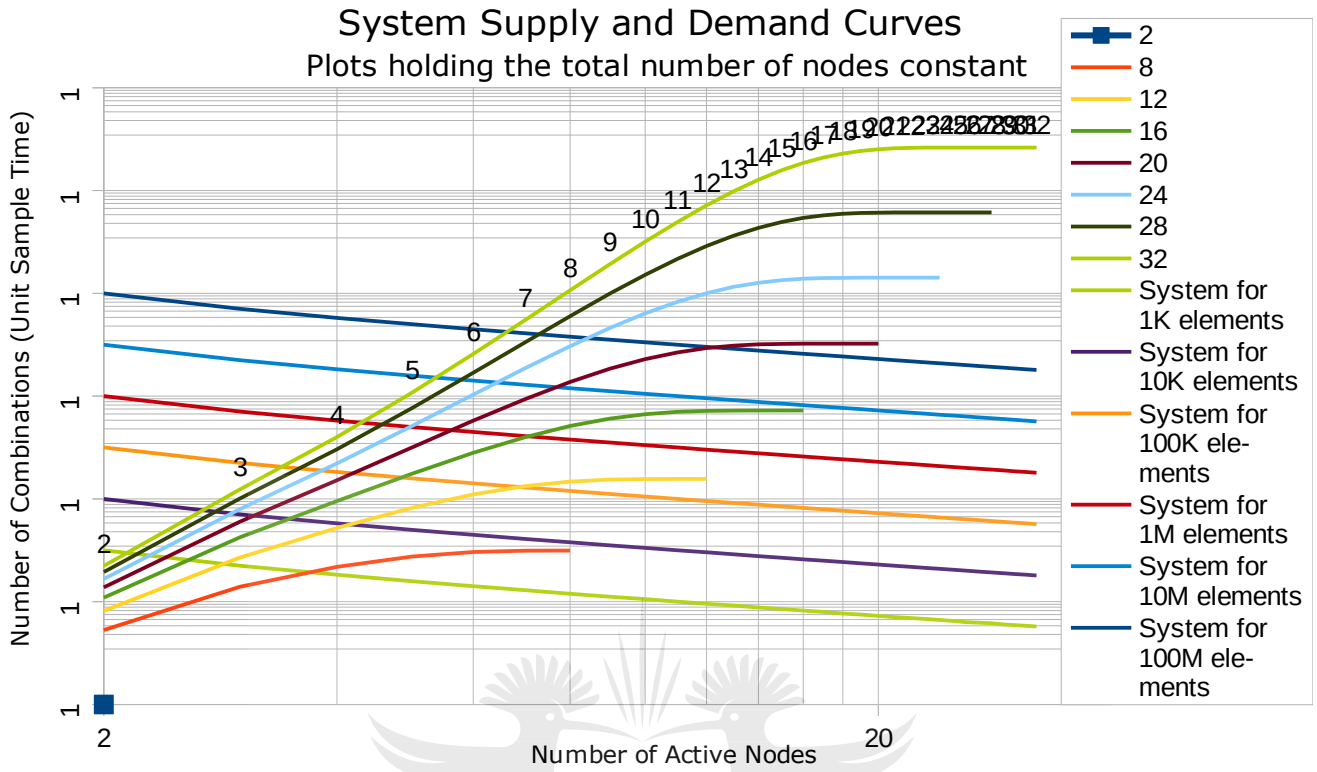


Figure 31: System supply and demand curves, plots holding the total number of nodes constant

There are also two further possibilities for system selection that are of interest to the general situation:

1. Taking a greater number of measurements for a given number of active and total nodes than the system supply curve would indicate. This region has non-unique (repeated) measurements and thus allows averaging or median filtering for noise reduction at the cost of sampling time.
2. Taking a lesser number of measurements for the given number of total nodes or taking a lesser number of measurements with a lesser number of total nodes, both at a point below the system demand curve. These constraints correspond to the region below the demand and supply curves, and does not have the required amount of information to resolve all the elements. Since the all the measurements contain distributed information about the entire field, a regularized solution can be estimated. This region is implicit when dealing with continuous media, where the maximum number of elements is inherently undefined, and it may be useful in discrete fields when the number of nodes is constrained due to physical or cost limitations.

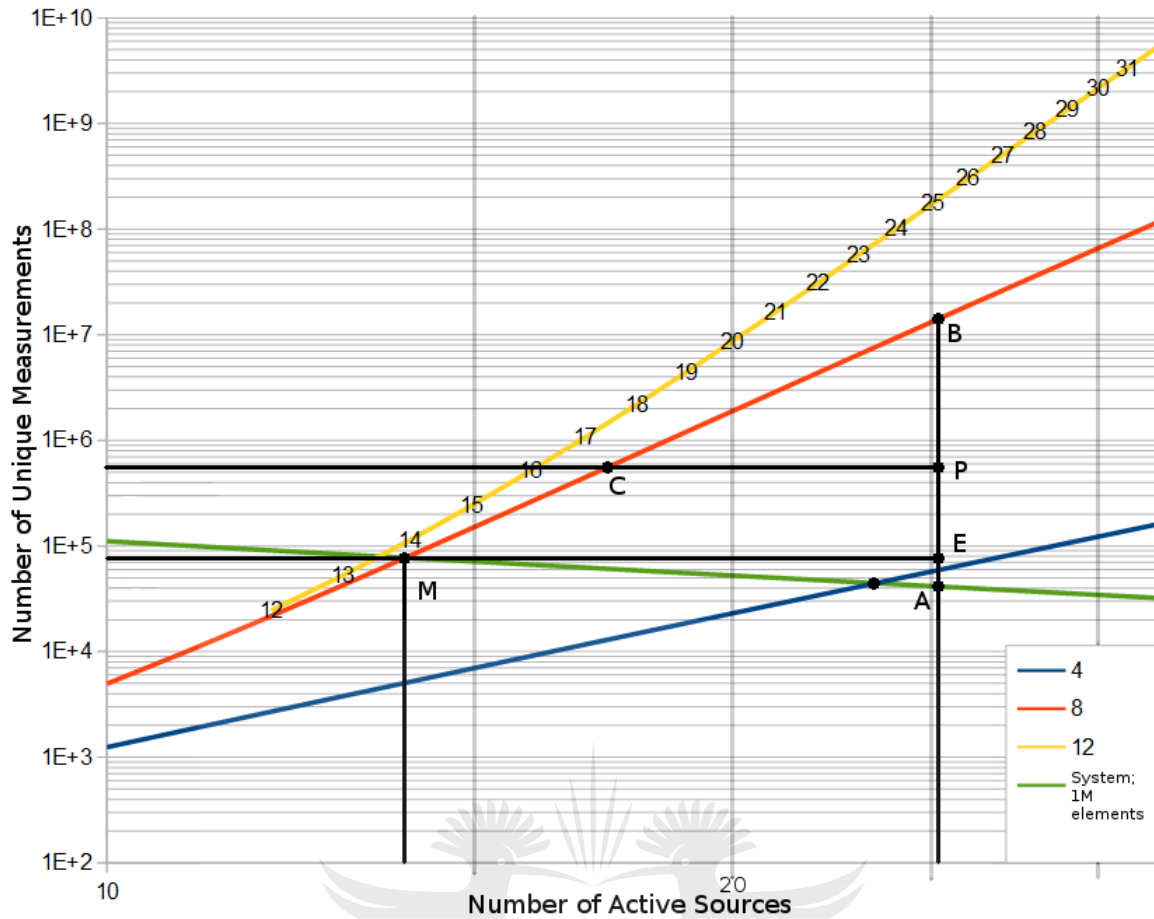


Figure 32: Plot showing the geometric properties of defined measures

Since the focus is a discrete field of a finite number of elements, it is possible to define metrics for sizing of systems and for characterisation of performance (the purpose of Figure 32, discussed below). *In the case of a continuous field there are an infinite number of elements in the field, and such definitions become meaningless, since the demand curve is undefined.* As a result, none of the metrics derived here appear to be used in the literature for previous techniques, which focus on measurement of continuous media rather than discrete elements.

The metrics are taken with regard to a point that lies between the demand and supply curves, to the right of the minimum defined measurement (refer to Figure 32 for the visual representation):

1. The ratio between the desired number of combinations (the point P) and the minimum number of combinations (the demand curve, point A), for the given number of total nodes (a vertical line on the plot). This will be called the **oversampling factor**, and is a measure of the ability of the measurements to deal with noise or the ability to increase sample rate:

$$(P_y/A_y)$$

2. The ratio of between the maximum number of unique combinations (the supply curve, point B) and the minimum number of unique combinations (the demand curve, point A), for a given number of total nodes (a vertical line on the plot). This will be called the **oversupply factor**, and measures the flexibility of the system to be configured in such a way to counteract noise and improve dynamic range:  $(B_y/A_y)$

3. The ratio between the desired number of nodes (the point P) and the minimum number of total nodes (the supply curve, point C), when holding the number of combinations constant (a horizontal line on the plot). This will be called the **node excess factor**, and is a measure of the increased node density on the field relative to the minimum requirement. It is also meaningful in situations where channels may be lost due to failure, indicating the amount of damage that can be sustained before the ability to resolve is affected at the desired sample rate:  $(P_x/C_x)$
4. The ratio between the desired number of nodes (the point P) and the number of nodes at the minimum defined measurement (point M), which is a horizontal ratio (M-E) between two vertical lines on the plot. This will be called the **system excess factor**, and is a measure of the excess system capacity and general reconfigurability:  $(P_x/M_x)$
5. The ratio between the desired number of combinations (the point P) and the number of combinations at the minimum defined measurement, which is a vertical ratio between two horizontal lines on the plot. This will be called the **sample rate factor**, and measures the sample rate in terms of the minimum system required for a completely defined reconstruction:  $(P_y/M_y)$

There are a number of derivative measures that can be useful in the context of comparison between system parameters, since they normalize against system dependent parameters and thus allow a degree of comparison:

1. The ratio between: the difference between the point and the minimum number of combinations, and the difference between the maximum and minimum number of combinations. This will be called the **oversampling utilization factor**, and is a measure of the ability of the sample rate to be reduced:  $(P_y - A_y)/(B_y - A_y)$
2. The ratio between the node excess factor and the system excess factor, which will be called the **system stress factor**. This factor is a measure of the ability to increase the number of unique measurements, and thus the accuracy of the measurements at the expense of sampling time:  $(P_x - C_x)/(P_x - M_x)$

The measures are intended to be useful in comparison between the performance of systems, by characterising them in a non-dimensional way. Through experimentation it may be possible to find relationships that can aid in the reasoning about possible configurations that are yet untested. Implicit in the formulation about such measures is an appreciation of dimensional analysis.

There are a number of non-dimensional groups that factor in the physical topology of the field, and the location of the sampling points in relation to each other and elements on the field. Some of these will be discussed later in the experimental design.

#### 4.5.4 Design considerations for sampler hardware

The second question can now be addressed; *how might the system configurations be differentiated in order to choose the most economically efficient option*. At a first optimization of the design of the sampling system itself, the component parts of the system must be considered in their effect on cost and performance.

### Considering multiplexer cell cost only

A non-dimensional ratio can be derived to indicate the amount of information obtained for a given complexity in the multiplexing system; a simple division of the number of unique measurement states by the number of flexibly connected multiplexing unit cells. This ratio is demonstrated in Figure 33, which is intended as a design aid for the hardware designer at this level. There is an inflexion point that would be a sensible point to size the system in terms of the number of driven nodes given the flexible multiplexing scheme demonstrated. This point is visually at approximately  $\text{round}(n/2)$  .

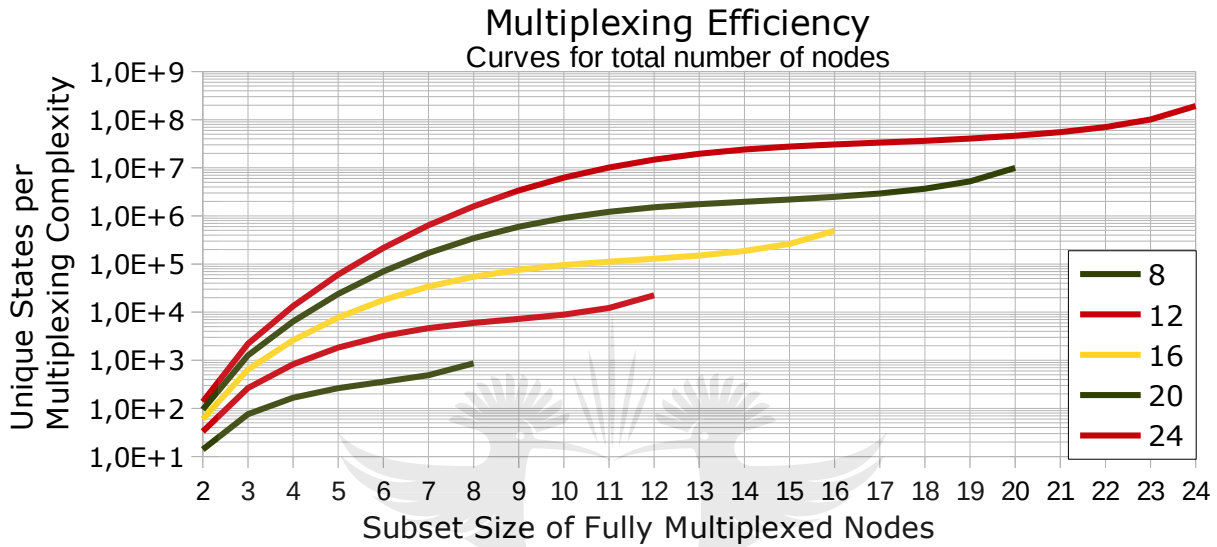


Figure 33: Graphs of information resolution relative to multiplexing complexity

The graph in Figure 33 is a first take on answering to the form that a sensible design would take. The series are for the total number of nodes, with an increase in the horizontal axis being an increase in the number of these nodes that can be driven actively. If preliminary cost relationships between the two subsets of the system are known, a better design decision can be made by plotting curves as demonstrated in Figure 34.

### Considering costs for channel routing, multiplexing, and drivers

In the previous plots such as Figure 31 the amount of unique measurement information can be determined for a given system information requirement. However, the design configuration is still indeterminate, since multiple combinations of total and active nodes will provide sufficient measurement information. The plot in Figure 34 allows a weighted relative cost structure to guide the most economical configuration, assuming flexible multiplexing interconnect as presented in Figure 29. The series are drawn for a given number of total nodes and cost structure in non-dimensional cost units for the interconnect lines, multiplexing cells, and drivers for active nodes. This process is a simple application of equations 67 and 71 with a linear sum of normalized weighted costs.

## Design Curves for a Given Information Resolution

Curves plotted for total number of nodes and cost scheme (Line : Multiplexer : Drivers), points are number of active drivers

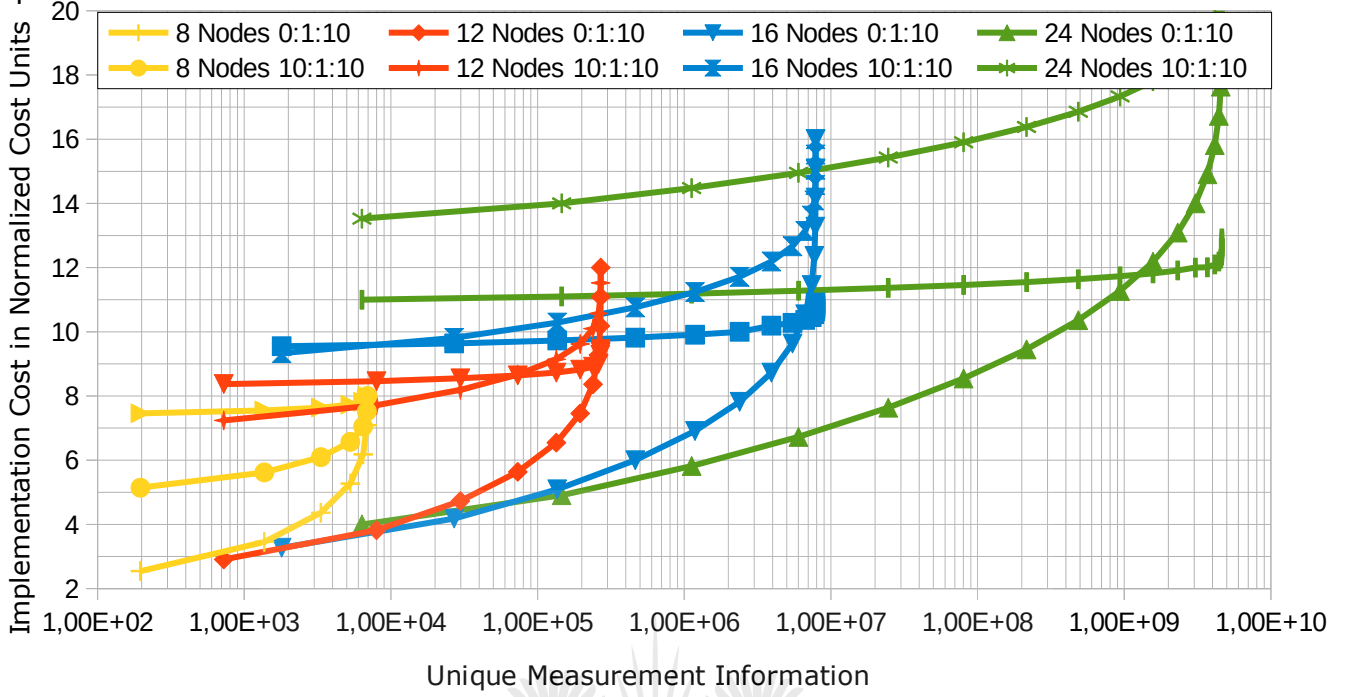


Figure 34: Cost relationships for a given information resolution, plotted in series for total number of nodes for cost structure for (Line : Multiplexer Cell : Active Driver)

In use; the designer selects a quantity of unique measurement information and traces up to the lowest curve that has the same cost structure as that of the application, then quantizes to the nearest number of active nodes which appear as points on the curve. For example; an information requirement of  $1.0 \times 10^6$  with a cost structure of (0 for Line, 1 for Multiplexer, 10 for Driver) meets the curve for 24 total nodes at the position for 4 active channels, rather than the higher curve for 16 total nodes and 6 active channels.

The cost structure used to plot Figure 34 is based on the following formula, where  $W_1$  is the unit cost for a multiplexer cell,  $W_2$  is the unit cost for a driver and  $W_3$  the unit cost for the line length servicing one channel:

$$C = W_1 \cdot \min((k \cdot (n - k + 1)), n) + W_2 \cdot k + W_3 \cdot n \quad (64)$$

The minimum serves to acknowledge that for any configuration the drivers need to be tristate, which is effected by a multiplexer through-switch at the base level. Thus there need to be at least as many multiplexer cells as drivers. In general the observations are that:

1. As the cost of a source increases relative to a multiplexing cell, the designer will prefer to implement a greater number of channels with a lower number of drivers. This would be the case for highly accurate sources and precision measurements, and would be true in any such application where the sources are becoming expensive relative to the lines or multiplexer: industrial or small-scale embedded.
2. As the cost of a source decreases, the design should move to eliminating multiplexing altogether and have the sources link directly. This would be equivalent to a system that does

not require high precision in the measurements and will not have long links to the field being measured. Such an example might be a tightly integrated sensor and sampler system that is miniaturized (or possibly embedded), where the speed of sampling and oversampling techniques can overcome imprecise measurements.

3. As the cost of the physical connection between each channel and the measurement system increases, this cost will tend to dominate and the design should move towards a reduction in multiplexing in order to be flexible and acquire a maximal amount of information. This would correspond to the industrial application of such a sensing methodology, where long lengths of shielded cable may be required between the measurement system and the array of sensors located on or near some equipment.

The illustration serves to show that the system design parameters matter greatly to the overall cost of implementation, and that further work on algorithms for reconstruction and associated issues should consider being tuned towards use cases of such systems that would make production sense. It is often better to select a system with a greater number of total nodes, and greater information resolution. There is no cost benefit to choosing a less capable design and the greater capacity affords greater options to the implementation at a later stage.

#### **4.5.5 Template system design procedure**

To summarize the initial investigations into design parameters; when the designing for system cost, the resource use can be accounted for by the following design procedure. This serves as a heuristic for more accurate methods:

1. Determine the technology used to create the sensor elements, which will determine the smallest size of these elements that can be manufactured.
2. Decide on the number of elements to be resolved based on the physical size of the field and the physical size of the sensor elements chosen, this is the theoretical minimum amount of information resolution required by the sampling system.
3. Take the practical required amount of unique measurement information as a multiple of the minimum (recommend 10-20x), since it cannot be assumed that the reconstruction is able to work effectively with a minimal amount of information. In addition to this, the time to sample the field must be taken into account; a greater degree of parallelism in the measurements will decrease the number of states required.
4. Once a target information resolution is determined a relative cost structure for the physical layout of the system is required. This will have to be found by summing the implementation cost of the board space and cell cost for the functional units in the design. These base units include the signal lines to the field, the multiplexing system, and the drivers for the active nodes.
5. Using this cost, normalized against a functional unit, plot a family of curves similar to Figure 34, for every number of possible nodes. These curves are used with the amount of unique measurement information to determine the most economical system configuration.



#### 4.5.6 Discussion of boundary scan in comparison to multiplexing and further conclusions

A method for an exponential decrease in the amount of interconnect that is required by a field of sensors has been shown. The benefits of combinatorially many sample states makes an unprecedented reduction in the amount of interconnect required to obtain systems measurement. This however does not come free of burden:

1. The combinatorial states by definition have to be sampled sequentially, in a finite amount of time. This dependence is an expectation by pigeon-hole principle and is acceptable if the rate at which measurements are made is sufficiently high for the purpose. However temporal aperture error and subsequent smearing in reconstructions will occur if this is violated, requiring a time normalized decision criterion for configuration selection.
2. The elements have been represented here as ideal resistors, in reality there are parasitic reactances between elements and across elements. The effect of these reactive elements is to generate waves of complex damped oscillations over the field, the nature of which is expected to be very difficult to predict. In general a certain time is required for the noise to settle after a combinatorial state is applied, before a useful measurement can be made. The size of the field will have a large impact on this factor: either in terms of numbers of discrete elements, or physical dimensions in the case where elements are taken to be infinitesimal.

The net effect is that the larger the field and the greater the parasitic reactances, the greater the sample time required and the lower the effective “frame rate” of the sensor as a whole.

The information about the individual elements is “spread” over the measurements in each combinatorial state, this hints at the possibility of partially accurate recovery using a regularization across the elements and/or across the combinatorial states against each other in time. It is expected that this property can be exploited to achieve:

1. Greater noise resistance by utilizing more combinatorial states than is theoretically required for a full recovery, thus offsetting limitations in the dynamic resolution of the sampling equipment.
2. A possible iterative method that does not solve the system outright but rather improves and estimate until a desired level of accuracy is achieved.
3. Loss-resistant transmission techniques that are able to withstand partial loss of combinatorial state vectors in the form of graceful loss of resolution rather than catastrophic information loss. This would be inherent in the signal itself, rather than a manipulation as is implemented in error-correction codes and codecs used in digital signal transmission.
4. Variable serialization, which is possible if the number of boundary nodes is greater than is required for reconstruction. The recovery would only require a subset of the combinatorial states made available, thus decreasing the amount of serialization required at the expense of greater complexity in the sensing hardware.

These ideas will be explored in later sections.



## 4.6 Optimization of the Tomographical Boundary Scan idea

In the previous discussions the layout of the field has been assumed to support a boundary scan, however there were no guarantees in this regard. In this section the aim is to determine conditions on the internal layout of a field of elements. Further, the nature of the boundary is explored so that the maximizing uniformity of element response with regard to measurements element response can be approached.

The way elements are connected throughout the layer will make measurements possible or impossible depending on what an observer is able to discern from a given location. The observer into the field from the boundary will always view the field from the outside, so any choke conditions will present themselves as barriers to information flow. A choke condition is a graph cut that does not present a sufficient number of boundary combinations, where the boundary is the set of ports created by the cut, in order to determine the state of elements within the cut. It is possible to demonstrate how to create topological arrangements that do not create choke conditions, allowing all elements to have the possibility of resolution using only measurements made at the boundary.

### 4.6.1 Connectivity requirement for measurability

In order to determine whether a field is measurable, a criterion can be applied that holds at all points in the field. Consider an arbitrary field of elements that are connected to each other in an arbitrary manner, modelled as a graph:

1. Select a number of nodes arbitrarily on the field. These nodes will be considered as being on the border, since there is no topological prerogative to assign a border in another way.
2. Assume and ensure that the number of nodes is sufficient to provide enough states of variety to match the variety (the number of edges) in the field graph.
3. Consider an arbitrary graph cut between the nodes defined as border nodes and any other nodes on the graph:
  1. This border defines a control volume through which the observations can be made.
  2. The cut variety is defined as the combinatorial number of binary states that the number of edges along this cut can be placed in, that is whether there is flow through the edge.
  3. If the cut variety is lower than the number of edges within the graph cut, not including the edges along the cut itself, then any set of observations made through the border cannot result in a solution for the number of elements within the border.
4. Since any observation of an edge has to be made through a border cut, and is made through any possible number of cuts that would separate the edges from the border nodes, all such cuts must have sufficient cut variety.

### 4.6.2 Minimal connectivity topology

The complexity of the field layout will have a direct impact on the reliability of manufacture, since for every connection there is a probability of failure. It is thus sensible to determine the minimum complexity in connectivity both for practical reasons and so that a theoretical lower bound on

complexity is obtained. By doing so the number of paths that are traversed between any two nodes in the field can be minimized, while remaining true to the measurability requirement.

#### *Construction of the minimal connectivity graph*

This can be satisfied if a field graph that is constructed with a number of requirements is considered. The minimal field connectivity is the minimum energy state of the energy (cost) function associated with an infinitely large field constructed on the following rules, with associated cost factors:

1. The graph must be represented on a two dimensional plane. Thus nodes must have coordinates with two degrees of freedom. (This represents the constraints on the system to be implemented in a system with two degrees of freedom.)
2. Every edge connection must not overlap any other edge connection, that is the line segment representing an edge must not intersect with any other line segment. (This represents the requirement of the device having to be manufactured fundamentally as a single layer.)
3. There is an energy associated with the presence of every edge except boundary edges. (This constraint is to reduce the number of edges in the system down to a minimum feasible number.)
4. The energy associated with a line segment is the deviation of the line segment away from unit euclidean length in the chosen coordinate system. (This constraint is to ensure a constant coverage over the domain.)
5. Every node must have the same number of edge connections to other nodes. (This constraint is to ensure a uniform structure with regards to later recovery.)
6. A boundary edge connection is theoretical, without being represented as a line segment.
7. There are a finite number of boundary edges, and the variety present in the boundary edges cannot be exceeded by the number of edges. (This constraint is to ensure that the field can be solved by boundary measurements.)
8. The connectivity requirement must be satisfied, in doing so the boundary edges may be relocated to any other node in the system when the requirement is evaluated.

While not a rigorous mathematical proof, by evaluation it becomes evident that the above system above anneals to the structure as shown in Figure 35 below, as a segment of an infinitely large field of elements.

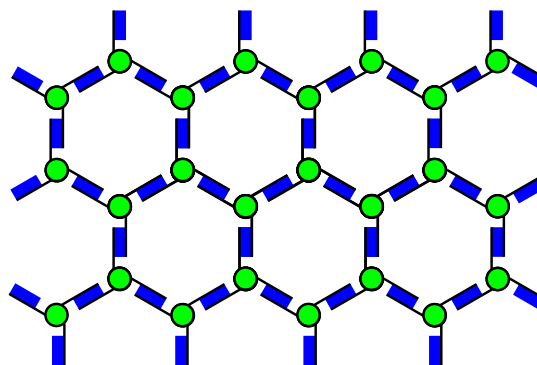


Figure 35: Minimal topology tiling

Any deviation from this structure will either increase the cost function or violate the rules of the construction. It is thus evident that this topology is a minima to the system, but is it the global minima?

#### *Evaluation of the global minima of the minimum connectivity graph*

Inspecting the conditions for the construction it is seen that every condition that incurs a cost is independent of the other conditions that incur a cost:

1. Increasing the number of edges, in this case from three to four, has no inherent impact on the cost of the edge lengths, and the overall cost will increase. The visual shape will change, which is due to symmetry bias in the eye of the reader, but this is not a topological property of the graph.
2. Increasing the length of edges beyond their base value is inherently independent on the number of edges themselves. The cost associated with the edges is a multiplier and thus is a monotonic function of the edge lengths, this is because there are no boundary effects that would make it preferential for a possible spread of edge lengths.

Since these two primary cost factors are the only possible sources of multiple minima in the model, and since it has been shown that they are both monotonic and independent the model is convex with respect to these factors. *It follows that this configuration is the global minimum of the system, and this topology is the simplest possible layout of a boundary scan field.*

#### **4.6.3 Boundary Inversion to Produce Continuous Fields**

Consider maximizing the response performance of the topology, since in section "4.4.2 - Device Layout" the requirements were identified; (see item 1.3, 2.1, and 3.3) that an interconnect scheme be able to provide suitable information on all elements in the field uniformly.

#### *Observations on the distribution of element sensitivities*

It is apparent when sensing a field of elements using boundary scan that the position of the probes will have a large impact on the degree to which each element will participate in a measurement, this is illustrated by some simple observations:

1. Consider two probes being placed on the boundary on adjacent nodes; the measurement taken at this location, when only considering the current passed, will be dominated by the element linking the two adjacent nodes (when all elements are of a value close to their mean).
2. Consider now two probes placed on nodes that are maximally far from one another; the measured current will be influenced by a large number of elements in different paths between the two nodes, to a similar degree if all elements are close to the mean element resistance.

This demonstrates a problem with boundary scan, which can be summarized as: *with regard to a particular elemental resistance, the bound of the mean fractional sensitivity of the measurement is at least inversely proportional to a function of; the average path distance between the element, and the nodes performing the sensing.* The nodes on the interior of the field will have a much lower fractional

contribution to the measurement, their effects are thus more likely to be masked by noise in the measurements and any iterative solution will likely solve for the elements near to the boundary before the interior. This problem is also true in the continuous case, where elements are differentially small.

#### *Reduction of variation in element sensitivities by field graph modification*

The remedy for this problem is looking at the nature of the boundary relativistically. Up until now the boundary nodes were discussed as being on the “exterior”, but what if this could be redefined as to what is exterior so that the boundary nodes can be a within a bounded distance from all other nodes? Consider this process:

1. First connect the field *as though it was continuous from edge to edge*, while maintaining uniformity of the structures in the field. This can be achieved by choosing a section of field that can be tiled, that is repeated to form a continuous pattern. The edges of this section can be connected to their opposites as if they were being tiled.
2. The field now has no obvious “exterior”, where the usual exterior was previously spatially defined by the discontinuity of field at its' edges there is now a contiguous whole. The structure formed has been made continuous just like the closed surface desired for sensing radiation.
3. The boundary nodes can now be connected by choosing a certain number of nodes to exist on the boundary, that is the boundary is now a set of curves enclosing certain node locations as the exterior, rather than a single curve that encloses the field as being interior.

The boundary nodes can be chosen as desired, since these nodes are no longer on a recognizable boundary, to avoid confusion they will be called “foveal nodes” (F-nodes). This terminology is chosen since the elements in the regions around these nodes have high fractional sensitivity in comparison to the other nodes in the field, which are now called hidden nodes (H-nodes).

A taxonomy of the types of continuous boundary connectivity is developed in an appendix: “8.6 - Boundary Connectivity” on page 181. A subset of the types of connectivity most likely to be useful is shown in Figure 36, below. The method of boundary connection is a subject of interest with regard to the geometry of projection, being the mapping between the physical and graph geometry.

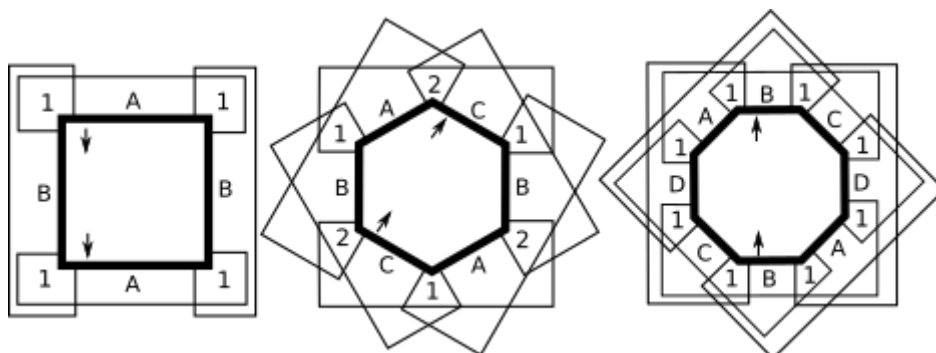


Figure 36: Three types of continuous boundary connectivity

### Use of Foveal Nodes in a discontinuous field

The addition of F-nodes to a discontinuous field will control the overall path length, however the border discontinuity means F-nodes cannot be used to sample the field effectively without nodes on the physical border. This can be demonstrated by considering a given host H-node and assuming the field is densely populated with a fine grid of nodes.

Figure 37 illustrates a field and 3 of the possible 8 virtual images that the field will produce when made continuous (one image for each edge and each corner). *This method of showing continuity will also be used in the representation of the field and in algorithmic methods that normally expect non-cyclical coordinates.*

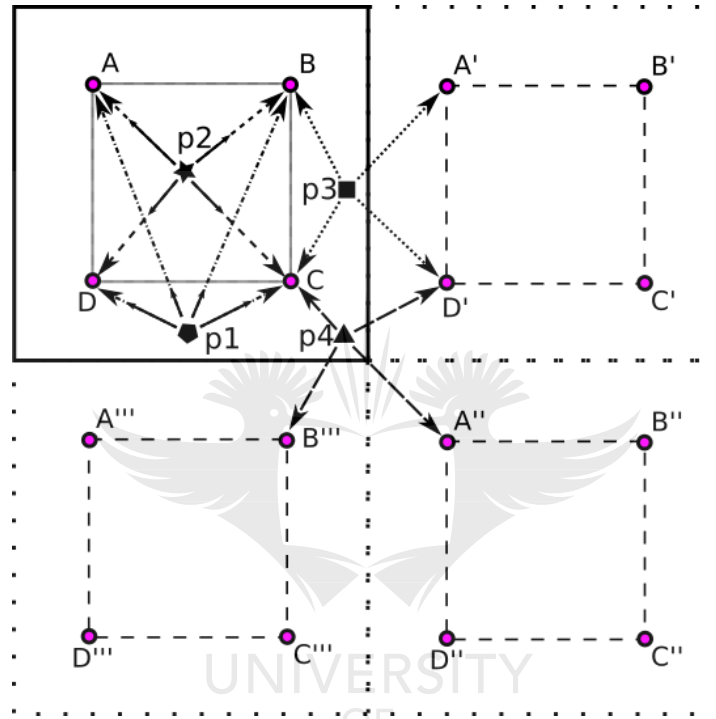


Figure 37: Effect of boundary continuity

Referring to Figure 37, consider investigation of the effect of the edge continuity. Starting by consideration of the possible H-node locations on the field with continuous edges, with Foveal nodes (A, B, C, D) and transposed images of the field formed by the right and bottom edges and the bottom right corner (A', B', C', D'), (A'', B'', C'', D''), (A''', B''', C''', D''').

It is possible to make a linear approximation of the effect of the voltage stimulus by linear interpolation between foveal nodes. Under this scheme the voltage gradient experienced by any point on the field can be qualitatively represented by a vector from the H-node being considered to the F-node that is either a source or sink stimulus, as it would be for a particular combinatorial state. The voltage gradient induced by the F-node is inversely proportional to the vector length, but for clarity the diagram does not show this effect on all the points (p1 to p4). This approximation is crude as it does not take into account the multiple path effect, which will be discussed further, rather only the shortest path effect. This approximation is first order, but serves to illustrate the idea.

Consider point p2, which is on the interior of the region between the foveal nodes (A, B, C, D). The amount of stimulus experience by this node over all the combinatorial states is the sum of the

inverse of the lengths of the vector difference between the first order approximation gradient-vectors. The degree of stimulus is proportional to the degree of influence an element at this location will have on the measurements at the F-nodes. This proportionality is shown in the equation below; where  $Y$  is the measure of stimulus,  $n$  is the total number of boundary nodes,  $F$  is a particular foveal node and  $H$  is the hidden node under inspection.

$$Y = \sum_i^n \sum_j^n [(F_i - H) - (F_j - H)]^{-1} \quad (65)$$

Now consider point p1, which has been drawn with gradient vectors resulting from a discontinuous field. The angles between the vectors have become more acute, indicating the vector difference between any two foveal nodes is reduced. This angle between any two F-nodes will be called the “view angle”.

The sum of view angles at p1 is less than the sum of view angles at p2, and the sum of the magnitudes of vector differences are lower. Since the phenomenon is bounded by the most interior nodes having the largest view angles, and the most exterior nodes having the smallest view angles; it is clear that the sensitivity of the field decreases significantly for nodes exterior to the smallest convex hull formed by the F-nodes. This manifests as a reduction of stimulus of H-nodes with regard to F-node locations

Consider now points p3 and p4 with vectors drawn as in a continuous field with wraparound edges. The virtual images of the nodes (A', B', C', D', etc.) have become the vertices for shortest paths, *this is possible since electrically the region is locally smooth*. The sum effect of stimulus is the same as if the points existed internal to the convex hull of the F-nodes, and the drastic diminishing sensitivity phenomenon no longer persists, regardless of the location of the candidate H-node on the field.

*The boundary region of a discontinuous field thus represents a loss of sensing efficiency* if a lower bound on sensitivity of elements is a design requirement. It also shows a loss of material efficiency in the resources used to populate the boundary region, which is a sizeable area in relation to the total field area. *It is for this reason that continuous fields should be investigated*, however for other applications of the technique discontinuous fields will be necessary, so further study is advised to characterize their performance.

#### *Node positioning on a continuous boundary*

It is possible to continue to improve the uniformity of measurements over the field. The positioning of the F-nodes can be made such that the variances in path distances between any H-node and its' nearest two F-nodes is controlled.

This positioning is a primary heuristic of the sensitivity of a measurement with respect to an element for the field with elements all at their mean values. However this sensitivity is entirely dependent on the values of the elements in the field. The heuristic is applicable since it cannot be assumed there is any particular prior average state of the values in the field, unless a very clear prior of the types of images imposed on the field is obtained. A uniform average is itself a prior that may be evaluated by simpler mechanisms.



If a prior is known, can be estimated by using generic layouts, or can be determined by other measurements; it is then possible to optimize node locations by a fitting process. In this process, an optimization loop would be used around;

1. the use of the intensities prior, the node locations, and the measurement combination scheme;
2. evaluation of the sensitivity of element locations to the measurement scheme by perturbation of elements in locations of interest, in order to develop a sensitivity profile; and
3. comparison of the sensitivity profile with a desired profile, or by maximization of global mean sensitivity, in order to provide an objective function for further iterations.

#### **4.6.4 Topological Properties of a Continuous Field with Regards Foveal Node Positioning**

The continuous field has shown properties that are beneficial to smoothing the measurability of elements under test. It maintains a bounded degree of sensitivity that is required for reliable estimates of element bounds, with regard to a given precision of measurement from the foveal nodes.

The representation of this field is more complicated than it would seem at first, especially if it is desired to optimize the measurement sensitivity over the field by ensuring a minimum variance of sensitivity for every element. The obvious starting point is minimizing the minimum distance from each hidden node in the field to the sum of the nearest two active foveal nodes. To achieve this a distance function must be defined appropriate to the graph domain, and this distance function must be appropriate to the field connectivity.

##### *Defining a distance function over the field*

The true minimal distance between two nodes is the minimum path distance over the graph connectivity of the field, however a good approximation would be useful. Since the general problem of node placement for any image that may be formed on the field is in question, it is suitable to assume all the elements are at their mean conductivity.

The distance function between two nodes can now be approximated by a number of norms, depending on the nature of the field connectivity (known types of connectivity realizable on a single layer will be addressed separately):

1. Euclidean distance  $L2 ( \sqrt{\Delta x + \Delta y} )$  is appropriate for nodes with great connectivity and fields that have conductive elements that have varying scale, that is their resistance is length dependent and thus directly dependent on the distance that the element spans between nodes. This norm is appropriate for fields with infinitesimal elements, made up of purely conductive films, a possibility that will be explained further.
2. Manhattan distance  $L1 ( |\Delta x| + |\Delta y| )$  is appropriate for minimal connectivity, with 3 elements terminating at each node, and square connectivity where 4 elements per node form a simple grid structure.



3. Scaled “Difference Counting”, an L0 norm with a multiplier (  $\min(\Delta x, \Delta Y)$  ) is appropriate for (6,4)-space and 6-space connectivity, where a grid is given diagonal cross-links on every other alternating node or every node is given diagonal cross-links that overlap.

#### *Modelling the continuous fields on flat arrays*

The understanding of distance across the field is complicated by the way in which the field wraps back to itself around its edges, the effect of which is to distort the field with regard to electrical distance given a uniform physical structure, much like the orthographical issues associated with representing a 3D shape on a flat plane. The most accurate method of accounting for this distortion is to ensure *local flatness* of the projection by imagining that the edges do not exist, using *virtual images* of the field that are transposed across each edge and each corner of the field's physical boundary. Under this arrangement, any node in the field can have the true distance to any other node easily computed, as the projection is continuous for a distance from every point of at least the maximal distance possible across the field.

This method works for shapes of field that are themselves able to pattern over a surface without leaving gaps or overlapping. Since the edges of the field are joined electrically, field shapes that are continuous must have an even number of sides. When these conditions are not met, the field is not continuous and creation of a distance function is much more difficult. There are a few cases to consider:

1. The number of sides in the field is even and no more than 6. These shapes can be modelled on flat arrays easily.
2. The number of sides in the field is odd and only an even number of sides are connected to each other. These field shapes may sometimes be represented on a plane without overlap, however the notion of distance will not map correctly due to gaps in the projection.
3. The number of sides in the field is even and larger than 6. These shapes will overlap and the notion of distance will be confused due to ambiguity between which image is to be used. An extreme example of this progression is modelling a circle with vary many even segments, in this case the only way to define a distance is to have the images exist in overlap and for every line drawn between two points from the real to the virtual field images an inspection must be made as to which image has the shorter line and whether the line passes through the “aperture of continuity” created by the joined sides.
4. The number of sides in the field is infinite and even. This would be the case when modelling a circular field, and since there are an infinite number of virtual images that overlap the problem must be approached from a different perspective.

#### **4.6.5 Element Value Distribution**

The construction of fields has been investigated, along with how they might be optimized in terms of connectivity and F-node layout, by assuming that the elements are relatively uniform. The assumption must be tested to determine bounds on element variation. In our application this depends on the chemistry of the photoresistive sensor elements, and is thus is a practical question.

The field of minimal connectivity is a uniform tiling with a ratio of 1.5 : 1 resistive elements to conductive nodes, this will be referred to as 3-space connectivity. This field is visualized in Figure 38.

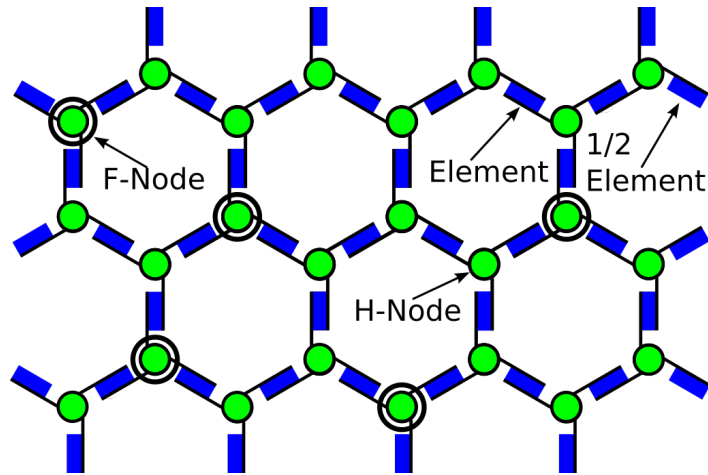


Figure 38: Field of minimal connectivity, 3-space connectivity

Greater levels of connectivity are solvable as long as no regions suffer choke conditions. The properties of the solution with respect to an increase in connectivity at this point are unknown, besides a few observations:

1. Consider a number of resistors in parallel between two nodes only:
  1. As the number of resistors increases, the change in any particular resistor about its mean value has a lower fractional change in the current experienced through the two nodes when a voltage stimulus is applied. The number of alternate paths increases as the connectivity rises.
  2. As any one resistor approaches zero resistance the fractional effect of the other resistors on the current flowing through the circuit rapidly diminishes. This effect will decrease the measurability of the effects of the other elements, and is due to "current stealing" effects.
  3. As any one resistor approaches infinite resistance, its measurability in terms of current with respect to other elements decreases to zero.
2. Consider a number of resistors in series, between 2 nodes only:
  1. As the number of resistors increases, the fractional change in effect by any particular resistor about its' mean decreases with increasing number of resistors in the chain. This loosely corresponds to a lowering of connectivity, since the minimal path length in a field increases with decreasing connectivity. This effect is on both the current through the path and the voltage that can be sensed on a subset of nodes in the path.
  2. As any one resistor decreases towards zero, the measurability of that resistor decreases rapidly with respect to the other resistors in the circuit since the fractional change will be dominated by the bulk effect of the other resistors in the chain. This measurability is both in terms of the current flowing through path and the voltages that can be sensed on nodes in the path.

These two effects (the serial and parallel) tend to pull the sensitivity of a field with respect to any particular element lower for a general increase in the number of elements, further investigations are needed to determine the net effect of the interaction with respect to the effect on measurements and subsequent reconstruction. The expectation is that there will be a marked falloff in relative element sensitivity with increasing path distance from a measurement location, which will become a dominating effect in the design of the density of points of measurement in any given field. *It is clear however that the falloff in sensitivity with path distance will be greater for fields with a larger number of total paths, which further reinforces the need to implement a minimal amount of connectivity on the field itself.*

The variational effects discussed indicate that the system cannot function effectively if sensor elements have too great or too low an effective resistance relative to one another. This phenomena is a bound on the ability of the system to resolve with respect to the variance of element resistances about the mean, experiments are needed to determine the empirical bound of resolvability as a function of this variance.

#### **4.7 The Literature on EIT**

The previous sections have taken the reader through the logical progression that was taken by the research. It was later discovered that; there is an existing class of methods that deal with the sampling and reconstruction from electrical measurements at the periphery of three dimensional physical objects. These were not introduced up until this point because the first principles development is necessary to understand the logic of the particular structural arrangement used.

Within this general paradigm of existing methods there are a number of methods that have been used in an array of applications, the three main methods are:

1. Electrical Resistance Tomography (ERT), where measurements are made by passing a direct current through a number of combinations of points on a body and measuring the effect of the body on the voltages experienced at the non-excited points, and the load effect on the excitation signal itself.
2. Electrical Impedance Tomography (EIT), where measurements are made by passing an alternating current through the body as in ERT. The signal is alternating and thus the properties are all complex-valued in nature, including the body under measurement that has elements that have both permittivity and permeability. This method is suitable for bodies that have elements with components of resistance, and capacitance or inductance. The increased number of variables in such a situation require measurements to be made over a sample space of combinations of boundary nodes and excitation frequencies. [103]
3. Electrical Capacitance Tomography (ECT), which applies an alternating stimulus in order to find the internal state of non-conductive media. The measurements may also be charge-inducing in certain situations, where the static charge distribution over the body is measured rather than alternating voltages.

These methods have been developed since the late 1970s and are targeted to the general problem of finding the internal state of inhomogeneous continuous matter. The applications for such a

technique are large since the electrical stimulus used can be small, this makes the prospects highly attractive in comparison with methods of tomography that use ionizing radiation or that require expensive equipment, such as Magnetic Resonance Imaging (MRI).

Since the methods of ERT and ECT can be achieved as special cases of EIT, this is the sensing methodology that will be referred to in this work. The problem definition is unusual in that it has developed from a more complex primary problem, that of the continuous domain. This formulation is a result of interactions and inspirations from the earlier development of Computed Tomography (CT), which uses the attenuation of “hard radiation” in the form of X-rays that pass through a continuous solid body. This genesis has coloured the understanding of the possibilities for passing soft radiation like electrical currents in a similar tomographical manner. The evidence for this history is in the techniques and methodology used in the development of EIT:

1. Investigations have been done into the solveability of the problem, this has shown that the in the discrete case of a finite number of resistive elements it is mathematically possible to solve for the elements exactly. However all indications as yet found have shown that this result has been the basis for proving the usefulness of further research into the general continuous problem, rather than a useful fact in its' own right.
2. The earliest reconstruction technique for finding an approximation of the continuous properties of the object was based on the early methods for reconstruction from CT [104], [105], [106], [107]:
  1. The original technique as used in CT, known as “backpropagation”, is based on the differential attenuation of the regions of the media to the hard radiation that it is exposed to from a point source (or as close a point-source as can be constructed). This results in three-dimensional images that map the sensitivity of attenuated radiation collected on an array of pixels to the differential contribution of the voxel to this attenuation. These images can be unwrapped and stacked to form a matrix of voxel sensitivities with regard to individual measurements”, where the measurements are pixels on the array measuring the attenuated radiation for a given rotation of the specimen.
  2. The earliest technique in reconstruction for EIT, also known as “backpropagation”, uses a very similar method to that in early CT. The radiation however is “soft”, and thus prefers to bend around the areas of attenuation. This results in an inaccurate reconstruction, since the information provided for reconstruction can only ever be an estimate. The sensitivities of measurement channels with regard to elemental resistances (admittances in the complex form) in the field are built up from estimates of the effect of these admittances on the channel. The field is assumed to be in a medium with only two degrees of freedom, though this is merely a simplification. The resulting images of “sensitivity with regard to a measurement channel” are unwrapped and stacked to form a matrix that can be inverted with suitable techniques and applied to the actual measurements. Since the radiation is soft, the current distribution assumptions in this method rely on the admittances not varying far from the mean level of admittance.

3. Later techniques have considered applying EIT with regard to an “open boundary”, where electrodes either cannot be placed on the edges of the object under measurement or may be moved over the body in an attempt to better resolve individual areas. The electrodes are typically arranged and held by a device that maintains their relative positions but allows the set to be repositioned. Such methods invariably involve an operator-interpreter in the a loop that involves iteratively:
  1. Imaging a suspect area.
  2. Interpreting the image for the information of interest to the application.
  3. Repositioning the array of electrodes to another area of interest, either in a search pattern for an area of interest or in an optimization pattern that seeks to better image an already found area of interest.

#### **4.7.1 The applicability of previous work on EIT to the current problem**

It must be strongly emphasized that the general case of EIT is one that is under-defined. Since the media being interrogated by the measurements is continuous there is an infinite possible number of elements that can be defined for the model. It is therefore impossible to ever have enough information for an “exact” reconstruction (technically it would be impossible to define this), and the task of the researcher is to find the best reconstruction possible by improving a combination of:

1. Determining the best resolution possible under the particular circumstances and quantify the quality of reconstructions in general [108], [109], [110], [111], [112], [113], [114], [115], [116], [117], [118], [119], [120]
2. Improvement of the forward problem as a system simulation, using both meshed [121], and meshless methods [122]. Discretization of the models of the continuous domain, which is used in estimating the reconstruction and is a fundamental factor in the trade between accuracy and computational time taken in reconstruction [123], [124], [125].
3. The accuracy of the boundaries (and thus internal discretizations) of the models with respect to the shape of the body being measured. This factor is important since the shape is often unavailable and thus required to be assumed, or is constantly changing and may require monitoring [126], [127], [128].
4. The location and interaction of electrodes in contact with the body, with respect to body shape and the regions of interest being imaged. This includes techniques that may only sample a subset of the possible boundary of a body. The electrode model has been a cause for great error in reconstruction and smart design of the electrode surfaces with regard to the problem being imaged can better shape the path of the soft radiation, and increase sensitivity to regions of interest. New applications require investigation into the current paths within the body in order to maximise the quality of information received given a finite number of measurement combinations [129], [130], [131], [132], [133], [134], [135], [136].
5. The sample pattern generated in the process of taking measurements, since the radiation is soft this has a large impact in which regions contribute to the measurements [137], [138], [139], [140], [141]

6. The performance of the sampling system, as exemplified by [142], [143], [144], [145], [146], [147], [148], [149], [149], [150], [151], [152], [153], [154], [155], [156], [157], [158], [159], [160] in terms of its' ability to:
  1. Be useful in form with regard to the target environment of use. This may range from remote sensing over long distances to internal use within body cavities.
  2. Deliver a precise stimulus to the body at the frequencies of interest.
  3. Account for and immunize itself against parasitic effects in the transmission of the probe signals and environmental noise.
  4. Measure the pattern of responses to the stimulus applied to the body.
  5. Account for the degradation due to drop-out of channels due to imperfect contacts.
7. The reconstruction of the internal properties of the body under measurement by:
  1. Improving the inherent regularization of the method of reconstruction. There is always a method of regularization present in reconstruction as a result of the system being under-defined. This includes the use of external priors, the formulation of internal priors, and the bounding of the reconstruction based on arbitrary rules [161], [162], [163], [164], [165], [166], [167], [168], [169], [170], [171], [172], [173], [174], [175], [176].
  2. Improving the accuracy of the reconstruction by using techniques that make better assumptions about the problem parameters and are able to adapt these parameters for a more precise image. While similar to regularization this includes parameters of model formulation rather than distribution of values within a model formulation. This may include the use of iterative optimizations that modify the understanding of the prior based on clustering and binning of the values found in previous iterations [177], [178], [179], [180], [181], [182], [183], [184], [185], [186], [187], [188], [189], [190], [191], [192].
  3. Improving the computational cost of reconstruction with regard to the amount of information available for reconstruction, thus enabling imaging at greater frame-rates or at greater complexities (and thus potential reconstruction resolution) given a target frame-rate. This may include massively parallel inverse function approximations based on neural network architectures, cellular automata or other methods [193], [194], [195], [196], [197], [187], [198], [199], [200], [201], [202], [203], [203], [204], [205], [206], [207], [208], [209]. Other increases in speed may be had by:
    1. Smart heuristics [210].
    2. Simplified inverse models mapped onto more complex forward models, as a type of prior.
    3. Partial reconstructions of local areas.
8. The inclusion and fusion of other sensor modalities into the reconstruction as either a prior or inherent in the reconstruction method. These may include methods such as measurements made by [211]:
  1. Ultrasound imaging [212], [213].



2. Structured light projection.
3. Intense light tomography [214].
4. Measurements of the magnetic fields induced by currents in EIT.

The body of work surveyed revealed a host of work that is not applicable to the current problem, and some mathematical analysis that is useful.

#### **4.7.2 Classification of applications in previous work with regard to EIT**

As a demonstration of scope, the method has been evaluated for use in:

1. Primary diagnosis of breast cancer nodules, with attention paid to the characterization of nodules as malignant or benign [215].
2. Imaging and determination of lung volume in patients with certain lung conditions that require continuous assessment [216].
3. Imaging the mixing of solids and liquids in chemical process plants [217], [218], [219], [220], [221], [222]
4. Imaging the distribution of bubble density of fluidized beds and general multi-phase flow [223], [224]
5. Imaging the distribution of water content of regions of earth dams and fluid-filled rock strata. [225], [226], [227]
6. Imaging the formation of cracks in composite materials by the addition of conducting fillers [228], [229]
7. Imaging the film quality and integrity of a layer of graphene by measurements on the boundary [230].
8. Determining gas and liquid composition in reaction mixtures [231].
9. Imaging the distribution of sediment in filter cakes used in chemical process plants [232].
10. Imaging the pressure profile on a conductive fabric [233].

#### **4.7.3 The current problem in light of EIT**

The reconstruction of the electrical properties from EIT have been shown to be an ill-posed inverse problem. This makes the method extremely sensitive to issues of:

1. Modelling errors in shape and the electrical properties of the electrodes.
2. Measurement accuracy and precision.

The problem at hand however does not have any ambiguity in the model whatsoever. The connectivity is completely known, and the discrete element model by definition is complete in electrical terms as long as the isolation between nodes and the internals of elements can be maintained. There is modelling error in the relationship between the radiation flux and the V-I transfer function of the sensor element, however this is not an issue in reconstruction from electrical measurements.



*The limitations in reconstruction will only be due to the errors in measurement, and the inherent nature of finding a solution to a highly non-linear problem. Errors can be mitigated by sampling excess measurements with respect to the number of elements in the field. Filtering of individual measurements can be done effectively by averaging or median filtering, and inaccuracy can in principle be mitigated to a certain extent by the complementary nature of measurement pairs. The extent to which the non-linearity of the problem will impact the reconstruction method is at this point difficult to predict, and experimentation will be required.*

#### **4.8 Sensor-Layer Manufacturing Methods**

It is now possible to consider the particulars of the manufacture of a prototype system. The details of which will highly influence the properties of the measurement system produced. The details of various manufacture methods will be expounded upon in an Appendix (8.3 - Sensor-Layer Manufacture Methods), the summary is given below. There are two types of field to consider, the first being the manufacture of finite elements:

1. Discrete-component implementations based upon either;
  - a) through-hole components mounted on a stiff substrate; or
  - b) surface-mount components mounted on either;
    1. stiff substrates; or
    2. flexible substrates of either the metal or polymer type
  - c) axial-leaded components mounted in a self-supporting mesh.
2. Printed-paste on a flexible or stiff substrate based upon either;
  - a) pastes held in suspension; or
  - b) pastes in solution and precipitated by evaporation.
3. Injet printing on a flexible or stiff substrate, with precipitation by gas-delivered developer.

The second type of field is that of infinitesimal elements, which can be produced either by:

1. dipping and surface painting of photoresistive materials; or
2. chemical vapour deposition.

The core purpose of the manufacture finite element methods (2. and 3.) is the production of a photoresistive pattern. Such forms are illustrated in Figure 39.

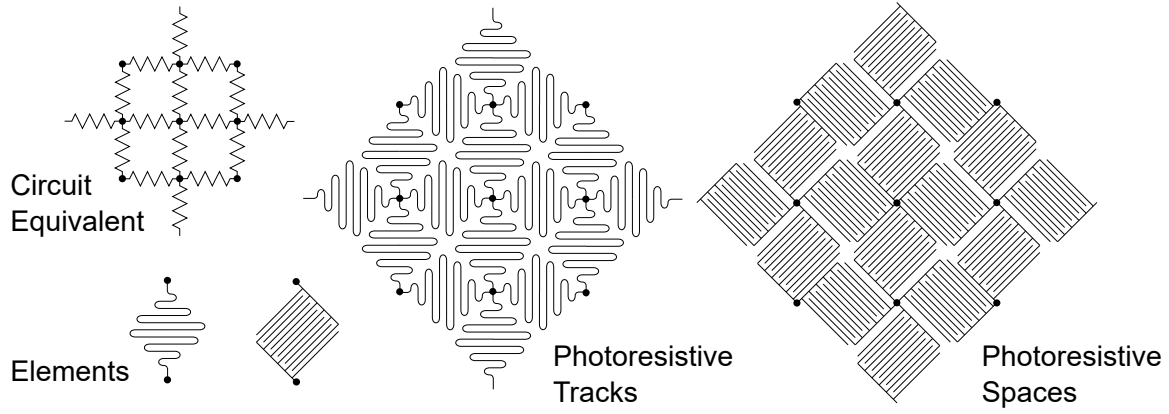


Figure 39: Printed photoresistive form examples

This may be implemented as the only conductive material or photoresistive pads deposited on an etched metal film that forms low resistance interconnect between the pixels. The use of an interconnect reduces the uncertainty and complexity in reconstruction, since photosensitive regions are defined in shape and electrical properties. The links between pixel elements are subject to their own photosensitive response when no conductive links are used, mitigating this response requires modifying the shape of the pixels to the detriment of sensitivity.

A prototype system would most easily use the finite element manufacture methods 1a and 1c, with particular interest in the self-supporting axial-led component method of (1c). *This approach is applicable as a technological form in it's own right, and suitable for measurement of solar flux in large systems like central receiver towers.*

#### 4.9 The Forward Transform

The device can be understood as a higher-order process that implements a mathematical transform. The process receives two sets of parameters and produces an output of two sets of vectors:

$$Q(\bar{c})(\bar{s}) \rightarrow (\bar{v}, \bar{p}) \quad (66)$$

where:

$$\bar{s} \in \mathbb{R}^M, \bar{v} \in \mathbb{R}^F, \bar{p} \in \mathbb{R}^F, \bar{c} \in [-1, 0, 1] \quad (67)$$

Variable  $\bar{c}$  is the vector of excitation states,  $\bar{s}$  the vector of conductances,  $\bar{v}$  the vector of measured voltages,  $\bar{p}$  the vector of measured currents,  $M$  the number of elements,  $N$  the number of nodes, and  $F$  the number of F-Nodes:

##### 4.9.1 The Conductivity-state view

The process is represented here as a higher-order functional (a “Curried” function), it receives arguments from right to left to produce a function:

$$Q(\bar{s}) \rightarrow Q_s() \quad (68)$$

The output is a function that can be evaluated on an input of a suitable form to produce an output of a known form:

$$Q_s(\bar{c}_i) = (\bar{v}_{si}, \bar{p}_{si}) \quad (69)$$

where  $i$  is a distinct combinatorial state. This process can be viewed in a different ordering, by a different process, that produces the same result:

$$W(\bar{c}_i) \rightarrow W_i() \quad (70)$$

and:

$$W_i(\bar{s}) = (\bar{v}_{si}, \bar{p}_{si}) \quad (71)$$

where the subscript  $i$  here is used to indicate the function  $W$  associated with the combinatorial state  $i$ . The function  $Q_s$  corresponds to a system of elements linking nodes. The values of the elements have been determined by passing the argument of  $\bar{s}$  to the functional  $Q$ . The function  $Q_s$  receives a vector of  $c_i$  describing the combinatorial state  $i$  and produces a vector of voltages  $\bar{v}_{si}$  and currents  $\bar{p}_{si}$  for the given input state of element configuration  $\bar{s}$ .

The transform can be viewed as the mapping performed by the function  $Q_s()$  from the ordered set of inputs  $\{\bar{c}\}$  to the ordered set of outputs  $\{\bar{v}\}, \{\bar{p}\}$ , which will be referred to as the "conductivity-state" ordered view:

$$Q_s(\{\bar{c}\}) \rightarrow \{\bar{v}\}, \{\bar{p}\} \quad (72)$$

The conductivity state process has its element values defined prior to the configuration by combinatorial states. It is known that for a given combinatorial state vector the process is partially linear, being multiplicatively linear. The process here is represented by the black-box function  $R()$  with scalar multiplier  $a$  on the input vector of a combinatorial state:

$$a \cdot R(\bar{x}) = R(a \cdot \bar{x}) \quad (73)$$

Full linearity is not present as the sum of responses to inputs is not equal to the response to the sum of inputs:

$$R(\bar{x}) + R(\bar{y}) \neq R(\bar{x} + \bar{y}) \quad (74)$$

Thus responses over combinatorial state vectors cannot be meaningfully combined in simple operations, however the response by scaling the applied voltages within a combinatorial state vector produces a linear effect. This non-linearity can be demonstrated by considering a circuit of two resistors in parallel. The current curve produced by varying one resistance while maintaining the other constant has the form of a square root, very close to logarithmic in response.

#### 4.9.2 Connectivity-state view

The connectivity-state ordered view is the mapping produced by a set of functions  $W_i()$  corresponding to the applied combinatorial states, that each receive the same input, being the state of the elements of the circuit. The set of functions are derived by measurement state vectors that configure the host functional. The connectivity-state ordered view can be formalized as:

$$\{W_i(\bar{s}) \forall i \in \{\bar{c}\}\} = \{\bar{v}_i, \bar{p}_i\} \forall i \in \{\bar{c}\} \quad (75)$$

The amount of information provided by the transform is slightly greater than the information provided to it as an element state vector  $\bar{s}$ , and if the redundant components are removed the transform has exactly equal information, thus is in theory reversible.

There are as many models produced as there are combinatorial states, with all sharing parameters in the form of the conductances of the elements. This multiplicity of models is the cause of the complexity, as such *there is no clean form matrix multiplication operation that can be constructed to describe the system, since a matrix operation is a linear function mapping*. Formulation in these functional terms indicates a number of similarities to techniques used in other systems which may be of use.

The functions all receive a vector of element conductivities, they can thus be viewed as a collection of models that share the weights of their connections. This weight sharing is important since it is an inherent form of regularization, being the constraint of model parameters against another model in order to reduce the variety needing solution. In the case of continuous EIT this would be almost immediately be interpreted as requiring something akin to Tikhonov methods, however in the discrete sense there is a possible excess of information rather than a chronic shortage of it. In this way functional formulation hints at a natural regularization that is inherently defined by the interactions between models within the formulation, rather than the arbitrary nature of regularization in under-determined systems.

This weight sharing leads immediately to the understanding that the model as a whole may be approximated with a bound in accuracy as the successive application of inputs to the collection of functions describing the model. This holds as long as the deviations of the mutually shared conditions of the functions are kept small.

#### 4.9.3 Simulation of the forward transform

The forward transform is implementable as a series of applications of the techniques used in SPICE circuit simulation, specifically the initial DC steady state analysis, which is described thus:

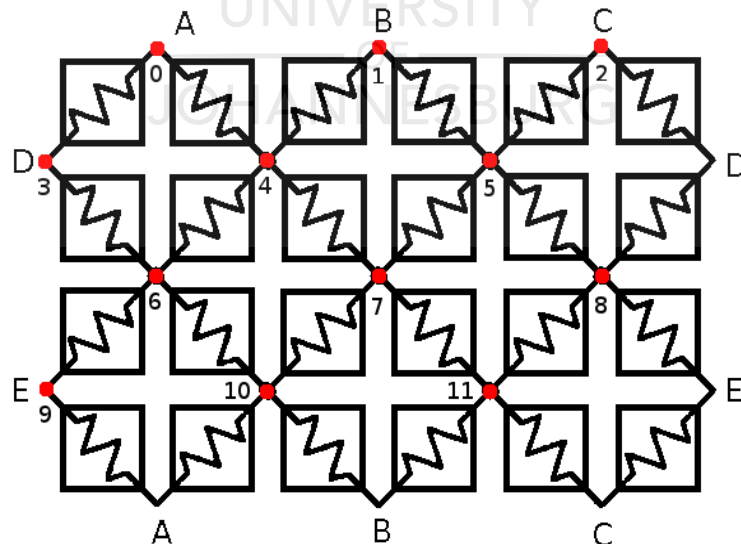


Figure 40: Parsing an image into an EITMSA graph

The normal method for circuit simulation in SPICE is to parse a graph of element relationships in list form. This set of textual directives is used to create an internal graph structure of matrix form. In this situation a list representation is however not ideal. It is better to parse an image directly by iterating over the pixels and using a state machine to determine which nodes are bridged by a pixel

element. The layout by which this is done is shown in Figure 40, where the nodes are labelled in red dots and the alphabetic labels are for nodes that will be connected to make the field continuous.

If the effects of a set of boundary conditions are to be simulated, the state of the field elements will have to either be known or assumed. Simulation is required to both to generate test sets of resulting voltages and currents at the boundaries, given an irradiation pattern, and in any reconstruction that uses iterative approximation. By indexing the nodes by row and column, it is possible to easily work with the node voltages as an image. The inter-node spacing is however twice the horizontal as it is in the vertical, which means any node voltage image requires resizing the image in the horizontal dimension to correspond to the field.

The system matrix is build up using node current relationships, that is for every node  $i$  with neighbours  $j$ ,  $k$ ,  $l$  and  $m$ ; there is a current balance such that:

$$s_{ij} \cdot (V_j - V_i) + s_{ik} \cdot (V_k - V_i) + s_{il} \cdot (V_l - V_i) + s_{im} \cdot (V_m - V_i) = i = 0 \quad (76)$$

where  $s_{ij}$  is the conductance of the element between nodes  $i$  and  $j$  such that  $s_{ij} = 1/R_{ij}$ . The above is manipulated to give the equations that apply for every node in the field:

$$s_{ij} \cdot V_j + s_{ik} \cdot V_k + s_{il} \cdot V_l + s_{im} \cdot V_m - (s_{ij} + s_{ik} + s_{il} + s_{im}) \cdot V_i = 0 \quad (77)$$

The matrix is constructed sequentially in the rows by copying the values of the pixels into the corresponding column locations, treating the pixel intensities as conductances rather than resistances for convenience. Using the state machine approach the rows of the matrix can be filled in one pass over the image of conductances, by directly addressing both the forward and reverse conductivity relationships formed by an element. After which the rows are summed and the inverse stored in the matrix diagonal. *This process is much faster than generating a list representation to be given to an existing SPICE code, and allows simulating in the loop for reconstruction algorithms.*

The process results in the form below, where  $\bar{r}$  is the result vector:

$$[S] \bar{V} = \bar{r} \quad (78)$$

This system  $[S]$  is stored persistently, copies of which are augmented for each measurement state, resulting in a set of systems, each of the form below:

$$\begin{bmatrix} \ddots & \cdots & s_j & \cdots \\ 0 & 1 & \cdots & 0 \\ \cdots & s_m & \cdots & \\ & & \vdots & \end{bmatrix} \bar{V} = \begin{bmatrix} 0 \\ V_i \\ \vdots \\ 0 \end{bmatrix} \quad (79)$$

Each system is inverted using an iterative solver in order to obtain  $\bar{V}$  for the voltages of all nodes in the field, for each measurement state, and is thus an expression of the conductivity-state process. The currents at each boundary node are determined by substitution of the node voltages in order to obtain the residual from the current balance relationship, which can be checked since all currents in the system must sum to zero.

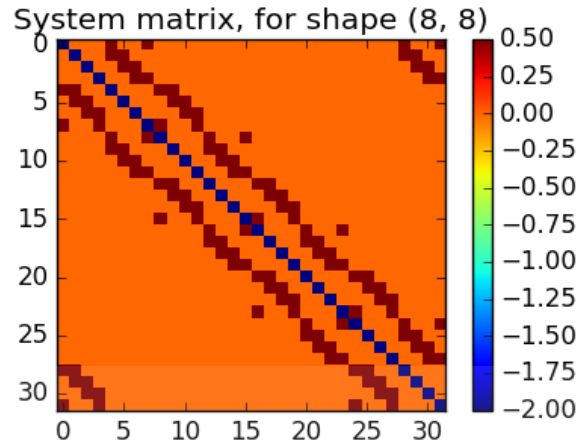


Figure 41: Map representation of example system matrix structure

The system matrix that results for a uniform field of 8×8 pixel elements is shown in Figure 41, this shows the banded structure is dominant but not universal, due to the boundary nodes. This sparseness and banded structure can be exploited to increase the efficiency of system simulations, and is important for memory and computation efficiency when handling large reconstructions.

It is also possible to use mesh-free simulation methods, since the problem is mathematically equivalent to heat flow, where techniques like that of [234] can be used. *These methods have not been considered in detail for this project.*

## 4.10 The Inverse Transform Recovery

The inverse to the forward transformation is dealt with in this section, being the fundamental problem addressed in the research.

### 4.10.1 Introduction

Primary interest is in the reconstruction of the vector of element conductivities used, given a known set of combinatorial state vectors associated with a known set of measured vectors for voltages and currents. Bearing in mind that there is no neat construction of linear algebra that can describe the forward process, a solution can be attempted in multiple possible ways:

1. Accept that the problem is non-linear and maintain its' entire non-linearity and global behaviour. This requires the approach needed for all non-linear systems, a guess-and-check method of iterative optimization.
2. Attempt to linearise the system in local regions, using methods of solution for linear systems on the simpler problem. This process may be repeated in iterative fashion, with the hope that each linearisation approaches the final solution such that error is minimized monotonically with iteration.



3. Attempt to linearise the global system, using methods of solution for linear systems and regularization to maintain the solution in a sensible region of the space of element conductivities.

Algorithms for all the approaches have been developed and will be proposed below, empirical investigations as to their performance are required since the complicated nature of the problems makes symbolic analysis difficult.

#### 4.10.2 Inverse by global optimization

Numerical optimization in the continuous domain is used to minimize some function over the space of its' inputs, which can be represented a vector hyperspace which spans the real numbers. There are a number of algorithms available, they may or may not require a black-box function that produces gradients with regard to the input. The algorithms that do not require a gradient function are termed "gradient-free methods" and are the subject of interest in this problem. Examples of unconstrained numerical optimization algorithms are [235], [236], [237], [238], [239], [240], [241], [242], [243].

This method of optimization has been used in work on EIT (as covered in the literature review) due to it's theoretical completeness, by not making any assumptions of linearity. It is thus a reference for comparison of other techniques. In our application a basic version can be expressed as by Figure 42, below:

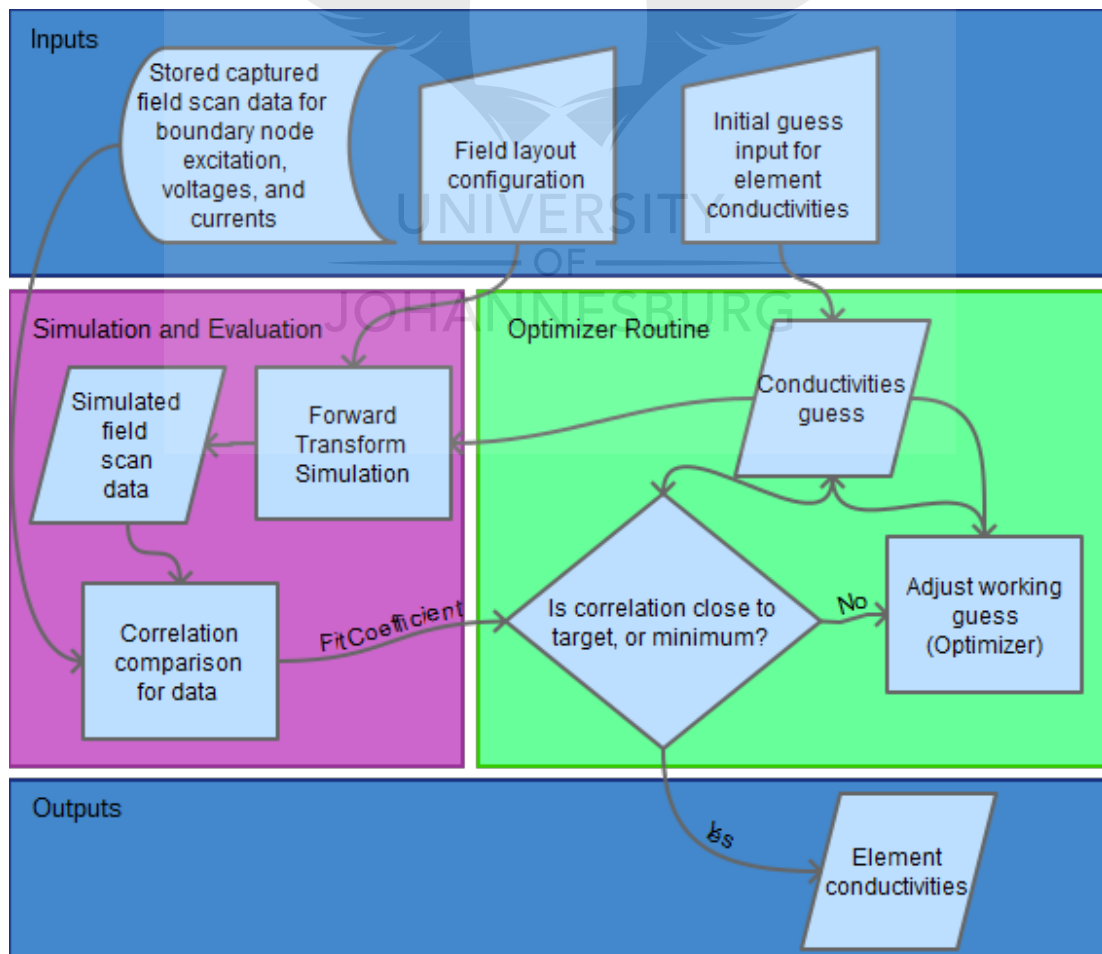


Figure 42: Reconstruction by optimization routine

Translating the reconstruction of our element conductivities into the general form of numerical optimization the problem can be defined, as per [244]:

1. The input of the function is the vector of element conductivities.
2. The function to be minimized is the cumulative error between:
  1. The output of the forward transform for all combinatorial states and
  2. The previously measured output from a device that has been probed with all combinatorial states.

This method has poor numerical efficiency. In static applications at low required rates for reconstruction the method may be suitable since in theory it may be possible to approach arbitrarily close to the actual answer. However, since the system is so non-linear it is highly likely that this method will become unstable as a result of local minima, as the size of the field increases. This will require a significant search time and meta-algorithms in order to find the global minima. *Experiments were performed on the use of global optimization in reconstruction, using small fields to reduce computational time requirements. The results were as follows:*

1. The continuous field borders result in multiple solutions: given a random prior, the fitting algorithm converges almost perfectly to alternate conductivity profiles that have no similarity with the original. This convergence is present despite a large excess of unique measurement information. Given a perfect prior convergence was achieved, thereby implying correctness.
2. No tests on discontinuous borders were performed, further research is required to determine if multiple solutions is an artefact as a result of continuous borders.

#### **4.10.3 The traditional approach of EIT – Backpropagation**

As mentioned previously the first reconstruction method proposed for EIT was a backpropagation approach that treated the soft radiation with an approximate hard radiation template. This method is quite similar to the optimization approach proposed, however the difference is in the assumptions made. In the backpropagation method a fundamental linearisation of the system in global terms is made, corresponding to method (3): the elements are assumed to be close to their mean value. This allows the system to be described in terms of linear equations and functions because the source of non-linearity in the system is removed, that of the current-stealing interactions between elements.

A single measurement on the boundary, for a given combination of boundary conditions, can then be viewed as a linear combination of the effects of the resistive elements in the field. A vector can be assigned to the component of a measurement as a list of coefficients of sensitivity with regard to element values. A similar vector can be assigned to every component of every measurement, thus building a matrix of sensitivity vectors for every component of every measurement in the set of measurements.

The result is a linear system that forms a subspace in the space of the element sensitivities. The actual measurement as found by the sampling process can be projected onto the subspace to find the solution, using a pseudonorm or a similar regularization-projection process such as LASSO. The

sensitivities with regard to elements are small, which makes the matrix ill-conditioned and the inverse numerically unstable. This can be mitigated to a certain extent by suitable transformations of the problem, but care is necessary. Since backpropagation is simply a large matrix-multiplication, once the inverse has been found it remains static and the method of reconstruction from measurements is relatively fast and deterministic in time.

The reconstruction in backpropagation results in a smooth regularized image, and is stable enough in practice to use despite violation of the theoretical bounds on its' validity. *It is of less interest in our purpose however, since it does not inherently exploit any known information about the structure of sampling nodes, and is already known for being unable to capture much detail.*

#### 4.10.4 Inverse by piecewise linearisation

*At this point it is possible to propose a new algorithm for reconstruction, motivated by the availability of information about the boundary nodes that is unlike that available to general EIT. The method uses weight-sharing in an over-constrained inverse to solve for element conductivities.*

This form of the inverse is based on the connectivity-oriented view. A set of functions  $W_i$  are present that are associated with the combinational states  $i$ . This approach arises from the question: Is it possible that an approximation of these functions can be viewed as linear operations on a vector of elemental conductivities?

At this point an assumption is made that the voltage state of the entire field at every measurement is known. Since the voltage and current through any element in the field are variables related by the resistance of the element, once one variable is obtained the other is implicit. Consider is given to a single state of the system, corresponding to a single measurement in our scheme. At each node  $i$  the current balance can be used to write relationships for the neighbouring nodes  $j, k, l$ , and  $m$  :

$$(V_j - V_i) \cdot s_{ij} + (V_k - V_i) \cdot s_{ik} + (V_l - V_i) \cdot s_{il} + (V_m - V_i) \cdot s_{im} = i = 0 \quad (80)$$

The relations between the elements and an assumed set of voltage stages can be used in order to build a system matrix that will solve for the element resistances directly, the system can be described by:

$$\begin{bmatrix} \bar{E}_1 \\ \bar{E}_2 \\ \bar{E}_3 \\ \vdots \end{bmatrix} [\bar{S}] = [\bar{r}] \quad (81)$$

where  $\bar{E}_n$  is the application of current balance at the node  $n$  by using the assumed node voltages, where the voltage applied over an element is the difference in the voltages of the nodes that it links. *In this method the nodes are not augmented with known voltages, that is only current information at the boundary nodes is being taken into consideration.* The vector  $\bar{r}$  is the result vector for the current balance at each node, and will be zero at internal nodes and non-zero at nodes where current is injected or removed. The sum of the elements in  $\bar{r}$  must be zero in order to conserve total current in the system. By inversion of the matrix the vector of conductivities  $\bar{S}$  for the system can be found, where conductivity is the reciprocal of resistivity  $1/R = S$ , thus:

$$\bar{S} = \begin{bmatrix} \bar{E}_1 \\ \bar{E}_2 \\ \bar{E}_i \\ \vdots \end{bmatrix}^{-1} [\bar{c}] \forall \{i \in \text{nodes}\} \quad (82)$$

or more simply:

$$\bar{S} = [E]^{-1} [\bar{c}] \quad (83)$$

In the case where the node voltages are already known, the system would solve for the conductivities perfectly. *In the problem at hand it is only possible to estimate the node voltages at each state, and in doing so exploit structure that is present in the F-node placement. In order to make the estimation the forward transform can be used to interpolate the voltage field based on a conductivity prior.*

In the case where the voltages are not perfectly known the matrix  $[E]$  may not ever be invertible, however it is possible to regularize the problem by using the pseudoinverse so that:

$$\bar{S} = [E^T E]^{-1} E^T [\bar{c}] \quad (84)$$

This approximation will improve as more information is available, as long as only current information is used. If node voltages are augmented with voltage information directly, direct contradictions are introduced that make any solution impossible. In order to gain such information it is possible to append the voltage estimates of other field states, since the aim is to attempt to solve for the element conductivities, which are constant over all measurements of the field. The system is now:

$$\begin{bmatrix} \bar{E}_i^j \\ \bar{E}_{i+1}^j \\ \vdots \\ \bar{E}_i^{j+1} \\ \bar{E}_{i+1}^{j+1} \\ \vdots \end{bmatrix} [\bar{S}] = \begin{bmatrix} c_i^j \\ c_{i+1}^j \\ \vdots \\ c_i^{j+1} \\ c_{i+1}^{j+1} \\ \vdots \end{bmatrix} \forall \{i \in \text{nodes}, j \in \text{measurements}\} \quad (85)$$

Which is simplified as:

$$\begin{bmatrix} [E^j] \\ [E^{j+1}] \\ \vdots \end{bmatrix} [\bar{S}] = \begin{bmatrix} \bar{c}^j \\ \bar{c}^{j+1} \\ \vdots \end{bmatrix} \forall \{j \in \text{measurements}\} \quad (86)$$

The corresponding inverse captures the interaction between estimations of the field voltage, via weight sharing, in a regularized inverse that is guaranteed to be invertible. It likely solves for the conductivities of the field while weighing the contributions of every measurement state equally. The performance of the inverse is a function of:

1. The accuracy of the estimation of the voltage field for each measurement state, this is a function of:
  1. The placement of F-node locations in terms of distance from the field elements and each other.

2. The model assumptions in the method of estimation, the most accurate being a SPICE-like solver (forward transform simulation) for node voltages based on an initial guess of element conductivities.

The regular L2 pseudonorm seeks to minimize the total energy in the solution and thus the variance between the elements in the resultant vector. This goal is true to most models of images and continuous, smooth phenomena in bodies.

### *Algorithmic Complexity*

Consideration is now given to the scaling of the proposed method in terms of algorithmic complexity and memory complexity, in order to determine the practical suitability of the method in a general sense.

There are as many estimates used to generate the matrix  $[E]$  as there are measurement states, and a matrix of  $N \times N$  for each measurement state. This results in a memory complexity of  $M \times N^2$  where  $M$  are the number of measurement states. Since the measurement states are expected to contain dissimilar information about different areas of the field, it is possible to restrict the number of measurements to use for each node to a constant:

$$C \times N^2 \quad (87)$$

Since this matrix must be first be constructed, with an algorithmic complexity of at least  $C \times N^2$ , and must be inverted, with a complexity of at least  $N^{2.373}$ . This results in a total algorithmic complexity of:

$$2 \cdot C^{2.373} + N^{4.746} + N^{2.373} \quad (88)$$

This algorithmic complexity is a problem as the number of nodes in the field grows, resulting in a slow reconstruction that has a comparatively high memory footprint. Multiple non-parallel steps are required in an iterative manner:

1. Interpolation of the boundary states over a conductivity prior.
2. Construction of the system matrix.
3. Regularized matrix solution against a zero vector.
4. De-linearisation of the indexing.
5. Comparison of the conductivity profile against the measured data.
6. Repetition of the inversion process using an updated conductivity prior.

*This makes the reconstruction difficult to scale using parallel computing techniques, and unsuitable to applications of specialized hardware.*

### *Interpolation for voltage field estimation*

At this point it is important to consider the value of in-place interpolation methods in the estimation of the H-node states from F-node boundary conditions, since this information is often required for reconstruction. A sufficiently accurate interpolation method would greatly reduce the time complexity of algorithms over the natural method of system simulation.

The field is expected to be smooth, since the current is dependent on the voltage field. This current locally contains information about the global conditions in its' path, as the current will avoid elements with high resistances. This benefits model fitting, however the information is nuanced and an insufficient number of foveal nodes will result in a poor estimation, which will be useless in aiding reconstruction.

A number of interpolation models were investigated by comparing the fit of the model to the known node voltage distribution in a continuously connected field (all implemented using virtual images). The models are listed here in order of performance, best to worst: Radial Basis Functions, Bivariate Cubic Interpolation, Bivariate Linear Interpolation, Piecewise Bivariate Splines, and Support Vector Machine Regression

*The details of these will not be covered since the best performance by far is the use of a field conductivity estimate in the forward model of the field (where the forward model is mathematically identical to heat-flow interpolation). The errors introduced by the other methods do not warrant the decreased computing resources required.*

#### **4.10.5 Inverse by global constant-current field interpolation**

The inverse by piecewise linearisation results in a large computational overhead, the focus is now to consider another reconstruction method that has a lower computational footprint.

This method first attempts to find the relative shape of the conductivity distribution over the field, rather than its' absolute values. This problem is inherently simpler, and is the most common approach to EIT in general. This is still valuable for our purposes, since:

1. The shape of a light distribution off a concentrating mirror is the primary value in its' ability to concentrate, in which case a relative measurement is acceptable if an aperture array for directional purposes is not used. *This approach is consistent with a number of measurement forms presented, most importantly the axial-leaded mesh.*
2. The actual distribution can be found by normalization against points that are known, implemented by a sparse distribution of photo-detectors that can be easily sampled using conventional techniques. In this case a simple least-squares model would fit a scaling and offset parameter for the entire conductivity image, which would also effect dynamic calibration of the field against the reference points.

Consider first the effect of a change in conductivity when full knowledge of all the nodes in the field is present, not just the boundary nodes. In Figure 43 the effect of a circular conductivity change on five different conductivity shape is demonstrated:



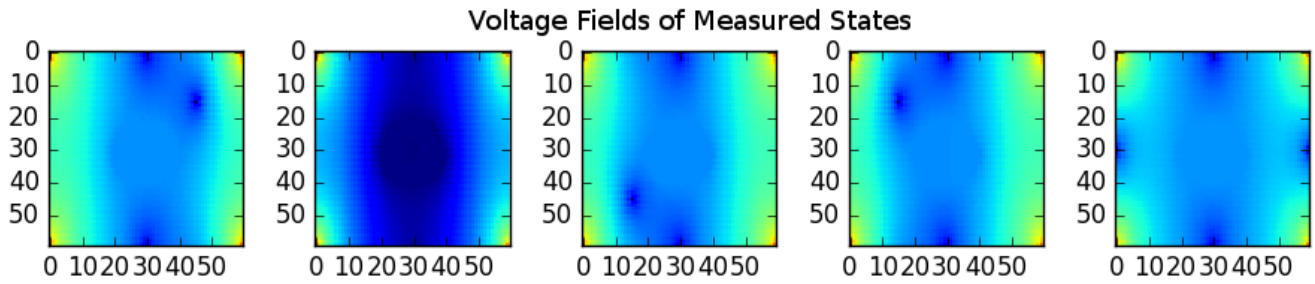


Figure 43: Voltage fields due to a conductivity change.

The effect of the conductivity change is primarily to modify the current distribution over the field, this can be found by finding the gradient of the voltage field. This gradient is calculated by application of the Sobel, Prewitt or Scharr methods, which are computationally simple as a hyperbolic mean of a set of convolutional filters. The Scharr operator is used on the voltage fields in Figure 43 to generate Figure 44, in which the effect of the conductivity change is clearly seen as a central tendency common to all the states.

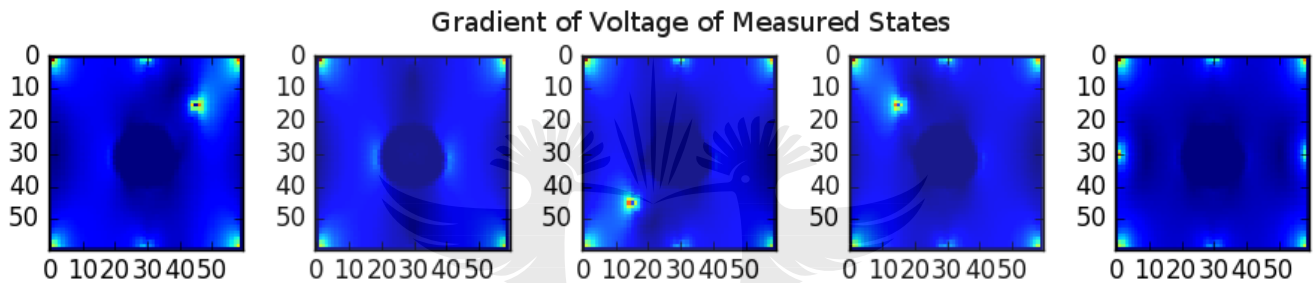


Figure 44: Gradient of voltage field of measured states

The voltage fields in Figure 43 can be *estimated by interpolation between the foveal nodes, which is best done by forcing the measurement state values at the F-nodes in a system simulation*. The points can be equally distributed in a regular pattern, which partition the surface into a triangulation of simplexes. The global state of the current flow over the surface is affected by the local changes of conductivity; the current will tend to bend around local obstructions. This effect makes small local conductivity changes detectable that would be smaller than the inter-node triangulation, the behaviour of which are not easy to predict.

The conductivity change is the common to all the voltage field states, so a simple operation of summing the gradient images effects a linearisation reconstruction. The averaging effect of the summing tends to diminish the errors introduced by any one particular measurement, and reinforce the wanted conductivity distribution. In addition to this the errors can be largely removed by determining the current distribution across a prior conductivity on the field. This may be constructed from a uniform prior or a previous image prior that is being improved upon.

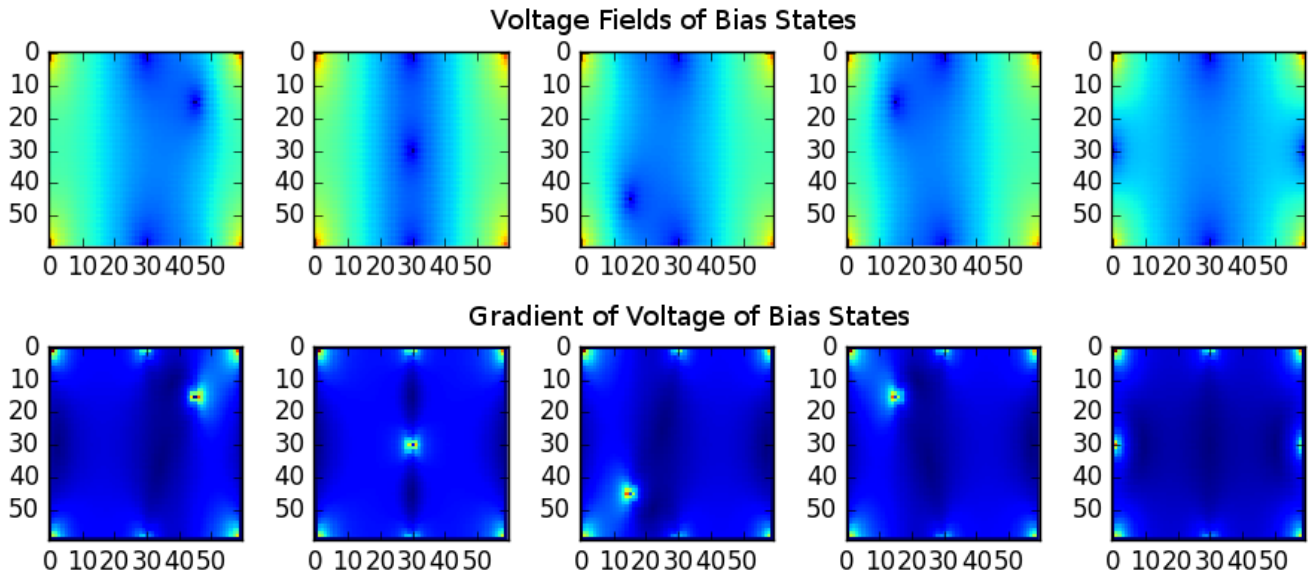


Figure 45: Bias images that form errors in reconstruction for a given prior

The voltage fields of measurement states and their respective gradients are shown in Figure 45, found using a uniform conductivity distribution. This form of error will be called the bias error, and must be calculated during reconstruction rather than being pre-calculated, since it depends highly on the particular measurement states used. The measurement states should be weighted in terms of use value, since the algorithm does not make use of current information in the reconstruction. States that have a predominant amount of information in F-node voltages are preferred, and where the active nodes are far from one another so that the voltage field is relatively uniform in large regions of the field.

*Overall this process of interpolation, summation and correction can be iteratively applied to improve the estimation of the conductivity field, since all forms of interpolation and error compensation used makes use of a prior conductivity distribution.*

#### *Observed Behaviour*

The above mentioned method is bolstered by accounting for all the combinations of applied measurement information available when a conductivity state is assumed. Using the simulation mechanism it is possible to produce a number of voltage fields for each state:

1. A heat-flow interpolation of the measured voltages into the field.
2. A simulation of the voltage field for the conductivity state using the state excitation vector for the voltage stimulus.
3. A simulation of the voltage field for the conductivity state using the actual measured currents at the F-nodes.

Using the available estimate of the conductivity state, it is possible to run an entirely new measurement process to generate the measured vectors for the conductivity state estimate. Using these measured vectors it is possible to generate a number of voltage fields:

1. A heat-flow interpolation of simulated measured voltages into the field.

## 2. The voltage field using the simulated currents at the F-nodes.

These fields are the only possible fields given an estimated conductivity state and a set of EITMSA measurements. *First-order interactions between all these fields and their gradients were investigated, as well as their reductions, and the method described is the only combination that gives useful results between these.*

### Formalizing the Inversion

The procedure thus described is a linearisation over the average current flow, as described below:

$$\bar{S}_{(x,y)} = \frac{\bar{I}_{(x,y)}}{\nabla \bar{V}(x,y)} \quad (89)$$

Where  $\bar{S}$  is the conductivity distribution,  $\bar{I}$  is the current distribution, and  $\bar{V}$  is the state voltage distribution. This linearization is simply an application of fundamental voltage-current relationships, and is aided by the nature of the continuous field that estimation is never extrapolation, only interpolation. Given known voltages at the F-nodes, even a first-order interpolation will be accurate to the average gradient between the two points. *This invariant is true no matter the shape of the voltage field between the points.*

The approximation is made that the field is continuous in order that the  $\nabla$  operator can be determined with discrete image gradient functions, however it would be a better generalization to use  $\nabla$  over the graph itself. The local current,  $I_{(x,y)}$ , can be kept relatively invariant by weighting according to the mean-expected local currents on a state-by-state basis, or by averaging over a sufficient number of independent states. Algorithmically this approximation is equivalent to:

$$\tilde{S}_{(x,y)} = \frac{1}{n} \sum_i^n \frac{I_{(x,y)}^i}{\nabla \bar{V}_{(x,y)}^i} \approx \text{norm} \left( \frac{1}{n} \sum_i^n \frac{1}{\nabla \bar{V}_{(x,y)}^i} \right) \quad (90)$$

where  $i$  is a state index, and  $n$  the total number of states.

In this investigation averaging was used, no attempt was made to adjust the local currents by weight. This would have otherwise increased the memory requirements of the reconstruction considerably.

This form of linearisation is considerably less prone to noise than other methods that have been used in EIT, with no direct need of current measurements. It is possible to determine the voltage field from either voltage or current boundary conditions, equivalent to Dirichlet and Neumann boundary types respectively. Experiments currently indicate that voltage conditions are superior in performance for this method. The continuous edges of the field ensure that voltage states are always being interpolated, which allows the gradient operator to function ideally with wrapping borders.

*The current distribution assumption is heavily impacted by the states used and thus performance of the reconstruction will vary depending on state selections.* Using all states for a measurement scheme is practically impossible (there are combinatorially-many), and the variation between iterations of selecting random states is appreciable. Thus any current distribution scheme will introduce error due to this effect alone. By randomizing the state selections a time-averaging effect over multiple

reconstructions can help to eliminate this, however ideally some form of state-specific compensation would provide the best results.

### *Field Scaling and Continuous Equivalence*

Since only the relative positions of the F-nodes need to be accurate, and a continuous approximation is used, it is possible to use lower resolutions during heat-flow interpolation and in bias compensation. The relative size of the field used for reconstruction purposes should be considered as an important parameter for a number of reasons:

1. The time taken for reconstruction is almost completely dominated by the steps of heat-flow interpolation and bias field simulation, a lower resolution is less computationally and memory-expensive.
2. A reduction in resolution brings with it an order of magnitude reduction in the degrees of freedom available for current flow, thus lowering resolution forms an effective regularization method that is natural to the system. Regularization is important when not enough base information is available, or cannot be utilized effectively.

A reduction in resolution does however change the nature of the field interactions that arise from the connectivity used, due to the reduction in the degrees of freedom in key locations. As the number of elements in a minimum path between any two F-nodes increases, the behaviour of current flow will tend toward that of a continuous medium. In the case of a large path distance the reduction in resolution would not change interactions much; however in regions close to F-nodes the current behaviour becomes substantially different.

Added to this error factor is the effect of the gradient operator, which in the "Sobel" and "Scharr" methods estimates gradients with Taylor coefficients for two points either side of a point in question. Thus as the resolution of reconstruction is reduced the gradient estimation produces further errors and edge location distortions. Reduction of the number of coefficients (using a simpler gradient operator) results in a lower accuracy of gradient estimation, but appears to be slightly more suitable for very low resolution reconstructions.

### *Implementation Caveats*

A limiting problem that occurs during simulation is that when two F-nodes are positioned with only one element between them, the system solution cannot be found. This was true for the BLAS and LAPACK routines called by the method of simulation, and is expected to be due to ill-conditioning of the system matrix under these circumstances. *So long as there are at least two elements in a path between any two F-nodes the problem does not present itself.*

Another problem that occurs is the iteration scheme walking itself into producing conductivity images that in turn produce unsolvable matrices. The conductivity estimate needs to be bounded by clipping operations to ensure conductivity does not go to zero, or become too large.

### *Modifications for Robustness and State Selection*

The performance of the method is dependent on the states used in the reconstruction, the selection of which should be more ideally performed by a sensitivity analysis. Element sensitivity is

dependent on the graph distance between active F-nodes, and there is a general parallel shunting effect between nodes. Thus an approximation can be made by ordering states with a descending hyperbolic mean of the distances between host and any sink nodes present, taking account of virtual images formed by wraparound.

*The errors caused by state selection alone will be reinforced in an iterative scheme, creating false images and what appear to be 'mirror image' duplicates in some tests. To avoid this, state selection should vary between conductivity state estimation iterations, and multiple models used in consensus. These effects are the cause for much of the implementation complexity described in the model below.*

#### *Description of the Resulting Model*

When the above observations are combined, these experiments have lead to the method shown in Figure 46 and in Figure 47. The diagram in Figure 46 is described below:

1. The upper-left block (orange block) contains all inputs to the algorithm, including all parameters and the data taken from field measurements. Parameters below the measurement vectors are scalars, integers and vectors in  $\mathbb{R}^1$  and shown in white.
2. The upper block (yellow block) contains a mechanism for dispatching lists of measurement state indices to many reconstruction models, one of which is shown below it (taupe block). State indices are dispatched as vectors (blue data), and are generated either deterministically or according to a random sampling mechanism.
3. The reconstruction model pictured (taupe block) takes parameters and assumes a uniform conductivity prior. All conductivity images and their gradients are two dimensional vectors (green data), which are transformed by processes (pink processes). Iteration within each model is terminated by an iteration counter.
4. The lowermost block (yellow) has a mechanism where the results of the multiple reconstruction models are reduced and combined for further iterations of multiple models. Processes and decisions here are in blue, with overall termination of the algorithm by an iteration counter.

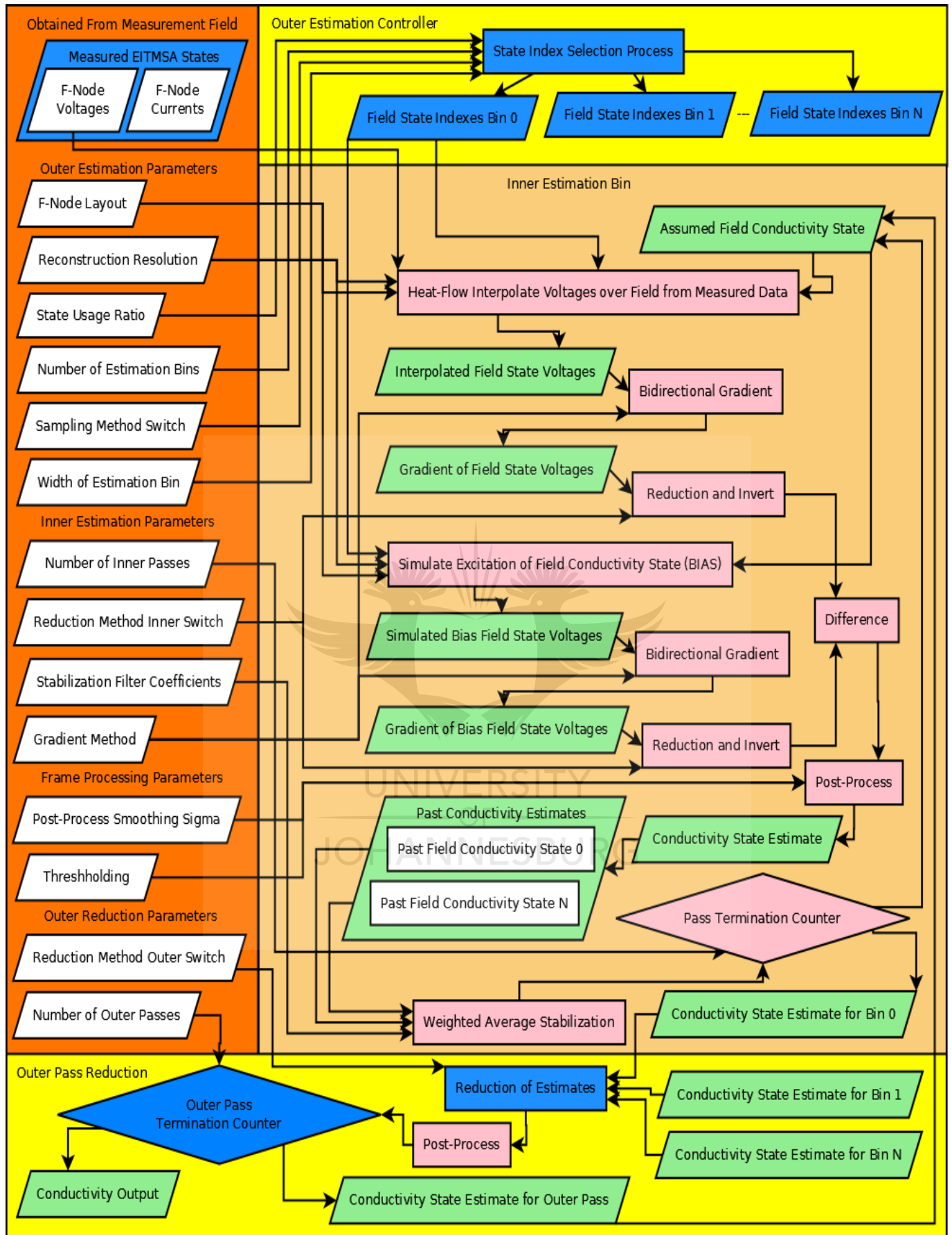


Figure 46: Iterative reconstruction using voltage-interpolated fields



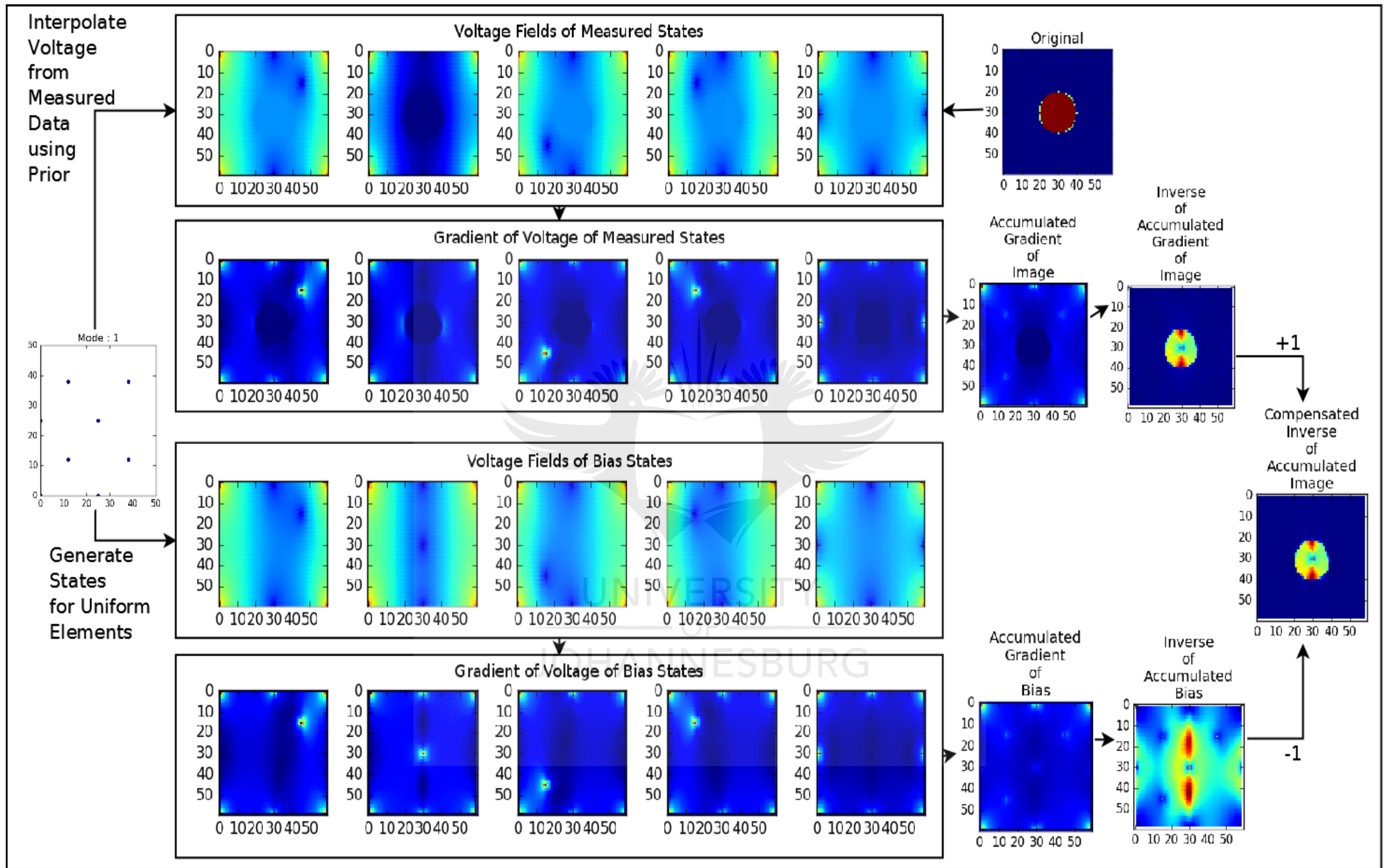


Figure 47: Alternative visualization of reconstruction process

The diagram in Figure 47 shows a single pass of reconstruction, and uses the actual conductivity distribution as a prior to demonstrate the process, the real process is substantially less accurate.. The scatter plot to the left has the foveal node locations, and five measurement states are shown. The conductivity projected onto the field is shown at the top right.

### Description of Reconstruction Procedure

The algorithm is described in Figure 46 on page 122, and also in Figure 47 on page 123, with reference to the former the operation is as follows:

1. The measurement states excitation vectors can either be stored as part of the data captured from the sampler hardware, or generated as part of a method common to both the sampler and the reconstruction. Generation is preferred since the excitation vector is an excess transmission requirement. The excitation vector is a linearisation of the normally two-dimensional F-node indexes:  $\bar{e}$  .
2. A conductivity state is assumed as the initiator to the iterative process; a uniform prior is a suitable starting point. This prior is in the form of a two-dimensional matrix:  $[s]$  .
3. An outer iterative loop is performed, in which multiple reconstruction models are dispatched and reduced in order to gain a better estimate against imbalances in the contributions from respective measurement states. Each reconstruction model is given a subset of state vector indexes, chosen either deterministically or by random sampling (either with or without replacement). The conductivity state estimates are reduced for each pixel by either averaging all the estimates images together, median selection, or correlating. The new estimate is filtered and used as a prior in a new pass of reconstructions. Each reconstruction model (sub-model) generates a reconstruction estimate according to the following method:
  - a) Two simulation processes occur independent of each other. Both use the conductivity prior  $[s]$  , and parse the conductivity state using the method shown in Figure 40 to generate a system matrix  $[q]$  for the conductivity graph. *The F-node current information is not used in this implementation, but can be easily included with relevant boundary conditions.* In each measurement state (corresponding to an activation  $\bar{e}$  ), the voltage field can be calculated independent of each other, in parallel. The system matrices are common to all measurement states, but since simulation requires the matrix be augmented a copy is made for each state  $m$  , producing  $[q_m]$  :
  - b) The voltage fields of the measurement states are found by simulation of the current flow over the conductivity graph, driven by the vector that describes the voltage state at the boundary nodes. Both the excited F-nodes and the normally passive F-nodes are driven as set voltages in the simulation,  $\bar{v}_m$  , with the same length as  $\bar{e}$  . The interpolation is thus exclusively to determine the H-node voltages between F-nodes. *This series of measurement states will be called the "measurement stream".*
  - c) The bias field state is found by simulating the current flow over the field graph using the excitation voltages at the field nodes,  $\bar{v}_e$  . The active F-nodes are driven to their excitation voltages and the interpolation determines the voltages at the high-impedance F-nodes, and at the H-nodes between them. *This will be called the "bias stream".*

- d) Both the measurement stream and the bias stream have their voltage fields differentiated by an image gradient magnitude operator. This can be done for each measurement state independently and directly after it is generated.
- e) After generation the gradient images for each stream are accumulated independently for their respective streams. This accumulation is a reduction operation that can only be partially parallelized. The measurement stream produces a conductivity image, and the bias stream produces an error compensation image.
- f) The conductivity image and error compensation image are each element-wise inverted, and the conductivity image has the error compensation image subtracted from it to produce a new conductivity estimate. The result is then post-processed by a successive application of:
- g) Element-wise clipping, to ensure that the conductivities remain in sane limits, without which infinities and errors in simulations over the graph will occur.
- h) Thresholding and quantization, which is only applied if the conductivity image is known to be quantized in nature. The parameters for thresholding are a subject for empirical investigation, and will not be considered here.
- i) The conductivity estimate is entered into a history, which is used to generate a conductivity estimate for further iterations of the algorithm. The estimate is generated by an element-wise application of a finite-response stabilization filter, formed by weighted kernel over the values of conductivities in the history for each element respectively.
- j) The model iterates in this way using its' own conductivity estimate before returning an estimate to the outer loop.

### Stabilization Filtering

Filtering is done on a per-pixel basis over a stored history of the pixel values from previous iterations. The finite response filter has the form below; where the response for the latest conductivity  $[s_{-1}]$  is determined by the history of conductivity images  $[s_0] \cdots [s_I]$ , where  $I$  is the index of the last coefficient,  $a$ , in the kernel:

$$[s_{-1}] = \frac{a_0 \cdot [s_0] + a_1 \cdot [s_1] + \cdots + a_I \cdot [s_I]}{\sum_0^I a_i} \quad (91)$$

*This kernel is applied since in initial testing, oscillations of the conductivity image occurred when the iterative routine used only the last produced estimate.* These oscillations were dependent on a number of factors, including the conductivity image being reconstructed. The optimal kernel for reconstruction is a parameter of the reconstruction that must be determined empirically, but in simple tests a hyperbolic fall-off shows sufficient stability.

### *Smoothing*

Stabilization filtering is useful to improve convergence behaviour, and prevent oscillating results that are present with small step changes in conductivity. In addition to this intra-frame smoothing can be done on the result of each iteration. Smoothing reduces the total variation available to the result and helps combat vanishing solutions that decay with further iterations rather than reinforce the desired result. The global current-bending effects that tend to make small conductivities difficult to reconstruct can be managed by smoothing, where small changes are spatially amplified so their footprint is larger.

### *Thresholding*

Simple experiments with the method indicate that if it is known that there are a finite number of conductivities a threshold process can be used on each estimate between iterations to improve the reconstruction of edges and forms, as a result of the reduction in degrees of freedom. In this case, instead of spatial smoothing; operations of erosion and dilation can be considered. This will not however be investigated further in this project.

### *Modifications to the basic form*

The initial investigations into this method of reconstruction show a number of behaviours that suggest modifications are required:

1. The foveal nodes are themselves locations of a high gradient, and thus present themselves as detail in the conductivity reconstruction. A clipping operation on the voltage field prior to differentiation will eliminate the highly distorted field around the F-nodes and reduce such artefacts.
2. The shape of reconstructions are slightly distorted, as if by an affine transformation. This can be attributed to a number of factors:
  1. The physical structure of the conductivity graph, which will distort the electric field especially at borders to step-changes in conductivity.
  2. A bias in the measurement states chosen in the average overall shape of the electric field produced, a problem that is exacerbated by using less measurements.

The changes in shape cannot be easily compensated during reconstruction, since the problem is largely due to a lack of information in a particular region, caused by the overall curvature of the electric field shadowing these regions. This information deficit is a problem best alleviated by a good choice in the particular excitation states used during a scan, balancing field interactions over all regions. It may however be possible to dynamically evaluate the quality of a particular measurement during reconstruction.

### *Algorithmic complexity of the reconstruction method*

Consider should now be given to the scaling properties of the algorithm, and comparison with the former proposed reconstruction, in order to determine its' general suitability. The algorithm thus described has a number of serial processes, which will be considered independently then integrated.

The generation of the system matrix for the conductivity graph can be done in parallel for each pixel, the total complexity is given by  $O(N^2)$ , while the parallelism is a constant  $O(C_1)$  to independent memory locations. This independence allows memory access parallelism. These graphs must be copied for later augmentation, taking  $O(M \cdot N^2)$  operations in total and has a parallelism of  $O(C_2)$  operations to independent memory locations.

The graph system matrices for each measurement are augmented for each F-Node, this is of order  $O(F \cdot M)$ , where  $F$  are the number of foveal nodes. Parallelism is of order  $O(C_3)$ , with independent memory locations. These can be solved independently with a total order of  $O(M \cdot N^{2.373})$ , the parallelism is limited to each measurement with order  $O(N^{2.373})$ . The gradient operations have an order of  $O(M \cdot C_4 \cdot N)$ , the parallelism is an order  $O(C_5)$  due to the reduction operation of the kernel convolution at each node pixel. These operations occur for the measurement and bias states independently.

The complexity of the reduction of summing over each measurement is  $O(M \cdot N)$  with a parallelism of  $O(M \cdot \log N)$ . The difference and inversion is performed in  $O(N)$  and filter stabilization in  $O(I \cdot N)$ , with a parallel order of  $O(C_6)$  and  $O(C_7 \cdot I)$  respectively.

Total algorithm complexity is thus an order of:

$$\begin{aligned} &O(2 \cdot (N^2 + M \cdot N^2 + F \cdot M + M \cdot N^{2.373} + M \cdot C_4 \cdot N + M \cdot N + N)) \\ &= \\ &O(2 \cdot (M \cdot N^{2.373} + N^2 \cdot (1 + M) + N \cdot (1 + M(1 + C_4)))) \end{aligned} \quad (92)$$

The parallelism is high, with a series order of:

$$O(2 \cdot (C_1 + C_2 + C_3 + N^{2.373} + C_5 + C_7 \cdot I)) \quad (93)$$

The memory complexity of the serial case is at a minimum:

$$O(2 \cdot N^2 + (2 \cdot M + I) \cdot N) \quad (94)$$

In comparing the algorithmic complexity with the previous reconstruction method, the dominating exponent is orders of magnitude smaller. The number of nodes that can be resolved is thus much greater for a given computing power. Memory use is also much reduced, since intermediate results can be reduced after they are generated. This makes the reconstruction method suitable for a memory-constrained platform. Overall the reconstruction method is suitable for implementation on comparatively low-power hardware, including embedded devices.

#### 4.11 Chapter Summary

This chapter covers the design of the measurement technique, starting with the necessary requirements and covering the steps taken to achieve the objectives for a novel characterization technique. The objectives were laid out as: a combination of cost-effectiveness for overall impact; being operable in production environments in order to track currently unquantified variables; being mouldable into a general surface to account for necessary variation in form; directly transducing the phenomena rather than transducing a transformed stimulus for better response time; technical



comparability with existing techniques for research impact; and theoretical completeness to facilitate a base for further development.

The sensing problem was described in terms of the information required, the physical constraints, the necessary optical quantities, the characteristics of the phenomena being sampled, applicable heuristics and simplifications, and the errors expecting in real implementation of the technique. The material characteristics for radiation sensing were covered, along with the methods and modes by which direct measurements can be made using semiconductor transducers. Despite extensive study into existing solar-related measurement techniques, the existing methodologies were found unsuitable for modification and application to the project goals.

Development of a solution was approached from first principles, referencing concepts located in the appendices which sample the plenoptic function with varying degrees of simplification. Light field capture was selected as most suitable, with a candidate device for measurement described. The device demonstrates the feasibility of the measurement technique in a specific application, with the primary problem in its' construction being the sensor array used. This array became the focus of design investigations as a result of the complexity in achieving a design suitable to requirements. Manufacturability of the array was considered, evaluating known techniques against the requirements.

The mathematical properties of the array were covered, with a focus on solving the scaling problem in transport of information between the sensor and primary capture device. The physical constraints were considered, and the necessity for a reduction in the amount of information transport was identified based on the reliability requirements for small-scale manufacture, and the scalability of the technique for characterization of large solar system forms. The reduction was achieved by moving information transport into the structure of the sensing elements themselves, thereby trading off complexity in manufacture for complexity in recovering the state of the sensors from inter-related measurements, taken at select points on the array.

This technique was dubbed Electrical Impedance Tomography Manifold Sensor Array (EITMSA). The properties being explored with investigations into the requirements on the linkage structure of sensor elements, the nature of the transform elicited by the construction, and how measurements of the structure are made distinct in order to provide sufficient information to resolve element resistances. Measurement of the structure was achieved by a fabric of switched low-impedance voltage-driven excitation and high-impedance sensor nodes, the properties of which were explored. The layout of these points were explored and the cost implications of variations in the number active of excitation and sensor resources. The conditions on how measurements were to be made were explored, with a resultant exponential relationship between the number of measurement channels and the information transport potential.

Exploration of the basic properties of continuous and discontinuous topologies determined that closed electrical manifolds have superior properties that align with the target manifold physical structure. A uniform spacing of sensing nodes over the electrically continuous manifold was identified as an optimal prior for maximal cost efficiency per sensing channel.



Measurements made on this construction and constraints result in a set of independent system matrices that are linked by common parameters, and subject to the effects of non-linear interactions within and between each other.

The applicability of prior research into Electrical Impedance Tomography was investigated, with the majority of research particular to the problems in sampling and modelling real-world continuous media. The EITMSA construction is subject to significantly less variation than EIT for continuous media due to a known topology, no ambiguity in the sensing locations or interface impedance, and natural constraints on the electrical degrees of freedom within the field.

Mathematical modelling and simulation of the construction (the forward transform) was covered, whereby a simplified uniform array mapping was chosen for the purposes of investigation by simulation. The inverse to this transformation is the subject of the main experimentation; due to the complexities in reversing the highly non-linear forward transform, and the opportunity to exploit the greater certainty provided by the discrete topology. The approaches to the inverse are covered in a number of algorithm expressions, with traditional EIT and novel approaches. A novel approach by way an iterative application of heat-flow interpolation and the continuous kirchoff current conservation law. This includes a number of in-loop tuning parameters that were investigated by simulation, whereby the reconstructions obtained by latin-hypercube sampled parameters were measured against a number of standard objective functions applicable to the final use case.



## 5 Experimental Design

The system that has been described has many layers of complexity and an extensive scope. The investigation will focus on the core enabling part of the system, that of the EITMSA and its reconstruction. The development of the details of the other sections will be neglected, which will be left to further investigations.

### 5.1 Experimental procedure

The experiment will seek to evaluate the EITMSA multiplexing method, since this is the enabling structure and forms a bound on the overall system accuracy. This will be done with a simulation of the system, forming a best case performance measurement on which further development of specific implementations can be based. The reconstruction method developed will be evaluated. Specific implementations will need to consider the effects of the transducer chosen for that application in addition to the reconstruction performance.

A number of image step functions of different locations and sizes are used as test inputs, since these are suitable for general characterization and approximate the expected conductivity profiles. The parameter space is large, and there is little prior information to inform an optimal slice pattern over the space. To accommodate this, a set of field configurations is chosen according to a method based on **latin-hypercube sampling** within the bounds of the parameter space, in order to maximize the generalization of the test results. *The set of responses of the field are acquired by circuit simulation, which are modified by degrees of quantization and given various levels of Gaussian noise that can reasonably be expected from the electrical environment.*

Latin hypercube sampling maximizes the spread and general uniformity of samples over a sample space, the particular procedure used was as follows:

1. The bounds of each input dimension are specified.
2. The dimensions are labelled with weights that are used to proportionately allocate sampling variance to the continuous dimensions relative to each other. A number of values are allocated in uniform strides spanning the dimension bounds, forming a candidate set.
3. The discrete dimensions are chosen deterministically or a uniform selection is made over a given array of discrete values to form a candidate set. In this case all discrete bins were deterministic.
4. A number of sampling rounds are made, for each the procedure is as follows:
  1. Entries for each dimension are drawn to make a single sample:
    1. Dimensions that have the largest number of items are sampled randomly with draws made *without replacement* from the candidate set for each dimension.
    2. All other dimensions have smaller sets, and are thus drawn with replacement.

## 5.2 Test Sample Space

The test being reported on here had the following hypercube generation parameters, chosen by compute time limitations:

Input Meta-Parameter	Value	Resulting Meta-Parameter	Value
Number of Dimension Divisions	15	Number of Samples	320
Number of Pick Iterations	15	Number of Ground-Truth Tests	15
Number of Test Images	5	Total Number of Tests	4800
Number of Test Image Locations	3		

In this test scheme the foveal node generator pattern will be kept constant in the general form of that demonstrated in Figure 47, a staggered layout with equal spacing in each dimension that takes account of the distance in wraparound on the edges. The actual parameters used in the test are listed below:

Parameter Name	Parameter Function	Sample Set Values
Host Image Shape	The size of the input image in pixels [x, y]	{[30, 30],}
Gradient Operator	The gradient method used to potential gradient images from the voltage field simulation on a per-state basis.	{Scharr,}
Resize Order	The order of interpolation used in resizing the simulated field [X, Y/2] to the input shape [X, Y]. This interpolation is required due to the graph map structure.	{1,}
Pass Coefficients	The stabilization filter coefficients used, in order from most recent frame to least recent frame.	{[2.5, 2.0, 2.0, 1.0],}
Sampling Mode	The method used to select forward transform measurements from those made available. "Deterministic" selects the states progressively according to weighted distance between F-nodes, from greatest to smallest. "Without Replacement" randomly samples without replacement from a window of measurement indexes made available, according to the "States Available Ratio"	{Deterministic, Without Replacement}
Dynamic Binning	The measurements are made available to the outer loop, and then partitioned out to the sub-models. This controls how often the selection occurs, and how random it is over the iterations of reconstruction.	{Inner, Outer, Static}
Noise	The magnitude of noise added to the results from the forward transform. This factor is total noise added to a full scale of 2 Volts.	{0, 0.00526, 0.0105, 0.0158, 0.0211, 0.0263, 0.0316, 0.0368, 0.0421, 0.0474, 0.0526, 0.0579, 0.0632, 0.0684, 0.0737, 0.0789, 0.0842, 0.0895, 0.0947, 0.1}
Quantization	Simulation of the effective numerical depth of the ADC of the electrical capture equipment.	{4096, 16384}
Inner Consolidation Method	Method of aggregation over gradient states used in the "inner bin" sub-models.	{Mean, }

Parameter Name	Parameter Function	Sample Set Values
Inner Blur Radius	Gaussian smoothing coefficient used in the filter stage within the "inner bin" sub-models.	{0, 0.63, 1, 1.26}
Inner Median	Median filter radius used in the filter stage within the inner sub-models.	{0, 1, 2}
Total Nodes	Number of sampling points in the field.	{16, 24, 32, 64}
Active Nodes	Number of nodes selected at any one time as current drivers.	{2, }
Outer-Loop Consolidation Method	The method of aggregating the resulting reconstruction images from the inner sub-models.	{Mean, Median}
Outer-Loop Blur Radius	Gaussian smoothing coefficient used in the filter stage in the outer loop, after sub-models have been aggregated.	{0, 0.0667, 0.133, 0.2, 0.267, 0.333, 0.4, 0.467, 0.533, 0.6, 0.63, 0.667, 0.733, 0.8, 0.867, 0.933, 1, 1.26}
Outer-Loop Median	The radius of the median filter used in the filtering stage after the sub-models are aggregated.	{1, 2, 3}
Shotgun Bins	The total number of reconstruction inner sub-models to use.	{1, 2, 3, 4}
Shotgun Passes	The number of iterations to use within each sub-model before aggregation in the outer loop.	{1, 2}
States Available Ratio	The ratio of the number of states made available for reconstruction, against the parity number of states based on the number of F-nodes and the total number of sensor elements in the grid.	{0.5, 0.526, 0.553, 0.579, 0.605, 0.632, 0.658, 0.684, 0.711, 0.737, 0.763, 0.789, 0.816, 0.842, 0.868, 0.895, 0.921, 0.947, 0.974, 1}
States Used Ratio	The ratio of the states made available which are actually used in reconstruction. The sampling mode 'without replacement' draws this number from the pool of states made available. (See row above)	{0.5, 0.526, 0.553, 0.579, 0.605, 0.632, 0.658, 0.684, 0.711, 0.737, 0.763, 0.789, 0.816, 0.842, 0.868, 0.895, 0.921, 0.947, 0.974, 1}
Resolution-Multiplier-X	The scale in the X dimension of the image actually used in simulation, resulting in a more or less constrained system graph.	{0.7, 1, 1.5}
Resolution-Multiplier-Y	As above, for the Y-dimension.	{0.7, 1, 1.5}

### 5.3 Objective Functions Used in Evaluation

A primary aim in the experiment is to non-dimensionally characterize the system by the ratios that have been outlined in section "4.5.3 - Design considerations for system configurations", which can be derived from the number of nodes and samples taken. In order to characterize the performance of reconstructions, a number of standard comparisons against the ground truth will be used in analysis. Spectral content measurements were performed but not included here due to space constraints, it is sufficient that the regularization inherent in reconstruction tends to eliminate the higher-frequency spectral content. The objective functions used were not entirely independent of each other, however each add relevant information that the others do not, these are as follows:

Comparison	Rationale for use
Mean Squared Error	General measure of accuracy of reconstruction on a per-pixel basis.
Error in Centroid	The image centroid deviation, chosen due to usefulness in solar mirror tracking performance evaluation.
Total Image Mass (Image Moment M00)	Total Image Mass is proportional to the total amount of energy that would impinge on the sensor, and is a primary quantity of concern in solar thermal systems.

## 5.4 Chapter Summary

This chapter has covered the design of the experiments in line with the design science approach elected. The key aspect investigated was the reconstruction of the flux image acquired from the sensor matrix. This was modelled as an ideal forward and inverse transform on the layer of the electrical resistance of the elements, thereby decoupling the investigations from the specific light transducer used.

Due to the complex interaction between the core and tuning parameters in the proposed reconstruction algorithm, characterization of the entire parameter space was required. The methodology taken was to pipeline a number of primitive image step functions, with variation in size and position, through a simulated capture and reconstruction pipeline. The difference between the imposed image on the simulated field being compared by well-known object functions.

Due to the relatively large number of dimensions to consider, the geometric increase in the number of samples made a grid sampling scheme untenable. A latin-hypercube method was used in response to the explosion in dimensionality, maximizing the coverage of the parameter space while limiting the total number of samples. The results of the simulated experiments were evaluated by high-dimensional slicing techniques, requiring interaction with the data due to little prior knowledge present to guide the interrogation.

The transducer field size was limited to 30 by 30 elements, being representative of a basic device and remaining manageable in terms of computing time. The interpolation steps used internal to the algorithm were selected based on interactive experiments, representing what appeared to be good average values. The effect of imperfect electrical sampling and uniform device imperfections were modelled as a noise addition to the output of the forward transform, being representative of the environmental noise expected as the primary mode of interference. Due to the known requirements of class of techniques to measurement sensitivity, the quantization noise of the Analogue to Digital Converter was modelled at bit depths representative of microcontrollers at 10 and 14 bits. The most important parameter with regard to sampling time; the number of excitation states used, was given a large relative sample allocation due to need to determine the asymptotic effect of information available to the reconstruction.

Overall the experimental setup was effective at covering the overall effect of the parameters on the reconstruction algorithm, while remaining computable in a reasonable amount of time.

## 6 Experimental Results and Discussion

In order to determine the overall performance of the method, a number of ground-truth input samples were used, over which the results are aggregated to determine performance. The input images were 2D step functions generated in 3 different locations on the field, for each location 5 different sizes of step function were used. The step function size is given by factor, that is the equivalent denominator in the ratio to the field width, such as  $factor(5) = width/5$ . The algorithm used requires a contrast within the input image, and cannot function if there is insufficient contrast present. It is for this reason that test images of  $factor(2)$  or less result in unstable reconstructions, and the largest test step function is chosen at  $factor(3)$ . The values used are listed below:

Image Locations:			Image Sizes:	
X	Y	Description:	Factor:	
0,5	0,5	Centre	3	6
0,2	0,2	Upper Left	4	7
0,2	0,5	Upper Centre	5	

Since Latin hypercube sampling is used to sample a maximal amount of input parameter space, statistical reductions are required to determine the effect of a parameter on the whole input space. Due to the non-linear behaviour exhibited by the forward transform and the reconstruction, a large number of outliers are present in the results and significantly non-Gaussian distributions. Robust statistical methods were used to combat this; primary aggregation is by L1-associated median rather than L2-associated mean. The results are first grouped according to the sample input vector, and aggregated according to median. Depending on the plot, aggregation using median occurs according to the classes found in the chosen X-axis of the plot. This depends on plot type.

### 6.1 Parameter-Space Slice and Aggregation Analysis

There are three main forms of plot present: The first is a combination of scatter plot and hexagonal binning (an improved 2D histogram) methods, where the scatter plot is aggregated and the hexbins are left unaggregated in order to show the properties of the distribution. The second type of plot is a regular scatter plot that corresponds with the aggregation method of the first, with the hexbins omitted since their distributions are consistent in nature with FigurePlot 1. The third type is a combination of box-and-whisker plots and scatter plots with linear regressions in overlay. The scatter points in overlay are aggregations according to median, and a number of fitted trend-lines are shown as candidate models for the progression of these aggregated points.

Only the results that indicate relationships will be presented, others can be assumed uninteresting or not conclusive in any direction. Plots will be presented and the results discussed in a section following shortly afterwards. The term “(Ground-Truth vs Resolve Actual)” refers to the performance for the reconstruction measured against the respective input test image. This label is attached because measurements also included the best reconstruction performance (given a perfect prior), but these results did not aid much in evaluation and have not been included.



Logarithmic scaling on frequency bins  
Series plotted are for dimension: 'Total Nodes'  
Grouping method 'median' used for dimensions: ('Test Original-Image')

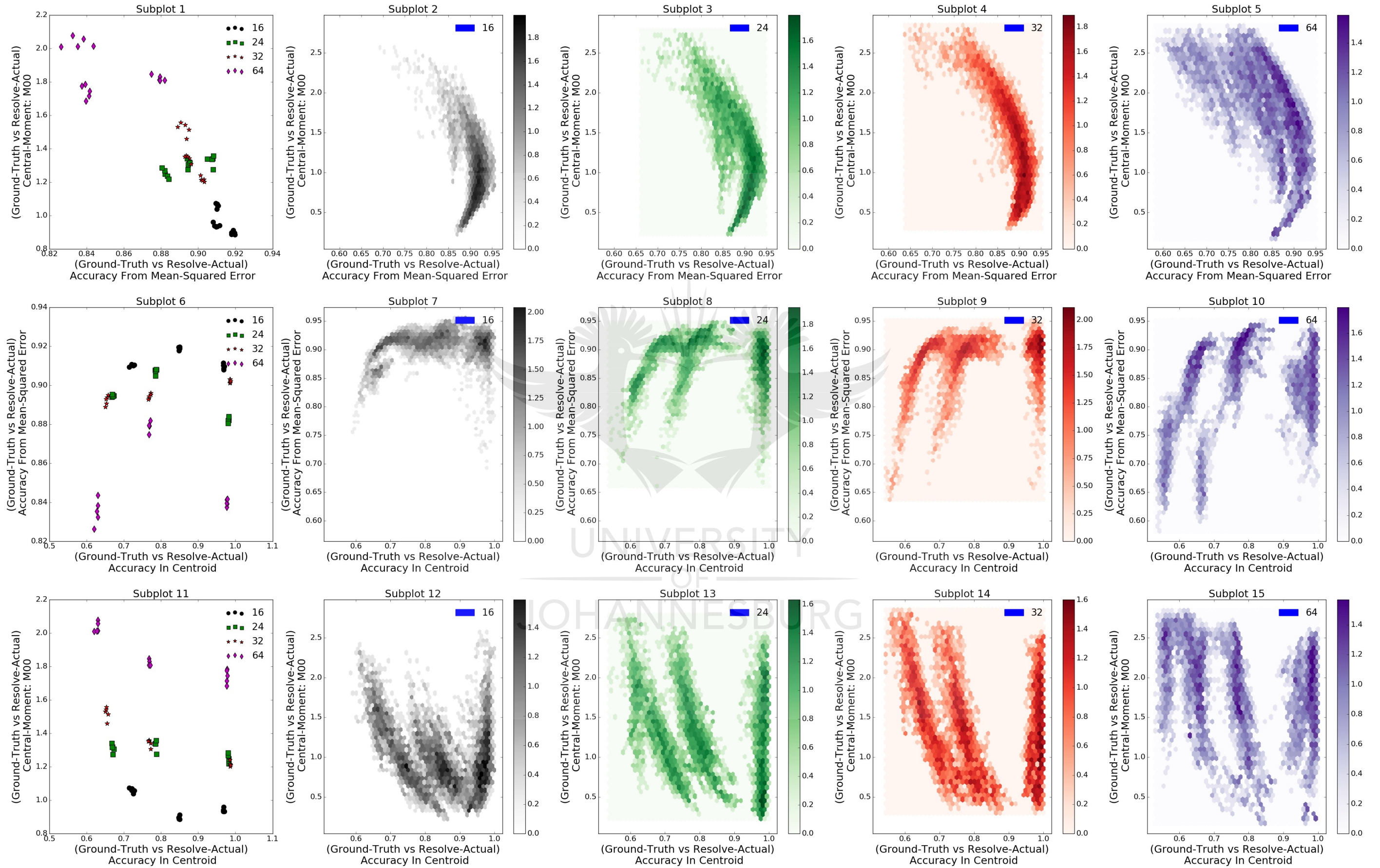


Figure 48: Performance plot for parameter "Total Nodes"

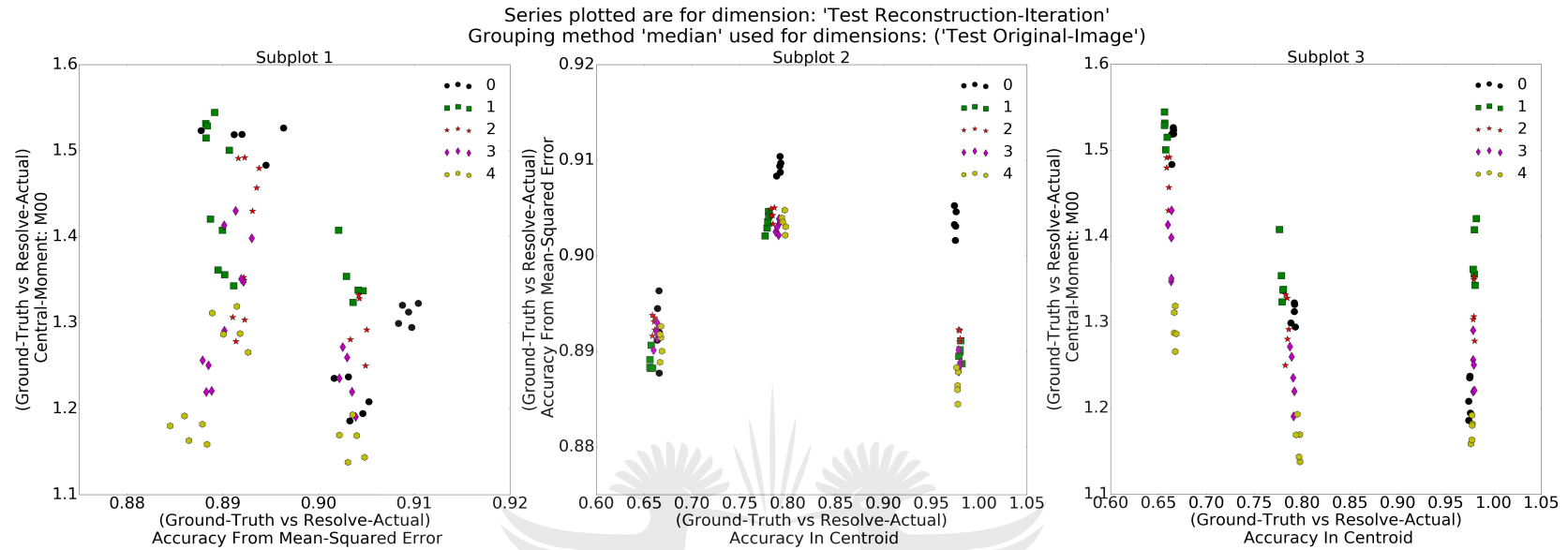


Figure 49: Performance for various numbers of chained iterations of the main algorithm.

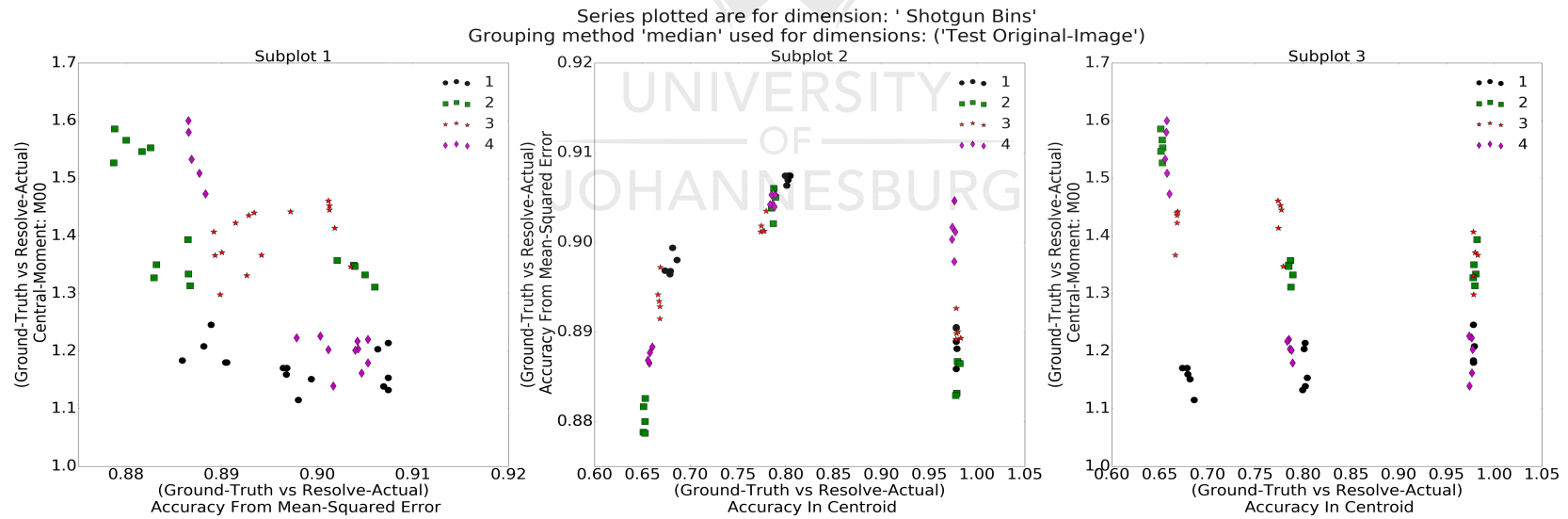


Figure 50: Performance for variations on the number of sub-models in the inner loop.

### 6.1.1 Discussion for Figure 48 – The total number of F-nodes

The performance of the reconstruction displays counter-intuitive behaviour with respect to the total number of nodes used to spatially sample the field in a sparse manner, with reference to Figure 48 it is evident that:

#### *Spatial Distortion*

There are three groups of reconstruction performance, these correspond to the spatial locations of the test images, and can be seen in Subplot 6 and Subplot 11. Within these groups there is a tight grouping among the variations in step function size. This grouping is primarily a result of distortions in the geometry of the field (similar to distortions in projecting a sphere onto a flat surface), this effect being evident in test functions during development. The group with the greatest accuracy corresponds to the central test image, and the least accurate the spot in the upper left corner.

There is no inherent bias in the scheme to reconstruct a particular image shape (there is no over-fitting on this particular set of test cases), so all distortions are due to the change in response as a result of variations in path geometry over the field. This illustrates the need for further experiments into the method of connecting the boundary, a taxonomy of which is included in the Appendix (8.6 - Boundary Connectivity on page 181). This result shows that is likely that connectivity of type 61 or type 81 would perform more consistently, being closer to a geometry with uniform distance between any two points.

This problem is also unexpectedly magnified with increasing number of F-nodes, this could be due to an unforeseen imbalance in the geometrical distribution of F-nodes with respect to the boundary connectivity. This would introduce greater error in the uniformity of the  $I_{(x,y)}$  estimate, thus generate an imbalance between contributions from various parts of the image after aggregation.

#### *Mass Estimation*

In reference to Subplot 1, a large amount of total mean-squared error is due to the contribution of over-estimation of the image mass, increasing with the number of F-nodes used. This could be due to a number of effects:

1. Increased deviation from continuous behaviour characteristics as a result of lower path lengths between any H-node and F-node, and a resulting decrease in freedom in the parallel paths for certain measurement state excitation patterns.
2. A mismatch between the amount of regularization and the F-node density. The increase in data available with increasing F-node density requires a decrease in the regularization provided by the filtering stages of Gaussian Blurring. Since the sampling scheme is uniform this compensation is not provided, and thus skews the aggregate results of the input parameter space.



The distribution of results between 64 F-nodes and 16 F-nodes demonstrates that despite general over-estimation of image mass there is a greater window of parameters that give good accuracies. The distribution for greater numbers of F-nodes has greater spread indicating that the tuning of other parameters becomes more sensitive with this parameter, most likely due to increased non-linearity in as a function of path length. Overall lower F-node density produces more stable results.

This discussion is continued after presentation of Figure 60, on page 148.

#### **6.1.2 Discussion for Figure 49 – The Total Number of Outer Loop Iterations**

In reference to Figure 49, the effect of the number of reconstruction iterations is to increase the accuracy of mass in the reconstructed image. The directionality is of interest more than the actual values, since the rate of convergence is dependent on the coefficients used in inter-frame stabilization.

The groupings in Subplot 13, due to test image location, show a general trend: at first iteration results in an overestimation of mass, which is then corrected by successive iterations and improves over the reconstruction based on a uniform prior. Iteration does not improve the accuracy of the reconstruction centroid to any appreciable extent. This behaviour is consistent with what is expected; that iteration would successively improve sharpness in the reconstruction without changing shape properties. Overall, iteration appears to be worthwhile; however more experiments are needed to determine what set of filter coefficients maximizes the joint goals of stability and computational efficiency in obtaining a better reconstruction.

#### **6.1.3 Discussion for Figure 50 – The Number of Sub-Models Used**

This series of plots in Figure 50 demonstrates the effect of including sub-models rather than a single grouping of measurements. The states are distributed as uniformly as possible over the sub-models, the purpose of which is to attempt to mitigate the inherent imbalances in estimation of

$$I_{(x,y)} \cdot$$

Subplot 1 has the grouping due to test image location, and indicates that having one large model performs in a more predictable result, this effect is likely purely due to having a larger pool over which aggregation occurs. Subplot 3 however shows that the case with 4 sub-models approaches the performance of the single case, which due to the aggregation in the outer loop starts to dominate.

The use of sub-models is likely only going to show significantly different results when non-linear operations such as thresholding are included within their filter stages, however the present test does not consider these cases. Overall this test indicates that for most cases a single model is best given a finite amount of measurement state data.

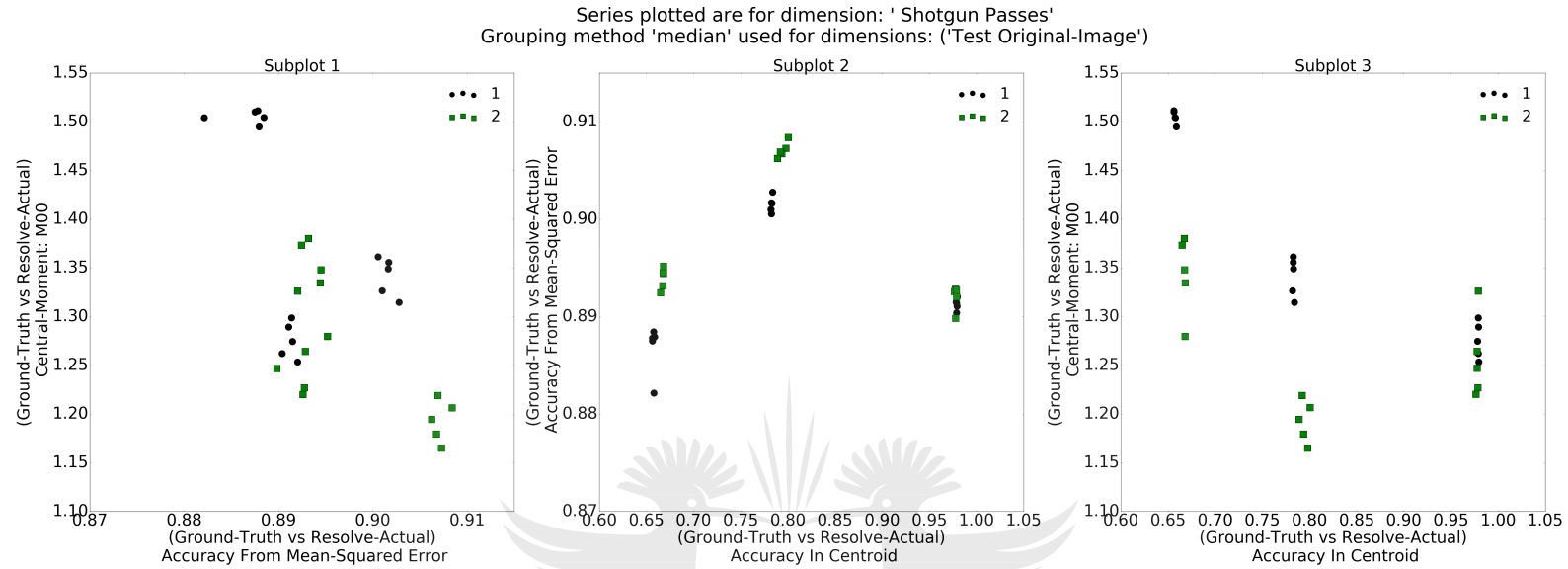


Figure 51: Performance for the number of iterations within the inner sub-models.

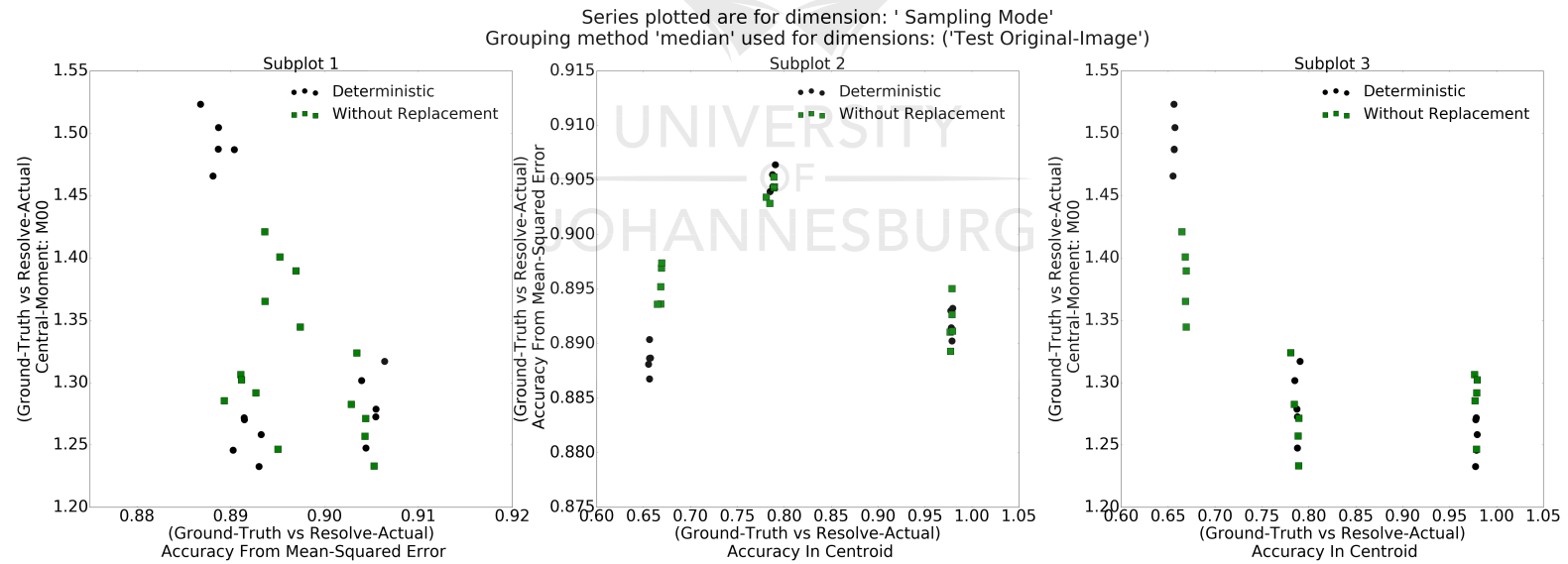


Figure 52: Performance for variations in method of measurement state selection.

#### 6.1.4 Discussion for Figure 51 – The Number of Iterations within Each Sub-Model

The series of plots in Figure 51 demonstrate an improvement in accuracy when iteration is used within the sub-models. The purpose of having iteration within the sub-models is to reinforce the particular sensitivities present in the particular set of measurements used by the sub-model. This allows regions with inherent insensitivity (as a result of field structure or measurement set choice) to have a better net weighting after final aggregation, thereby improving the estimate of  $I_{(x,y)}$ .

This result, particularly with regard to image mass in Subplot 3, indicates that the use of sub-models is beneficial when internal iteration is used. However; the combination of the choice of a conservative set of frame filtering coefficients, and an insufficient coverage of the parameter space make further testing necessary to determine the net value of using sub-models. It is recommended that the use of non-linear filtering functions like thresholding be investigated further with consideration of this parameter.

#### 6.1.5 Discussion for Figure 52 – The Method of Measurement State Selection

The sampling mode is the method by which measurement states are selected for use in reconstruction, the choice of which determines the nature of the estimate of the current distribution over the field. There is a marginal improvement in the general error, and an appreciable improvement in estimating the image mass that correlates with the grouping due to test image location. Random sampling is often used as a form of regularization in many algorithms, increasing the statistically expected performance. In this case the window for selection depends on the sample availability ratio, and thus the selection is less random for lower allocations. This represents a scheme that would occur in physical sampling hardware, where only a subset of samples is available.

These results indicate that a stochastic sampling scheme in the hardware over successive frames would likely result in a greater expected performance as a streaming device, though ideally a state sensitivity weighting scheme should be employed.



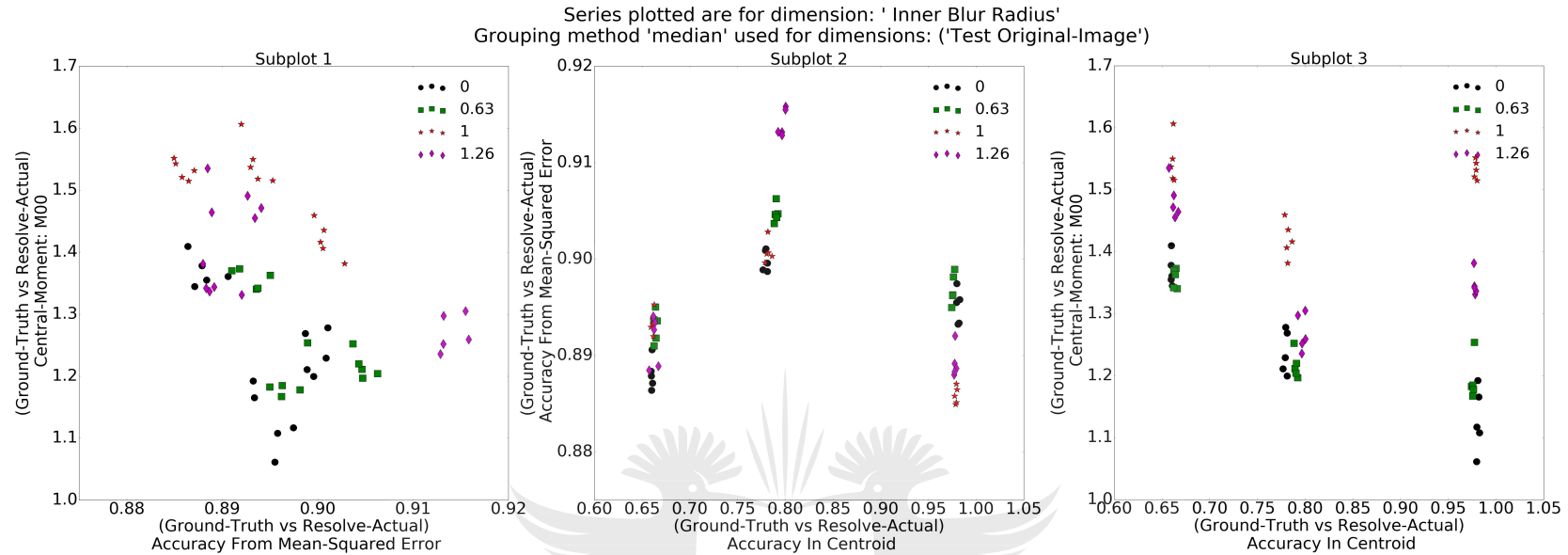


Figure 53: Performance for variations in magnitude of Gaussian blurring within inner sub-models.

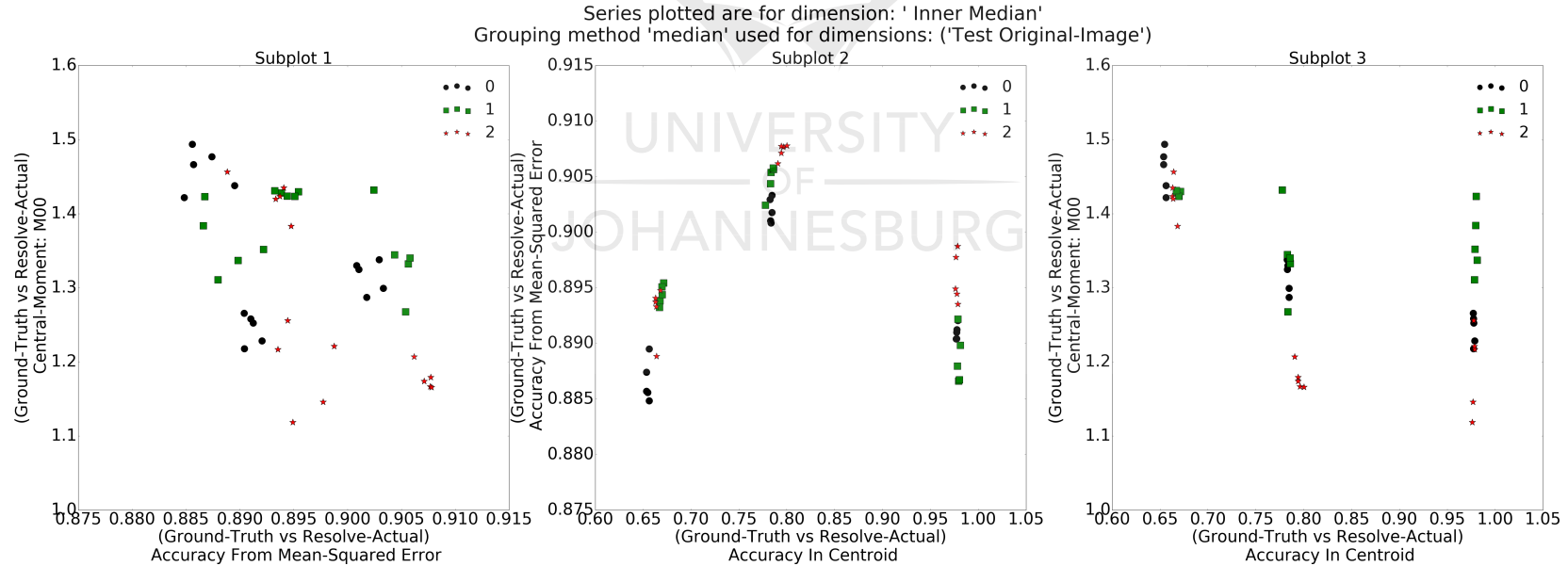


Figure 54: Performance for variations in median filter radius within inner sub-models.

#### **6.1.6 Discussion for Figure 53 – The Radius of Gaussian Blur Used within Sub-Model Filtering**

The use of a Gaussian blur in filtering during iteration of the inner stages is the subject of Figure 53. Performance varies between the groupings between test image location, indicating that this form of regularisation has some impact in managing distortions in field geometry. In general performance is best when either using no blur entirely, or a lower value such as indicated by 0.63.

The test functions used are insensitive to this parameter, and further evaluations should best be done on a test set with greater spatial frequency content. In initial experiments the blur was found to be good at improving stabilization of images with non-conservative inter-frame filter coefficients, however comparison is best performed against the median filter in the same stage.

The increased overestimation of image mass with increasing blur radius shows that ideally a stage of sharpening be used as a final post-processing step to balance the change in mass while retaining the regularisation that the blur provides. In the case of thresholding, a morphological operation of erosion can be used to the same effect.

#### **6.1.7 Discussion for Figure 54 – The Median Filter as a Function of Morphological Radius**

Median filtering is used within the sub-models as a form of regularization, primarily to enhance edges and remove spurious noise. The shape of the window over which filtering occurs is an implicit parameter to this method, and a source of optimization non-linearity in the small window possible due to field size constraints. The particular variant used here attempted to maintain a monotonically-increasing circular window by varying between circular and square morphological templates. A radius of 0 indicates that median filtering was not performed at all.

In Figure 54 the improvement in performance is evident primarily in the effect on image mass, an increase in radius being beneficial also to stability in reconstruction. At such low absolute radii the nature of the morphological template means that this result could easily be linked to the shape of the filter window, rather than its coverage area. In order to investigate the shape effects, a much larger field should be used to reduce the effect of pixel-level variations, however this comes a much greater computational time and memory footprint for the algorithm.

In general median filtering should be considered before the use of a Gaussian blur for regularisation, both from these results and qualitative metrics in experimenting with the output results.

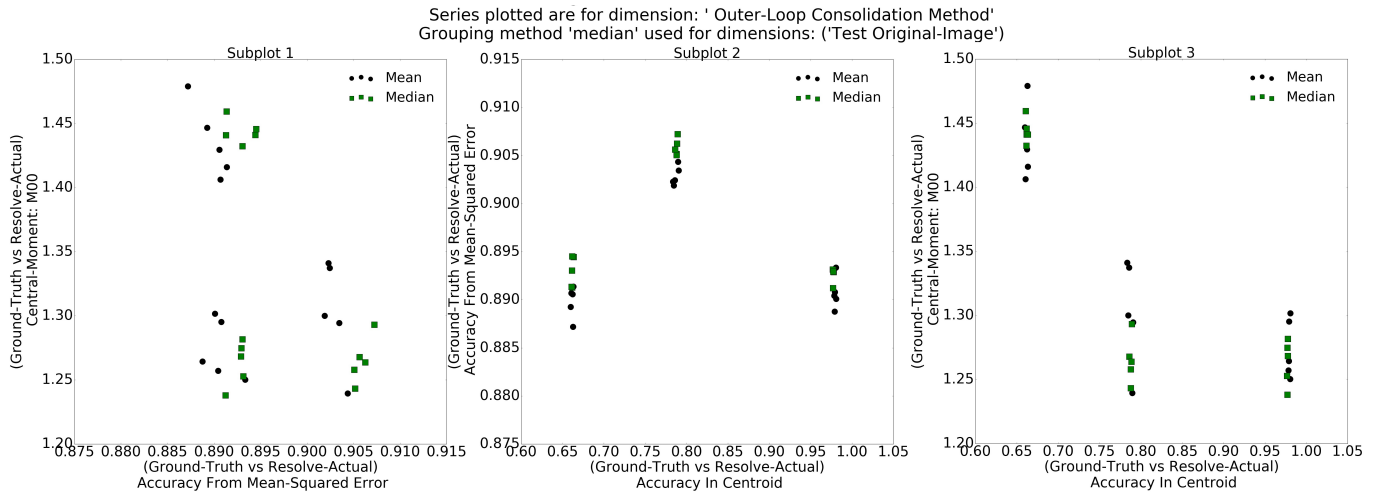


Figure 55: Performance for method of aggregation of the results of the sub-models in the outer loop.

### 6.1.8 Discussion for Figure 55– The Method of Aggregation of the Sub-Model Results

Figure 55 indicates that taking a per-pixel median of the results from the sub-models is more consistent than using a mean. The overall performance of a median is slightly better than a mean, even though a low number of sub-models is being used here the median is likely to be more robust an indicator even at larger numbers of sub-models.

The use of a median does however increase memory requirements, as a median cannot be calculated continuously. Further tests targeting low-memory footprint variants of the algorithm should focus on the use of a mean aggregation, as results here indicate insufficient performance gains for the alternative.

### 6.1.9 Discussion for Figure 56 – The Effect of Oversampling Factor

The overall sampling ratio is a non-dimensional measurement that was shown as the “oversampling factor” in section “4.5.3 - Design considerations for system configurations”, on page 82. Despite previous expectations, there appears to be no performance relationship to this non-dimensional ratio. This ratio is the only such that makes sense given the limitations of the test performed, however it is likely that the expectations of predictability based on unique information are flawed. In general reconstruction methods for EIT have to make many assumptions and regularizations in order to be stable or even exist. It is likely that the informational content between different states is fractional and disappears in the noise introduced by these assumptions.

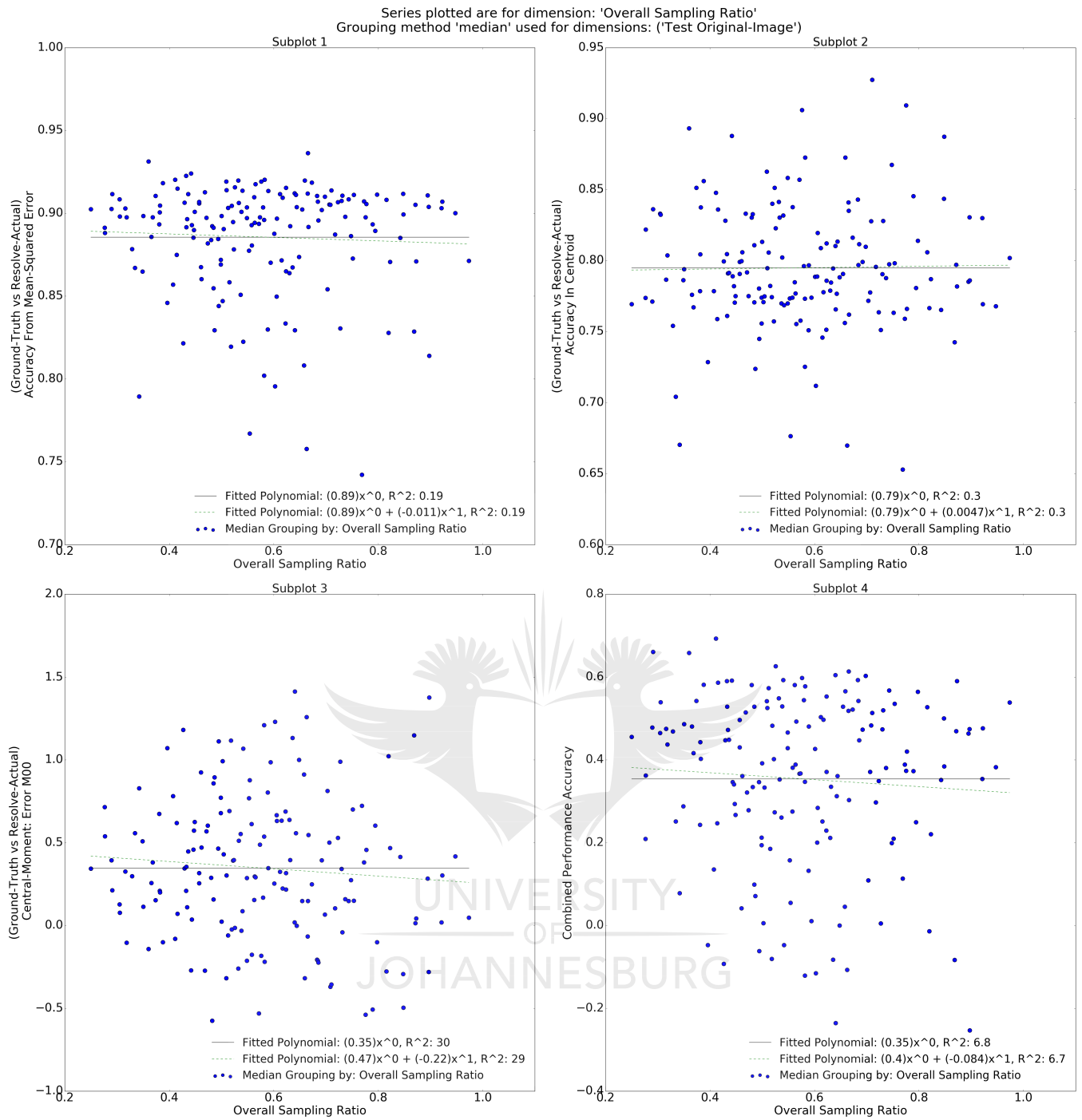


Figure 56: Scatterplot of medians for classes of parameter for the number of states used as a ratio to total information required, with fitted lines up to the first order to show mean and trend.

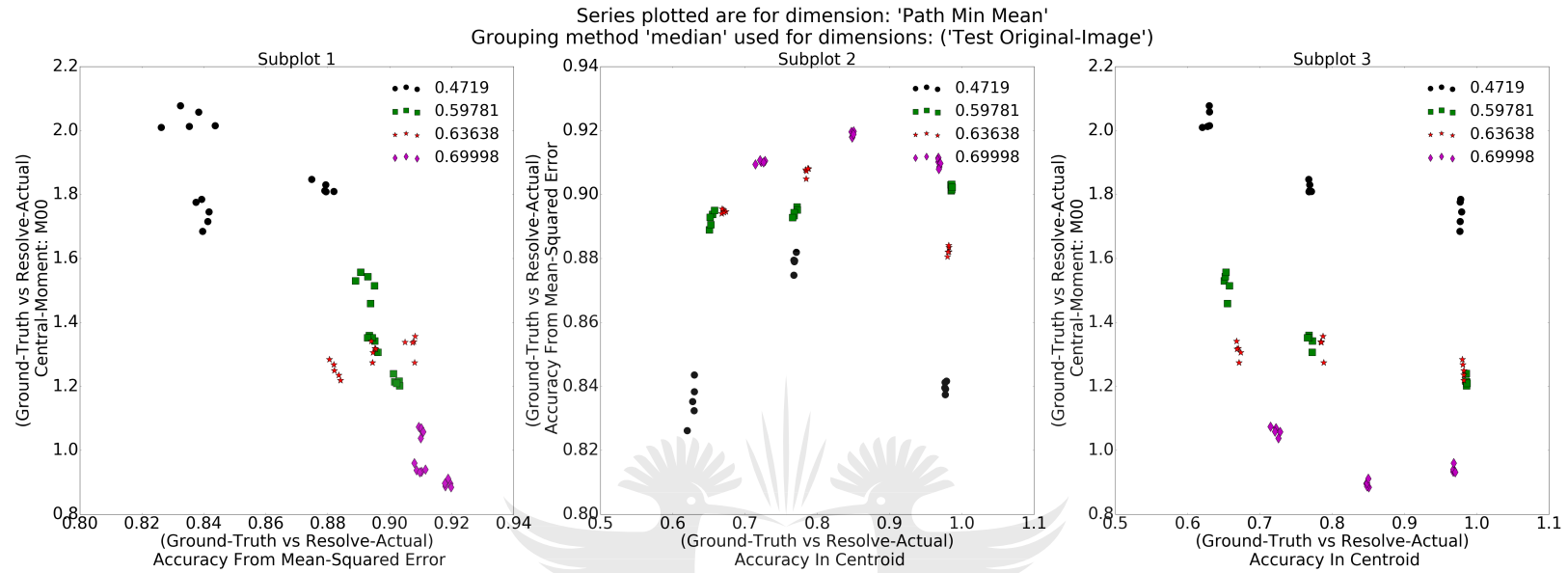


Figure 57: Performance for variations in the mean of the minimum path length between any H-node and the nearest F-node.

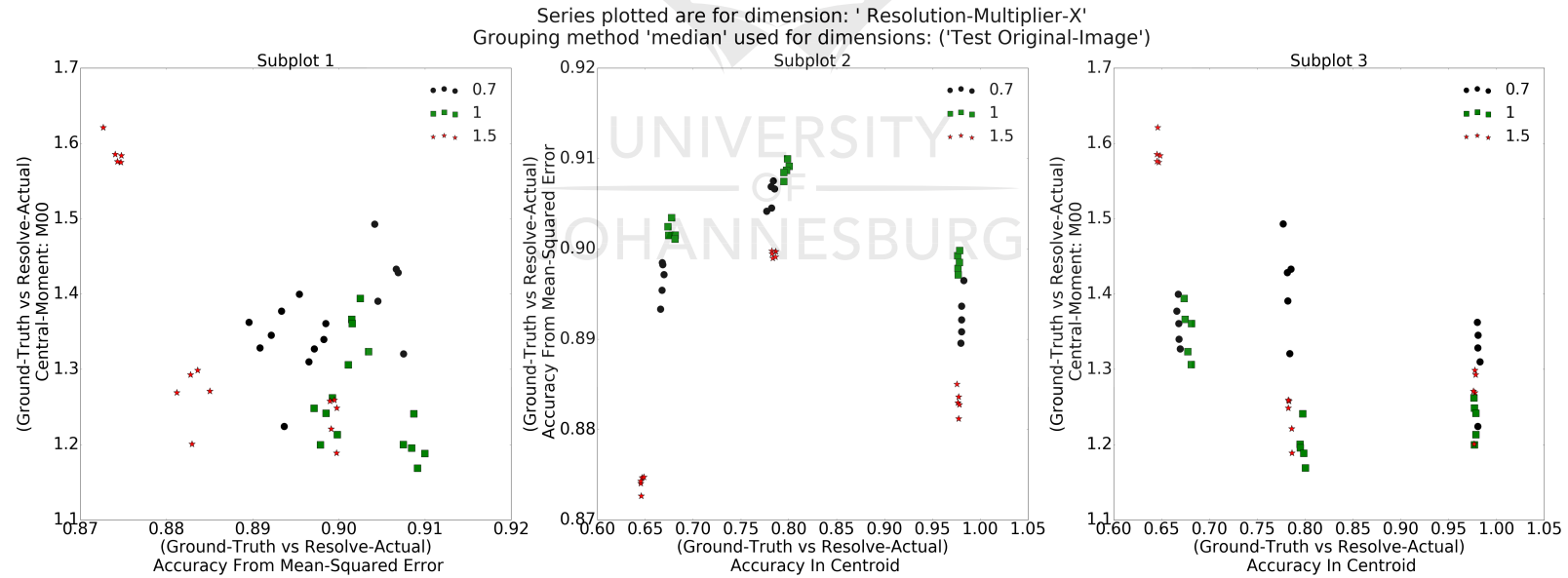


Figure 58: Performance for scaling of the field size in the X axis during reconstruction.

#### **6.1.10 Discussion for Figure 57 – The Electrical Path Distance Between H and F-Nodes**

This plot demonstrates the correlation of improved performance with a decrease in non-linearity caused by the current density in the immediate location of an F-node, but should only be considered as complimentary to Figure 48. There is tight coupling with the total number of nodes, since there was only one F-node spacing method used in the test. The only source of variation in path length statistics besides the total number of nodes is the method of spacing the sampling nodes on the field.

#### **6.1.11 Discussion for Figure 58 – The Multiplier of the Field Width X-Axis**

The effect of reconstruction at fields constructed at multiples of the base resolution is shown in Figure 58, the dimension that is kept at a 1 to 1 ratio with the input image when parsed into the field structure. The effect of which depends on the scaling ratio.

Ratios below one show a reduction in performance in comparisons to a direct mapping, the however this drop in performance is fairly consistent across test images locations. There is some instability in one sector of the field, and a tendency to overestimate image mass to a greater extent.

Ratios above one show a reduction in performance with regard to mean-squared error, and in image mass. The grouping of results is however tighter, indicating a more stable reconstruction in general. One test image location does however perform very poorly, indicating that the problems of projection are magnified with greater field sizes.

The overall indication is that if computational complexity is a concern, especially for fields that are constructed with continuous films, then a reduction in field complexity may be worthwhile. The results for larger ratios indicate that in developing the algorithm it is likely better to test at larger field sizes, and once relationships are found, determine their validity in scaling to smaller sizes. This fits with the understanding that non-linear and edge effects increase in prominence with smaller field sizes. The computational cost scales rapidly with larger field sizes however, so it is recommended that parallelisation be achieved beforehand.



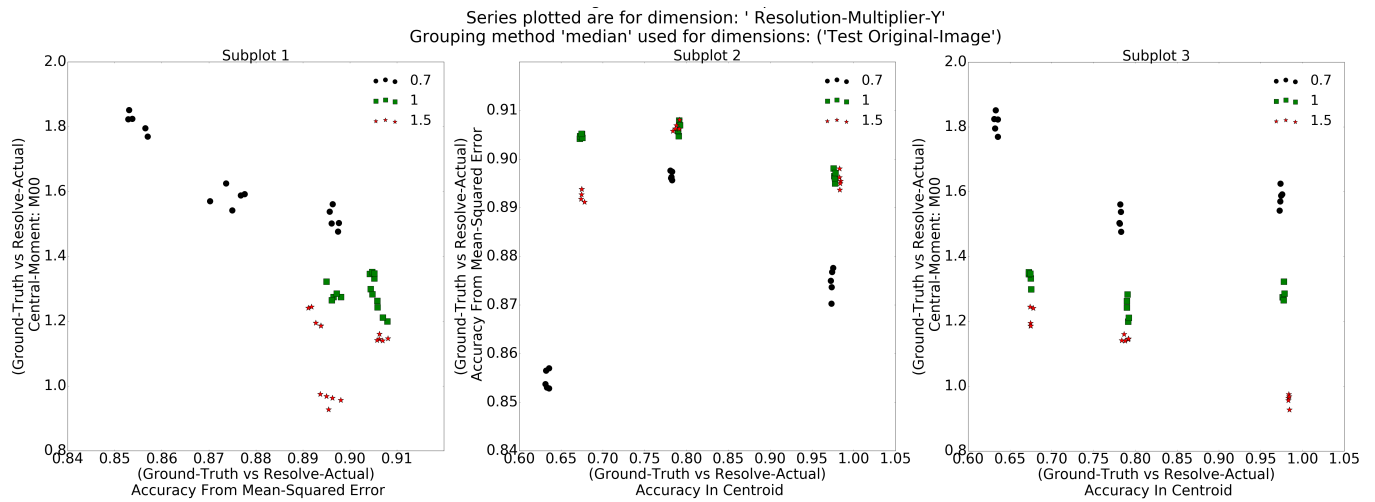


Figure 59: Performance effects for scaling field shape in the Y axis during reconstruction.

### 6.1.12 Discussion for Figure 59 – Field Width Multiplier in the Y-Axis

The scaling factor in this series is for the dimension that is halved by parsing into the field structure, as such it behaves in a distinct manner in comparison to Figure 59 above. The effect of downscaling is a general reduction in all metrics of performance, while up-scaling has increased performance and stability for all test image locations.

This effect is likely due to an interaction in the gradient operations, which assume uniform geometry of the pixel elements, and the actual gradient effects on the field. The process of up-scaling is to better match the behaviour of these two processes at the geometric level. This can likely be remedied by using gradient operators that are defined on the field graph structure itself, and thereby consistent with its geometry.

These results may also be due to similar effects in reducing non-linearity such as in Figure 58, however the overall increase in all performance indicators indicate that it is more likely due to a structural effect. It is recommended that further investigations consider the use of a native graph Laplacian, which would also introduce less error when considering different forms of continuous connection at the borders.

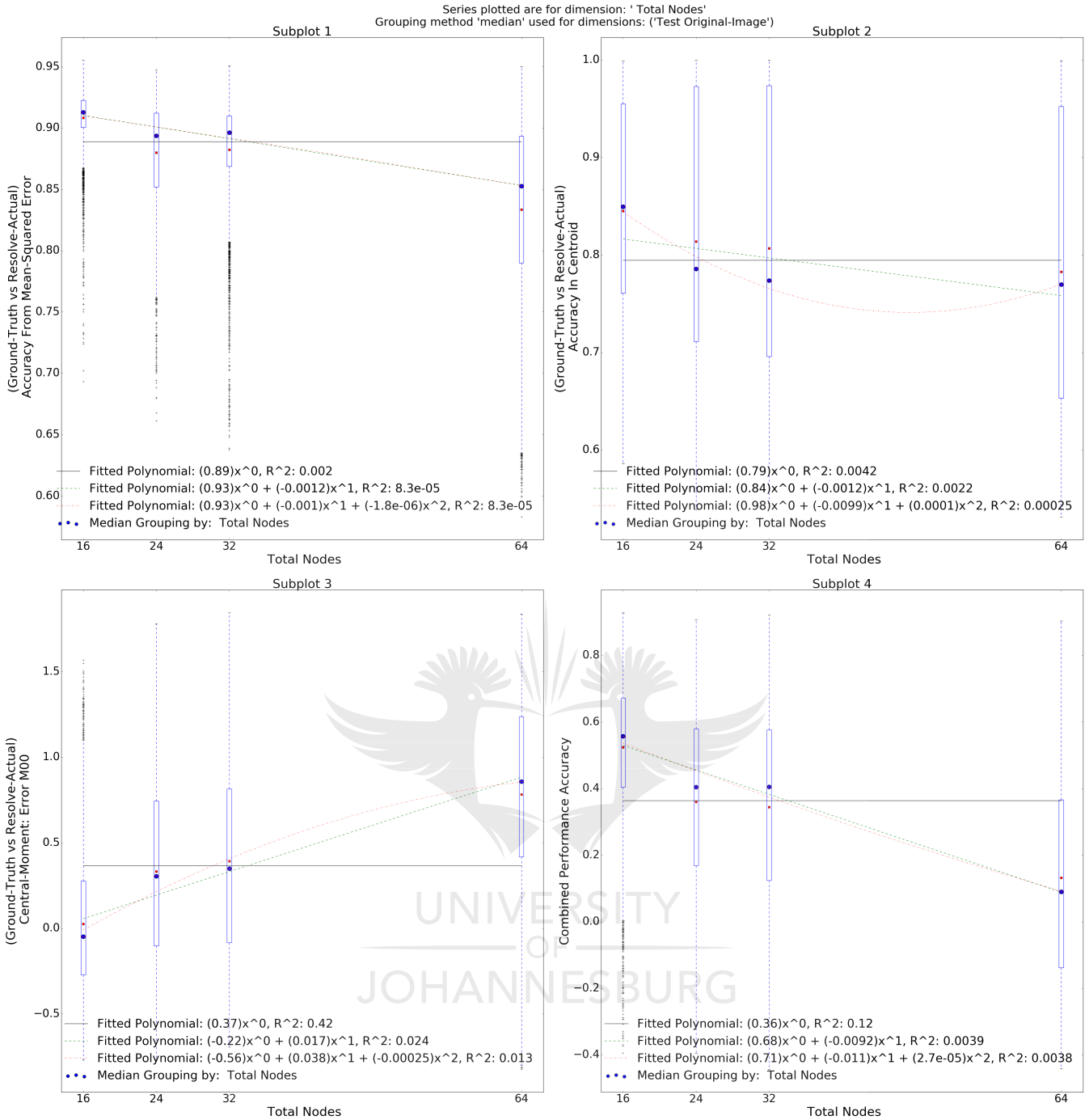


Figure 60: Box-and-whisker plot for the effect of the number of F-nodes used.

### 6.1.13 Discussion for Figure 60 – The Effect of Total F-Nodes

The effect of increasing available spatial data of the voltage field was shown first in Figure 48 and now in Figure 60, however the results are surprising. Since at the sample location voltages are acquired high-impedance with no distortion of the generated field, it was expected that an increase in available data from these locations would be only beneficial. The opposite effect is observed, with a clear trend in both the median and mean of the classes toward an overestimation of image mass and a decrease in centroid accuracy. The number of data points visually represented on the graph is low, however the trend is for the central tendencies which are supported by many data points, and is thus still significant. In addition to the possible causes presented in the discussion of Figure 48, there are a number of possible explanations:

A likely cause for this behaviour is the relationship with the heat-flow interpolation and the solver to obtain the voltage field given the Dirichlet boundary conditions imposed. During development it was observed that a direct solver for the system was required, the numerical sensitivity of the problem being such that successive approximation approaches such as conjugate gradient produced very poor results. Since the operation is fundamentally interpolation, it is unlikely that over-fitting is the cause.

Another cause may be the effects of spacing on the relative geometrical distances over the field between F-nodes. However, since the layout is in powers of 2 and scales evenly the relative locations of F-nodes to each other are fairly consistent. A further analysis of performance against spacing pattern would help in determining the contribution of this factor.

Due to the numerical sensitivity issues outlined, this result may be as likely an artefact of the specific implementation of the method as it is a fundamental property of its' behaviour. However if the result is true to the nature of this type of reconstruction, it indicates that there is likely to be an asymptotic upper limit to accuracy that is yet to be discovered. This result is in line with the significant computational numerical problems inherent with EIT reconstruction; which now may be apparent even when the boundary conditions are Dirichlet rather than Neumann conditions present in usual applications of EIT.

#### **6.1.14 Discussion for Figure 61 – the number of measurement states used**

This plot (below on page 150) is an absolute measurement of the number of measurement states used, rather than the relative measurement of Figure 56. There is a clear learning curve in the central tendency, despite a few outliers, showing a non-monotonic relationship. At first increasing the total number of measurements used improves the mean-squared accuracy, with most of the error being a function of an overestimation of image mass. The overestimation is improved until approximately 30 measurement states, where mass is estimated correctly, and further measurement information results in underestimation of image mass.

There appears to be increased variance in median performance with increasing the number of measurement states used after 30, however there is insufficient data in this region to draw many conclusions. The plot shows fitted lines for average, linear and quadratic relationships against the median. There is however no prior as to what form of fit is appropriate; it may be that a plateau in performance is reached, or alternatively the algorithm starts over-fitting and performance suffers with increasing measurement information. The inter-quartile distance decreases with regard to mean-squared accuracy with increasing measurements, and is expected due to a better and more stable estimate of current distribution. Since measurements are picked stochastically, increasing measurements results in less particular cases of bias due to sensitivity imbalances.

*The number of measurements used is overall the most pertinent factor in overall algorithm performance.* The underestimation in mass is likely due to uncompensated sensitivity biases being increased in relative magnitude by aggregation, as noted in previous discussions.

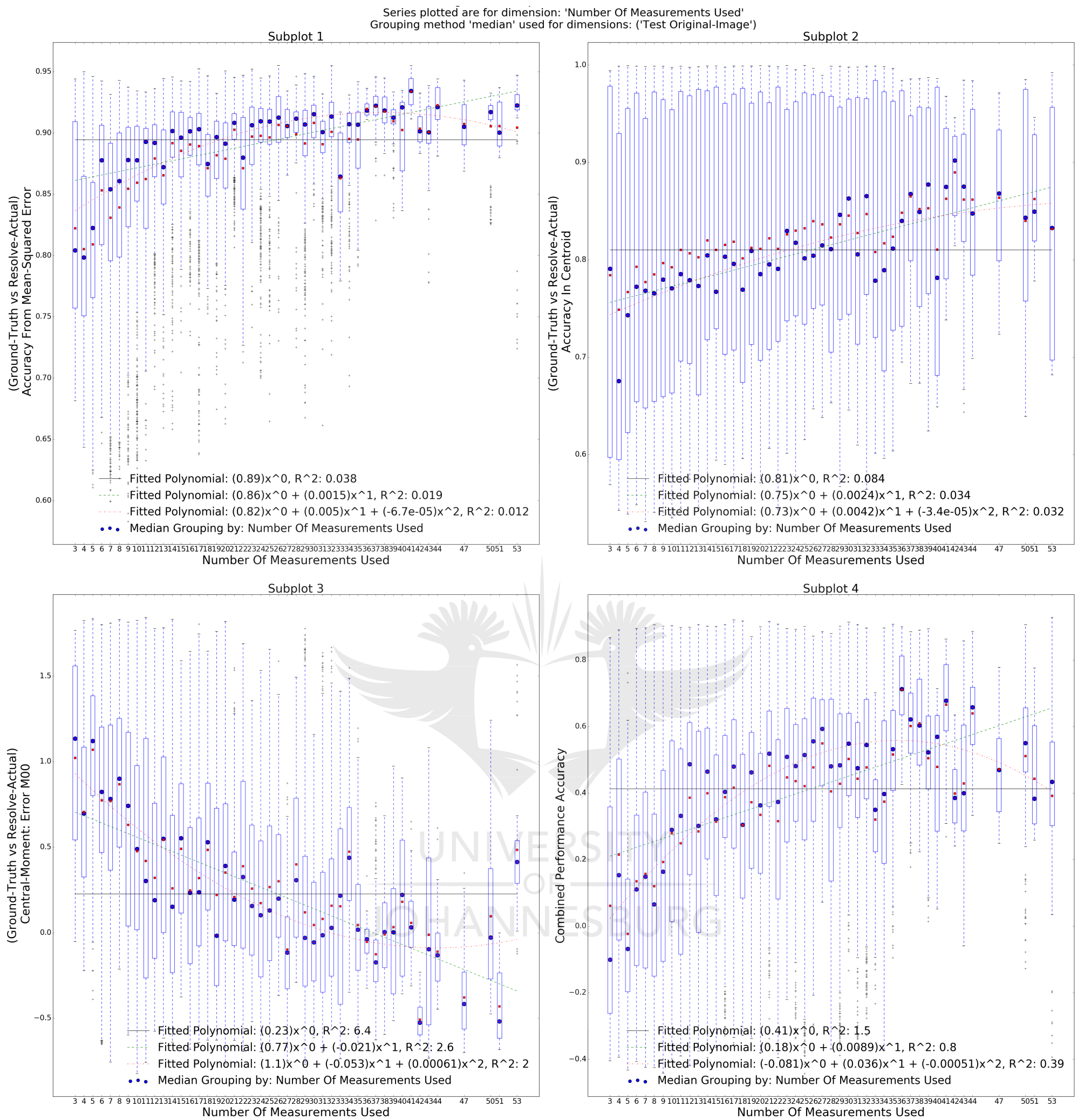


Figure 61: Box-and-whisker plot for the effect of measurement data quantity.

## 6.2 Principal Component Analysis Results

Principal component analysis (PCA) is a method often used in reducing the number of effective dimensions in a problem, and in determining fundamental relationships between measurement dimensions. The process essentially pivots the data to produce a new set of orthogonal unit vectors, oriented such that there is a decreasing amount of variance in the observed data with successive unit vectors used.

The use of Latin-hypercube sampling complicates the use of PCA, since by definition the variance of the input dimensions has been made approximately uniform across all the input dimensions. This mismatch is managed by subdividing the data into performance-labelled classes before applying PCA. Further complications arise in that PCA cannot handle discrete dimensions, so the input dimensions that effect mode switches cannot be analysed.

The unit vectors obtained are useful in describing relationships, since their components best describe competing factors from a covariance standpoint. The classes used can be plotted against the data transformed according to these unit vectors, and by using pairs of such vectors a projection slice taken that may be highly meaningful in determining causal relationships. The unit vectors are ordered by the amount of variance explained, the degree of falloff in variance is a descriptor for the separability of the data with regard to a strictly linear manifold.

A high rate of variance falloff indicates a set of data that has lower effective rank than the original dimensionality, and indicates compression of the data and thus the problem space. A lower rate of variance falloff indicates a lower degree of separability and more non-linear behaviour in the problem space. Other techniques such as Kernel PCA, Non-Negative Matrix Factorization and Linear Discriminant Analysis are complementary and provide a dimensionality reduction under different assumptions. These have however not been applied to the problem at hand.

Normalization is a requirement of PCA so that variance is truly comparable between dimensions, in this case a standard normalization of  $z_i = (x_i - u_i) / \sigma_i$  was used for each column  $i$  in the dataset. As a result all numerical plots are in units of standard deviation, the colour being used to show value of the objective function used in the grouping for the plot. The slices used in the following visualizations are only for the first three highest-variance PCA component vectors. All data points are aggregate results over the test image locations and sizes, determined for each set of input parameters.

Referring to Figure 62, below on page 152: Since the falloff in the explained variance ratio is approximately linear (and not a power relationship), the data is linearly incompressible. The description of the results in linear terms is thus limited when using PCA, and this is also true for the other objective functions in the set. Since Latin-hypercube sampling requires a sectioning by objective function, the PCA component vectors are different for each objective function used. *The analytical value of the technique in this application is low, being insufficient to develop distinctions. The distinctions obtained in previous discussions are of greater value to the final conclusions.*

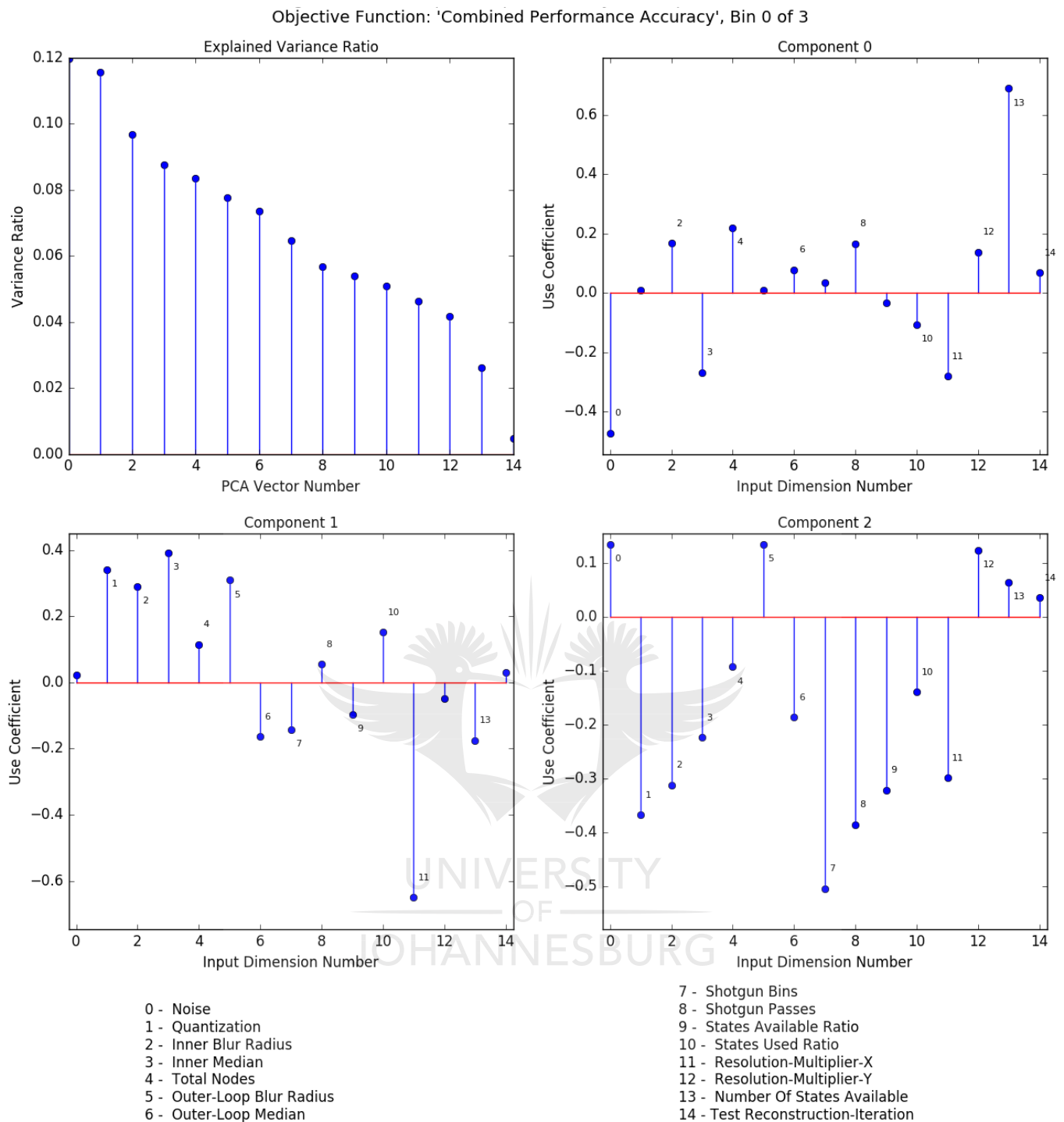


Figure 62.1: PCA Components for objective function - "Combined Performance Accuracy"

### 6.2.1 Discussion for Plots of PCA Vectors and Distributions

Inspecting the stem plot for "Component 0" in Figure 62.1 and Figure 62.2, and with reference to previous plots for each of the dimensions, it can be seen that: The primary driver of inaccuracy is the number of measurements used in reconstruction (due to mass under-estimation), with secondary drivers being the number of iterations within the sub-models, the total number of F-nodes in the field, the Gaussian blur within the sub-models and the scaling in reconstruction resolution for the y-axis. The drivers of accuracy include measurement noise, median filtering in the inner sub-models and scaling in reconstruction resolution in the X-axis.



Visualizing against dimension: 'Combined Performance Accuracy' with 'Log'-scale HexBins

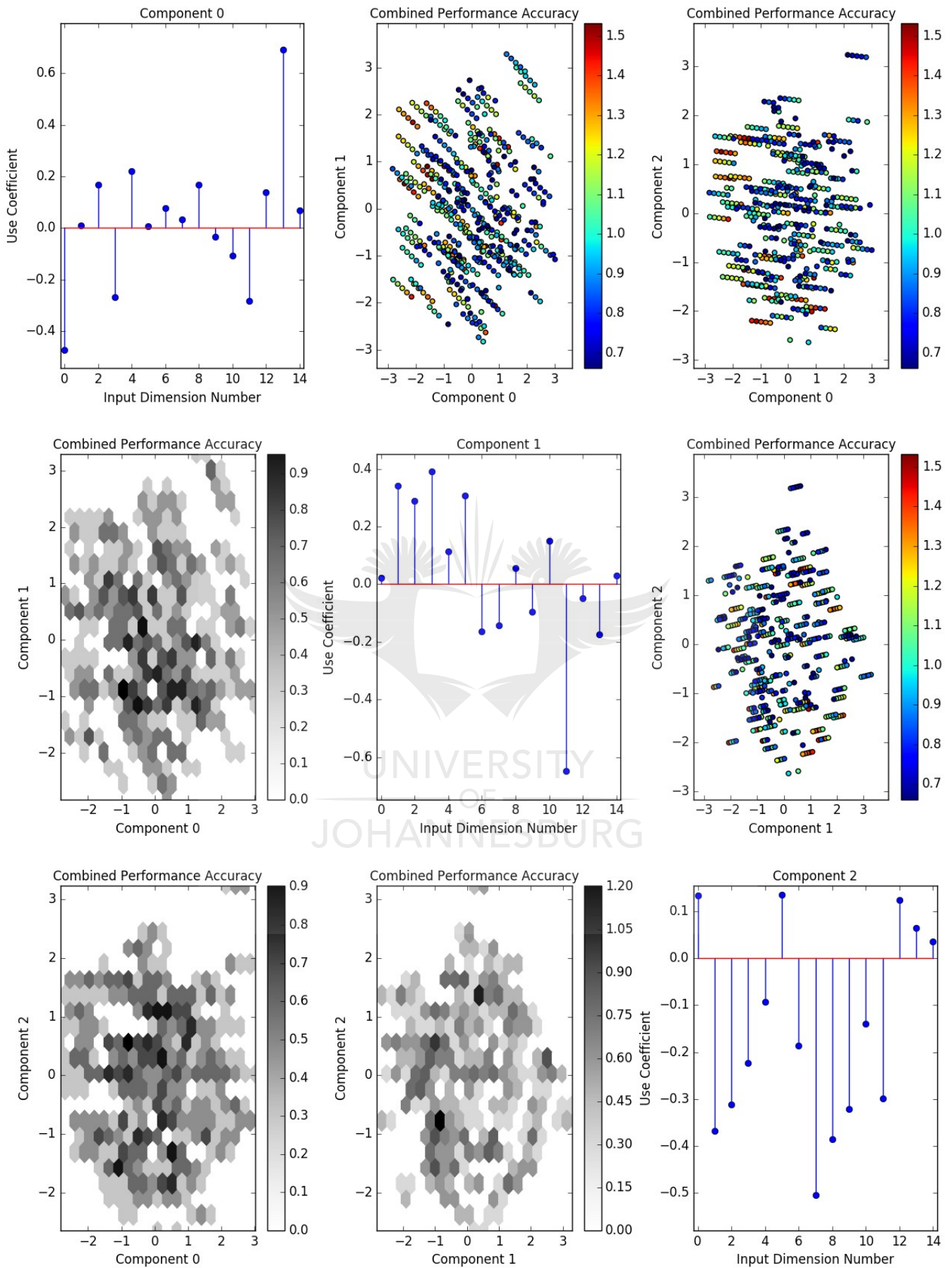


Figure 62.2: Combined Hexbin and Scatter-plots for groupings with respect to objective "Combined Performance Accuracy"

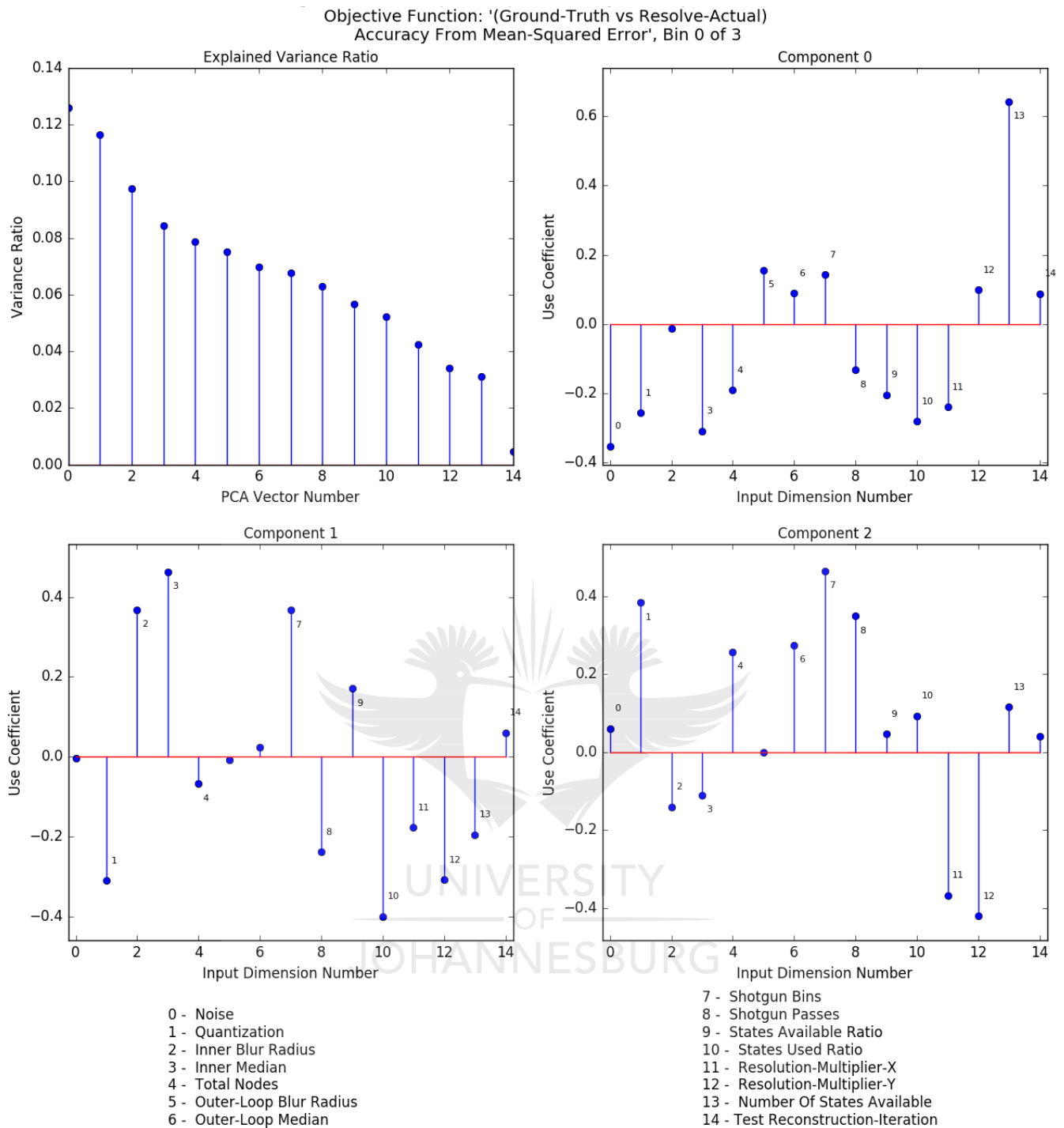


Figure 63 PCA Components for objective function - "Mean-Squared Accuracy"

The plot in Figure 62.2 shows the first three component vectors, which are sufficient to demonstrate some grouping in the best performance characteristics. The groupings are not well defined; which is expected given the non-linear nature of the reconstruction, and the described variance of the PCA vectors.

The pair of plots in Figure 63.1 and Figure 63.2 show a similar set of relationships, PCA being applied to the topmost performance class of the objective accuracy against the mean-squared error. *There is however little grouping to make any distinctions from, and the situation is similar for the other objective measurements. The other plots have been omitted for this reason.*

Visualizing against dimension: '(Ground-Truth vs Resolve-Actual)  
Accuracy From Mean-Squared Error' with 'Log'-scale HexBins

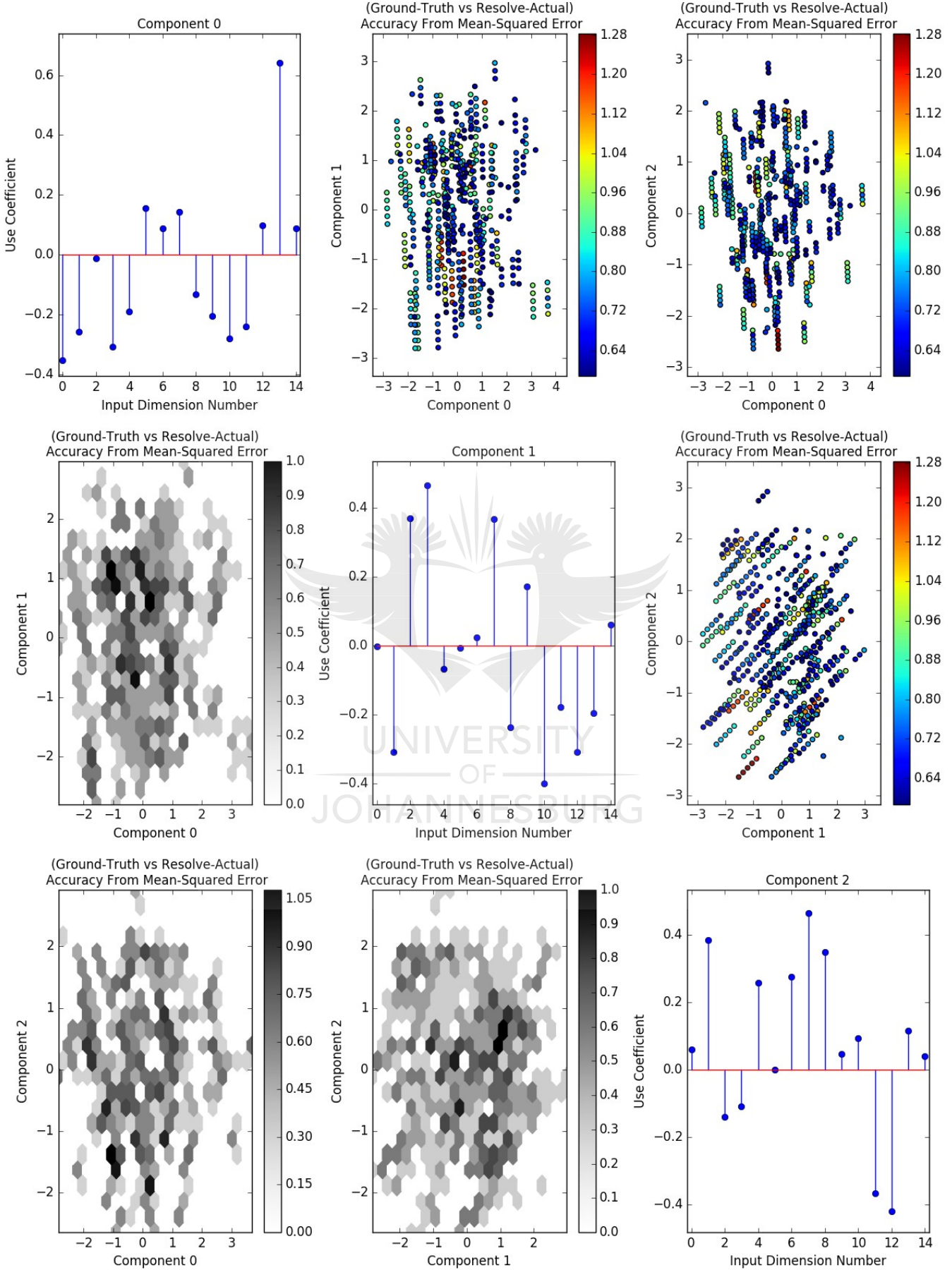


Figure 63.2: Combined Hexbin and Scatter-plots for groupings with respect to objective mean-squared accuracy.

### 6.3 Chapter Summary

The results of the simulation experiments were interrogated using robust-statistical techniques, being necessitated by the use of latin hypercube sampling and the highly nonlinear interactions between parameters, the system and the stochastic elements of the reconstruction algorithm. Slices were taken along axes in the parameter space, with projection of the out of plane points to the slice layer. Visualization was in the majority by the use of scatter plots and hexbin plots for maximal representational density. Aggregations were done by robust methods and performed on groupings associated with the test image used.

The plots shown here were a part of a much larger corpus produced as part of relationship investigations. The overall performance characteristics of the pipeline with respect to key design factors was established, along with lines of investigation for improvement of the algorithm in a number of areas.

The most interesting phenomena observed were:

1. Spatial distortion due to what is believed to be topological layout of the transducer elements resulting in warping of the image in reconstruction away from the centre of the image.
2. Image mass is affected by the number of sensor nodes, and tuning of the reconstruction is required to ensure that image mass correspondence is maintained.
3. The iterative approach to the algorithm needs stabilization, however is effective at improving the reconstruction accuracy. The efficiency of the iteration with respect to the stabilization requirements needs further study.
4. Key factors in improving stability of the iteration and overall effectiveness are the use of filtering between iterations, and the choice of filtering methods used.
5. The predictability of the reconstruction capability based on amount of information is subject to errors, and it is likely that information available between measurement states is lost due assumptions made in the reconstruction process.
6. As per expectations, the number of measurement states is the dominant factor in algorithm performance. An increase in the number of states used has a positive effect on the accuracy of the reconstruction.

Dimensionality reduction was investigated using principle component analysis in order to find out of plane relations. The linear drop in described variance between components indicates that PCA is unsuitable, and inspection of the vectors yielded no direct insight into possible relationships.

The effect of noise on the reconstructions was as expected, with increasing noise reducing the quality. The algorithm did however prove robust against noise with regard to stability, and tolerating large total amounts of noise.



## 7 Conclusion

This chapter discusses the research as a whole, including the finding and future possible developments.

### 7.1 A Brief Review of the Investigation Process

The process of this investigation began with a justification of the research premises based on general problems experienced in the design of concentrating solar power systems. The design science methodology was selected, since the most valuable product of the intended research would not be a particular device, but rather a family of possible devices that could be tailored to particular situations.

The main types of concentration methods for solar thermal applications were surveyed, in order to determine the optical and physical structure that a measurement device would have to interface with. In addition to this, applications of solar thermal power were surveyed. This was in order to determine the general characteristics required of a measurement scheme that could be used for informing the parameters of their control.

Existing measurement technologies were surveyed and the history of solar measurement devices was investigated in order to discover the principles of operation of existing methodologies, in order that they might be adapted for the intended purposes. This resulted in the selection of a direct measurement strategy due to size and interface constraints previously identified. The conventions in measurement quantities were identified and their applicability to the current problem evaluated.

The analytical techniques used in solar thermal system design were surveyed, along with the modelling methods used for predictions of heat transfer and power output. This was to determine the types of information required to better inform these methods, and how local information might benefit such analyses.

Modelling methods for optical systems were considered, along with the limitations in resolution and how lensing might be accomplished given the large flux levels present as a result of concentration. The distribution and variation of solar energy was considered with regard to the effects that a measurement device would have to resolve, and what quantities might be assumed constant.

General surface metrology was surveyed, with the aim being to adapt any existing technological forms to the problem at hand. The representation of light fields was surveyed, along with Image-Based Rendering in order that existing light-field technologies might inform the structure of the intended device. Holography was briefly surveyed in order to determine applicability of the technique to metrology of large, reflective concentrating surfaces. The combination of Holography and Light Field ideas resulted in principles for general measurement that the intended method must conform to, and structurally shaped the design form.

Design specifications were developed based on the surveys done on environment, purposes and analytical use of the intended measurement technique. Material limitations in transducers proved to be severely limiting to the number of options available; the heat and intensity of concentrated

solar flux precluding many of the usual approaches to imaging methods. In addition to this, the dynamic range of most sensor materials would practically limit the useful response due to saturation. A number of candidates for prototype were proposed based on a taxonomy derived from light field techniques, and the form of the most complete and practically-implementable technology was chosen for further development.

The key component required for function of the model was identified as the imaging array. This was a result of the component being the largest source of complexity presented during manufacture, and the largest cost when using discrete components. This complexity was as a result of the number of routes and connections required when using traditional multiplexing techniques. The structure of the sensing array was considered from first principles and the method of identification of particular element response (the interconnect layer) was determined to be the greatest cause of complexity. Due to the material factors and the simpler mathematical properties, the design was based around the use of passive resistive materials, either with photo-sensitive or thermo-sensitive effects.

The interconnect layer was investigated from first principles, and a method of enabling exponentially increasing interconnect capacity was proposed in order to counteract the increasing complexity in the physical problem. This proposal relied on a boundary scan technique that was developed from first principles and algorithms proposed, before existing research on a similar boundary scan idea was discovered. Bounds on the technique were determined for the structural form, such that guarantees of solveability for all elements are upheld. The method of boundary scan was investigated, and a criterion for extracting a maximal amount of information was determined to ensure unique measurements.

The technique elicits a non-linear forward transform that receives a vector of field conductivities and produces a set of boundary voltages and current. The transform processes were characterized in functional terms, along with the types of linearisation that could be applied. A number of inverses were proposed, some novel and others based on standard techniques used in non-linear systems. The most straightforward technique of global optimization was applied initially. These tests shown multiple solutions despite the guarantees of unique measurements and an excess number of measurements provided, the reasons for which are likely an artefact of the non-linear nature of the transform.

An inverse reconstruction based on weight-sharing and pseudo-inverse was proposed, utilizing the estimates of the voltage field based on heat-flow interpolation. This was analysed for its' computational and memory complexity and found to require a large number of resources in the intended use case. This would have violated the design targets, and be unsuitable as a technological base for further development.

A different algorithm for the inverse was investigated based on an averaging linearisation of the current distribution, and determination of the conductivity distribution by a non-linear interpolation of the voltage field from known points. This method showed general success using perfect information, though further optimizations based on state selection were identified as a requirement for better performance. Due to the continuous borders and interpolation, this method



proved stable even in the presence of low amounts of noise. The particulars of the implementation were non-obvious and identified as a set of parameters that could only be optimized by experiment.

This inverse was tested by application of a pipeline whereby measurements of an actual device were simulated, and the effects of converter quantization and Gaussian noise were applied. The pipeline was fed with image step functions in a number of sizes and locations, generating a test measurement set. The parameter space of the inverse transform was the subject of the test, being sampled in a stochastic yet uniform manner using latin-hypercube sampling. The performance of the inverse transform in reconstructing the original test image was evaluated on a number of objective aggregate functions, applicable to the intended use in measurement of concentrated solar flux distributions.

The results of the tests were visualized using a slice, projection and aggregation technique that allowed the effects of each parameter to be visualized against their effect on the whole sample space. Dimensionality reduction in the form of Principal Component Analysis was performed, however the distribution was found to be linearly incompressible and thus the dimensionality reduction of low analytical value.

## 7.2 Results of the Tests

The characteristics of the inverse transform used were shown to be generally favourable to the intended application, however further improvements are recommended before implementation is attempted:

1. The field boundary connectivity needs modification to reduce artefacts and skew as a result of geometrical distortions. A taxonomy of possible boundary connectivity configurations has been developed and recommendations made according to this scheme.
2. The performance of the reconstruction method be investigated with regard to continuity of the field elements, since this appears to be a factor in reconstruction performance.
3. An Implementation of the algorithm be tested utilizing the gradient over the graph structure as a native Laplacian, rather than the discrete image gradient operators used in this implementation.
4. Investigations be made into improving the estimate of the current distribution by weighted scaling, in order to solve the issues identified with estimation of mass and to improve efficiency. By optimizing the current distribution estimate, improvements will also be made to the reconstruction accuracy as a result of variable sensitivity with regard to element position.

*A reduced form of implementation would be feasible given the development of the method at the current state: An array of discrete thermistor sensors arranged to form a porous net; which can be placed in the path of an operating solar concentrating mirror to determine the distribution of flux through a surface region, neglecting directional measurements. This has direct and pertinent applications in the control of solar thermal concentrating systems, especially designs utilizing adaptive mirrors. The technique in its' current form can currently provide a reasonably accurate measurement with speed suitable for feedback*

*control of systems with concentration overcapacity. Implementation can be done with very low cost hardware and sensor materials.*

Further improvements of the method should be considered in order to scale the algorithm up to solution of comparatively high-resolution fields, as would be required for the intended measurement technique form.

1. Parallelisation of the algorithm be investigated for use in grid-computing and multi-processor applications. The algorithm is inherently amenable to parallelisation by design, and tests indicate that the inclusion of greater amounts of measurement information would benefit reconstruction accuracy.
2. Optimization of the size of field segments suitable for reasonable reconstruction in the intended Lytro-style device. Since the complexity of the heat-flow interpolation step scales rapidly with field size, either:
  1. Multiple independent fields should be tiled over the measurement surface, under each aperture, in order that flux directionality be measured.
  2. A single large measurement field be used as the light sensitive surface, with sampling of the patches done in a semi-local manner. The boundaries would be discontinuous, and a border of buffer elements set at mean value be used to estimate current flow at the patch edges. This allows smaller *overlapping* patches to be reconstructed at a much reduced computational cost, before being stitched together.

### **7.3 Final Remarks and Main Contributions**

Despite the complexity that arose during the project: a measurement technique has been proposed that is able to scale to a wide range of concentrating solar thermal systems, has a form that is able to capture a near-maximal amount of information with regard to the light fields present in real-world conditions. This technique can be implemented with low cost sensor technologies and electronic hardware, and can operate in field conditions to measure real-world effects.

A subset of the intended technique was simulated and characterized, with the results showing good potential for fruitful further development. The technique as it stands can be implemented in a less capable but still valuable form, that introduces possibilities for tighter control of concentrating solar thermal systems.

The transform used in the technique, along with the proposed inverse, is likely to be useful in any application where a passive sense-resistive manifold might be useful. This example is the only known method thus far, as best can be determined, to use such methods in optical measurement applications.

### **7.4 Chapter Summary**

The overall aims of the project were achieved in that a prototype technique was developed for the quantification of light made available by a solar collector. The technique is applicable to a broad class of forms of concentrating solar collector. The key pieces of the technology were investigated, and the core mathematical process relied upon was found suitable in a bounding characterization.

## **8 Appendices**

This section contains supplementary material that is either extra to requirements or better fitted into the structure of the presentation by way of reference.

### **8.1 Concepts for Measurement**

This section will cover concept implementation of sensing techniques in order to obtain intensity, direction and wavelength information over a surface.

The progression of ideas will be according to the unwrapping of the problem, starting with a solution with high bias and low descriptive power before adding on complexity and descriptive power, until a point of maximum descriptive power with practical feasibility is reached. During this process, models of systems were proposed and qualitatively evaluated in order to determine a rough understanding of their descriptive power, implementation complexity and expected performance characteristics. The origin point of this process is the calorimetric approach used as current (the ASHRAE method), described in terms of spatial complexity.

#### **8.1.1 Zeroth Generation “Scanning”**

The system in two degrees of freedom, being the surface of the receiver, is simplified to have an aggregate measurement over the region of interest. In the case of a calorimetric method, this aggregate is the energy in the system, acquired by a high-emissivity coating and measured as a temperature difference. This type of measurement could also be performed by a photosensitive surface the same shape as the receiver tube.

Implementation of a uniform photosensitive surface directly is not practical in a monolithic sensor layer due to inconsistencies in sensitivity over the surface, which by itself could not be removed by calibration. If the surface were to be segmented into regions, calibration could be achieved at manufacture or dynamically by sensing the regions, however this is a deviation into another sensing model.

#### **8.1.2 First Generation Scanning**

First generation scanning is a measurement solution to a system with two degrees of freedom by having each degree of freedom accounted for by a coordinate positioning system, and a point intensity sensor. This can either be in terms of directional degrees of freedom or spatial degrees of freedom, with most existing systems being directional (e.g. barcode scanners).

A spatial sampling device using the principle can be implemented by a point flux intensity sensor such as a photodiode. This would be mounted on a Cartesian, polar or cylindrical positioning system that sweeps over a surface of interest. A cylindrical positioning system is suitable for most concentrators, but requires the measured property be transmitted wirelessly in order to avoid slip rings or long lengths of cable. Design considerations require accurate indexing of the sensor position, and a stiff structure to minimize error due to vibration.

Measurement speed is a function of overall accuracy in dynamic positioning and the response time of the sensor element. The response time can be affected by high irradiances due to the element

being driven near to saturation, or by significant memory effects that are present in photoresistors. The memory effect in particular is a significant limitation, since it can result in large errors in estimates of image mass, and as such photoresistors should be avoided in this configuration. These factors necessitate silvered attenuating filters and active cooling of the sensor element.

#### *Energy-Integrating First Generation Scanning*

The use of a sensor that responds to irradiance directly is fast, but results in an indicator variable that is contingent on expected spectral content, an undesirable property for the measurement. It is possible to integrate over the spectral content using an indirect sensor with a high-emissivity coating. This sensor is heated by received solar irradiance and the temperature measured electrically. A probe of low thermal capacity that is shielded from convective effects is required. The temperature of the probe is then dependent on radiative heat exchange in equilibrium and optical efficiency. It can be moved between locations and allowed to reach equilibrium for successive measurements. This method would have a long response time; requiring steady phenomena and results compensated by reference instrumentation to normalize against global direct flux.

#### *Direction-Sensitive Point Scanning*

An extension of first generation spatial scanning can account for directional information at each surface location by use of a number of points with different directional sensitivities. Since sensors have inherent directionality in their sensitivity as a function of angle, it is sufficient to sweep a number of oriented point sensors over every location, using a range of relative angles to the reference sensor. Given that directional sensitivity of the sensor can be modelled as a discrete vector against angle of incidence; it is possible to reconstruct for the true directional distribution given sufficient numbers of sensors and an expected form in the directional distribution. A less computationally intensive approach would be to modify the angular sensitivity pattern using shrouds and/or lenses on each sensor.

### **8.1.3 Second Generation Scanning (Line Scanners)**

A linear array of sensors can be swept parallel to their axis, as in the pushbroom camera. This exchanges dimensional complexity in positioning with dimensional complexity in the linear array, with the benefit of increased frame rate. Resolution in the direction of the linear array is a function of the layout and individual size of the sensor elements, which is a manufacturing limitation. It is possible to use a staggered array of sensors to overcome sensor size issues, this however introduces a greater complexity and uncertainty in the reconstruction.

#### *Direction sensitive line scanning*

Directional sensitivity can be added as in the first generation system. The calibration of each element is required due to inevitable errors in positioning during manufacture, along with the positioning mechanism.

#### 8.1.4 Third Generation Scanning (Imaging Sensors)

The degrees of freedom on the surface can be taken up by a collection of sensors located on the surface. This description is the approach of the construction of focal plane arrays used in camera technology. Implementation of a focal plane array for solar applications can be based on either:

1. Existing CMOS imaging chips as are commercially available. The small footprint of these sensors requires a pattern of such sensors over a flat surface to cover the area of a typical focal region of a concentrating mirror. The position of the active area of the imaging devices needs to be determined after assembly due to inactive border zones and imprecision in placement. Resolution available on even the cheapest low-resolution CMOS imaging devices far exceeds the expected variation over the focal region, and is thus a wasted resource. Silvered attenuating filters will be required to reduce high concentrated solar irradiances to levels that will not damage or saturate the sensors.
2. Arrays of discrete photodiode sensors. The resolution afforded by such an arrangement is poor, due to tolerances in the diodes and device positioning. Silvered attenuating filters are required, however saturation is less of a problem as devices are better able to deal with temperature and high irradiances. Curved surfaces can be manufactured with a flexible circuit substrate, this is not however compatible with automatic placement machines and any significant bending of a substrate post-positioning will result in cracking of solder joints. Alternately, curved surfaces can be approximated by flat sections at the expense of additional modelling complexity and imperfection in sampling the desired surface. Sampling must be done by multiplexing technique.
3. Arrays of discrete or custom manufactured photoresistors. This has poor resolution in the discrete case, which can be improved by a custom-manufactured array using gravure or photolithographical printing techniques. Both discrete and custom arrays can be curved given a suitable substrate. Response to irradiance is suitable for low to medium concentration levels, as long as the sensor is cooled to avoid damaging temperatures. Sampling must be done by multiplexing technique, which will be discussed further.

Direct use in finding solar flux levels on the collector requires that either:

1. The sensor array would be positioned in the focal region of interest as a curved surface in place of the actual receiver tube, and shrouded with a silvered attenuating filter. The LANSIR method of determining the statistical properties of a mirror uses a synthetic parallel-ray light source on a concentrating mirror of interest. The statistical properties of the spread of concentrated irradiance is measured by a focal plane array in terms of intensity.
2. The sensor array in planar form would be positioned by a mechanism such that the centre-line or centre-point of the planar array would be located at a point on the desired measurement surface, with the array being tangential to the measurement surface. This point of contact would then be rotated to give a number of measurements at various angles. Given a sufficient but finite number of measurement points the irradiance on the curved surface can be estimated by interpolation of irradiances in the planes onto the surface in a 3D reconstruction. A best implementation would however require a model of fair complexity

(most likely based on a Hough-like transform or Maximum-A-Priori) in order to globally fuse the information provided at every pixel in the array for every plane angle measured.

#### *Directionally-sensitive surface arrays*

It is possible to include directional sensitivity to the array by the use of an ensemble of mounting directions for the sensor elements in the array. The orientation of the sensors creates inherent directional sensitivity with unmodified sensor elements due to Lambertian optical properties of flat surfaces (or the built-in lenses often present on discrete sensors). However, directionality can be further improved using element-associated shrouds. Each sensor element codes for a different “angular response vector” in discrete representation, and a full complement of representative angular response vectors can be estimated for each location by interpolating missing responses from neighbouring locations. The use of sparse or smooth fitting models can reasonably reconstruct for a good estimate of overall angular response from these vector estimates, as long as certain properties of the distribution of irradiance hold. Accuracy of device construction will have a significant impact on overall performance, requiring extensive calibration in order to determine actual position and angular response in order to gain maximal performance. The tolerances of typical manufacture methods may be suitable to ignore calibration if relative sensor position and direction error is made low by having a large overall device, as would be used in monitoring larger focal areas.

This model can be adapted to the arthropod eye model, where the element shrouds or lenslets are oriented to cover the range in angle in a fan-like continuous distribution, rather than an interleaved arrangement of directional bins.

#### *Single-aperture imaging focal plane arrays and light-field capture*

Positioning a third generation planar imaging sensor behind an aperture and/or lensing system allows the measurement of radiation direction through the aperture. The use in solar measurement is more concerned with spatial measurement over the surface of interest, which would require the imaging sensor to be passed over the surface with a positioning mechanism.

This provides a single point of spatial addressing in the local sense and directional addressing in the global sense, and thus a five-dimensional sampling of the plenoptic function (a light-field image) acquired serially. The aperture itself is an attenuating mechanism that can be tuned to the expected concentration ratio.



## 8.2 Sample time consideration design

The designer may have the primary limitation being minimization of the time to sample the required amount of unique measurement information. This constraint is a concern when time related effects are of interest, requiring a well defined capture time window. In this case the total number of nodes will need to be maximized, since every additional node increases the amount of information available at every measurement. Since additional nodes are a large cost factor this will have to be simultaneously minimized. The plot in Figure 64 is taken holding the number of active sources constant, while increasing the total number of nodes.

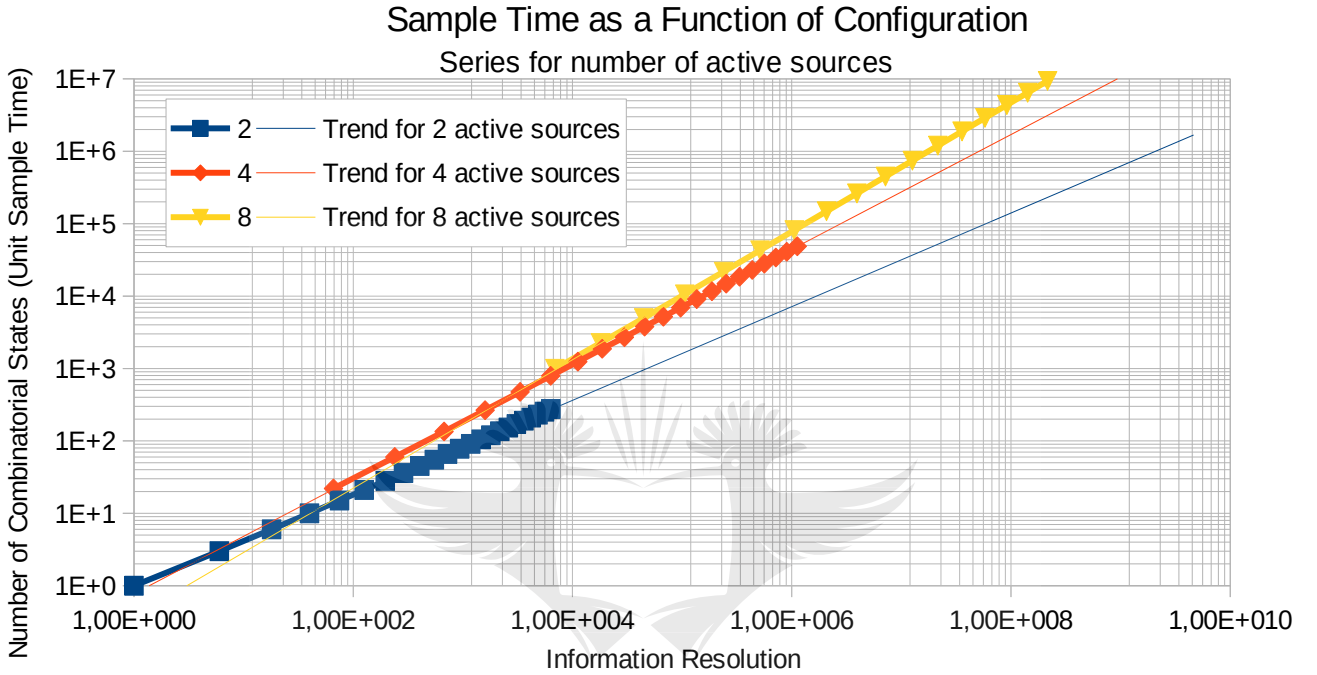


Figure 64: Sample time as a function of information resolution for system configurations

The points are ascending total number of nodes with increasing number of combinations, the lines demonstrate the continuity of the series of discrete points and the ability to sample a subset of the maximum amount of information present. The minimum sampling time is provided by the lowest number of active nodes for any given information resolution, however this may come at the cost of a large number of total nodes.

A power law hypothesis gives a perfect fit to both the relationship between the number of combinations for a given number of total nodes, and the meta-relationship between these coefficients. This gives the following relationship:

$$t_s = (1.52 \cdot n_t^{-1.12}) \cdot q_{\text{symmetric}} \quad (95)$$

where  $t_s$  is the sample time for a set of measurements, and  $n_t$  the total number of boundary nodes being measured, for a given quantity of unique measurement information  $q_{\text{symmetric}}$ .

This demonstrates that it is possible to get an arbitrary sample time at given information resolution, however the logic of this arrangement is practically bounded by the limit where every node is sampled directly.

### 8.3 Sensor-Layer Manufacture Methods

There are a number of ways to manufacture photoresistive elements on the sensor layer, these will be detailed below:

#### 8.3.1 Discrete Component Implementation

For our purposes, a prototype system would be implemented using discrete components, rather than the conceptual manufacture framework of a deposited photoresistive film. Implementation of a prototype array using discrete semiconductors routed and jointed using manual job-shop production techniques is necessary for evaluation of the system performance in real terms. There are a number of options available to the designer with current packages used in discrete components:

##### *Through-Hole Mount on Substrate*

Through hole leaded photoresistive components are currently available despite their violation of RoHS directives, and are implemented as ceramic wafers on which a copper layer is deposited, leads attached and the copper etched with a serpentine groove. The surface of the copper and groove is coated with a photoresistive semiconducting material such as Cadmium Sulphide, the region in the groove thus forming the photoresistor that is sensitive to visible light radiation. The coated surface is sealed with a translucent epoxy to prevent damage to the coating and loss to the environment of the toxic semiconducting layer.

Due to the method of construction and expected areas of use, the photoresistor manufactured in this way varies in optical performance characteristics and the mounting is subject to not insignificant tolerances due to variation in lead placement and the side thickness of the epoxy coating. The devices are large in relation to other discrete components due to the age of the target printed circuit board technology for which they were designed.

The concerns of this construction method are:

1. Inconsistencies in the orientation of the surface angle of the photoresistors to the substrate normal.
2. Inconsistencies in the photoresistive response and the calibration concerns with these.
3. Large pixels associated with the relatively large photoresistive elements.
4. Incomplete optical coverage of the region being sensed due to the inter-element spacing required due to manufacturing tolerances, and the fractional response of the elements due to their internal serpentine grooves.
5. The large manual placement labour required to feed most components of this type due to packaging methods that are incompatible with pick-place machinery.

### *Surface Mount Device on Substrate*

Discrete photoresistive devices compatible with surface mount techniques are not common, investigations up to the current point have shown no such components commercially available to this project, though in principle there is no physical reason that such devices cannot be manufactured.

Discrete photodiodes and phototransistors are commonly available in surface mount packages. Currently theory to handle the non-symmetric photo-optical response of semiconductor photodiodes has not been developed, though in principle is possible given some modifications to the technique. In order to create the required electrical symmetry, two photodiodes or phototransistors may be connected back-to-back or front-to-front in series. In this configuration the reverse-bias response of the semiconductor dominates the response, this however has some caveats:

1. The effective sensor area is double the size of the discrete element, which is already large in comparison with some technologies. This size is not a problem for integrated sensors developed on the technique, where process technologies are the limitation rather than commercial device binning procedures. These back-to-back pairs however appear to be non-existent.
2. The two sensors are implemented as two junctions in two areas. Their electrical appearance is as one symmetrical non-linear device which should ideally have equal responses in both quadrants. However, spatially the junctions respond to different stimuli and thus are likely to be non-symmetrical, especially when one junction is separated from the other in the image being sensed by an edge. This asymmetry is not a problem in aggregate, since the voltage over many measurements is expected to balance. The symmetry of measurements cannot be guaranteed however, with reconstruction applying greater sensitivity to one quadrant of the pair than the other. This would result in a value skewed to the element that is more sensitive in the sampling scheme, rather than an equal average of the two spatially distinct elements. This problem is not apparent when effective resolution of the variation is less than the actual resolution of the local region of the pair of elements.
3. Unless special reconstruction methods are implemented, the response over many measurements will aggregate the stimuli at both junctions and the effective pixel will have a non-square shape that is subject to rotation due to the connectivity requirements over the field. This will be awkward to handle in the reconstruction, though not of great concern if it is managed in the intermediate steps for reconstruction, which does add complexity to the solution.

### *Surface Mount on Flexible Substrate*

Flexible substrates available currently are based on either metal or polymer films of various thickness. A copper layer is formed on the substrate or on an insulating film in the case of the metal films such as aluminium. The characteristics of the surface mount devices carry over to this section, in addition to this there are a few design issues to address:

### *Metal film flexible substrates*

The metal film varieties are useful when dissipation of heat is a problem, the board itself being effective at removing heat from high-power components, without the use of additional heatsinks or areas of copper for dissipation.

The radius of curvature available with metal film substrate is less than the polymer film variants, in addition to this the insulating film may be compromised by excessive manipulation of the surface. The stiffness of the film material (the Young's modulus) is not insubstantial with respect to the materials of the packaging of discrete devices and the materials. This results in the substrate being able to put a great amount of stress on packages that are mounted onto the substrate before it is bent. This will fracture the packages, the solder joints and lead to greater unreliability otherwise.

The primary problem is thus: The substrate is bent before the components are mounted, components are mounted afterwards. However, reflow ovens are not designed to handle non-planar substrates, which complicates the mounting process. The action of gravity in a non-usual direction complicates the matter further, since the epoxies used to hold the components is designed to soften during reflow to allow the surface tension of the melting solder to pull the components into better alignment.

*The use of metal film substrates is thus practically limited to lower curvatures than the polymer film varieties unless the mounting problems are solved.*

### *Polymer film substrates*

Polymer film substrates are used extensively in the automotive car industry, where they serve to route signal lines for instrumentation and the electrical connections are made by screw-connection terminals that clamp the substrate to form a junction.

The primary difficulty in using the films with surface mount devices is the warping and melting of the substrate under reflow. The use of polymers that are stable is a fundamental requirement, this is not however a current feature of commercially available films and would require further development before use.

A benefit to the use of polymers is the lower stiffness than that of the metal films, which allows components to be mounted before the film is bent, and the greater curvature of the result. In doing such the placement of the components is important; since the substrate is less stiff a local warping occurs that needs to be balanced in order to effect a substantially smooth curvature.

### *Axial-Leaded Component Mesh*

*A great benefit for the method is the possibility for the sensor material itself being the structural support that defines the location of the sensor elements in space, only one layer is required:- that of the sensor material.*

In this method axial-leaded thermistors are used to sense a saturation temperature as a result of solar irradiation. In order to construct a sensing field, the leads are soldered against each other so the components form the links of a square or triangular grid, which then forms a wire-like mesh that can be formed over a shape or held in a plane by low but sufficient tension.

The sensor is only able to react to stimuli that travels through the package or leads, radiation requires a glass casing and temperature is most effectively transported via conduction through the leads. In this case the temperature sensed will be the average of the temperature gradient across the two leads, this in effect a convolution over the field, and can be mathematically reversed by deconvolution.

An interesting development using this method is the concept of a porous sensor manifold, where the sensor elements that would normally be dense and obstruct the path of radiation or gas flows are now present over the same area, but only interfere with a very low fraction of the system. The effect is a low resolution but distributed sensing pattern over the region that has minimal effect on the normal behaviour of the system.

### **8.3.2 Printed-Paste Method**

A simple method to construct a sensor without using discrete components or complicated and expensive semiconductor process technologies is the use of printing techniques to deliver a semiconductor ink in a pattern that effects the multiplexing technique. The desired result is a coating of photoresistive material in a pattern with the desired resolution. This pattern is maintained in an even film and with even junction density such that the photoresistive effect is uniform. If the surface being coated is not a good insulator, subject to absorbing water or otherwise prone to loss of dielectric; the photosensitive resistance will be shorted in unpredictable ways. The substrate should be stable and able to hold an ink, so paper that is printed with a semiconducting ink and later coated to make it hydrophobic is a cheap and effective proposal.

#### *Pastes in suspension*

Since semiconductor compounds are generally non-soluble in ionic media a suspension, the paste may be composed of micronised grains of photoresistive semiconducting material. Examples of such photoresistive compounds are Lead Sulphide (PbS), primarily sensitive in the infra-red region, and Cadmium Sulphide (CdS), sensitive in the visible region and used in discrete photoresistors. These compounds are well known since the early research into semiconductors, more modern photo-polymers have been discovered that are organic and non-ionic.

The use of sulphides creates a that microstructure consists of grains of ionic salts. Upon evaporation of the suspending fluid these form non-crystalline ionic bonds in proximity contact. The electrical effect is a large number of semiconductor junctions that are in series-parallel and in opposite directions, the use as a sensor in the reverse-current flow of electrons suitably excited by incoming radiation to jump their band-gap.

Pastes can be delivered by various methods used in printing [245]:

1. Silkscreen, where a membrane is varnished with a negative of the pattern and the ink pressed through the unvarnished areas onto the surface being printed [102].
2. Gravure, where a drum or plate is etched or stamped with a pattern to be printed and the resulting grooves holding ink by surface tension to be delivered on contact with the surface being printed [246].

3. Photolithography, where a drum is etched by photolithographical means in order to deliver a pattern of ink onto a rubberised roller that delivers it onto the surface being printed.
4. Drafting pen, a slower process where ink is delivered by a needle or pen-like tip that is actuated in 3 dimensions in order to build up the pattern on the surface.
5. Spray coating, where the ink is deposited on the surface by a nozzle and passes through a screen that defines the inverse of the pattern, thereby allowing only the pattern to be deposited.

The relative ease by which a photoresistive pattern can be created using these methods is offset by the relatively low resolution available in comparison to other semiconductor technologies. There is also the need for more extensive testing to calibrate the device against drift due to process parameters. Resolution is a key parameter, and manufacturing processes will decrease the reliability of the photoresistive circuit links due to shorting and open circuits, as a result of imperfect distribution. In addition to this, for the photosensitive elements to be modelled as a discrete lumped body the elements must have a far greater effect on response than the nodes. This dominance is possible if the elements are effected by serpentine lengths of photoresistor material, thus having orders of magnitude greater resistance than the nodes and dominating the response.

Since the layer formed by the process can be made thin, and on flexible substrates, this method is ideal for creating light resolving surfaces that have substantial curvature and complex shapes. The photosensitive film should be protected with a coating that stabilizes the semiconductor mechanically and resists expected abrasion, weather effects and temperature fluctuations.

The drafting pen and spray coating techniques can work on surfaces that are already moulded with complex curvatures that are either open or closed surfaces. In this way it would be possible to create photosensitive manifolds like spheres and cylinders.

#### *Pastes in solution*

Non-ionic organic semiconductors have the prospect of being delivered by an inorganic solvent, producing a much finer structure than that of suspended pastes; thus more uniform photoresistive properties and structural integrity. By proper control of the viscosity of the solution such that the pattern shape is maintained on the surface, delivery of the solution can be made by techniques used in ink printing. The surface is then allowed to dry with the evaporation and temperature of the solvent controlled by the drying environment so as to allow more uniform and stable crystal microstructure growth. Due to limitations in availability of such semiconductors and current project scope this avenue has been identified but not appreciably investigated.

### **8.3.3 Inkjet Printing + Gas Developer Method**

Sulphide semiconductors are ready candidates for application to the problem, manufacturable in ionic form and come with a beneficial property that they are very sparingly soluble in water. The semiconductor cation can be delivered in solution to the surface to be coated, such as cadmium, lead or tin, paired with an anion such as a chloride or nitrate. The sulphide can be formed by delivery of Hydrogen-Sulphide gas which will precipitate out the semiconductor in surface reaction with the liquid.



The use of inkjet (or bubblejet) method of printing is an implementation of the inkjet method by a micro electrical mechanical system (MEMS) for the pumping of small droplets of ink using a thermally generated gas bubble from the ink itself. Small chambers hold ink by surface tension and a heating coil is activated to heat the microdrop, pumping it out onto the surface as the print head scans the surface. This method was commercialized for home and office printer applications, the print head is disposable and can be cleaned and refilled as a way to deliver the cation solution [247].

Inkjet is a technique also used in commercial printing at scale, where drops of ink are produced by a nozzle, given an electrostatic charge and accelerated using voltage fields to the surface being printed. The drops are either created on-demand or a continuous stream is produced that is either directed toward the surface or to an ink-catch that captures the drops for reuse, thus giving the print head control of delivery. Magnetic fields are used in such systems to scan the droplet stream perpendicular to the print head direction. The inkjet method of delivery is thus also able to deliver the cation solution at scale [247].

#### **8.3.4 Conductive Film Continuous-Element Fields**

Continuous fields are possible by applying the Electrical Impedance Tomography method to surfaces coated with uniform photoresistive layers. A special application of printing in the general sense, with application of other surface coating methods. A basic method of testing this principle is the use of selenium rollers used in photocopiers and “laser” printers, which are photoconductive by construction.

##### *Dipping and Surface Painting*

A simple method of application of a semiconducting photoresistor is by suspension of micronised grains in a solvent, as has already been covered. Delivery of this suspension in a uniform way over a surface can be effected by printing through an unvarnished silkscreen, spray deposition by nozzle, or dipping in the suspension. Once the photosensitive surface is stable it should be protected with a transparent coating to prevent mechanical and weather damage to the surface. It should be apparent that the ease and scale of these methods allow large regions to be covered and captured, allowing capture at such scales.

##### *Chemical Vapour Deposition (CVD)*

If very thin layers of photoresistive material are required, as would be to reduce total current draw by the array at the expense of signal to noise ratio, the use of vapour deposition is an expensive but worthwhile possibility. There are process variants of the base method particular and tuned to various requirements. A vapour is heated to a temperature where a chemical reaction occurs on the surface, creating a very thin layer of the desired material. There have been no requirements in the current project to have such thin layers, so further investigation as to how to implement CVD and what semiconductors are compatible has not been made.

## 8.4 Electrical Layout

The electrical apparatus for the excitation of the field can now be addressed, along with the measurement of the boundary properties at each state. A straightforward cell can be used for the measurement of both current and voltage, switched and unswitched. An analogue switch is actively controlled by the outputs of a serial-in parallel-out shift register, thereby switching F-nodes from being able to source or sink current. Level shifting is required to interface any control logic with the analogue switches.

The analogue switch is effectively a voltage controlled resistor, when gated ON it represents a near-linear resistance and will pass current in both directions. A survey of commercially available production analogue switches show ON resistances from  $45\Omega$  to  $200\Omega$ , and a voltage swing not exceeding  $30V$  and most typically,  $15V$ . This component is a limiting factor in design due to its' attenuating effect on the signals being measured. The switch resistance is very low in comparison with the typical sensor element resistance, however the Thevenin equivalent resistance of the circuit with these elements will be much lower than the individual sensor elements due to the parallel paths present.

The switch resistance may be easily accounted for in modelling the circuit as a system of equations, however it reduces the accuracy of methods that may approximate the circuit rather than solve it directly. In addition to this, the resistance is a function of current through the switch, which despite the best efforts of the manufacturer is still slightly non-linear due to the properties of MOSFET transistor technology.

### 8.4.1 The Foveal Node Sensing Cell

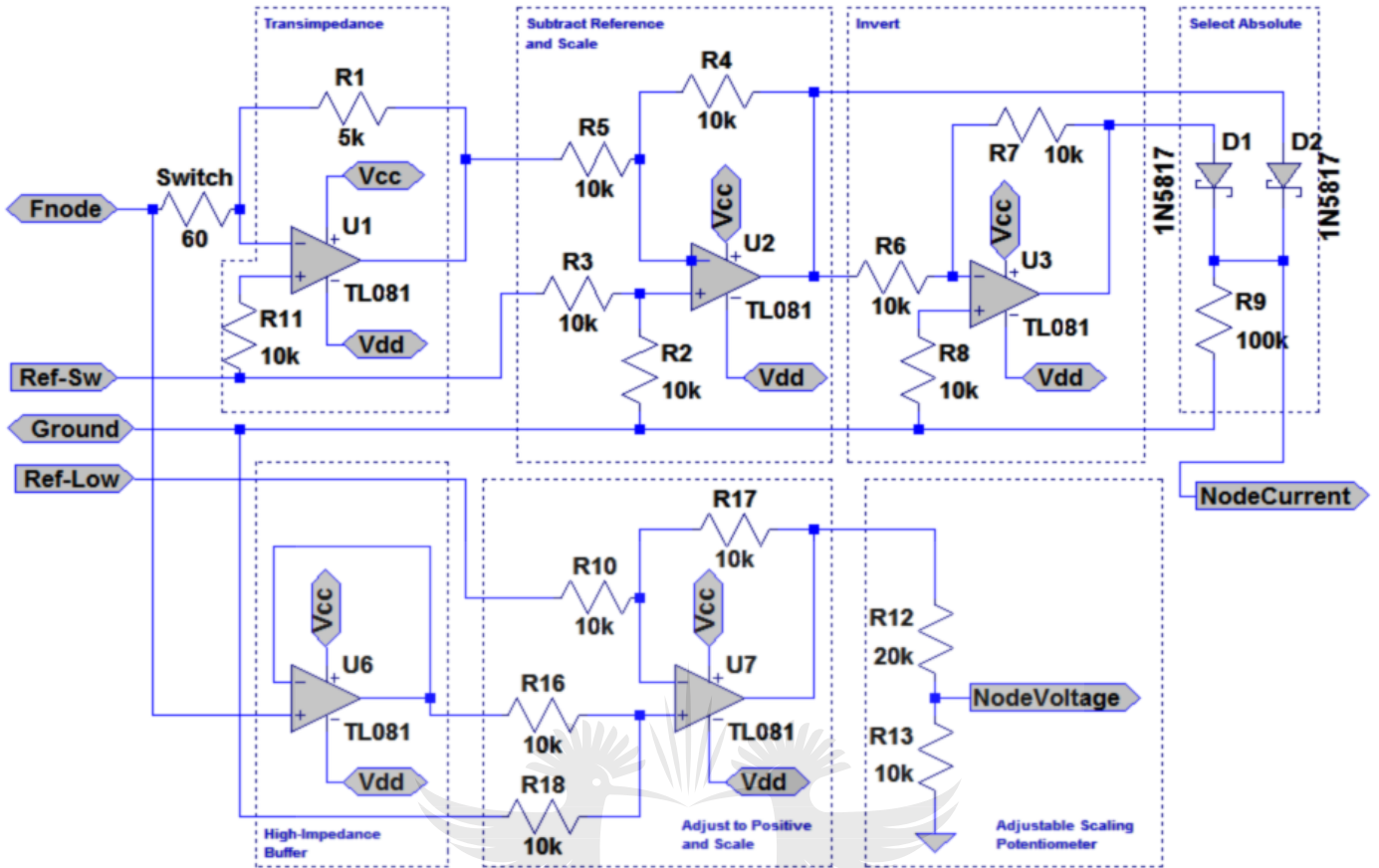


Figure 65: Sense cell for one Foveal Node

Please refer to Figure 65, which describes a partial model of an active sensing scheme for one F-node. The field is sensed with differential voltages, the voltage at the F-node is buffered by an operational amplifier which is connected directly to the node and thus unswitched. The current sourced or sunk from the F-node is sensed by a very low impedance current-to-voltage converter, implemented by negative feedback through a resistor from the output of an OPAMP to the inverting terminal summing with the current being sensed.

The circuit applies an excitation voltage to the field that is at points intermediate from the rail voltages provided to the OPAMPs. Thus for rails of  $[-15, +15]$ , excitation voltages are  $[-7, +7]$  or similar. In order to apply the excitation voltage, the current-to-voltage converter has its' non-inverting terminal shifted by a push-pull switch that selects a voltage reference by way of the direction of the current. *Since the OPAMP in negative feedback will drive its' output to make the inverting and non-inverting voltages equal, this shift in non-inverting voltage creates a "virtual source" or "virtual sink", that is inherently low impedance.*

The output of the current sensing OPAMP in transimpedance that forms the source or sink will swing above the virtual source voltage or below the virtual sink voltage within the gap between these high and low points and the supply rails. It became apparent that in order to get sufficient resolution while keeping the system cost down, an analogue zoom block is required to tailor the signal to the ADC. This must be implemented by either switched resistances, in the form of digital potentiometers, or switched capacitor designs. The former require calibration and the latter must

be implemented in integrated designs. An analogue zoom would allow an iterative selection of the best sensing window for the ADC, given the particular field being sensed.

#### **8.4.2 Management of electrical noise**

Any practical measurement scheme must from the outset account for sources of error in the design, in order to be stable in real-world conditions. In our case, the field of sensor elements is large antenna for picking up radio signals and stray electromagnetic radiation. The signal lines from the foveal nodes will also be subject to electromagnetic interference. This interference is an important consideration in electrically noisy environments, as might be the case with servo-actuated solar tracking on mirrors.

A grounded plane underneath the entire sensor array is advised, with grounded sheath shielding for the bundle from the foveal nodes to the primary source of measurement. Since the sum of all currents must be a loop zero, bringing all the wires in close electromagnetic contact with each other in a twisted bundle provides natural differential pairs for currents flowing in the active nodes. The nodes not switched active are left “high-impedance”, which would ordinarily make them susceptible to induced noise. However, in this case it must be remembered that the node is still subject to a Thevenin equivalent resistance for the field of elements at the sensor mean value.

Electrical noise can be managed further by series inductive filtering and capacitive shunt filtering to ensure only low frequency components are present, since measurements are desired when the field is at steady state. This will however reduce the frequency at which switching of combinatorial states may occur. The frequency at which states may be switched is inherently limited by the ringing present due to the parasitic reactive elements in the field itself, a source of self-induced noise in the form of a damped transient.

#### **8.4.3 Sources of Measurement Error**

Consider the causes of inaccuracy in the measurement system:

1. Offset errors
2. Non-linearity of response
3. Scaling error
4. Quantization error

By taking a measurement with its’ direct twin (in terms of excitation potential), the effects of offset can be eliminated by subtraction between pairs, or cancel each other indirectly in the reconstruction. This methods can be used to account for differences in offset error between channels.

Scaling error is a more difficult issue, there are two cases to consider:

1. The source of the scaling error is uniform over the channels being sensed, as would be the case for a multiplexed digitizing sampler. This would result in relative measurements being accurate and absolute measurements being in error. This should be counteracted by calibration against a reference field with known absolute properties.

2. The source of the scaling error is non-uniform over the channels. This will skew measurements since the influence of certain channels will be unbalanced in the reconstruction. There is very little work investigating the effects of this on reconstruction, and little incentive to do so since the ill-posed nature of the problem is great enough to warrant a high degree of calibration and manufacture quality in EIT systems. It is expected that the image will become distorted under these conditions, and the reconstruction more unstable.

## 8.5 Calibration and characterisation

The use of a photoresistive imaging field is contingent on a number of model assumptions, violations of which will make reconstruction unreliable, with deviations that will require calibration compensation. These are listed here, and form design criteria for application of the method in a physical measurement device.

### 8.5.1 Overview of assumptions in base model

There are a number of assumptions in the base model, deviations from which need to be calibrated against:

#### *Zero parasitic conductivity*

There are two possible sources of parasitic conductivity with regard to the intended EITMSA imager, which will be considered accounted for by the construction of the device:

1. Leakage conductivity from the field to the environmental ground or current sources. This may occur as a result of:
  1. Conducting aqueous and liquid films that form a bridge to the device casing.
  2. Stress-induced breakdown of the dielectric relative to a ground plane that may be present in order to provide system resistance to environmental electrical noise.
2. Leakage conductivity over the field itself. This occurs between the nodes and is modelled as a resistive bridge between the nodes adjacent to one another, a number in parallel with the sensor elements. This loss is exacerbated with greater impedance of the sensor elements, and is not insubstantial given the multiple conditions of:
  1. High environmental humidity and possible conductive liquid films (most likely aqueous), present on or within the substrate on which the sensor elements are supported.
  2. Dusting over the surface of the field, forming bridge connections between sensor cells.
  3. A substrate material that will degrade under environmental stress conditions of light, heat, mechanical stress and chemical stress.

The first type of parasitic conductivity cannot be reliably compensated for with calibration, and must be specifically avoided in design. The second type can be calibrated for to a certain degree if the field can be sampled at more points than are foveal nodes using a probe array capable of being repositioned, with calibration requiring reconstruction of the parasitic resistive elements. Once known the parasitic elements can be incorporated in the model, however the increase in conductivity will mask the sensitivity of the photosensitive elements.

### *Element homogeneity*

The sensor elements are assumed to be within small tolerance regarding shape, chemistry, thickness and other factors that have major influence on the flux and temperature response characteristics. This assumption is unreasonable in the target field application for a production system, however in order to compensate for these variations an intensive calibration routine would be required. In fields manufactured out of discrete components a suitable matching and binning procedure would be required to ensure homogeneity.

A case study for this assumption is that typical discrete Light-Dependent Resistors available from commercial manufacturers have significant variation in characteristics (+/-20%). It is not yet understood whether this variation is a symptom of an economised manufacture process, or is a result of fundamental physical problems in depositing uniform films of photoresistive semiconductor material.

In order to map out empirical calibration curves for each sensor element, the field would need extensive iterations of being:

1. Held uniformly at various temperatures for each test cycle.
2. A number of test patterns of calibrated light applied, such that each element is subject to a minimum number of different flux levels.
3. The field sampled and reconstructed using the test pattern as a regularization prior for high accuracy in reconstruction, so as to minimise error due to reconstruction issues.

### *Zero self-heating*

In a body typical of inspection by EIT, the effect of the electrical current is assumed to be negligible in terms of changing the conductivities of region of the body. In the case of EITMSA the sensor elements are likely to be under a prolonged series of excitations in most use cases. The resistive losses in these elements will cause a heating effect. It is however clear that in the current application the power consumed by the field will not have any significance unless large excitation voltages are applied. Self-heating is only likely to be a concern if the EITMSA method is ported to integrated devices that need to be operated in low temperatures.

### *Homogeneity of thermal conditions for light-sensitive fields*

The effect of differential heating of an EITMSA field for optical measurement is likely to lower the accuracy bound, and presents a real issue when considering that the field will be subject to intense radiation. In order to combat this a number of strategies may be employed:

1. Manufacture of each sensor element as a series combination of the light-sensitive region and a positive-temperature coefficient (PTC) thermistor of a tuned size. The semiconducting light-sensitive region has a negative temperature coefficient (NTC) that is partially compensated by the thermistor which is thermally very near to it. This will afford partial compensation, however the NTC and PTC are unmatched in their responses. Use of further combinations of NTC and PTC thermistors in series and parallel will better compensate.



However, conductivities in parallel will desensitize the boundary measurements with regard to the sensor elements and reduce overall dynamic resolution.

2. Use of a thermal mass behind the EITMSA field, which is in good contact with the field and has good thermal conductivity in order to make the temperature gradient across the field close to uniform.
  1. The temperature of this thermal mass can be measured by thermistor or thermocouple at a number of locations and a basic heat flow finite element method used to get a good approximation of the temperature over the field.
  2. This temperature can be used in the calibration compensation of the field elements based on a temperature-calibration curve for:
    1. A typical element representative of the average response.
    2. A binned element based on classes of response, as determined by previous calibration of the field against a constant luminous flux.
    3. An individual element, as determined by a full calibration against various light fluxes under various operating temperatures.
3. Use of a thermal regulator with an extended heatsink or active temperature regulator system. This requires a material of good thermal conductivity and a mechanism to aggressively exchange heat with either the ambient air. Also required is another heat reservoir or heat pump, such that there is good regulation of the temperature with regard to heat input into the system. This allows a simple temperature compensation based only on the average temperature of the field. Calibration can be done according to the methods previously mentioned. The principles of such are well understood, two examples of such a design would include:
  1. A sleeve backing the field substrate through which liquid coolant is circulated to a heat exchanger.
  2. A finned heatsink backing the field substrate, over which air is blown in to form a direct heat exchanger with the environment.

#### *Maximal Inhomogeneity for thermal-sensitive field*

The assumption of homogeneity under thermal conditions is definitely not true when using a spectrally “integrating” coating; such as a low-emissivity paint over a thermal-sensitive field of thermistors or resistors. Such sensors intend the thermal effects and thus require that as little heat spread as possible is maintained across the field, the direct opposite of the heat-transfer objectives in a light-sensitive design. The use of an integrating coating implies an error due to the imperfect nature of the coating, in terms of:

1. Error due to variations in emissivity over the spectral content of the radiation being measured.
2. Change in emissivity of the coating with regard to different wavelengths of light, as a function of the temperature of the coating.

It has been found in devices for the measurement of general solar properties and in solar collector systems that degradation of the coating is a significant weathering effect. This will limit the life of the device between applications of low-emissivity coatings, since calibration in this situation is difficult.

#### *Thermal Stability*

The sensor elements are likely to degrade under elevated temperatures, however this process will be assumed to be slow and will be compensated for by periodic re-calibration based on empirical experience with the device. This requirement is true for both light-sensitive and thermal-sensitive designs, due to degradation of the semiconductors and possible high-emissivity coatings.

#### *Colour masking of the light-sensitive field*

In order to achieve spectral differentiation either:

1. A mask of spectral filters placed over the photosensitive area of the elements, as used in commonly available focal plane CCD and CMOS imagers. Filters are made by a dye-impregnated plastic or by plastics manufactured with specific granularity at the molecular level. It is assumed that the consistency of such acquired filters will be good and their calibration compensation will not be required.
2. The sensor elements are manufactured with variation in semiconductor chemistry in order to provide differing spectral response, either by variation of the semiconductor used or by inclusion of a dye that subtractively modifies response to different wavelengths. Issue of manufacture consistency arise, with required compensation by calibration on a per-element or regional basis. This method of manufacture is out of the scope of this project, however for many possible applications this method is likely to be the most practical way of achieving spectral differentiation.

### **8.5.2 Identifying sources of deviation from the model**

#### *Memory-effect*

The typical photoresistive semiconductor has a conductance that is a function of the past history of irradiance on the sensor. This has been found to be significant, making precise measurements only possible after settling times of up to an hour. This effect can be reduced by having generally lower irradiances on the surface. It is possible that parameters of construction can alleviate the problem, however there appears to be little work in this area.

#### *Thermal noise*

So-called Johnson noise is the generation of a voltage over a resistor due to thermal dislocation of electrons. This noise factor is prevalent when using high impedance measurements and high values of resistance, and forms a noise floor that cannot be avoided in analogue design. Thermal noise is often reduced by cryogenically cooling analogue circuit stages. High value resistors are to be avoided in most cases, while avoiding the power consumption of low value resistors. The models of

thermal noise will be omitted here, since the effects of Johnson noise will be low in comparison with other errors.

#### *Response of analogue-to-digital converters*

The analogue to digital conversion process is particular to the type and implementation, the error due is primarily due to non-linearity and noise in the quantization levels. It is common to lump these into a single noise estimate as a distribution about the true value, unless higher performance is required. It can be fairly assumed that this source of noise is lower than the general noise in the analogue stages.

### **8.5.3 Calibration Routines**

Calibration is applicable to multiple levels of the system; beginning with the method of applying an electrical stimulus and measuring F-node properties, and on to characterization of the elements in the measurement field itself. Calibration of the sampler hardware is a function of electrical design and component quality and drift, while the measurement field is a function of reference light sources and light shape modifiers.

#### *Calibration of the sampler*

The electrical sampler mechanism has three components that must be calibrated:

1. A reference for high and low voltages. This can be done at construction against a reference Voltmeter and is not a problem with regards drift, since measurements are normalized.
2. The current measurement for each channel, which is a function of the values of feedback elements used in construction at the current temperature and age.
3. The voltage measurement for each channel, which is a function of analogue signal conditioning components and the performance of the Analogue-to-Digital-Converter.

Calibration of the EIT sampler can be effected by a reference array of ohmic resistors. Multiplexing the different channels into the array at known points will provide a range of reference voltages and currents based on their position. This provides a calibration of sources against each other, but requires accurate high and low references.

If a voltage stimulus and voltage measurements are used without the need for current measurement, both the hardware and the calibration are simplified since there is no need for any sort of transimpedance amplifier. The accurate measurement of current is a design problem for EIT systems in general.

#### *Artificial Light Sources*

A uniform light source is suitable for calibrating the absolute response of the elements, rather than their relative response. This can be achieved by a planar array of light sources located at a sufficient distance from the device, with shrouding to prevent other environmental light influence. Cross calibration against a calibrated light intensity measurement is required along with a stable power source. This routine is required for a number of temperatures in the expected range. If a single calibrated light level is available without variability, attenuation of the light can be effected by

stacking known filters. If the atmospheric conditions are known to be clear and close to the normal spectral profile, the sun itself can be used as source with normalization against a pyrometer.

#### *Sources of Ground-Truth*

A basic form of calibration of elements against one another can be effected by opaque masks placed over field in contact, in order to avoid image-forming effects (not diffraction). This can be effected on an element-by element basis or in a shotgun sequencing approach with a set of random matrix patterns. A pyrometric flux measurement is suitable for a calibrated reference, a calorimetric approach that is well known for light measurement.

#### *Measurement of Drift by Supplementary Sensors*

It is possible to use easily-sampled controlled sensor elements for assessing:

1. weathering of elements in the field
2. local noise levels
3. thermal drift and calibration-curve adjustment
4. moisture-related drift and calibration adjustment

These sensors should be located on their own channels for direct measurement, located both on the field and in the environment. *This provides a normalized measurement against the unconcentrated sun, which is acceptable for concentration estimation.*

#### **8.5.4 Device failure modes**

There are a number of failure modes for the system, which can be investigated:

##### *Stochastic photosensitive element failure*

In order to model failure of sensor elements, a Monte-Carlo simulation can be used to sample the effects of disconnection of random photosensitive elements in the field according to a component failure probability. This approach is suitable to plot the aggregate properties of the field against component failure probability.

##### *The loss of either the voltage, or current, or both channels of an F-node as a blind failure*

The resolving ability of the system is algorithm dependent when the loss or misbehaviour of an F-node measurement goes undetected, that is stuck at some level of voltage and current. This mode of failure is likely debilitating to regions of the field associated with the F-node. Due to the global information in the voltage field, incorrect information from a channel will have a large effect on reconstruction.

##### *The loss of either the voltage or current channels as a detected failure*

When the loss of a channel is detected the reconstruction can be reconfigured to omit the faulty node. This condition occurs due to failure of a source driver, or more likely the physical channel. The reconstruction methods presented can be made overall somewhat resilient to failures of a channel when it is detected; by isolating a channel the reconstruction routine can ignore such information and reconstruction will still be effective for unaffected regions. Since it is relatively easy

to detect a channel failure, the sampling method is thus generally robust even during post-processing of existing data.

## 8.6 Boundary Connectivity

The process of making a field continuous has been described, however this process has not been defined adequately. The various methods should be considered due to their effects on physical construction. In a field that does not physically wrap into a continuous manifold in 3D space, some layouts go further toward reducing the amount of connecting conductors than others, and will have different behaviours. This consideration is important over wide areas, in order to reduce material costs.

There are various different types of boundary reflectivity, as in Figure 66, below: The vertices of the facets are points that are directly electrically connected when the facets are connected in order to create a continuous field. The annotating numbers indicate the same electrical point, the letters enumerate the distinct sides of the polygon. The arrows indicate the direction and location of a single vector of flow over the continuously connected boundary.



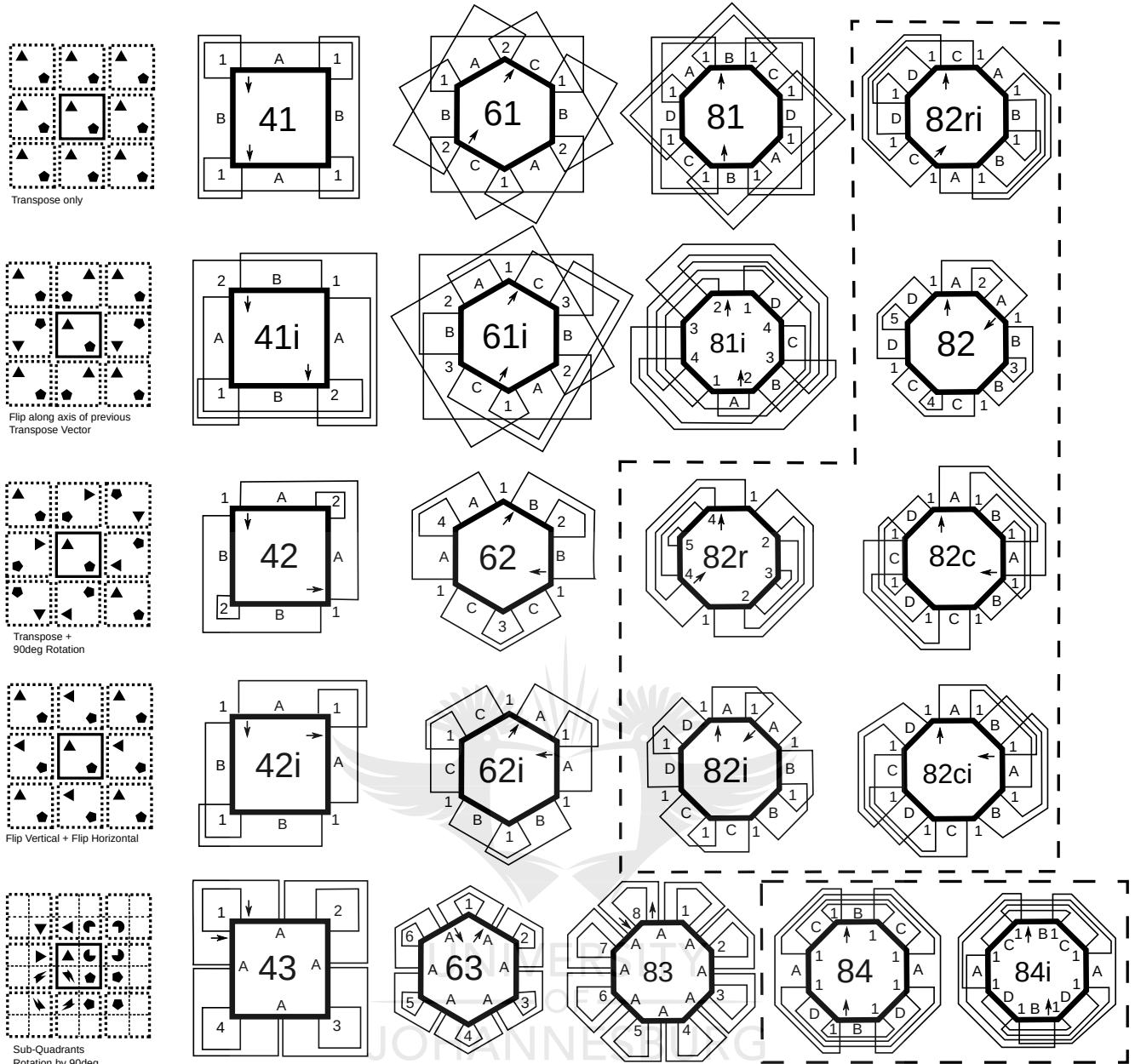


Figure 66: Types of continuous boundary connectivity

A basic taxonomy is given by a two letter code with a modifier, according to: [number of geometrical sides][number of unique border nodes][modifier of either {"i" for inverse flipping of border connections}{"r" for rotational connections}]. These are mentioned in passing, *the field is assumed to be connected according to the "41" method*. Further investigation is required in order to characterize the behaviour of other types.

### 8.6.1 Path Length Sensitivity Profiles

The effects of node positions on the sensitivity profile are profound, both in the context of other work in EIT and by inspection. In order to get an understanding of the sensitivity effects a first-order approximation was made with regard to the element sensitivities based on path length. The diagram in Figure 67 serves to illustrate the effects of the continuous connectivity at the boundaries and as visualization of the first-order effects of the node locations on the element sensitivities.



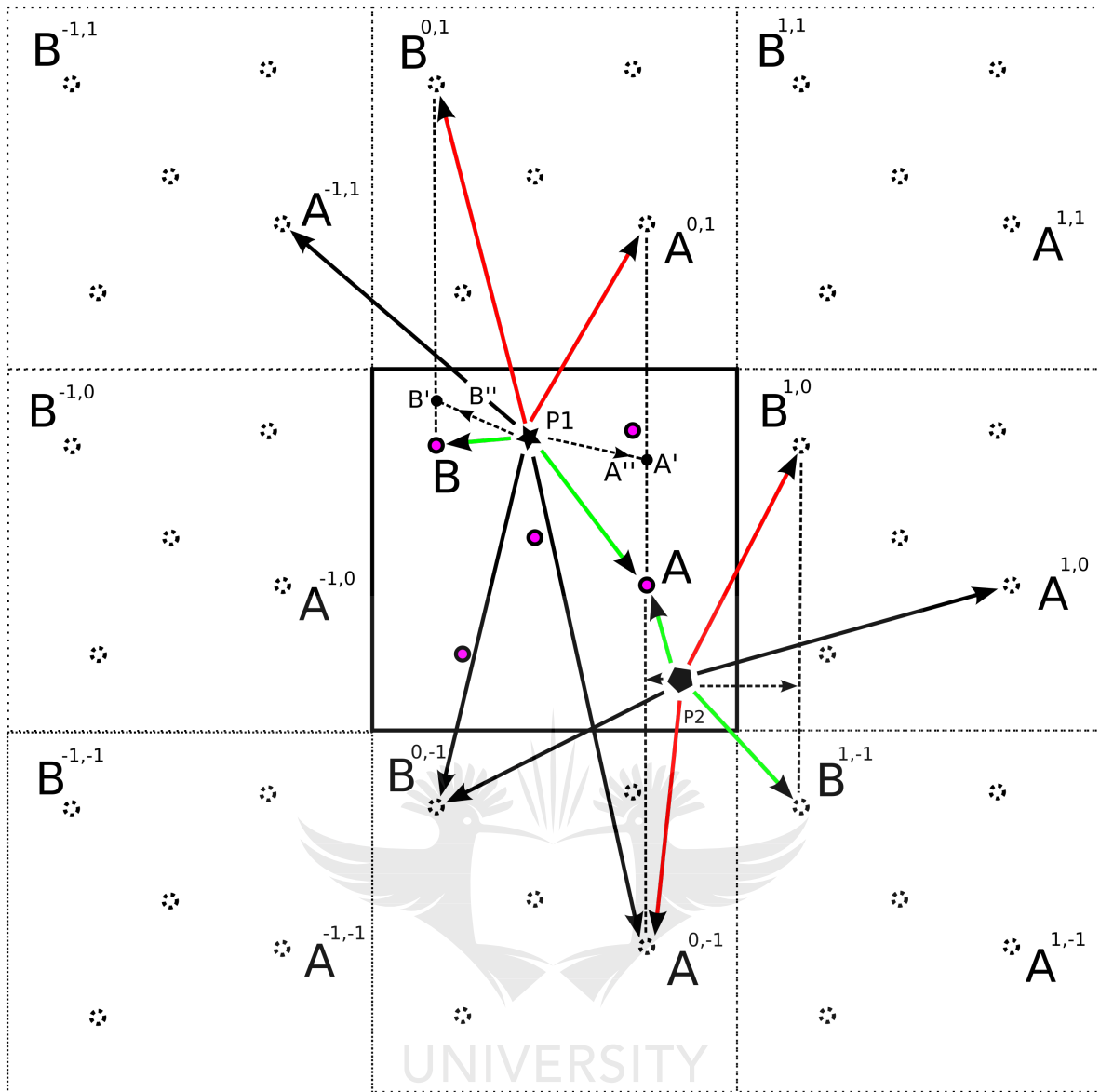


Figure 67: Virtual image principle demonstrating first order sensitivity analysis

The figure is thus described:

1. The figure shows two prospective points on the field, P1 and P2, which are being excited by a current passing through the F-nodes A and B, which have indexing superscripts to indicate when they exist on a virtual image of the field.
2. The black lines indicate influence that would not occur, since the voltage field is determined by the closest F-nodes, these lines indicate flows of potential that would not occur.
3. The green vectors indicate the shortest path over the field to the F-nodes A and B, for P2 this path to B one of the virtual images of the F-node.
4. The red lines indicate the parallel path to the virtual node, since the node can be viewed either directly on the field or through the continuously defined border (much like how there are two directions to the opposite side of a sphere when sitting on its' surface).
5. Since there is current contributed by the effects represented by both the green and red vectors, the net effect of the parallel combination is somewhere in-between, as represented

by A' and B' for P1. The ratio of the distances B-B' and B'-B<sup>01</sup> is proportional to some function of the ratio between the some functions of the length of vectors P1-B and P1-B<sup>01</sup>.

This shows that the parallel combinations created by the continuous boundaries have a significant effect on smoothing the effect of electrical potential on the field. *The representation here is a foundation of a sensitivity analysis for every hidden node in the field, in which every combination of two active F-nodes is considered:*

1. The path lengths from a hidden node to the two closest virtual images of the active node are mapped. The path lengths were found according to the connectivity profile of the field, three such connectivity profiles were separately used, being the 3-space, 4-space and 6-space configurations.
2. Applied a parallel weighting method to the two paths to a virtual node based on the equivalent resistance for two resistors in parallel, with the resistance being the length of the path.  $\frac{1}{R^T} = \frac{1}{R^1} + \frac{1}{R^2}$  .
3. Summed the parallel-weighted paths in order to get a measure of the total electrical path length (and thus sensitivity).
4. Statistically aggregated the resistance-sensitivity image formed by the above process for all elements in the field, for all combinations of the F-nodes.

#### *Sensitivity Profiles Visualised*

The method described above produced the plots in Figure 68, Figure 69, and Figure 70, which show the path distance for all types of field connectivity. Unit of measure is the distance over the field in terms of elements traversed, which in this case of pixels.

The plot in Figure 70 uses a euclidean distance calculation which is applicable to a field based on a continuous medium, rather than the discrete distances used in the other plots. It should be considered that the size of the elements in a discrete system are finite, while the elements in a continuous system are infinitesimal and thus subject to a normalization based on the scale of their representation. The euclidean distance plots are thus only comparable to their own counterparts.

PARAMETERS :  
 DISTANCE METRIC : MANHATTAN  
 FIELD SHAPE (x,y) : (200, 200)  
 MAXIMUM :  
 CONSISTENCY : 0.871659371069  
 LOWER VALUE : 149.993333333  
 UPPER VALUE : 172.077922078  
 MEAN :  
 CONSISTENCY : 0.90896735724  
 LOWER VALUE : 112.12082774  
 UPPER VALUE : 123.349674603  
 MINIMUM :  
 CONSISTENCY : 0.615172851563  
 LOWER VALUE : 49.995  
 UPPER VALUE : 81.2698412698  
 VARIANCE :  
 CONSISTENCY : 0.350353733675  
 LOWER VALUE : 418.447335666  
 UPPER VALUE : 1194.3567185

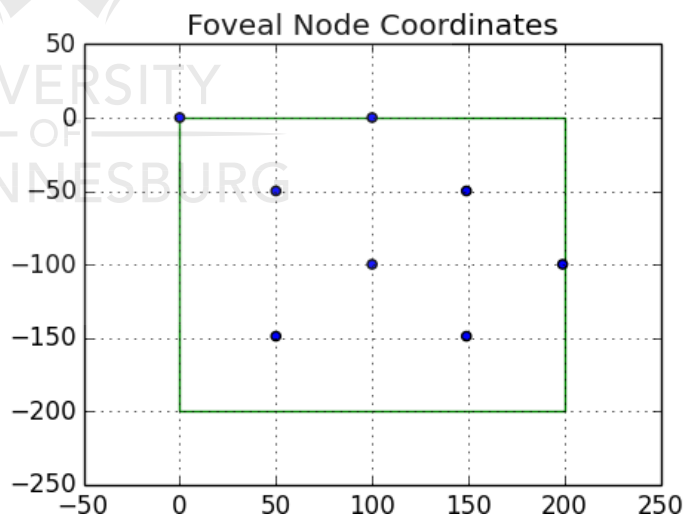
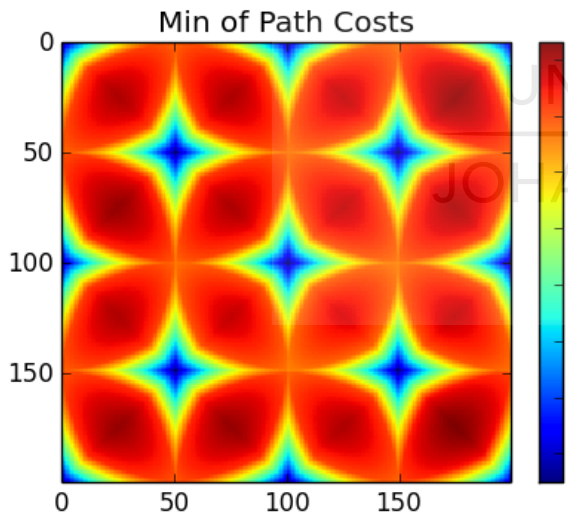
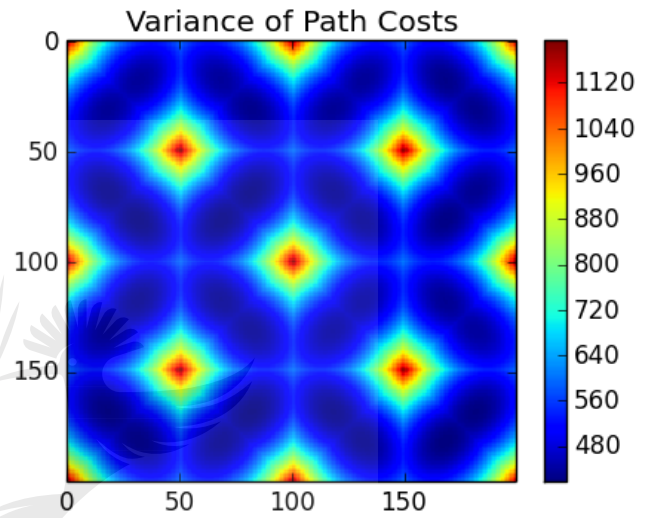
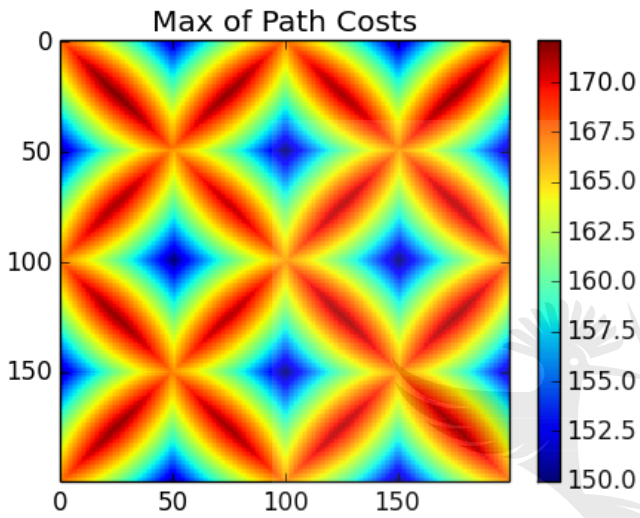
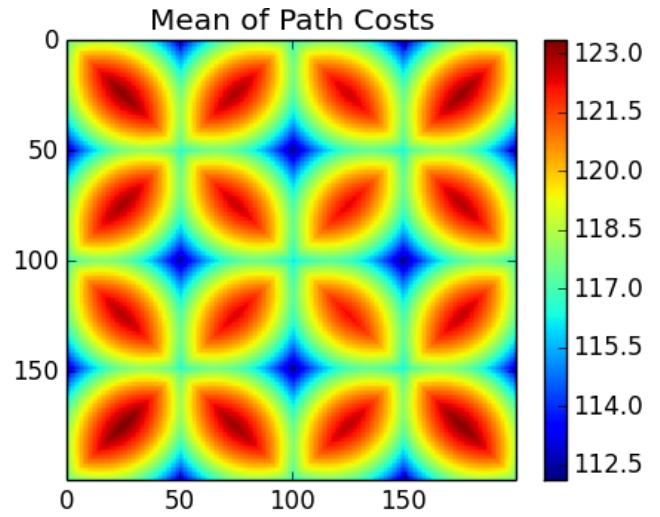


Figure 68: Manhattan connectivity path sensitivity analysis for F-node pattern A

PARAMETERS :  
 DISTANCE METRIC : BRIDGED\_MANHATTAN  
 FIELD SHAPE (x,y) : (200, 200)  
 MAXIMUM :  
 CONSISTENCY : 0.9375  
 LOWER VALUE : 93.75  
 UPPER VALUE : 100.0  
 MEAN :  
 CONSISTENCY : 0.854477239333  
 LOWER VALUE : 74.8725  
 UPPER VALUE : 87.62375  
 MINIMUM :  
 CONSISTENCY : 0.493266666667  
 LOWER VALUE : 36.995  
 UPPER VALUE : 75.0  
 VARIANCE :  
 CONSISTENCY : 0.16330901021  
 LOWER VALUE : 65.6313046875  
 UPPER VALUE : 401.88416183

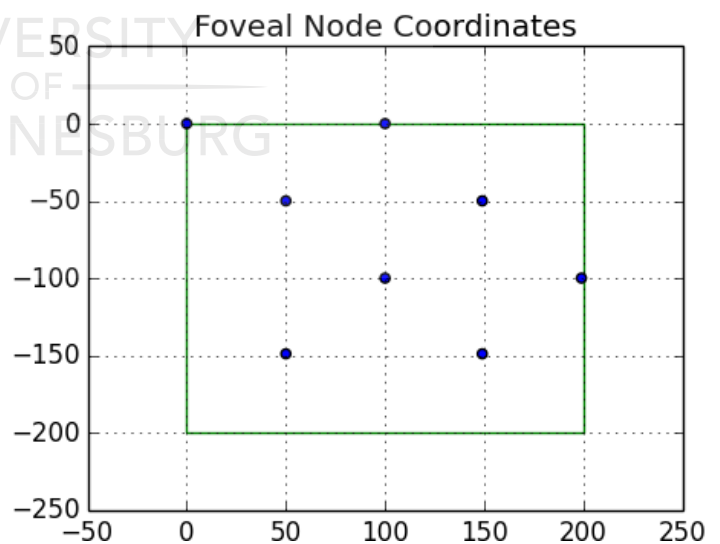
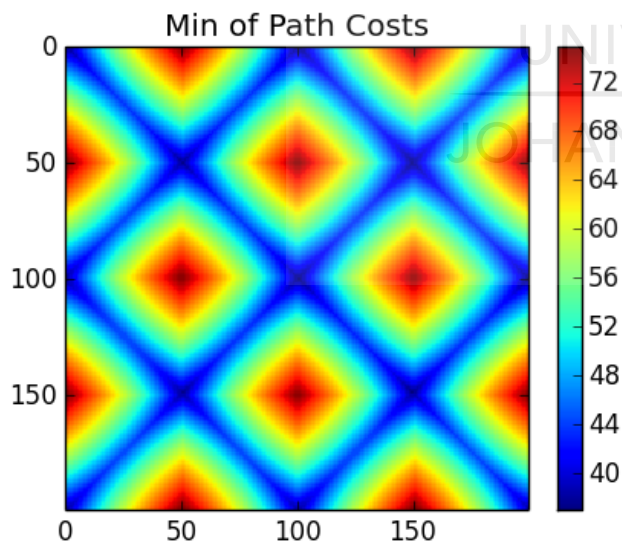
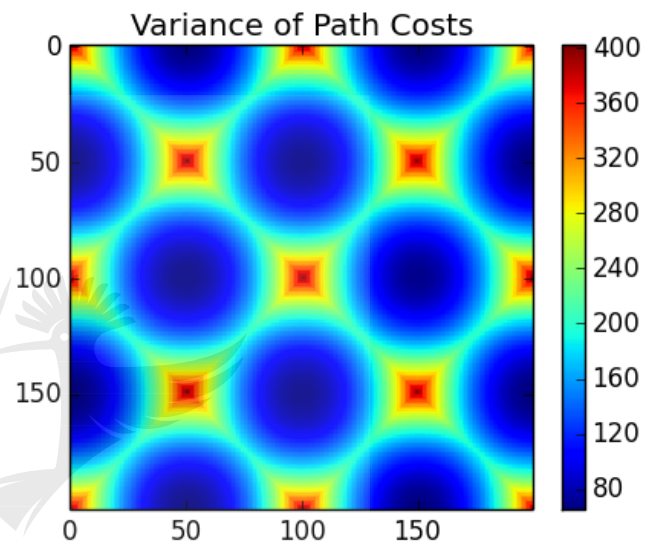
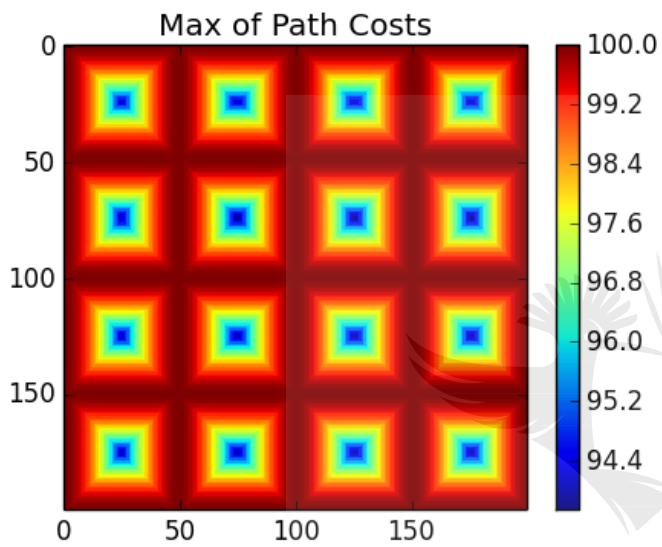
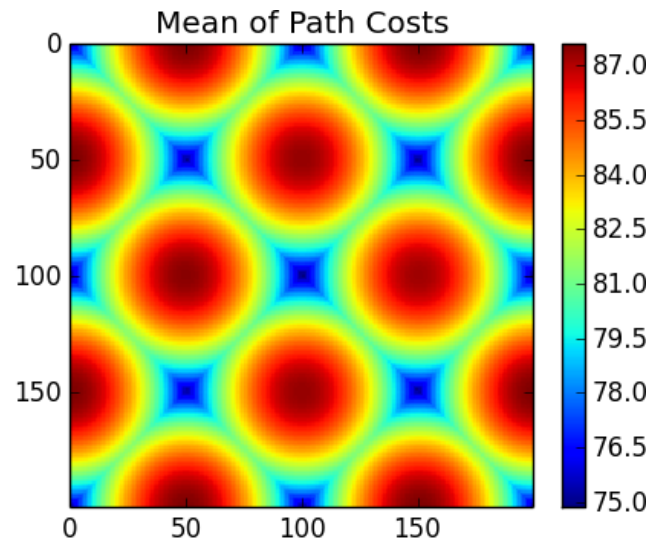


Figure 69: Bridged-Manhattan connectivity layout for F-node pattern A

PARAMETERS :  
 DISTANCE METRIC : EUCLIDEAN  
 FIELD SHAPE (x,y) : (200, 200)  
 MAXIMUM :  
 CONSISTENCY : 0.907444136543  
 LOWER VALUE : 111.79713811  
 UPPER VALUE : 123.200022578  
 MEAN :  
 CONSISTENCY : 0.96504723119  
 LOWER VALUE : 91.1979479053  
 UPPER VALUE : 94.5010202173  
 MINIMUM :  
 CONSISTENCY : 0.643093037484  
 LOWER VALUE : 48.2394795513  
 UPPER VALUE : 75.0116650929  
 VARIANCE :  
 CONSISTENCY : 0.238727881365  
 LOWER VALUE : 143.138296602  
 UPPER VALUE : 599.587680261

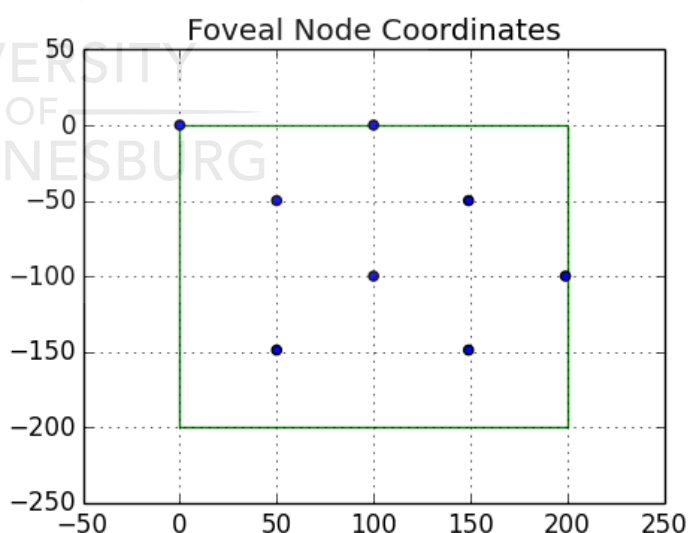
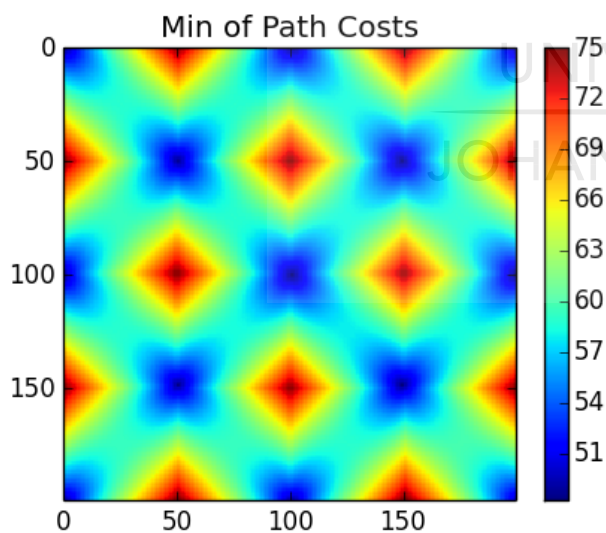
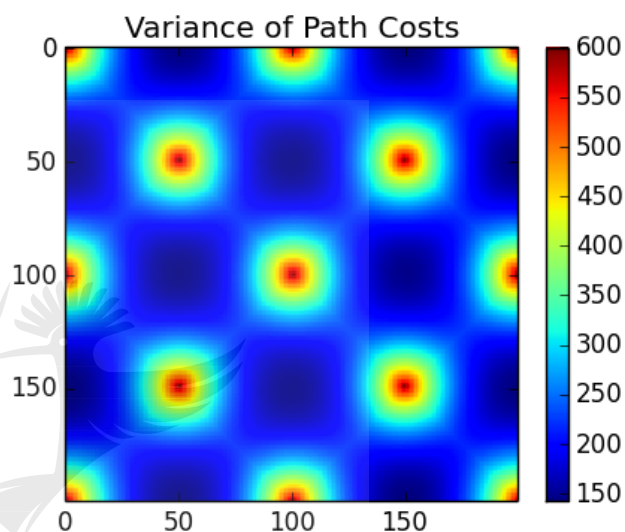
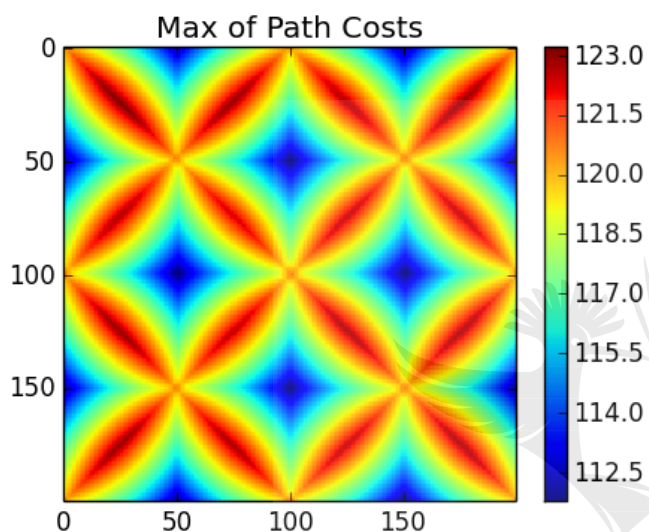
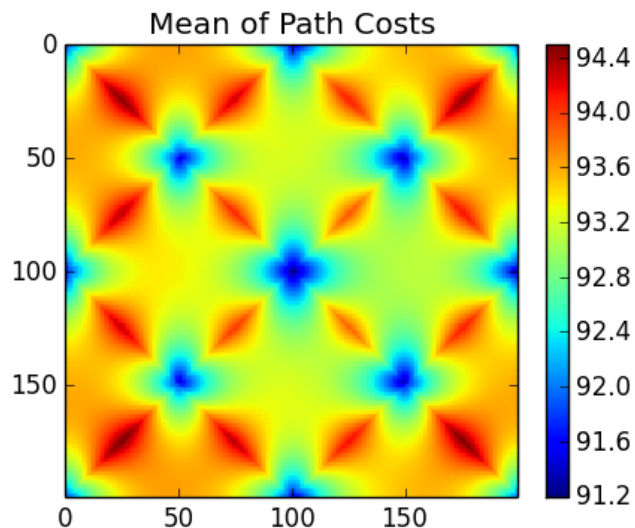


Figure 70: Euclidean connectivity sensitivity analysis for F-node pattern A



## 8.7 Proposed Methods of Reconstruction

This section contains a few methods of reconstruction that were theorized and are unique in comparison to traditional EIT since they can exploit structure inherent in the node placement. *They are candidate methods that have not been implemented as yet.*

### 8.7.1 Inverse by linearity of response

This method focusses of the interpretation of the model as a connectivity state. The processes implementing the transform have been shown to be non-linear with regard to a particular combinatorial state, however there is a possibility that the non-linearities of each combinatorial state will counter each other and produce an approximate linear response when averaged together. This statement is likely extremely difficult to prove, an empirical investigation should suffice.

Consider the response of a particular combinatorial state to a configuration of element conductivities. A dictionary of responses is produced that are the result of the mappings of each of the connectivity state functions to a set of inputs. The set of inputs is desired to span the input space, that is the set of input vectors of element conductivities is desired to be a basis for the input space.

The basis functions used to describe the inputs are spatial, there is nothing preventing the use of any particular wavelet basis for the element conductivity space (although this requires empirical investigation), a partial list of candidates for a spatial basis are:

1. Walsh-Hadamard
2. Fourier / Hartley
3. Noiselets
4. Discrete Cosine Transform
5. Vectors defined by an application of Principle Component Analysis (PCA) on a database of expected images

Once a dictionary of responses of outputs for inputs of the spatial basis is obtained, construction is possible of a fitting scheme that will regularize the inverse, the system in the form  $A\bar{x}=\bar{b}$  is described:

$$\begin{bmatrix} \begin{bmatrix} B_1 \\ C_1 \end{bmatrix} \begin{bmatrix} B_2 \\ C_1 \end{bmatrix} \begin{bmatrix} B_3 \\ C_1 \end{bmatrix} \begin{bmatrix} B_4 \\ C_1 \end{bmatrix} \begin{bmatrix} B_5 \\ C_1 \end{bmatrix} \\ \begin{bmatrix} B_1 \\ C_2 \end{bmatrix} \begin{bmatrix} B_2 \\ C_2 \end{bmatrix} \begin{bmatrix} B_3 \\ C_2 \end{bmatrix} \begin{bmatrix} B_4 \\ C_2 \end{bmatrix} \begin{bmatrix} B_5 \\ C_2 \end{bmatrix} \\ \begin{bmatrix} B_1 \\ C_3 \end{bmatrix} \begin{bmatrix} B_2 \\ C_3 \end{bmatrix} \begin{bmatrix} B_3 \\ C_3 \end{bmatrix} \begin{bmatrix} B_4 \\ C_3 \end{bmatrix} \begin{bmatrix} B_5 \\ C_3 \end{bmatrix} \\ \vdots \end{bmatrix} \cdots \begin{bmatrix} BC_1 \\ BC_2 \\ BC_3 \\ BC_4 \\ BC_5 \\ \vdots \end{bmatrix} = \begin{bmatrix} MC_1 \\ MC_2 \\ MC_3 \\ MC_4 \\ MC_5 \\ \vdots \end{bmatrix} \quad (96)$$



where  $\begin{bmatrix} B_i \\ C_j \end{bmatrix}$  is the output response associated with basis function  $i$  and combinatorial state  $j$ , the vector of terms  $BC_i$  is the vector of coefficients of the spatial basis functions for the state of the device and the vector in the place of  $\bar{b}$  in the form is a concatenation of the responses measured in the test state for the device.

#### *Least-Squares regularization*

In order to find the coefficients of the spatial basis functions the problem can be inverted using a pseudoinverse (L2 -norm based):

$$A\bar{x}=\bar{b}$$

$$\bar{x}\approx[A^T A]^{-1} A^T \cdot \bar{b} \quad (97)$$

This process guarantees a solution to the system of equations, since it effects a nearest projection of the solution onto the hyperplane that defines feasible solutions. The guarantee covers the finding of a solution only, whether this solution is suitable is another matter. The hyperplane of feasible solutions regularizes the vector  $\bar{x}$  to have the lowest possible energy, and thus the lowest degree of internal variance.

The compressive sensing theory has shown the L2 reconstruction to be very poor for vectors  $\bar{x}$  that are sparse or nearly sparse. This observation is pertinent since when using a spatial basis, since real images are most often sparse. In the case of noiselets however, this method would be appropriate.

#### *L1 regularization*

A method of inverting the problem  $A\bar{x}=\bar{b}$  is desired that is robust and allows determination of the sparsest or closest sparse vector  $\bar{x}$  that satisfies. The framework of compressive sensing (via its' sparse modelling approach) does just this, there are now a host of algorithms that are able to deal with noise and sub rank matrices. The core of all these methods is the minimization of the L1 norm of the error;

$$\sum_{k=0}^n |y_k - x_k|^1 \quad (98)$$

This approach is the desired method of reconstruction given that our  $\bar{x}$  is indeed expected to be sparse.

### **8.8 The Linear Pinhole Model**

A camera model requires a set of intrinsic parameters, with regard to the nature of the camera structure and optics. In addition to this are extrinsic parameters, with regard to the camera position in the environment [82]. The model linearly maps the points in the world to points on the image plane  $(I, J)$  [82]:

$$\begin{bmatrix} c_{11} & c_{12} & c_{13} & c_{14} \\ c_{21} & c_{22} & c_{23} & c_{24} \\ c_{31} & c_{32} & c_{33} & c_{34} \end{bmatrix} \begin{bmatrix} x \\ y \\ z \\ 1 \end{bmatrix} = \begin{bmatrix} i \\ j \\ t \end{bmatrix} \text{ where } I = i/t, J = j/t \quad (99)$$

The matrix  $c$  is a compound transformation of the intrinsic and extrinsic parameters:

$$c = \begin{bmatrix} \frac{f}{s_i} & 0 & i_c & 0 \\ 0 & \frac{f}{s_j} & j_c & 0 \\ 0 & 0 & 1 & 0 \end{bmatrix} \begin{bmatrix} R_{11} & R_{12} & R_{13} & T_x \\ R_{21} & R_{22} & R_{23} & T_y \\ R_{31} & R_{32} & R_{33} & T_z \\ 0 & 0 & 0 & 1 \end{bmatrix} \quad (100)$$

where  $f$  is the focal length,  $(i_c, j_c)$  the centre of the image,  $R_i$  a component of the rotation,  $T_i$  a component of the translation, and  $s_i, s_j$  the sensor resolution in the image plane.

By expansion and recognition that the focal point of the camera is at the intersection of three planes, all which pass through the focal point: a plane parallel to the image plane, a plane passing through all points where, and another for all points. This results in equations for the focal point, given a  $c$  matrix [82]:

$$\begin{aligned} x &= \frac{(c_{33}c_{12} - c_{32}c_{13})(c_{33}c_{24} - c_{34}c_{23}) - (c_{33}c_{22} - c_{32}c_{23})(c_{33}c_{14} - c_{34}c_{13})}{(c_{33}c_{22} - c_{32}c_{23})(c_{33}c_{11} - c_{11}c_{13}) - (c_{33}c_{12} - c_{32}c_{13})(c_{33}c_{21} - c_{31}c_{23})} \\ y &= \frac{(c_{31}c_{13} - c_{11}c_{33})(c_{31}c_{24} - c_{21}c_{34}) - (c_{31}c_{23} - c_{21}c_{33})(c_{31}c_{14} - c_{11}c_{34})}{(c_{31}c_{23} - c_{21}c_{33})(c_{31}c_{12} - c_{11}c_{32}) - (c_{31}c_{13} - c_{11}c_{33})(c_{31}c_{22} - c_{21}c_{32})} \\ z &= \frac{(c_{31}c_{22} - c_{21}c_{32})(c_{31}c_{14} - c_{11}c_{34}) - (c_{31}c_{12} - c_{11}c_{32})(c_{31}c_{24} - c_{21}c_{34})}{(c_{31}c_{12} - c_{11}c_{32})(c_{31}c_{23} - c_{21}c_{33}) - (c_{31}c_{22} - c_{21}c_{32})(c_{31}c_{13} - c_{11}c_{33})} \end{aligned} \quad (101)$$

The orientation of the camera can be found from applying the plane equations where  $i=0$  and. The focal length to sensor resolution ratios can be found by the following procedure [82]:

$$\begin{aligned} v_1 &= \sqrt{c_{11}^2 + c_{12}^2 + c_{13}^2} & \theta_1 &= \frac{\pi}{2} - 2 \sin^{-1} \left[ \frac{1}{2} \sqrt{\left(\frac{c_{31}}{v_3} - \frac{c_{11}}{v_1}\right)^2 + \left(\frac{c_{32}}{v_3} - \frac{c_{12}}{v_1}\right)^2 + \left(\frac{c_{33}}{v_3} - \frac{c_{13}}{v_1}\right)^2} \right] & \frac{s_i}{f} &= \tan \frac{\theta_1}{i_c} \\ v_2 &= \sqrt{c_{21}^2 + c_{22}^2 + c_{23}^2} & \theta_2 &= \frac{\pi}{2} - 2 \sin^{-1} \left[ \frac{1}{2} \sqrt{\left(\frac{c_{31}}{v_3} - \frac{c_{21}}{v_2}\right)^2 + \left(\frac{c_{32}}{v_3} - \frac{c_{22}}{v_2}\right)^2 + \left(\frac{c_{33}}{v_3} - \frac{c_{23}}{v_2}\right)^2} \right] & \frac{s_j}{f} &= \tan \frac{\theta_2}{j_c} \\ v_3 &= \sqrt{c_{31}^2 + c_{32}^2 + c_{33}^2} \end{aligned} \quad (102)$$

The model may be used to inverse map a point on the image plane to a vector that directs toward the point in 3D space, this map is done by an inverse perspective transformation [82]:

$$\begin{bmatrix} p_{11} & p_{12} & p_{13} \\ p_{21} & p_{22} & p_{23} \\ p_{31} & p_{32} & p_{33} \end{bmatrix} \begin{bmatrix} i \\ j \\ 1 \end{bmatrix} = \begin{bmatrix} x_v \\ y_v \\ z_v \\ w \end{bmatrix} \text{ where } p = \begin{bmatrix} R_{11} & R_{12} & R_{13} & T_x \\ R_{21} & R_{22} & R_{23} & T_y \\ R_{31} & R_{32} & R_{33} & T_z \\ 0 & 0 & 0 & 1 \end{bmatrix} \begin{bmatrix} s_i & 0 & -i_c s_i \\ 0 & -s_j & j_c s_j \\ 0 & 0 & f \\ 0 & 0 & 0 \end{bmatrix} \quad (103)$$

The calibration of a camera according to the model requires at least six points with known relative location in 3D space. The procedure is to use the point to image transform, manipulating to get a system of equations for each point [82]:

$$\begin{aligned} c_{11}x+c_{12}y+c_{13}z+c_{14}-I c_{31}x-I c_{32}y-I c_{33}z &= I \\ c_{21}x+c_{22}y+c_{23}z+c_{24}-J c_{31}x-J c_{32}y-J c_{33}z &= J \end{aligned} \quad (104)$$

where the parameter  $c_{34}$  only affects the scaling of the transform matrix, which does not matter in the transformation itself, and has been set to 1 for convenience. By building a system of equations for six points in known 3D space, all 11 unknowns can be solved using a least-squares matrix inverse on the  $I, J$  coordinates in the image plane.



## Bibliography

- [1] A. Dresch, D. P. Lacerda, and J. A. V. Antunes Jr, *Design Science Research - A Method for Science and Technology Advancement*. London: Springer, 2015.
- [2] A. M. Novikov and D. A. Novikov, "Means and Methods of Scientific Research," in *Research Methodology*, J. Y.-L. Forrest, Ed. 2013.
- [3] R. Leutz and A. Suzuki, *Nonimaging Fresnel Lenses - Design and Performance of Solar Concentrators*. Berlin: Springer-Verlag, 2001.
- [4] R. Foster, M. Ghassemi, and A. Cota, "Solar Thermal Systems and Applications," in *Solar Energy - Renewable Energy and the Environment*, Boca Raton: CRC Press, 2010.
- [5] I. Dincer and T. Abdul Hussain Ratlamwala, "Exergy analysis of solar energy systems," in *Solar Energy Sciences and Engineering Applications*, Boca Raton: CRC Press, 2013.
- [6] R. Petela, "Exergy analysis of solar radiation processes," in *Solar Energy Sciences and Engineering Applications*, Boca Raton: CRC Press, 2013.
- [7] A. Fong and J. Tippet, "Technology basics," in *Project Development in the Solar Industry*, Boca Raton: CRC Press, 2013.
- [8] T. Hirsch *et al.*, "Advancements in the Field of Direct Steam Generation in Linear Solar Concentrators — A Review," *Heat Transf. Eng.*, vol. 35, no. 2014, pp. 258–271, 2014.
- [9] J. Chaves, "Étendue and the Winston-Welford Design Method," in *Introduction to NonImaging Optics*, Boca Raton: CRC Press, 2008, pp. 55–116.
- [10] J. Chaves, "The Miñano Design Method Using Poisson Brackets," in *Introduction to NonImaging Optics*, Boca Raton: CRC Press, 2008.
- [11] J. Chaves, "Stepped Flow-Line Nonimaging Optics," in *Introduction to NonImaging Optics*, Boca Raton: CRC Press, 2008.
- [12] J. Chaves, "Design of Two-Dimensional Concentrators," in *Introduction to NonImaging Optics*, Boca Raton: CRC Press, 2008.
- [13] D. Chemisana and T. K. Mallick, "Building integrated concentrating solar systems," in *Solar Energy Sciences and Engineering Applications*, Boca Raton: CRC Press, 2013.
- [14] G. Manzolini and P. Silva, "Solar energy conversion with thermal cycles," in *Solar Energy Sciences and Engineering Applications*, Boca Raton: CRC Press, 2013.
- [15] A. Nemet, Z. Kravanja, and J. J. Klemes, "Integration of solar thermal energy into processes with heat demand," *Clean Techn. Env. Policy*, vol. 14, pp. 453–463, 2012.
- [16] S. Licht, "The solar thermal electrochemical production of energetic molecules: Step," in *Solar Energy Sciences and Engineering Applications*, Boca Raton: CRC Press, 2013.
- [17] E. R. Bandala and B. W. Raichle, "Solar driven advanced oxidation processes for water decontamination and disinfection," in *Solar Energy Sciences and Engineering Applications*, Boca Raton: CRC Press, 2013.
- [18] Z. Wang and G. F. Naterer, "Solar hydrogen production and CO<sub>2</sub> recycling," in *Solar Energy Sciences and Engineering Applications*, Boca Raton: CRC Press, 2013.
- [19] Q. Liao, C. Guo, R. Chen, X. Zhu, and Y. Wang, "Photobiohydrogen production and high-performance photobioreactor," in *Solar Energy Sciences and Engineering Applications*, Boca Raton: CRC Press, 2013.

- [20] S. Malato, I. Oller, P. Fernández-ibáñez, and M. Ignacio Maldonado, "Decontamination of water by combined solar advanced oxidation processes and biotreatment," in *Solar Energy Sciences and Engineering Applications*, Boca Raton: CRC Press, 2013.
- [21] N. Enteria, "Solar-desiccant air-conditioning systems," in *Solar Energy Sciences and Engineering Applications*, vol. 2030, Boca Raton: CRC Press, 2013.
- [22] K. Fong, "Solar hybrid air-conditioning design for buildings in hot and humid climates," in *Solar Energy Sciences and Engineering Applications*, Boca Raton: CRC Press, 2013.
- [23] B. Norton, "Solar energy collection and storage," in *Solar Energy Sciences and Engineering Applications*, Boca Raton: CRC Press, 2013.
- [24] R. Costa-Castello, J. D. Álvarez, M. Berenguel, and L. J. Yebra, "A repetitive control scheme for distributed solar collector field," *Int. J. Control*, vol. 83, no. No 5, May 2010, pp. 970–982, 2010.
- [25] J. M. Lemos, "Adaptive control of distributed collector solar fields," *Int. J. Syst. Sci.*, vol. 37, no. NO. 8, June 2006, pp. 523–533, 2006.
- [26] B. A. Costa, J. M. Lemos, and L. G. Rosa, "Temperature control of a solar furnace for material testing," *Int. J. Syst. Sci. Tempera*, vol. 42, no. No. 8, August 2011, pp. 1253–1264, 2011.
- [27] K. Wang, Y. He, and Z. Cheng, "A design method and numerical study for a new type parabolic trough solar collector with uniform solar flux distribution," *Sci. China Technol. Sci.*, vol. 57, no. 3, pp. 531–540, 2014.
- [28] N. R. E. Laboratory, "Thermal Systems Group: CSP Capabilities - Collector / Receiver Characterization," 2010.
- [29] M. Pfänder, M. Röger, and P. Heller, "Solar blind pyrometric temperature measurement on pressurized volumetric power tower receivers," *Quant. Infrared Thermogr. J.*, vol. 3, no. No 1, 2006, pp. 5–24, 2012.
- [30] B. Prior, "Market study: Current state of the US solar market," in *Project Development in the Solar Industry*, Boca Raton: CRC Press, 2013.
- [31] A. Tovar, "Development: Design considerations of photovoltaic systems," in *Project Development in the Solar Industry*, Boca Raton: CRC Press, 2013.
- [32] R. Foster, M. Ghassemi, and A. Cota, "Photovoltaic System Sizing and Design," in *Solar Energy - Renewable Energy and the Environment*, Boca Raton: CRC Press, 2010.
- [33] R. Foster, M. Ghassemi, and A. Cota, "Photovoltaic Conversion Systems," in *Solar Energy - Renewable Energy and the Environment*, Boca Raton: CRC Press, 2010.
- [34] L. Schnatbaum, "Solar thermal power plants," *Eur. Phys. J. Spec. Top.*, vol. 176, no. 1, pp. 127–140, 2009.
- [35] R. Foster, M. Ghassemi, and A. Cota, "Solar Resource," in *Solar Energy - Renewable Energy and the Environment*, no. 2004, Boca Raton: CRC Press, 2010.
- [36] A. Genç, İ. Kinacı, G. Oturanç, A. Kurnaz, S. Bilir, and N. Ozbalta, "Statistical Analysis of Solar Radiation Data Using Cubic Spline Functions," *Energy Sources*, vol. 24, no. January 2014, pp. 1131–1138, 2002.
- [37] D. R. Myers, "Modeling Clear Sky Solar Radiation," in *Solar Radiation - Practical Modelling for Renewable Energy Applications*, A. Ghassemi, Ed. Boca Raton: CRC Press, 2013.
- [38] I. Niknia, M. Yaghoubi, and R. Hessami, "A novel experimental method to find dust deposition effect on the performance of parabolic trough solar collectors," *Int. J. Environ. Stud.*, vol. 69, no. January 2014, pp. 233–252, 2012.

- [39] N. R. E. Laboratory, "Thermal Systems Group: CSP Capabilities - Advanced Reflector and Absorber Materials," 2010.
- [40] L. Qibin, W. Yalong, G. Zhichao, S. Jun, J. Hongguang, and L. Heping, "Experimental investigation on a parabolic trough solar collector for thermal power generation," *Sci China Tech Sci*, vol. No. 1, no. January, pp. 52–56, 2010.
- [41] E. Dikmen, M. Ayaz, H. H. Ezen, E. U. Kucuksille, and A. S. Sahin, "Estimation and optimization of thermal performance of evacuated tube solar collector system," *Heat Mass Transf.*, no. December, 2013.
- [42] H. U. Peng, Z. Qian, L. I. U. Yang, S. Chunchen, C. Xiaofang, and C. Zeshao, "Optical analysis of a hybrid solar concentrating Photovoltaic / Thermal ( CPV / T ) system with beam splitting technique," *Sci China Tech Sci*, vol. 56, no. 6, pp. 1387–1394, 2013.
- [43] V. H. Benitez, J. Pacheco-ramirez, and N. Pitalua-diaz, "Developing a Mini-heliostat Array for a Solar Central Tower Plant: A Practical Experience," *Intell. Autom. Soft Comput.*, pp. 37–41, 2013.
- [44] P. Gevorkian, "Solar Thermal Power," in *Large-Scale Solar Power System Design: An Engineering Guide for Grid-Connected Solar Power Generation*, McGraw-Hill Professional, 2011.
- [45] P. Gevorkian, "Solar Power System Technologies," in *Large-Scale Solar Power System Design: An Engineering Guide for Grid-Connected Solar Power Generation*, McGraw-Hill Professional, 2011.
- [46] S. Kalogirou, "Thermal modelling of parabolic trough collectors," in *Solar Energy Sciences and Engineering Applications*, Boca Raton: CRC Press, 2013.
- [47] R. Battisti, H. Schweiger, W. Weiss, and J. H. Morehouse, "Solar Thermal Energy Conversion," in *Handbook of Energy Efficiency and Renewable Energy*, 2007.
- [48] M. Romero-alvarez and E. Zarza, "Concentrating Solar Thermal Power," in *Energy Conversion*, Boca Raton, 2007.
- [49] S. Shanmugam, M. Eswaramoorthy, and A. R. Veerappan, "Mathematical Modeling of Thermoelectric Generator Driven by Solar Parabolic Dish Collector," *Appl. Sol. Energy*, vol. 47, no. 1, pp. 31–35, 2011.
- [50] C. Wu, "Vapor Cycles," in *Thermodynamic Cycles - Computer-Aided Design and Optimization*, 2004.
- [51] E. Logan, "Steam Power Plants," in *Thermodynamics*, Boca Raton: Taylor & Francis, 1999.
- [52] C. Wu, "Gas Open-System Cycles," in *Thermodynamic Cycles - Computer-Aided Design and Optimization*, Boca Raton: Taylor & Francis, 2004.
- [53] L. . Faulkner, "Gas Turbine Power Plants," in *Thermodynamics*, Boca Raton: Marcel Dekker, 1999.
- [54] C. Wu, "Gas Closed-System Cycles," in *Thermodynamic Cycles - Computer-Aided Design and Optimization*, Boca Raton: Marcel Dekker, 2004, pp. 3–4.
- [55] S. R. Kalbande, S. Kothari, R. G. Nadre, and A. N. Mathur, "Design Theory and Performance Analysis of Paraboloidal Solar Cooker," *Appl. Sol. Energy*, vol. 44, no. 2, pp. 103–112, 2008.
- [56] E. Bilgen, "Conduction and convection heat transfer in composite solar collector systems with porous absorber," *Warme- und Stoffiibertragung*, vol. 28, pp. 267–274, 1993.
- [57] A. Baghernejad and M. Yaghoubi, "Thermoeconomic Methodology for Analysis and Optimization of a Hybrid Solar Thermal Power Plant," *Int. J. Green Energy*, vol. 10, pp. 588–609, 2013.



- [58] J. Blanco, P. Palenzuela, D. Alarcon-Padilla, G. Zaragoza, and M. Ibarra, "Preliminary thermoeconomic analysis of combined parabolic trough solar power and desalination plant in port Safaga (Egypt)," *Desalin. Water Treat.*, vol. 51, pp. 1887–1899, 2013.
- [59] A. J. Kolios, S. Paganini, and S. Proia, "Development of thermodynamic cycles for concentrated solar power plants," *Int. J. Sustain. Energy*, no. January 2014, pp. 37–41, 2012.
- [60] N. Dushkina, "Propagation of Light," in *Handbook of Optical Metrology*, T. Yoshizawa, Ed. Boca Raton: CRC Press, 2009.
- [61] D. Malacara-Hernandez and Z. Malacara-Hernandez, "Geometrical Optics Principles," in *Handbook of Optical Design*, 3rd ed., Boca Raton: Taylor & Francis, 2013.
- [62] R. S. Sirohi, "Waves and Beams," in *Optical Methods of Measurement, Wholefield Techniques*, 2nd ed., vol. 0, Boca Raton: Taylor & Francis, 2009.
- [63] T. Yoshizawa, "Diffraction," in *Handbook of Optical Metrology*, T. Yoshizawa, Ed. Boca Raton: CRC Press, 2009.
- [64] R. S. Sirohi, "Diffraction," in *Optical Methods of Measurement, Wholefield Techniques*, 2009.
- [65] F. Vignola, J. Michalsky, and T. Stoffel, "Solar Resource Definitions and Terminology," in *Solar and Infrared Radiation Measurements*, Boca Raton: CRC Press, 2012.
- [66] F. Vignola, J. Michalsky, and T. Stoffel, "Appendix A: Modeling Solar Radiation," in *Solar and Infrared Radiation Measurements*, Boca Raton: CRC Press, 2012.
- [67] F. Vignola, J. Michalsky, and T. Stoffel, "Measuring Global Irradiance," in *Solar and Infrared Radiation Measurements*, Boca Raton: CRC Press, 2012.
- [68] F. Vignola, J. Michalsky, and T. Stoffel, "Net Radiation Measurements," in *Solar and Infrared Radiation Measurements*, Boca Raton: CRC Press, 2012, pp. 217–226.
- [69] F. Vignola, J. Michalsky, and T. Stoffel, "Diffuse Irradiance," in *Solar and Infrared Radiation Measurements*, no. 1942, Boca Raton: CRC Press, 2012, pp. 161–170.
- [70] F. Vignola, J. Michalsky, and T. Stoffel, "Direct Normal Irradiance," in *Solar and Infrared Radiation Measurements*, Boca Raton: CRC Press, 2012.
- [71] F. Vignola, J. Michalsky, and T. Stoffel, "Solar Spectral Measurements," in *Solar and Infrared Radiation Measurements*, Boca Raton: CRC Press, 2012, pp. 227–254.
- [72] F. Vignola, J. Michalsky, and T. Stoffel, "Historic Milestones in Solar and Infrared Radiation Measurement," in *Solar and Infrared Radiation Measurements*, Boca Raton: CRC Press, 2012, pp. 35–76.
- [73] D. R. Myers, "Introduction to Solar Radiation Measurements," in *Solar Radiation - Practical Modelling for Renewable Energy Applications*, A. Ghassemi, Ed. Boca Raton: CRC Press, 2013.
- [74] D. R. Myers, "Introduction to Modeling Spectral Distributions," in *Solar Radiation - Practical Modelling for Renewable Energy Applications*, A. Ghassemi, Ed. Boca Raton: CRC Press, 2013, pp. 103–119.
- [75] A. R. Jha, "Design Expressions and Critical Performance Parameters for Solar Cells," in *Solar Cell Technology and Applications*, pp. 39–69.
- [76] Y. Garini and E. Tauber, "Spectral Imaging: Methods, Design, and Applications," in *Biomedical Optical Imaging Technologies*, Boca Raton: Taylor & Francis, 2013, pp. 111–161.
- [77] P. R. Hall, "Lenses, Prisms, and Mirrors," in *Handbook of Optical Metrology*, T. Yoshizawa, Ed. Boca Raton: CRC Press, 2009.

- [78] C. Zhang and T. Chen, "A survey on image-based rendering—representation, sampling and compression," *Signal Process. Image Commun.*, vol. 19, no. 1, pp. 1–28, 2004.
- [79] J. Feng and H. G. Leighton, "Broadband solar radiances from visible band measurements: A method based on ScaRaB observations and model simulations," *Int. J. Remote Sens.*, vol. 26, no. 22, 20 November 2005, pp. 5125–5148, 2005.
- [80] J. Ye and J. Yu, "Ray geometry in non-pinhole cameras: a survey," *Vis Comput*, vol. 30, pp. 93–112, 2014.
- [81] Y. M. Song *et al.*, "Digital cameras with designs inspired by the arthropod eye," *Nature*, vol. 497, no. 7447, pp. 95–99, 2013.
- [82] K. M. Dawson-Howe and D. Vernon, "Simple Pinhole Camera Calibration," *Int. J. Imaging Syst. Technol.*, vol. 5, pp. 1–6, 1994.
- [83] G. Indebetouw and W. P. Shing, "Scanning Optical Reconstruction of Coded Aperture Images," vol. 76, pp. 69–76, 1982.
- [84] R. Raskar, "Less Is More: Coded Computational Photography," *ACCV*, vol. Part I, no. LNCS 4843, pp. 1–12, 2007.
- [85] O. Bimber, H. Qureshi, A. Grundh, M. Grosse, and D. Danch, "Adaptive Coded Aperture Photography," *ISVC*, vol. Part 1, no. LNCS 6938, pp. 54–65, 2011.
- [86] H. Nagahara, C. Zhou, T. Watanabe, H. Ishiguro, and S. K. Nayar, "Programmable Aperture Camera Using LCoS," *ECCV*, vol. Part 6, no. LNCS 6316, pp. 337–350, 2010.
- [87] C. Lee and S. Ogura, "Optical Thin Film and Coatings," in *Handbook of Optical Metrology*, T. Yoshizawa, Ed. Boca Raton: CRC Press, 2009.
- [88] F. Surface, "Film Surface and Thickness Profilometry," in *Handbook of Optical Metrology*, T. Yoshizawa, Ed. Boca Raton: CRC Press, 2009.
- [89] Y. Shuai, X. Xia, and H. Tan, "Numerical simulation and experiment research of radiation performance in a dish solar collector system," *Front. Energy Power Eng. China*, vol. 4, no. 4, pp. 488–495, 2010.
- [90] H. Kevin, "Optical Metrology Overview," in *Handbook of Optical Dimensional Metrology*, K. Harding, Ed. Boca Raton: CRC Press, 2013, pp. 3–36.
- [91] F. Chen, G. M. Brown, and M. Song, "Three-Dimensional Shape Measurement," in *Handbook of Optical Metrology*, T. Yoshizawa, Ed. Boca Raton: CRC Press, 2009.
- [92] E. Novak and B. Guenther, "Automation in Interferometry," in *Handbook of Optical Dimensional Metrology*, K. Harding, Ed. Boca Raton: CRC Press, 2013, pp. 369–394.
- [93] V. Badami and P. De Groot, "Displacement Measuring Interferometry," in *Handbook of Optical Dimensional Metrology*, K. Harding, Ed. Boca Raton: CRC Press, 2013, pp. 157–238.
- [94] D. A. Page, "Introduction," in *Handbook of Optical Metrology*, T. Yoshizawa, Ed. Boca Raton: CRC Press, 2009.
- [95] D. Brown and J. F. Laurie, "Portable Metrology," in *Handbook of Optical Dimensional Metrology*, K. Harding, Ed. Boca Raton: CRC Press, 2013, pp. 265–286.
- [96] Y. Zhang, Z. Xiong, P. Cong, and F. Wu, "Robust depth sensing with adaptive structured light illumination," *J. Vis. Commun. Image Represent.*, vol. 25, no. 4, pp. 649–658, 2014.
- [97] J. Salvi, S. Fernandez, T. Pribanic, and X. Llado, "A state of the art in structured light patterns for surface profilometry," *Pattern Recognit.*, vol. 43, no. 8, pp. 2666–2680, 2010.

- [98] W. Li, S. Fang, and S. Duan, "Optik 3D shape measurement based on structured light projection applying polynomial interpolation technique," *Opt. - Int. J. Light Electron Opt.*, vol. 124, no. 1, pp. 20–27, 2013.
- [99] S. Mrvoš, J. Salvi, and T. Pribanic, "Efficient multiple phase shift patterns for dense 3D acquisition in structured light scanning," *Image Vis. Comput.*, vol. 28, pp. 1255–1266, 2010.
- [100] S. Sandwith and S. Kyle, "Laser Tracking Systems," in *Handbook of Optical Dimensional Metrology*, K. Harding, Ed. Boca Raton: CRC Press, 2013.
- [101] G. Pedrini, "Holography," in *Handbook of Optical Metrology*, T. Yoshizawa, Ed. Boca Raton: CRC Press, 2009.
- [102] F. C. Krebs *et al.*, "A complete process for production of flexible large area polymer solar cells entirely using screen printing — First public demonstration," *Sol. Energy Mater. Sol. Cells*, vol. 93, pp. 422–441, 2009.
- [103] G. J. Saulnier, "EIT instrumentation," in *Electrical Impedance Tomography - Method, History and Applications*, D. S. Holder, Ed. Bristol: Institute of Physics Publishing, 2005.
- [104] W. Lionheart, N. Polydorides, and A. Borsic, "The reconstruction problem," in *Electrical Impedance Tomography - Method, History and Applications*, D. S. Holder, Ed. Bristol: Institute of Physics Publishing, 2005.
- [105] A. Adler, R. Gaburro, and W. Lionheart, "Electrical Impedance Tomography," *Handb. Math. Methods Imaging*, pp. 599–654, 2011.
- [106] O. Scherzer, *Handbook of Mathematical Methods in Imaging*. 2011.
- [107] O. Scherzer, *Handbook of Mathematical Methods in Imaging*. Boca Raton: CRC Press, 2011.
- [108] S. Nordebo *et al.*, "Fisher information analysis and preconditioning in electrical impedance tomography," *J. Phys. Conf. Ser.*, vol. 224, p. 12057, 2010.
- [109] T. K. Bera and J. Nagaraju, "Studying the Elemental Resistivity Profile of Electrical Impedance Tomography ( EIT ) Images," pp. 621–630, 2011.
- [110] B. Harrach and M. Ullrich, "Resolution Guarantees in Electrical Impedance Tomography," *IEEE Trans. Med. Imaging*, vol. 34, no. 7, pp. 1513–1521, 2015.
- [111] S. V. Gavrilov, "Numerical solution of the electrical impedance tomography problem with piecewise-constant conductivity and one measurement on the boundary," *Comput. Math. Model.*, vol. 24, no. 4, pp. 1–7, 2013.
- [112] S. Kim, E. J. Lee, E. J. Woo, and J. K. Seo, "Asymptotic analysis of the membrane structure to sensitivity of frequency-difference electrical impedance tomography," *Inverse Probl.*, vol. 28, no. 7, p. 75004, 2012.
- [113] A. Boyle, A. Adler, and W. R. B. Lionheart, "Shape Deformation in Two-Dimensional Electrical Impedance Tomography," *IEEE Trans. Med. Imaging*, vol. 31, no. 12, pp. 2185–2193, 2012.
- [114] B. Grychtol, W. R. B. Lionheart, M. Bodenstein, G. K. Wolf, and A. Adler, "Impact of model shape mismatch on reconstruction quality in electrical impedance tomography," *IEEE Trans. Med. Imaging*, vol. 31, no. 9, pp. 1754–1760, 2012.
- [115] M. Hintermüller, A. Laurain, and A. A. Novotny, *Second-order topological expansion for electrical impedance tomography*, vol. 36, no. 2. Springer, 2012.
- [116] B. Harrach and J. K. Seo, "Exact Shape-Reconstruction by One-Step Linearization in Electrical Impedance Tomography," *SIAM J. Math. Anal.*, vol. 42, no. 4, pp. 1505–1518, 2010.

- [117] B. Harrach, J. K. Seo, and E. J. Woo, "Factorization Method and Its Physical Justification in Frequency-Difference Electrical Impedance Tomography," *IEEE Trans. Med. Imaging*, vol. 29, no. 11, pp. 1918–1926, 2010.
- [118] A. Ave, "Error Study of EIT Inverse Problem Solution Using Neural Networks," *IEEE Int. Symp. Signal Process. Inf. Technol.*, vol. 7, pp. 894–899, 2007.
- [119] M. C. Costa, D. De Werra, and C. Picouleau, "Using graphs for some discrete tomography problems," *Discret. Appl. Math.*, vol. 154, no. 1, pp. 35–46, 2006.
- [120] A. Imiya, A. Torii, and K. Sato, "Tomography on Finite Graphs," *Electron. Notes Discret. Math.*, vol. 20, pp. 217–232, 2005.
- [121] X. Zhang *et al.*, "A Numerical Computation Forward Problem Model of Electrical Impedance Tomography Based on Generalized Finite Element Method," *IEEE Trans. Magn.*, vol. 50, no. 2, pp. 2–5, 2014.
- [122] A. Kumar Khambampati, R. Li Wang, B. Seok Kim, K. Youn Kim, Y.-G. Leea, and S. Kim, "A mesh-less method to solve electrical resistance tomography forward problem using singular boundary distributed source method," *Flow Meas. Instrum.*, pp. 1–9, 2015.
- [123] P. D. Ledger, "hp-Finite element discretisation of the electrical impedance tomography problem," *Comput. Methods Appl. Mech. Eng.*, vol. 225–228, pp. 154–176, 2012.
- [124] J. Li and Y. Yuan, "Numerical simulation and analysis of generalized difference method on triangular networks for electrical impedance tomography," *Appl. Math. Model.*, vol. 33, no. 5, pp. 2175–2186, 2009.
- [125] M. Chan Kim, K. Youn Kim, K. Jin Lee, Y. Joo Ko, and S. Kim, "Electrical impedance imaging of phase boundary in two-phase systems with adaptive mesh regeneration technique," *Int. Commun. Heat Mass Transf.*, vol. 32, no. 7, pp. 954–963, 2005.
- [126] F. Yang, J. Zhang, and R. Patterson, "Development of an Anatomically Realistic Forward Solver for Thoracic Electrical Impedance Tomography," *J. Med. Eng.*, vol. 2013, pp. 1–7, 2013.
- [127] S. V. Gavrilov and a. M. Denisov, "Iterative method for solving a three-dimensional electrical impedance tomography problem in the case of piecewise constant conductivity and one measurement on the boundary," *Comput. Math. Math. Phys.*, vol. 52, no. 8, pp. 1139–1148, 2012.
- [128] A. Nissinen, V. P. Kolehmainen, and J. P. Kaipio, "Compensation of modelling errors due to unknown domain boundary in electrical impedance tomography," *IEEE Trans. Med. Imaging*, vol. 30, no. 2, pp. 231–242, 2011.
- [129] W. He, B. Li, C. He, H. Luo, and Z. Xu, "Open Electrical Impedance Tomography: Computer Simulation and System Realization," *LSMS / ICSEE*, vol. CCIS 97, no. 97, pp. 163–170, 2010.
- [130] M. Hadinia and R. Jafari, "An element-free Galerkin forward solver for the complete-electrode model in electrical impedance tomography," *Flow Meas. Instrum.*, vol. 45, pp. 68–74, 2015.
- [131] a. Nissinen, D. Sbarbaro, L. M. Heikkinen, and M. Vauhkonen, "Reduced forward models in electrical impedance tomography with probe geometry," *Inverse Probl. Sci. Eng.*, vol. 22, no. 8, pp. 1259–1284, 2014.
- [132] M. Leinonen, H. Hakula, and N. Hyvönen, "Application of stochastic Galerkin FEM to the complete electrode model of electrical impedance tomography," *J. Comput. Phys.*, vol. 269, pp. 181–200, 2014.
- [133] P. Ghaderi Daneshmand and R. Jafari, "A 3D hybrid BE-FE solution to the forward problem of electrical impedance tomography," *Eng. Anal. Bound. Elem.*, vol. 37, no. 4, pp. 757–764, 2013.



- [134] J. Sun and W. Yang, "Evaluation of fringe effect of electrical resistance tomography sensor," *Meas. J. Int. Meas. Confed.*, vol. 53, pp. 145–160, 2014.
- [135] H. Hakula, N. Hyvönen, and T. Tuominen, "On the hp-adaptive solution of complete electrode model forward problems of electrical impedance tomography," *J. Comput. Appl. Math.*, vol. 236, no. 18, pp. 4645–4659, 2012.
- [136] Z. Szczepanik and Z. Rucki, "Field analysis and electrical models of multi-electrode impedance sensors," *Sensors Actuators, A Phys.*, vol. 133, no. 1, pp. 13–22, 2007.
- [137] J. Liu, H. Xiong, L. Lin, and G. Li, "Evaluation of measurement and stimulation patterns in open electrical impedance tomography with scanning electrode," *Med. Biol. Eng. Comput.*, vol. 53, no. 7, pp. 589–597, 2015.
- [138] R. Yerworth and R. Bayford, "The effect of serial data collection on the accuracy of electrical impedance tomography images," *Physiol. Meas.*, vol. 34, no. 6, pp. 659–69, 2013.
- [139] W. He, P. Ran, Z. Xu, and B. Li, "3D electrical impedance tomography represented by reconstructed planes in a semispherical electrode array model," vol. 41, pp. 433–446, 2013.
- [140] A. Javaherian and M. Soleimani, "Compressed sampling for boundary measurements in three-dimensional electrical impedance tomography," *Physiol. Meas.*, vol. 34, no. 9, pp. 1133–1149, 2013.
- [141] J. Nasehi Tehrani, T. I. Oh, C. Jin, a. Thiagalingam, and a. McEwan, "Evaluation of different stimulation and measurement patterns based on internal electrode: Application in cardiac impedance tomography," *Comput. Biol. Med.*, vol. 42, no. 11, pp. 1122–1132, 2012.
- [142] Z. Cao, H. Wang, W. Yang, and Y. Yan, "A calculable sensor for electrical impedance tomography," *Sensors Actuators, A Phys.*, vol. 140, no. 2, pp. 156–161, 2007.
- [143] M. Cousineau, A. Adler, A. E. Hartinger, and S. Member, "A Resistive Mesh Phantom for Assessing the Performance of EIT Systems," vol. 57, no. 9, pp. 2257–2266, 2010.
- [144] P. O. Gaggero, A. Adler, A. D. Waldmann, Y. Mamatjan, J. Justiz, and V. M. Koch, "Automated robust test framework for electrical impedance tomography," *Physiol. Meas.*, vol. 36, no. 6, pp. 1227–1244, 2015.
- [145] L. Constantinou, I. F. Triantis, R. Bayford, and A. Demosthenous, "High-power CMOS current driver with accurate transconductance for electrical impedance tomography," *IEEE Trans. Biomed. Circuits Syst.*, vol. 8, no. 4, pp. 575–583, 2014.
- [146] B. Seok, A. Kumar, Y. Jun, K. Youn, and S. Kim, "Image reconstruction using voltage-current system in electrical impedance tomography," *Nucl. Eng. Des.*, vol. 278, pp. 134–140, 2014.
- [147] E. J. Lee *et al.*, "Design of a microscopic electrical impedance tomography system for 3D continuous non-destructive monitoring of tissue culture," *Biomed. Eng. Online*, vol. 13, no. 142, pp. 1–15, 2014.
- [148] A. S. Tucker, R. M. Fox, and R. J. Sadleir, "Biocompatible, high precision, wideband, improved howland current source with lead-lag compensation," *IEEE Trans. Biomed. Circuits Syst.*, vol. 7, no. 1, pp. 63–70, 2013.
- [149] N. Li, H. Xu, Z. Zhou, J. Xin, Z. Sun, and X. Xu, "Reconfigurable Bioimpedance Emulation System for Electrical Impedance Tomography System Validation," *IEEE Trans. Biomed. Circuits Syst.*, vol. 7, no. 4, pp. 460–468, 2013.
- [150] T. R. Qureshi, C. Chatwin, and W. Wang, "Bio-impedance Excitation System: A Comparison of Voltage Source and Current Source Designs," *APCBEE Procedia*, vol. 7, pp. 42–47, 2013.

- [151] A. Adler, B. Grychtol, P. Gaggero, J. Justiz, V. Koch, and Y. Mamatjan, "A Novel Method for Monitoring Data Quality in Electrical Impedance Tomography," *J. Phys. Conf. Ser.*, vol. 434, p. 12077, 2013.
- [152] T. K. Bera and J. Nagaraju, "Common Ground Method of Current Injection in Electrical Impedance Tomography," *ObCom 2011*, vol. Part II, no. CCIS 270, pp. 574–587, 2011.
- [153] F. Dong, C. Xu, Z. Zhang, and S. Ren, "Design of parallel electrical resistance tomography system for measuring multiphase flow," *Chinese J. Chem. Eng.*, vol. 20, no. 2, pp. 368–379, 2012.
- [154] M. Khalighi, B. V. Vahdat, M. Mortazavi, and H. Wei, "Practical Design of Low-cost Instrumentation For Industrial Electrical Impedance Tomography (EIT)," *IEEE*, 2012.
- [155] K. Georgi, "Conductivity reconstructions using real data from a new planar electrical impedance tomography device," *Inverse Probl. Sci. Eng.*, vol. 21, no. 5, pp. 801–822, 2011.
- [156] T. Sun, S. Tsuda, K.-P. Zauner, and H. Morgan, "On-chip electrical impedance tomography for imaging biological cells," *Biosens. Bioelectron.*, vol. 25, no. 5, pp. 1109–1115, 2010.
- [157] C. Qiu, B. S. Hoyle, and F. J. W. Podd, "Engineering and application of a dual-modality process tomography system," *Flow Meas. Instrum.*, vol. 18, no. 5–6, pp. 247–254, 2007.
- [158] B. G. Buss *et al.*, "Quantifying resistivity using scanning impedance imaging," *Sensors Actuators, A Phys.*, vol. 137, no. 2, pp. 338–344, 2007.
- [159] M. Soleimani, "Electrical impedance tomography system: an open access circuit design," *Biomed. Eng. Online*, vol. 5, no. 28, 2006.
- [160] H. Benjamin, S. Bhansali, S. B. Hoath, W. L. Pickens, and R. Smallwood, "A planar micro-sensor for bio-impedance measurements," *Sensors Actuators B*, vol. 111–112, pp. 430–435, 2005.
- [161] Q. Wang, H. Wang, Z. Cui, and C. Yang, "Reconstruction of electrical impedance tomography (EIT) images based on the expectation maximum (EM) method," *ISA Trans.*, vol. 51, no. 6, pp. 808–820, 2012.
- [162] M. Gehre *et al.*, "Sparsity reconstruction in electrical impedance tomography: An experimental evaluation," *J. Comput. Appl. Math.*, vol. 236, no. 8, pp. 2126–2136, 2012.
- [163] H. Gagnon, B. Grychtol, and A. Adler, "A comparison framework for temporal image reconstructions in electrical impedance tomography," *Physiol. Meas.*, vol. 36, no. 6, pp. 1093–1107, 2015.
- [164] B. S. Kim, K. Y. Kim, and S. Kim, "Image reconstruction using adaptive mesh refinement based on adaptive thresholding in electrical impedance tomography," *Nucl. Eng. Des.*, vol. 270, pp. 421–426, 2014.
- [165] C. H. Antink, R. Pikkemaat, J. Malmivuo, and S. Leonhardt, "A shape-based quality evaluation and reconstruction method for electrical impedance tomography," *Physiol. Meas.*, vol. 36, no. 6, pp. 1161–1177, 2015.
- [166] O. K. Lee, H. Kang, J. C. Ye, and M. Lim, "A non-iterative method for the electrical impedance tomography based on joint sparse recovery," *Inverse Probl.*, vol. 31, no. 7, p. 75002, 2015.
- [167] A. Javaherian, A. Movafeghi, and R. Faghihi, "Reducing negative effects of quadratic norm regularization on image reconstruction in electrical impedance tomography," *Appl. Math. Model.*, vol. 37, no. 8, pp. 5637–5652, 2013.
- [168] M. Gehre, T. Kluth, C. Sebu, and P. Maass, "Sparse 3D reconstructions in electrical impedance tomography using real data," *Inverse Probl. Sci. Eng.*, vol. 22, no. 1, pp. 1–14, 2013.



- [169] B. Jin and P. Maass, "An analysis of electrical impedance tomography with applications to Tikhonov regularization," *ESAIM Control. Optim. Calc. Var.*, vol. 18, pp. 1027–1048, 2012.
- [170] J. Wang, J. Ma, B. Han, and Q. Li, "Split Bregman iterative algorithm for sparse reconstruction of electrical impedance tomography," *Signal Processing*, vol. 92, no. 12, pp. 2952–2961, 2012.
- [171] J. Nasehi Tehrani, a. McEwan, C. Jin, and a. van Schaik, "L1 regularization method in electrical impedance tomography by using the L1-curve (Pareto frontier curve)," *Appl. Math. Model.*, vol. 36, no. 3, pp. 1095–1105, 2012.
- [172] T. Lee, M. Leok, and N. H. McClamroch, "Geometric numerical integration for complex dynamics of tethered spacecraft," *Proc. 2011 Am. Control Conf.*, no. August 2011, pp. 1885–1891, 2011.
- [173] W. R. Fan and H. X. Wang, "Maximum entropy regularization method for electrical impedance tomography combined with a normalized sensitivity map," *Flow Meas. Instrum.*, vol. 21, no. 3, pp. 277–283, 2010.
- [174] D. Flores-Tapia and S. Pistorius, "Electrical Impedance Tomography Reconstruction Using A Monotonicity Approach Based On A Prior Knowledge," *32nd Annu. Int. Conf. IEEE EMBS*, vol. 10, pp. 4996–4999, 2010.
- [175] G. Steiner and D. Watzenig, "Logarithmic parameter reconstruction in electrical tomography," *COMPEL Int. J. Comput. Math. Electr. Electron. Eng.*, vol. 28, no. 4, pp. 879–891, 2009.
- [176] E. Chung, T. Chan, and X. Tai, "Electrical impedance tomography using level set representation and total variational regularization," *J. Comput. Phys.*, vol. 205, no. 1, pp. 357–372, 2005.
- [177] E. Malone, G. Sato dos Santos, D. Holder, and S. Arridge, "A Reconstruction-Classification Method for Multifrequency Electrical Impedance Tomography," *IEEE Trans. Med. Imaging*, vol. 34, no. 7, pp. 1486–1497, 2015.
- [178] B. S. Kim, A. K. Khambampati, S. Kim, and K. Y. Kim, "Improving spatial resolution of ERT images using adaptive mesh grouping technique," *Flow Meas. Instrum.*, vol. 31, pp. 19–24, 2013.
- [179] T. de C. Martins, A. V. Fernandes, and M. de S. G. Tsuzuki, "Image Reconstruction By Electrical Impedance Tomography Using Multi-Objective Simulated Annealing," *IEEE Trans. Med. Imaging*, no. 1, pp. 185–188, 2014.
- [180] R. R. Ribeiro, A. R. S. Feitosa, R. E. de Souza, and W. P. dos Santos, "Reconstruction of Electrical Impedance Tomography Images Using Genetic Algorithms and Non-Blind Search," *IEEE Trans. Med. Imaging*, pp. 153–156, 2014.
- [181] X. Zhang, W. Wang, G. Sze, D. Barber, and C. Chatwin, "An Image Reconstruction Algorithm for 3-D Electrical Impedance Mammography," *IEEE Trans. Med. Imaging*, vol. 33, no. 12, pp. 2223–2241, 2014.
- [182] M. Gehre and B. Jin, "Expectation propagation for nonlinear inverse problems - with an application to electrical impedance tomography," *J. Comput. Phys.*, vol. 259, pp. 513–535, 2014.
- [183] K. Hoffmann and K. Knudsen, "Iterative Reconstruction Methods for Hybrid Inverse Problems in Impedance Tomography," *Sens. Imaging*, vol. 15, no. 1, p. 96, 2014.
- [184] M. A. Heravi, L. Marin, and C. Sebu, "The method of fundamental solutions for complex electrical impedance tomography," *Eng. Anal. Bound. Elem.*, vol. 46, pp. 126–139, 2014.

- [185] E. Malone, G. Sato Dos Santos, D. Holder, and S. Arridge, "Multifrequency Electrical Impedance Tomography using spectral constraints," *IEEE Trans. Med. Imaging*, vol. 33, no. c, pp. 1–12, 2013.
- [186] T. D. C. Martins and M. de S. G. Tsuzuki, "Electrical Impedance Tomography Reconstruction Through Simulated Annealing with Multi-Stage Partially Evaluated Objective Functions," *Annu. Int. Conf. IEEE EMBS*, vol. 35, pp. 6425–6428, 2013.
- [187] A. Carpio and M.-L. Rapún, "Hybrid topological derivative and gradient-based methods for electrical impedance tomography," *Inverse Probl.*, vol. 28, no. 9, p. 95010, 2012.
- [188] C.-Y. Kim, J.-M. Kang, J.-H. Kim, B.-Y. Choi, and K.-Y. Kim, "Modified newton-raphson method using a region of interest in electrical impedance tomography," *J. Korean Phys. Soc.*, vol. 61, no. 8, pp. 1199–1205, 2012.
- [189] Y. Shihong, W. Teresa, C. Lijun, and W. Huaxiang, "Clustering mechanism for electric tomography imaging," *Sci. China Inf. Sci.*, vol. 55, no. 12, pp. 2849–2864, 2012.
- [190] L. Zhang, "Image Reconstruction Algorithm for Electrical Impedance Tomography Using Updated Sensitivity Matrix," *Int. Conf. Soft Comput. Pattern Recognit.*, vol. 11, pp. 248–252, 2011.
- [191] M. Dolgin and P. D. Einziger, "Stable Reconstruction of Piecewise Continuous Plane Stratified Biological Tissues via Electrical Impedance Tomography," *IEEE Trans. Biomed. Circuits Syst.*, vol. 57, no. 5, pp. 1227–1233, 2010.
- [192] H. Kim and C. Boo, "Intelligent Optimization Algorithm Approach to Image Reconstruction in Electrical Impedance Tomography," *ICNC 2006, Part I, LNCS 4221*, vol. 4221, pp. 856–859, 2006.
- [193] M. Chen, G. Hu, W. He, Y. Yang, and J. Zhai, "A Reconstruction Method for Electrical Impedance Tomography Using Particle Swarm Optimization," *LSMS/ICSEE 2010, Part II, LNCS*, vol. 6329, pp. 342–350, 2010.
- [194] M. Michalikova, R. Abedt, M. Prauzek, and J. Koziorek, "Image Reconstruction in Electrical Impedance Tomography Using Neural Network," *Int. Biomed. Eng. Conf.*, vol. 7, pp. 39–42, 2014.
- [195] C. Boo, H. Kim, M. Kang, and K. Y. Lee, "Stochastic Optimization Approaches to Image Reconstruction in Electrical Impedance Tomography," *ICCSA 2010, Part II, LNCS*, vol. 6017, pp. 99–109, 2010.
- [196] B. S. Kim and K. Y. Kim, "Estimation of conductivity distribution based on fast inversion using eigenvalue and eigenvector in electrical impedance tomography," *Flow Meas. Instrum.*, pp. 1–8, 2015.
- [197] a Fouchard, S. Bonnet, L. Hervé, and O. David, "Inversion without Explicit Jacobian Calculations in Electrical Impedance Tomography," *J. Phys. Conf. Ser.*, vol. 542, p. 12002, 2014.
- [198] Q. Wang, H. Wang, Z. Cui, Y. Xu, and C. Yang, "Fast reconstruction of electrical resistance tomography (ERT) images based on the projected CG method," *Flow Meas. Instrum.*, vol. 27, pp. 37–46, 2012.
- [199] T. D. C. Martins and M. D. S. G. T. Sales, "Electrical Impedance Tomography Reconstruction Through Simulated Annealing with Total Least Square Error as Objective Function," *Int. Conf. IEEE EMBS*, vol. 34, pp. 1518–1521, 2012.
- [200] A. Voutilainen, A. Lipponen, T. Savolainen, A. Lehtikoinen, M. Vauhkonen, and J. P. Kaipio, "Fast Adaptive 3-D Nonstationary Electrical Impedance Tomography Based on Reduced-Order Modeling," *IEEE Trans. Instrum. Meas.*, vol. 61, no. 10, pp. 2665–2681, 2012.
- [201] Q. Wang, H. Wang, and Y. Yan, "Fast reconstruction of computerized tomography images based on the cross-entropy method," *Flow Meas. Instrum.*, vol. 22, no. 4, pp. 295–302, 2011.

- [202] L. A. M. Mello, E. de Sturler, G. H. Paulino, and E. C. N. Silva, "Recycling Krylov subspaces for efficient large-scale electrical impedance tomography," *Comput. Methods Appl. Mech. Eng.*, vol. 199, no. 49–52, pp. 3101–3110, 2010.
- [203] P. Wang, L. Xie, and Y. Sun, "Electrical Impedance Tomography Based on BP Neural Network and Improved PSO," *Proc. Eighth Int. Conf. Mach. Learn. Cybern.*, no. July, pp. 12–15, 2009.
- [204] P. Wang, "The Implementation of FEM and RBF Neural Network in EIT," *Int. Conf. Intell. Networks Intell. Syst.*, vol. 2, no. 3, 2009.
- [205] P. Wang, L. Xie, and Y. Sun, "Application of PSO Algorithm and RBF Neural Network in Electrical Impedance Tomography," *Int. Conf. Electron. Meas. Instruments*, vol. 9, no. 3, pp. 517–521, 2009.
- [206] N. S. Mera, L. Elliott, and D. B. Ingham, "The use of neural network approximation models to speed up the optimisation process in electrical impedance tomography," *Comput. Methods Appl. Mech. Eng.*, vol. 197, no. 1–4, pp. 103–114, 2007.
- [207] M. Stasiak, J. Sikora, S. F. Filipowicz, and K. Nita, "Principal component analysis and artificial neural network approach to electrical impedance tomography problems approximated by multi-region boundary element method," *Eng. Anal. Bound. Elem.*, vol. 31, no. 8, pp. 713–720, 2007.
- [208] H. Kim, C. Boo, and M. Kang, "Image Reconstruction Using Genetic Algorithm in Electrical Impedance Tomography," *ICONIP 2006, Part III, LNCS*, vol. 4234, pp. 938–945, 2006.
- [209] Y. Wu *et al.*, "Tissue Conductivity Estimation in Two-Dimension Head Model Based on Support Vector Machine," *IEEE EMBS Annu. Int. Conf.*, vol. 28, pp. 1130–1133, 2006.
- [210] T. D. C. Martins, E. D. L. B. De Camargo, R. G. Lima, M. B. P. Amato, and M. D. S. G. Tsuzuki, "Image reconstruction using interval simulated annealing in electrical impedance tomography," *IEEE Trans. Biomed. Eng.*, vol. 59, no. 7, pp. 1861–1870, 2012.
- [211] D. Gürsoy, Y. Mamatjan, A. Adler, and H. Scharfetter, "Enhancing impedance imaging through multimodal tomography," *IEEE Trans. Biomed. Eng.*, vol. 58, no. 11, pp. 3215–3224, 2011.
- [212] B. Harrach, E. Lee, and M. Ullrich, "Combining frequency-difference and ultrasound modulated electrical impedance tomography," *Inverse Probl.*, vol. 31, no. 9, p. 95003, 2015.
- [213] M. Soleimani, "Electrical impedance tomography imaging using a priori ultrasound data," *Biomed. Eng. Online*, vol. 5, p. 8, 2006.
- [214] J. Sikora, T. Grzywacz, and S. Wojtowicz, "Object shape virtualization in impedance tomography," *Int. J. Comput. Math. Electr. Electron. Eng.*, vol. 28, no. 1, pp. 221–230, 2009.
- [215] P. Kantartzis, M. Abdi, and P. Liatsis, "Stimulation and measurement patterns versus prior information for fast 3D EIT: A breast screening case study," *Signal Processing*, vol. 93, no. 10, pp. 2838–2850, 2013.
- [216] D. Holder, "Other clinical applications of electrical impedance tomography," in *Electrical Impedance Tomography - Method, History and Applications*, D. S. Holder, Ed. Bristol: Institute of Physics Publishing, 2005.
- [217] Y. Abdul Wahab *et al.*, "Non-invasive process tomography in chemical mixtures – A review," *Sensors Actuators B Chem.*, vol. 210, pp. 602–617, 2015.
- [218] P. Tervasmäki, J. Tiihonen, and H. Ojamo, "Comparison of solids suspension criteria based on electrical impedance tomography and visual measurements," *Chem. Eng. Sci.*, vol. 116, pp. 128–135, 2014.

- [219] S. Hosseini, D. Patel, F. Ein-Mozaffari, and M. Mehrvar, "Study of solid-liquid mixing in agitated tanks through computational fluid dynamics modeling," *Ind. Eng. Chem. Res.*, vol. 49, no. 9, pp. 4426–4435, 2010.
- [220] D. R. Stephenson, M. Cooke, A. Kowalski, and T. A. York, "Determining jet mixing characteristics using electrical resistance tomography," *Flow Meas. Instrum.*, vol. 18, no. 5–6, pp. 204–210, 2007.
- [221] A. Seppänen, L. Heikkinen, T. Savolainen, A. Voutilainen, E. Somersalo, and J. P. Kaipio, "An experimental evaluation of state estimation with fluid dynamical models in process tomography," *Chem. Eng. J.*, vol. 127, no. 1–3, pp. 23–30, 2007.
- [222] A. R. Ruuskanen, A. Seppänen, S. Duncan, E. Somersalo, and J. P. Kaipio, "Using process tomography as a sensor for optimal control," *Appl. Numer. Math.*, vol. 56, no. 1, pp. 37–54, 2006.
- [223] D. Liu, A. K. Khambampati, S. Kim, and K. Y. Kim, "Multi-phase flow monitoring with electrical impedance tomography using level set based method," *Nucl. Eng. Des.*, vol. 289, pp. 108–116, 2015.
- [224] A. Nissinen, A. Lehtikainen, M. Mononen, S. Lähteenmäki, and M. Vauhkonen, "Estimation of the bubble size and bubble loading in a flotation froth using electrical resistance tomography," *Miner. Eng.*, vol. 69, pp. 1–12, 2014.
- [225] J. Kummerow and S. Raab, "Temperature Dependence of Electrical Resistivity – Part II: A New Experimental Set-up to Study Fluid-saturated Rocks," *Energy Procedia*, vol. 76, pp. 247–255, 2015.
- [226] G. Bouchette, P. Church, J. E. Mcfee, and A. Adler, "Imaging of Compact Objects Buried in Underwater Sediments Using Electrical Impedance Tomography," *IEEE Trans. Geosci. Remote Sens.*, vol. 52, no. 2, pp. 1407–1417, 2014.
- [227] J. a. Gutiérrez Gnechi, a. G.-T. Chávez, G. M. Chávez Campos, V. H. O. Peregrino, and E. Marroquin Pineda, "Soil water infiltration measurements using electrical impedance tomography," *Chem. Eng. J.*, vol. 191, pp. 13–21, 2012.
- [228] G. J. Gallo and E. T. Thostenson, "Spatial damage detection in electrically anisotropic fiber-reinforced composites using carbon nanotube networks," *Compos. Struct.*, 2015.
- [229] D. Zhang, L. Ye, D. Wang, Y. Tang, S. Mustapha, and Y. Chen, "Assessment of transverse impact damage in GF/EP laminates of conductive nanoparticles using electrical resistivity tomography," *Compos. Part A Appl. Sci. Manuf.*, vol. 43, no. 9, pp. 1587–1598, 2012.
- [230] B. R. Loyola, V. La Saponara, K. J. Loh, T. M. Briggs, G. O'Bryan, and J. L. Skinner, "Spatial sensing using electrical impedance tomography," *IEEE Sens. J.*, vol. 13, no. 6, pp. 2357–2367, 2013.
- [231] M. Wang, N. P. Ramskill, S. Barns, G. Raynel, C. Qiu, and C. M. Rayner, "A feasible process tomography and spectroscopy measurement system to determine carbon dioxide absorption," *Flow Meas. Instrum.*, vol. 31, pp. 77–85, 2013.
- [232] S. R. Aw, R. A. Rahim, M. H. F. Rahiman, F. R. M. Yunus, and C. L. Goh, "Electrical resistance tomography: A review of the application of conducting vessel walls," *Powder Technol.*, vol. 254, pp. 256–264, 2014.
- [233] A. Y. M. Soleimani, "A pressure mapping imaging device based on electrical impedance tomography of conductive fabrics," *Sens. Rev.*, vol. 32, no. 4, pp. 310–317, 2014.
- [234] V. M. Kolodyazhny and D. O. Lisin, "Meshless Method to Solve Nonstationary Heat Conduction Problems Using Atomic Radial Basis Functions," vol. 49, no. 2, pp. 434–440, 2013.
- [235] S. K. Mishra and B. B. Upadhyay, "Basic Concepts in Convex Analysis," in *Pseudolinear Functions and Optimization*, London: Springer, 2015.

- [236] K. G. Murty, *Optimization for Decision Making - Linear and Quadratic Models*. New York: Springer, 2010.
- [237] B. Baudry, F. Fleurey, J. Jézéquel, and Y. Le Traon, "Automatic Test Case Optimization: A Bacteriologic Algorithm," *IEEE Software*, pp. 76–82, 2005.
- [238] M. J. D. Powell, "A view of algorithms for optimization without derivatives," *DAMTP*, vol. NA03, pp. 1–12, 2007.
- [239] R. Saab and O. Yilmaz, "Sparse recovery by non-convex optimization – instance optimality," (*Preprint*), no. August 2009, pp. 1–32, 2009.
- [240] M. J. D. Powell, "The BOBYQA algorithm for bound constrained optimization without derivatives," *DAMTP*, vol. NA06, 2009.
- [241] Z. Harchaoui, A. Juditsky, and A. Nemirovski, "Conditional gradient algorithms for norm-regularized smooth convex optimization," *Math. Program.*, vol. Ser. A, 2014.
- [242] Y. Nesterov, "Universal gradient methods for convex optimization," *Math. Program., Ser. A*, 2014.
- [243] B. Borchers, "An Overview Of Software For Convex Optimization," *Department of Mathematics - New Mexico Tech*, 2009.
- [244] K.-T. Fang, R. Li, and A. Sudjianto, "Metamodeling," in *Design and Modeling for Computer Experiments*, New York: Springer, 2006.
- [245] F. C. Krebs, "Fabrication and processing of polymer solar cells: A review of printing and coating techniques," *Sol. Energy Mater. Sol. Cells*, vol. 93, pp. 394–412, 2009.
- [246] M. Pudas, J. Hagberg, and S. Leppävuori, "Gravure offset printing of polymer inks for conductors," *Prog. Org. Coatings*, vol. 49, no. September 2003, pp. 324–335, 2004.
- [247] N. Phiwpha and T. Fangsuwannarak, "Surface Passivation of Point-Contacted Solar Cells by Inkjet Printing," *Integr. Ferroelectr. An Int. J.*, vol. 149, no. January 2014, pp. 102–106, 2013.
- [248] D. Y. Goswami, "Solar Energy Resources," in *Energy Conversion*, Boca Raton: Taylor & Francis, 2007, pp. 1–10.
- [249] M. R. Patel, "Solar Thermal System," in *Wind and Solar Power Systems*, 2006.